

# Ultrasonic Spot Welding of Dissimilar Metal Sheets: An Experimental, Numerical and Metallurgical Investigation

Mantra Prasad Satpathy



Department of Mechanical Engineering  
National Institute of Technology Rourkela

# Ultrasonic Spot Welding of Dissimilar Metal Sheets: An Experimental, Numerical and Metallurgical Investigation

*Dissertation submitted in partial fulfillment*

*of the requirements of the degree of*

***Doctor of Philosophy***

*in*

***Mechanical Engineering***

*by*

***Mantra Prasad Satpathy***

(Roll Number: 512ME631)

*based on research carried out*

*under the supervision of*

***Prof. Susanta Kumar Sahoo***

*and*

***Prof. Saurav Datta***



Department of Mechanical Engineering  
**National Institute of Technology Rourkela**  
April, 2017



**Prof. Susanta Kumar Sahoo**  
Professor

**Prof. Saurav Datta**  
Assistant Professor

April 04, 2017

## **Supervisors' Certificate**

This is to certify that the work presented in the dissertation entitled *Ultrasonic Spot Welding of Dissimilar Metal Sheets: An Experimental, Numerical and Metallurgical Investigation* submitted by *Mantra Prasad Satpathy*, Roll Number 512ME631, is a record of original research carried out by him under our supervision and guidance in partial fulfilment of the requirements for the degree of *Doctor of Philosophy in Mechanical Engineering*. Neither this dissertation nor any part of it has been submitted earlier for any degree or diploma to any institute or university in India or abroad.

---

Saurav Datta  
Assistant Professor

---

Susanta Kumar Sahoo  
Professor

# **Dedication**

**Dedicated to my family, friends, and teachers  
For their love, guidance and support**

*Mantra Prasad Satpathy*

# Declaration of Originality

I, *Mantra Prasad Satpathy*, Roll Number *512ME631* hereby declare that this dissertation entitled *Ultrasonic Spot Welding of Dissimilar Metal Sheets: An Experimental, Numerical and Metallurgical Investigation* presents my original work carried out as a doctoral student of NIT Rourkela and, to the best of my knowledge, contains no material previously published or written by another person, nor any material presented by me for the award of any degree or diploma of NIT Rourkela or any other institution. Any contribution made to this research by others, with whom I have worked at NIT Rourkela or elsewhere, is explicitly acknowledged in the dissertation. Works of other authors cited in this dissertation have been duly acknowledged under the sections "Reference" or "Bibliography". I have also submitted my original research records to the scrutiny committee for evaluation of my dissertation.

I am fully aware that in case of any non-compliance detected in future, the Senate of NIT Rourkela may withdraw the degree awarded to me on the basis of the present dissertation.

April 04, 2017  
NIT Rourkela

*Mantra Prasad Satpathy*

# Acknowledgment

Before I dwell on the amount of hard work, long hours and sometimes infuriating moments which have littered the last few years. I am very fortunate to come across with a great number of people whose inspiration, guidance, help, and support helped in my field of research, and they deserve special thanks. Without them, I would never have been able to finish this dissertation.

First and foremost, my deepest sense of gratitude and indebtedness to my supervisors **Prof. Susanta Kumar Sahoo** and **Dr.Saurav Datta** for their countless advises and patient encouragement. They shared with me their brilliant insight and great vision on my research. They showed me as an example how to be a good researcher but at the same time a great leader and personnel. I have been really fortunate to have these advisors who could provide me such a wonderful guidance to this long journey.

I especially owe my heartfelt thankfulness to **Prof. Susanta Kumar Sahoo** for inspiring the work that follows in this dissertation. I am honoured to have studied and worked in his laboratory for the last four years. He not only gave me the freedom to explore on my own but also guided me when my steps flattered. His patience and insightful advice helped me to conquer a number of hurdles over time. These abilities, as well as his passion for science and learning, will continue to affect my future endeavours. I remain grateful to him forever.

Besides my supervisors, I am highly obliged to **Prof. Animesh Biswas**, our Honourable Director, **Prof. Sunil Kumar Sarangi**, former Director and **Prof. Banshidhar Majhi**, Dean (Academic Affairs) of National Institute of Technology Rourkela for giving an opportunity to be a part of this institute of national importance and provided me the academic support.

I would like to express my deepest gratitude to **Prof. S.S. Mohapatra**, Head of the department, Department of Mechanical Engineering, for his moral support. He shared his vast knowledge and experience in thereseach field and provided me tremendous help to counter the tough and trying moments. I am also incredibly grateful to the members of my doctoral scrutiny committee (DSC):**Prof. K.P. Maity** (Chairman, DSC), Department of Mechanical Engineering, **Prof. S.K. Patel**, Department of Mechanical Engineering, **Prof. C.K. Biswas**, Department of Mechanical Engineering and **Prof. A. Basu**, Department of Metallurgical and Materials Engineering for their indebted help and valuable suggestions during the research work.

I extend my heartfelt thanks to the faculty and staff members of the Mechanical Engineering as well as Metallurgical and Materials Engineering for their continuous

encouragement and suggestions. Among them, I especially acknowledge **Mr S.S. Samal** and **Mr A. Khuntia**, technical staff members of the central workshop and production engineering laboratory and **Mr S. Hembram** and **Mr S. Pradhan** (Department of Metallurgical and Materials Engineering) for their help in carrying out this work.

I would like to thank **Sushanta Kumar Sahoo, Bikash Ranjan Moharana, Srikar Potnuru, V.B Shaibu, Vivekananda Kukkala, Kasinath Das Mohapatra, Irshad K.T.** and **Rudra Narayan Kandi**, who apart from becoming lab mates over the last few years, (almost) always opened their door to me when I needed someone to bounce ideas off, subdue frustrations or just have a coffee with. Meanwhile, without these researchers, many problems would have taken a longer to solve. I would give thanks to my close friends **Ashutosh Pattanaik, Swayam Bikash Mishra, Sambit Kumar Mohapatra, Manoja Kumar Mohanty, Alok Ranjan Biswal, P.T.R. Swain, Sumant Samal, Subrat Bhuyan** and **Saroj Kumar Samantray** for their support and cooperation, which is hard to express in words. The time spent with them will remain in my memory for years to come.

I am thankful for the financial support provided by **CSIR**, Govt. of India. The major part of this research work is the outcome of the sponsored project (Grant no. 22(0593)/12/EMR-II dated 2.4.2012). I am also grateful to **MHRD**, Govt. of India for the fellowship provided during my tenure of staying at National Institute of Technology Rourkela.

Parents are the living idols of the God. None of this would have been possible without the love and support from my family. I owe a lot to my parents **Mr Debesh Chandra Satpathy** and **Mrs Susama Satpathy** for their blessings and a constant source of unconditional love, concern, support, and strength all these years. A stock of loving appreciation is reserved for **Mr Ajaya Chandra Satpathy**, my uncle and friend for his extreme affection, unfathomable belief and moral support for me. Words fail to express my thanks to my younger brother **Hara Prasad Satpathy** who encouraged me through every step of my student life. Last but not the least; I thank the almighty for giving me strength during the course of research work.

April 04, 2017  
NIT Rourkela

*Mantra Prasad Satpathy*  
Roll Number: 512ME631

# Abstract

Ultrasonic metal welding (USMW) is a new and emerging concept used in the industries over the past twenty years and serving to the manufacturing sectors like aviation, medical, microelectronics, automotive and much more due to various hurdles faced by conventional fusion welding process. USMW is a clean and reliable technique in which the welding takes place with a high energy, no flux or filler metal needed, longer tool life and it takes very short time (less than one second) to weld materials in a perfect controllable environment with greater efficiency.

To acquire high vibration amplitude in USMW, there is a necessity to design a welding system that consists of components like a booster and horn. The principal purpose of these parts is to amplify the input amplitude of vibration so that the energy transferred to the welding spot should be sufficient for creating a joint. In the present study, new type of booster and horn are proposed and modelled with adequate precision not only to produce high-quality welds but also to solve a lot of issues faced while designing these types of ultrasonic tools. The modal analysis module of finite element method (FEM) is used to analyze the effects of different step lengths and fillet radius on its natural frequency of 20 kHz, ensuring that these components will be in a resonating condition with other parts of the system. It is found that there were 1.11 % and 2.52 % errors in the length calculation of both parts. Similarly, 0.61 % error is obtained for both while calculating the magnification ratio. However, such low levels of errors may be considered to be insignificant. The dynamic analysis has also been performed to find out the stress distribution in both parts under cyclic loading conditions. Due to these cyclic loading conditions, the nodal regions (hot areas) are under highly stressed, and the relevant temperature field is consequently determined. The results obtained from the simulation, and experimental results were found to be close to each other and an error of 2% was noticed. Other welding components are also fabricated such as anvil, specimen-holder and backing plate for producing a satisfactory weld. Meanwhile, the complex mechanism behind the USMW has been addressed and modelled analytically. This model can predict the forces as well as temperatures those occur during the welding process and also explains the effects of various material properties and surface conditions on the weld behaviour.

The experiments have been performed on the aluminium, copper, brass and stainless steel metal sheets with a number of different configurations, anvil designs, and surface conditions. The fundamental aspect of this study is to control the process parameters like vibration amplitude, weld pressure and weld time so that, an appreciable weld strength



can be obtained. Thus, tensile shear and T-peel failure load studies suggest that increase in vibration amplitude means the increase of scrubbing action between the faying surfaces, resulting a better bonding strength. Similarly, increase in weld pressure also increases these weld failure loads and reach a peak value at a particular pressure. But, subsequently, these failure loads decrease due to suppression of relative motion between sheets and initiation of cracks. Excessive weld time also causes cracks around the weld spot. Likewise, if the thickness of the sheets increased, weld strengths are also increased due to absorption of more amount of ultrasonic energy. Moreover, the highest weld interface temperatures and weld areas are observed at the end of weld time because of the larger plastic deformation at the mating surfaces. For all the experiments, first anvil design shows maximum failure loads due to its non-cutting width and angle of knurls. Likewise, on the increase of surface roughness, the tensile shear, and T-peel failure loads decrease. It is found that, in lubricating condition, the highest failure loads are obtained.

Furthermore, the polynomial regression, artificial neural network (ANN) and adaptive neuro-fuzzy inference system (ANFIS) methods are developed and compared for each performance measure so that the whole welding process can be accurately described by a best predictive model. A welding mechanics based numerical model has been developed which can predict the temperatures during USMW process for various surface conditions. For all the experimental investigations, the predictive results show good agreement with the experimental values. In addition to it, acoustic softening during ultrasonic welding is found to very significant for the reduction in yield strength of the weld material up to 95 %.

It is seen that the quality of welding depends on the material properties, process parameters, and thickness of the workpiece. The present investigation also explains in details the effect of process parameters on the responses through metallurgical analysis. A quality lobe of welding like “under weld”, “good weld” and “over weld” is proposed after observing the fractured samples in optical microscopy and scanning electron microscopy (SEM). Meantime, energy dispersive spectroscopy (EDS) and X- ray diffraction (XRD) analyses are also used to reveal the thickness of interatomic diffusion and IMCs along the weld interface.

***Keywords:*** *USMW; Tensile shear failure load; T-peel failure load; ANN; ANFIS; Finite element method; Microscopy.*



# Contents

Supervisors' Certificate	iii
Dedication	iv
Declaration of Originality	v
Acknowledgment	vi
Abstract	viii
List of Figures	xv
List of Tables	xxvii
Nomenclature	xxix
<b>Chapter 1 Introduction</b> .....	<b>1</b>
1.1 Introduction.....	1
1.2 Brief Description of USMW Equipment .....	3
1.2.1 Lateral drive spot welding system	3
1.2.2 Wedge-reed spot welding system	4
1.2.3 Ultrasonic vibration assisted other welding processes	5
1.3 USMW Principles.....	5
1.4 USMW Applications.....	7
1.5 Requirements of Dissimilar Metal Sheets Welding.....	8
1.6 Objectives of the Present Research.....	9
1.7 Thesis Outline .....	10
<b>Chapter 2 Literature Review</b> .....	<b>13</b>
2.1 Introduction.....	13
2.2 Ultrasonic Welding System Component Design.....	14
2.3 Bonding Mechanism in USMW .....	16
2.4 Materials and Its Geometries .....	19
2.5 Process Parameters .....	21
2.5.1 Frequency of vibration	21
2.5.2 Weld pressure	21
2.5.3 Vibrational amplitude	22
2.5.4 Weld time, energy and power	22
2.6 Effect of Process Parameters in USMW .....	23
2.7 Numerical and Acoustic Softening Analysis in USMW .....	26
2.8 Research Gaps Identified from the Literature Review .....	28
2.9 Novelty of the Present Research Objectives and Methodology .....	29
2.10 Summary .....	31
<b>Chapter 3 Numerical Analysis on Component Design and Thermo-Mechanical Analysis of USMW</b> .....	<b>33</b>
3.1 Introduction.....	33
3.2 Theoretical Design of Horn and Booster .....	34
3.3 Background Theories for Numerical Design of Booster and Horn .....	38

3.4 FEM Application Strategy .....	40
3.4.1 Modal analysis	41
3.4.2 Frequency response analysis	46
3.4.3 Horn amplitude uniformity	48
3.4.4 Fatigue analysis of components	49
3.4.5 Vibro-thermographic analysis of components	50
3.4.6 Simultaneous simulation of both components	52
3.5 Manufacturing of Various Horns and A Booster .....	53
3.6 Design of Sonotrode Tip and Anvil .....	53
3.6.1 Material selection	53
3.6.2 Equipment employed for anvil development	56
3.7 Introduction to Thermo-Mechanical Analysis of USMW .....	59
3.8 Structural Analysis .....	60
3.8.1 Shear force exerted by horn	62
3.8.2 Shear force at weld interface	64
3.8.3 Significance of forces	69
3.9 Thermal Analysis .....	70
3.9.1 Heat generation inside the welding spot	70
3.9.2 Heat generation outside the welding spot	72
3.10 Acoustic Softening Analysis .....	72
3.10.1 Preparation of material model	73
3.10.2 Acoustic softening term calculation	74
3.11 Summary .....	74
<b>Chapter 4 Experimentation and Planning for Experimental, Numerical and Metallurgical Investigations on USMW .....</b>	<b>77</b>
4.1 Introduction .....	77
4.2 Ultrasonic Metal Welding Equipment.....	77
4.3 Universal Tensile Test Machine .....	78
4.4 Weld Materials for USMW .....	79
4.4.1 Mechanical properties extraction	79
4.4.2 Yield strength variation with temperature	80
4.4.3 Weld coupon thickness	81
4.4.4 Weld coupon length	81
4.4.5 Sheet hardness	83
4.4.6 Sheet roughness	83
4.4.7 Co-efficient of friction determination	84
4.5 USMW Parameters .....	85
4.6 Performance Measures in USMW .....	86
4.7 Summary .....	87

<b>Chapter 5 Experimental and Numerical Investigations on Al-Cu Weld Coupons .....</b>	<b>89</b>
5.1 Introduction.....	89
5.2 Problem Definition .....	89
5.3 Experimentation .....	90
5.3.1 Design of experiment	90
5.3.2 Workpiece and tool material	91
5.3.3 Welding performance evaluation characteristics	93
5.4 Results and Discussion .....	94
5.4.1 0.3 mm Al-Cu and 0.45 mm Al-Cu similar thickness weld coupons	94
5.4.2 0.6Al-0.4Cu and 0.7Al-0.4Cu dissimilar thickness weld coupons	101
5.4.3 Weld quality determination for 0.7Al-0.4Cu weld coupons	108
5.4.4 Prediction of responses for 0.7Al-0.4Cu weld coupons	116
5.4.5 Impact of various anvil designs for 0.7Al-0.4Cu weld coupons	129
5.4.6 Impact of different surface conditions for 0.7Al-0.4Cu weld coupons	136
5.4.7 FE simulation of temperature based on USMW mechanics for 0.7Al-0.4Cu weld coupons	145
5.4.8 Acoustic softening effect on top part for 0.7Al-0.4Cu weld coupons	161
5.5 Summary .....	164
<b>Chapter 6 Experimental and Numerical Investigations on Al-Brass Weld Coupons.....</b>	<b>169</b>
6.1 Introduction.....	169
6.2 Problem Definition .....	169
6.3 Experimentation .....	170
6.3.1 Design of experiment	170
6.3.2 Workpiece and tool material	171
6.3.3 Welding performance evaluation characteristics	171
6.4 Results and Discussion .....	173
6.4.1 0.3Al-0.3Brass and 0.45Al-0.45Brass similar thickness weld coupons	173
6.4.2 0.6Al-0.4Brass and 0.7Al-0.4Brass dissimilar thickness weld coupons	180
6.4.3 Weld quality determination for 0.7Al-0.4Brass weld coupons	186
6.4.4 Prediction of responses for 0.7Al-0.4Brass weld coupons	192
6.4.5 Impact of various anvil designs for 0.7Al-0.4Brass weld coupons	203
6.4.6 Impact of different surface conditions for 0.7Al-0.4Brass weld coupons	204
6.4.7 FE simulation of temperature based on USMW mechanics for 0.7Al-0.4Brass weld coupons	211
6.4.8 Acoustic softening effect on top part for 0.7Al-0.4Brass weld coupons	222
6.5 Summary .....	224
<b>Chapter 7 Experimental and Numerical Investigations on Al-SS Weld Coupons.....</b>	<b>227</b>
7.1 Introduction.....	227
7.2 Problem Definition .....	227
7.3 Experimentation .....	228

7.3.1 Design of experiment	228
7.3.2 Workpiece and tool material	228
7.3.3 Welding performance evaluation characteristics	229
<b>7.4 Results and Discussion</b>	<b>231</b>
7.4.1 0.45Al-0.1SS and 0.7Al-0.2SS dissimilar thickness weld coupons	231
7.4.2 Weld quality determination for 0.7Al-0.2SS weld coupons	236
7.4.3 Prediction of responses for 0.7Al-0.2SS weld coupons	243
7.4.4 Impact of various anvil designs for 0.7Al-0.2SS weld coupons	254
7.4.5 Impact of different surface conditions for 0.7Al-0.2SS weld coupons	256
7.4.6 FE simulation of temperature based on USMW mechanics for 0.7Al-0.2SS weld coupons	262
7.4.7 Acoustic softening effect on top part for 0.7Al-0.2SS weld coupons	272
7.5 Summary	275
<b>Chapter 8 Comparison of Results for Various Weld Coupon Combinations</b>	<b>279</b>
8.1 Introduction	279
8.2 Comparison of Various Performance Characteristics	279
8.2.1 Results from tensile shear and T-peel failure loads analyses	279
8.2.2 Results from interface temperature analysis	280
8.2.3 Results from weld area analysis	282
8.2.4 Results from microhardness analysis	283
8.2.5 Results from energy dispersive X-ray spectroscopy (EDS) analysis	283
8.3 Summary	284
<b>Chapter 9 Conclusions</b>	<b>287</b>
9.1 Introduction	287
9.2 Executive Summary	287
9.3 Conclusions	290
9.4 Contributions to Knowledge Enhancement	290
9.5 Scope for Further Research	291
<b>Appendix A Drawings</b>	<b>293</b>
<b>Appendix B Equipment used</b>	<b>299</b>
<b>References</b>	<b>305</b>
<b>Dissemination</b>	<b>315</b>

# List of Figures

1.1 Classifications of sound waves according to the frequency range [1] .....	2
1.2 Schematic diagram of a USMW system showing different parts .....	2
1.3 Schematic diagram of lateral drive ultrasonic metal welding system [14].....	4
1.4 Schematic diagram of wedge-reed ultrasonic metal welding system [14] .....	4
1.5 Ultrasonic seam welder [14] .....	5
1.6 Ultrasonic torsion welder [14] .....	5
1.7 Development of microwelds during the ultrasonic welding (a) initial contact with asperities and (b-d) increase in contact area due to progression in shearing, deformation and yielding of weld zones [14] .....	6
1.8 Various applications of USMW (a) MAS type terminals, (b) multiple stranded aluminium wire to copper eyelet, (c) heavy duty copper-aluminium connection, (d) ultrasonic torsion welded bolt to conductor [20].....	7
2.1 Research issues in USMW.....	13
2.2 Percentage of literature in the relevant fields surveyed in this work .....	14
2.3 Ultrasonic metal weldability chart [75] .....	19
2.4 Weld power curve in USMW [14].....	22
2.5 Overall methodology of the current research work.....	30
3.1 (a) Tapered, axisymmetric and slender bar, (b) Changes in stress distribution after plane wave propagates through it .....	34
3.2 Classifications of mode shapes with contours (a) longitudinal mode, (b) bending mode, (c) torsional mode .....	41
3.3 Modeled booster and horn with amplitude profiling.....	43
3.4 Meshed 3D models for finite element analysis.....	43
3.5 Mesh independence test of natural frequency for different numbers of elements.....	44
3.6 Natural frequencies from modal analysis.....	45
3.7 Variation of natural frequencies with shortening of lengths from theoretical ones .....	45
3.8 Variation of natural frequencies with radius of curvatures.....	46
3.9 Harmonic analysis of the components showing amplitude distribution.....	47
3.10 Amplitude variation plot with respect to length of both parts .....	47
3.11 Von Mises stress distributions for both components .....	48
3.12 Stress variation plot with respect to length of both parts .....	48
3.13 Variation of FE simulated normalized amplitude of horn tip with horn tip length excited at 20.04 kHz .....	49
3.14 Cumulative damage calculation from fatigue analysis .....	51
3.15 Predicted temperatures from vibro-thermographic analysis .....	52

3.16 Simulated results of amplitude and stress distributions for booster with horn .....	54
3.17 Manufactured various spot welding horns and booster .....	54
3.18 Stages of cutting operation on the surface of anvil using wire EDM .....	57
3.19 Detailed schematic presentation of weld area growth with time .....	60
3.20 Detailed analysis of forces acting on individual components during the welding [18] .....	61
3.21 Stress distribution under the knurls pattern during [18] .....	61
3.22 Small element of top workpiece under the sonotrode knurl .....	62
3.23 A 3D element for representation of principal stress.....	62
3.24 Free body diagram of workpieces, horn, and anvil [18] .....	64
3.25 Free body diagram of both top and bottom workpieces [18].....	65
3.26 Free body diagram of welded part with it's forced vibrated elongated part [18].....	66
3.27 A small element of weld area subjected to both plastic deformation and friction .....	68
3.28 Small element under shear strain for heat generation.....	70
3.29 Sinusoidal ultrasonic wave .....	71
3.30 Schematic diagram of different areas .....	72
3.31 Variation in power law constants with respect to temperature for AA1100 .....	73
3.32 Contour plot of sheet with initial sheet width and deformed sheet dimension .....	74
3.33 Flow chart representing the thermo-mechanical model to quantify acoustic softening .....	76
4.1 USMW machine setup .....	78
4.2 Schematic diagram of different parts .....	78
4.3 (a) INSTRON® 1195 universal testing machine, (b) Extensometer set-up on universal testing machine .....	79
4.4 Dog bone specimens before and after tensile testing.....	80
4.5 Linear approximation of yield strength with temperature .....	81
4.6 (a) Schematic diagram showing extension length, (b) lap welded samples of different dimensions.....	82
4.7 Effect of extension length on tensile shear strength and power consumed .....	82
4.8 Surface roughness profile showing $R_a$ .....	83
4.9 Static coefficient of friction determination setup .....	84
4.10 Coefficient of friction for different materials with various surface conditions .....	85
4.11 (a) Lap-shear coupon test fixture, (b) T-peel coupon test fixture .....	86
5.1 Schematic diagram of ultrasonic weld system with thermocouples attached to the specimen .....	91
5.2 Schematic diagrams of weld coupons (a) for tensile shear test, (b) T-peel test .....	93
5.3 Welded samples .....	93



5.4 Tensile shear and T-peel failure loads of 0.3Al-0.3Cu weld coupons for different vibration amplitudes.....	96
5.5 Tensile shear and T-peel failure loads of 0.45Al-0.45Cu weld coupons for different vibration amplitudes.....	96
5.6 Weld areas of 0.3Al-0.3Cu weld coupons for different vibration amplitudes.....	97
5.7 Weld areas of 0.45Al-0.45Cu weld coupons for different vibration amplitudes.....	98
5.8 Weld interface temperatures for 0.3Al-0.3Cu weld coupons at different vibration amplitudes .....	99
5.9 Weld interface temperatures for 0.45Al-0.45Cu weld coupons at different vibration amplitudes .....	100
5.10 SEM micrographs of weld cross-sections for (a)-(c) 0.3Al-0.3Cu joints and (d)-(f) 0.45Al-0.45Cu joints .....	101
5.11 Tensile shear and T-peel failure loads of 0.6Al-0.4Cu weld coupons for different vibration amplitudes.....	103
5.12 Tensile shear and T-peel failure loads of 0.7Al-0.4Cu weld coupons for different vibration amplitudes.....	104
5.13 Weld areas of 0.6Al-0.4Cu weld coupons for different vibration amplitudes.....	105
5.14 Weld areas of 0.7Al-0.4Cu weld coupons for different vibration amplitudes.....	106
5.15 Weld interface temperatures for 0.6Al-0.4Cu weld coupons at different vibration amplitudes .....	107
5.16 Weld interface temperatures for 0.7Al-0.4Cu weld coupons at different vibration amplitudes .....	107
5.17 SEM micrographs of weld cross-sections for (a)-(c) 0.6Al-0.4Cu joints and (d)-(f) 0.7Al-0.4Cu joints .....	109
5.18 Optical microscopic images of 0.7Al-0.4Cu weld specimens with increase in weld time .....	110
5.19 Average microhardness of peaks beneath sonotrode tip for different weld times...	111
5.20 Hardness distribution along the horizontal direction for 0.7Al-0.4Cu weld samples	111
5.21 Hardness distribution along the vertical direction for 0.7Al-0.4Cu weld samples....	111
5.22 Typical SEM image of top surface of Al sheet under sonotrode tip showing peak and valley regions.....	112
5.23 Overall fractured surface SEM images of tensile shear failed samples (a) Al side and (b) Cu side; (c) magnified image of (a) showing weld spots; (d) magnified image of (b) indicating squeezed-out eutectic liquid feature; (e) and (f) magnified pictures of spot A denoted in (c) and (d); (g) and (h) higher magnification images of spot B indicated in (e) and (f).....	113
5.24 EDS analysis of fractured surfaces of good weld sample .....	114

5.25 (a) High magnification SEM image and (b) EDS line analysis of weld interface for good weld joint .....	115
5.26 XRD results showing the presence various elements on (a) Al fractured surface, (b) Cu fractured surface.....	115
5.27 Various residual plots for TS.....	119
5.28 Various residual plots for TP.....	120
5.29 Schematic illustration of multi-layer feed forward neural network.....	121
5.30 Optimal number of hidden neurons for TS and TP in ANN model .....	122
5.31 MSE variation with number of iterations for (a) TS and (b) TP.....	122
5.32 Schematic illustration of a typical ANFIS architecture .....	123
5.33 A demonstration of bell type MFs for each input parameters in USMW process ...	124
5.34 Optimal number of MFs for TS and TP in ANFIS model.....	125
5.35 Graphical representation of fuzzy reasoning procedure of ANFIS controller using MATLAB .....	125
5.36 Error profile of validation data on TS for different models.....	126
5.37 Error profile of validation data on TP for different models.....	126
5.38 Comparison of various model predicted values with experimental results for TS ..	127
5.39 Comparison of various model predicted values with experimental results for TP ..	128
5.40 Tensile shear and T-peel failure loads of 0.7Al-0.4Cu weld coupons with weld time for various anvil patterns .....	130
5.41 Weld area as a function of weld time of 0.7Al-0.4Cu weld coupons for different anvil patterns.....	131
5.42 SEM photographs of impressions on copper sheet by anvils a) for anvil 1, b) for anvil 2, (c) for anvil 3 .....	133
5.43 Temperatures measured at weld interface with time of 0.7Al-0.4Cu weld coupons for different anvil patterns.....	133
5.44 Hardness distribution along the horizontal direction for anvil 1.....	134
5.45 Hardness distribution along the vertical direction for anvil 1 .....	134
5.46 SEM images of different weld conditions a) under weld, b) good weld, c) over weld .....	136
5.47 SEM images revealing wake features for various anvils (a) anvil 1, (b) anvil 2, (c) anvil 3 .....	136
5.48 Tensile shear and T-peel failure loads of 0.7Al-0.4Cu weld coupons for different surface conditions (a) Tensile shear failure load; (b) T-peel failure load .....	138
5.49 Interface temperatures of welded specimens at various surface conditions .....	140
5.50 Microhardness distribution across the 0.7Al-0.4Cu interface for different surface conditions.....	140

5.51 Fractured surfaces of ultrasonically welded specimens in lubricating surface condition (a) Al side surface with 30X zoom; (b) Magnified image of a; (c) Cu side surface with 30X zoom; (d) Magnified image of c.....	141
5.52 Fractured surfaces of ultrasonically welded specimens in normal surface condition (a) Al side surface with 25X zoom; (b) Magnified image of a; (c) Cu side surface with 25X zoom; (d) Magnified image of c.....	142
5.53 Fractured surfaces of ultrasonically welded specimens in EP surface condition (a) Al side surface with 30X zoom; (b) Magnified image of a; (c) Cu side surface with 30X zoom; (d) Magnified image of c.....	143
5.54 Fractured surfaces of ultrasonically welded specimens in emery surface condition (a) Al side surface with 30X zoom; (b) Magnified image of a; (c) Cu side surface with 30X zoom; (d) Magnified image of c.....	143
5.55 Complete setup for shear force measurement during welding .....	144
5.56 Shear force variation of 0.7Al-0.4Cu weld coupons with weld time for different surface conditions.....	144
5.57 Schematic model used for thermo-mechanical analysis .....	146
5.58 Illustrating various mesh elements used in proposed FE model .....	146
5.59 Deformation and stress distributions of 0.7Al-0.4Cu weld coupons along normal direction (Y-axis) during delay time .....	146
5.60 Compressive stress distributions along lines parallel to normal force direction for one weld spot .....	147
5.61 Comparison of total compressive load obtained by FE analysis and lathe tool dynamometer.....	147
5.62 Distribution of peak contact stress on bottom sheet for various thickness of top part .....	148
5.63 Peak contact stress prediction on quarter section of weld samples (a) for lubricating condition; (c) for normally polished condition; (e) for electrolytically polished condition; (g) for emery polished condition; (b, d, f, h) are cross-sectional image of (a, c, e, g) showing distribution of contact stress.....	151
5.64 Normal static load variation with respect to weld time.....	152
5.65 Weld area variation vs. weld time for various surface conditions with curve fitting equations.....	152
5.66 Boundary conditions applied to thermo-mechanical model.....	155
5.67 Contour plots and isolines of temperature for lubricating surface condition .....	156
5.68 Contour plots and isolines of temperature for normally polished surface condition	158
5.69 Contour plots and isolines of temperature for electrolytic polished surface condition .....	158

5.70 Contour plots and isolines of temperature for emery polished surface condition ...	159
5.71 Predicted average weld interface temperatures for various surface conditions .....	159
5.72 Predicted average sonotrode temperatures for various surface conditions .....	159
5.73 Variation of temperature along the weld interface (X-direction) at the end of weld time for various surface conditions .....	160
5.74 Variation of temperature in sonotrode (Y-direction) at the end of weld time for various surface condition .....	160
5.75 Comparison of weld interface temperatures between experimental results and numerical results for different surface conditions .....	161
5.76 Boundary conditions of the numerical model used for acoustic softening analysis	162
5.77 Sample image used to calculate average width after welding in Image J .....	162
5.78 Comparison of $\Delta W/W_0$ between modelled and experimental results using three acoustic softening parameter ( $\beta$ ) values for various surface conditions .....	163
5.79 Comparison of reduced top part thickness values between modelled and experimentally measured results for various surface conditions .....	163
6.1 Welded samples .....	173
6.2 Tensile shear and T-peel failure loads of 0.3Al-0.3Brass weld coupons for different vibration amplitudes .....	175
6.3 Tensile shear and T-peel failure loads of 0.45Al-0.45Brass weld coupons for different vibration amplitudes .....	175
6.4 Weld areas of 0.3Al-0.3Brass weld coupons for different vibration amplitudes.....	177
6.5 Weld areas of 0.45Al-0.45Brass weld coupons for different vibration amplitudes....	177
6.6 Weld interface temperatures for 0.3Al-0.3Brass weld coupons at different vibration amplitudes .....	178
6.7 Weld interface temperatures for 0.45Al-0.45Brass weld coupons at different vibration amplitudes .....	179
6.8 SEM micrographs of weld cross-sections for (a)-(c) 0.3Al-0.3Brass joints and (d)-(f) 0.45Al-0.45Brass joints .....	180
6.9 Tensile shear and T-peel failure loads of 0.6Al-0.4Brass weld coupons for different vibration amplitudes .....	181
6.10 Tensile shear and T-peel failure loads of 0.7Al-0.4Brass weld coupons for different vibration amplitudes .....	182
6.11 Weld areas of 0.6Al-0.4Brass weld coupons for different vibration amplitudes.....	183
6.12 Weld areas of 0.7Al-0.4Cu weld coupons for different vibration amplitudes .....	183
6.13 Weld interface temperatures for 0.6Al-0.4Brass weld coupons at different vibration amplitudes .....	185

6.14 Weld interface temperatures for 0.7Al-0.4Brass weld coupons at different vibration amplitudes .....	185
6.15 SEM micrographs of weld cross-sections for (a)-(c) 0.6Al-0.4Brass joints and (d)-(f) 0.7Al-0.4Brass joints.....	186
6.16 Optical microscopic images of 0.7Al-0.4Brass weld specimens with increase in weld time .....	187
6.17 Average microhardness of peaks beneath sonotrode tip for different weld times... 188	
6.18 Hardness distribution along the horizontal direction for 0.7Al-0.4Brass weld samples .....	188
6.19 Hardness distribution along the vertical direction for 0.7Al-0.4Brass weld samples .....	188
6.20 Typical SEM image of top surface of Al sheet under sonotrode tip showing peak and valley regions.....	189
6.21 Overall fractured surface SEM images of tensile shear failed samples (a) Al side and (b) Brass side; (c) magnified image of (a) showing weld spots; (d) magnified image of (b) indicating squeezed-out eutectic liquid feature; (e) and (f) magnified pictures of spot A denoted in (c) and (d); (g) and (h) higher magnification images of spot B indicated in (e) and (f).....	190
6.22 EDS analysis of fractured surfaces of good weld sample .....	191
6.23 (a) High magnification SEM image and (b) EDS line analysis of weld interface for good weld joint.....	191
6.24 XRD results showing the presence various elements on (a) Al fractured surface, (b) Brass fractured surface.....	192
6.25 Various residual plots for TS .....	195
6.26 Various residual plots for TP .....	197
6.27 Optimal number of hidden neurons for TS and TP in ANN model .....	198
6.28 MSE variation with number of iterations for (a) TS and (b) TP .....	198
6.29 Optimal number of MFs for TS and TP in ANFIS model .....	199
6.30 Error profile of validation data on TS for different models .....	200
6.31 Error profile of validation data on TP for different models .....	200
6.32 Comparison of various model predicted values with experimental results for TS ...	200
6.33 Comparison of various model predicted values with experimental results for TP ...	201
6.34 Tensile shear and T-peel failure loads of 0.7Al-0.4Brass weld coupons with weld time for various anvil patterns .....	203
6.35 Weld area as a function of weld time of 0.7Al-0.4Brass weld coupons for different anvil patterns .....	204

6.36	Temperatures measured at weld interface with time of 0.7Al-0.4Brass weld coupons for different anvil patterns.....	205
6.37	Tensile shear and T-peel failure loads of 0.7Al-0.4Brass weld coupons for different surface conditions (a) Tensile shear failure load; (b) T-peel failure load .....	206
6.38	Interface temperatures of welded specimens at various surface conditions .....	206
6.39	Microhardness distribution across the 0.7Al-0.4Brass interface for different surface conditions.....	207
6.40	Fractured surfaces of ultrasonic welded specimens in lubricating surface condition (a) Al side surface with 30X zoom; (b) Magnified image of a; (c) Brass side surface with 30X zoom; (d) Magnified image of c.....	208
6.41	Fractured surfaces of ultrasonic welded specimens in normal surface condition (a) Al side surface with 35X zoom; (b) Magnified image of a; (c) Brass side surface with 35X zoom; (d) Magnified image of c.....	209
6.42	Fractured surfaces of ultrasonic welded specimens in EP surface condition (a) Al side surface with 30X zoom; (b) Magnified image of a; (c) Brass side surface with 30X zoom; (d) Magnified image of c.....	210
6.43	Fractured surfaces of ultrasonic welded specimens in emery surface condition (a) Al side surface with 30X zoom; (b) Magnified image of a; (c) Brass side surface with 30X zoom; (d) Magnified image of c.....	210
6.44	Shear force variation of 0.7Al-0.4Brass weld coupons with weld time for different surface conditions .....	211
6.45	Deformation contour plots on quarter section of weld samples (a) for lubricating condition; (c) for normally polished condition; (e) for electrolytic polished condition; (g) for emery polished condition; (b, d, f, h) are cross-sectional image of (a, c, e, g) showing distribution of resulting deformation.....	213
6.46	Normal static load variation with respect to weld time .....	214
6.47	Weld area variation vs. weld time for various surface conditions with curve fitting equations .....	214
6.48	Contour plots and isolines of temperature for lubricating surface condition .....	218
6.49	Contour plots and isolines of temperature for normally polished surface condition	218
6.50	Contour plots and isolines of temperature for electrolytic polished surface condition .....	219
6.51	Contour plots and isolines of temperature for emery polished surface condition ...	219
6.52	Predicted average weld interface temperatures for various surface conditions .....	220
6.53	Predicted average sonotrode temperatures for various surface conditions .....	220
6.54	Variation of temperature along the weld interface (X-direction) at the end of weld time for various surface conditions .....	221

6.55 Variation of temperature in sonotrode (Y-direction) at the end of weld time for various surface condition .....	221
6.56 Comparison of weld interface temperatures between experimental results and numerical results for different surface conditions .....	221
6.57 Sample image used to calculate average width after welding in Image J.....	222
6.58 Comparison of $\Delta W/W_0$ between modelled and experimental results using three acoustic softening parameter ( $\beta$ ) values for various surface conditions.....	223
6.59 Comparison of reduced top part thickness values between modelled and experimentally measured results for various surface conditions.....	223
7.1 Welded samples .....	229
7.2 Tensile shear and T-peel failure loads of 0.45Al-0.1SS weld coupons for different vibration amplitudes.....	232
7.3 Tensile shear and T-peel failure loads of 0.7Al-0.2SS weld coupons for different vibration amplitudes.....	233
7.4 Weld areas of 0.45Al-0.1SS weld coupons for different vibration amplitudes.....	234
7.5 Weld areas of 0.7Al-0.2SS weld coupons for different vibration amplitudes .....	234
7.6 Weld samples with positions of thermocouples for temperature measurement.....	235
7.7 Weld interface temperatures for 0.45Al-0.1SS weld coupons at different vibration amplitudes .....	235
7.8 Weld interface temperatures for 0.7Al-0.2SS weld coupons at different vibration amplitudes .....	236
7.9 SEM micrographs of weld cross-sections for (a)-(c) 0.45Al-0.1SS joints and (d)-(f) 0.7Al-0.2SS joints .....	237
7.10 Optical microscopic images of 0.7Al-0.2SS weld specimens with increase in weld time .....	238
7.11 Average microhardness of peaks beneath sonotrode tip for different weld times...	239
7.12 Hardness distribution along the horizontal direction for 0.7Al-0.2SS weld samples .....	239
7.13 Hardness distribution along the vertical direction for 0.7Al-0.2SS weld samples ...	239
7.14 Typical SEM image of top surface of Al sheet under sonotrode tip showing peak and valley regions.....	240
7.15 Overall fractured surface SEM images of tensile shear failed samples (a) Al side and (b) SS side; (c) magnified image of (a) showing weld spots; (d) magnified image of (b) indicating squeezed-out eutectic liquid feature; (e) and (f) magnified images of spot A denoted in (c) and (d); (g) and (h) higher magnification images of spot B indicated in (e) and (f).....	241
7.16 EDS analysis of fractured surfaces of good weld sample .....	242

7.17 (a) High magnification SEM image and (b) EDS line analysis of weld interface for good weld joint .....	242
7.18 XRD results showing the presence various elements on (a) Al fractured surface, (b) SS fractured surface.....	243
7.19 Various residual plots for TS.....	246
7.20 Various residual plots for TP.....	248
7.21 Optimal number of hidden neurons for TS and TP in ANN model .....	249
7.22 MSE variation with number of iterations for (a) TS and (b) TP.....	249
7.23 Optimal number of MFs for TS and TP in ANFIS model.....	250
7.24 Error profile of validation data on TS for different models.....	250
7.25 Error profile of validation data on TP for different models.....	250
7.26 Comparison of various model predicted values with experimental results for TS ..	251
7.27 Comparison of various model predicted values with experimental results for TP ..	252
7.28 Tensile shear and T-peel failure loads of 0.7Al-0.2SS weld coupons with weld time for various anvil patterns .....	254
7.29 Weld area as a function of weld time of 0.7Al-0.2SS weld coupons for different anvil patterns.....	255
7.30 Temperatures measured at weld interface with time of 0.7Al-0.2SS weld coupons for different anvil patterns.....	255
7.31 Tensile shear and T-peel failure loads of 0.7Al-0.2SS weld coupons for different surface conditions (a) Tensile shear failure load; (b) T-peel failure load .....	257
7.32 Interface temperatures of welded specimens at various surface conditions .....	257
7.33 Microhardness distribution across the 0.7Al-0.2SS interface for different surface conditions.....	258
7.34 Fractured surfaces of ultrasonic welded specimens in lubricating surface condition (a) Al side surface with 30X zoom; (b) Magnified image of a; (c) SS side surface with 30X zoom; (d) Magnified image of c .....	259
7.35 Fractured surfaces of ultrasonic welded specimens in normal surface condition (a) Al side surface with 30X zoom; (b) Magnified image of a; (c) SS side surface with 30X zoom; (d) Magnified image of c .....	260
7.36 Fractured surfaces of ultrasonic welded specimens in EP surface condition (a) Al side surface with 30X zoom; (b) Magnified image of a; (c) SS side surface with 30X zoom; (d) Magnified image of c .....	260
7.37 Fractured surfaces of ultrasonic welded specimens in emery surface condition (a) Al side surface with 30X zoom; (b) Magnified image of a; (c) SS side surface with 30X zoom; (d) Magnified image of c .....	261



7.38 Shear force variation of 0.7Al-0.2SS weld coupons with weld time for different surface conditions.....	262
7.39 Deformation contour plots on quarter section of weld samples (a) for lubricating condition; (c) for normally polished condition; (e) for electrolytic polished condition; (g) for emery polished condition; (b, d, f, h) are cross-sectional image of (a, c, e, g) showing distribution of resulting deformation .....	265
7.40 Normal static load variation with respect to weld time.....	266
7.41 Weld area variation vs. weld time for various surface conditions with curve fitting equations.....	266
7.42 Contour plots and isolines of temperature for lubricating surface condition .....	269
7.43 Contour plots and isolines of temperature for normally polished surface condition	269
7.44 Contour plots and isolines of temperature for electrolytic polished surface condition .....	270
7.45 Contour plots and isolines of temperature for emery polished surface condition....	270
7.46 Predicted average weld interface temperatures for various surface conditions .....	271
7.47 Predicted average sonotrode temperatures for various surface conditions .....	271
7.48 Variation of temperature along the weld interface (X-direction) at the end of weld time for various surface conditions.....	271
7.49 Variation of temperature in sonotrode (Y-direction) at the end of weld time for various surface condition .....	271
7.50 Comparison of weld interface temperatures between experimental results and numerical results for different surface conditions .....	272
7.51 Sample image used to calculate average width after welding in Image J.....	273
7.52 Comparison of $\Delta W/W_0$ between modelled and experimental results using three acoustic softening parameter ( $\beta$ ) values for various surface conditions.....	274
7.53 Comparison of reduced top part thickness values between modelled and experimentally measured results for various surface conditions.....	274
8.1 Comparison of tensile shear and T-peel failure loads results for different weld coupons.....	280
8.2 Comparison of microscopic photographs for different weld coupons .....	281
8.3 Comparison of interface temperature results for different weld coupons.....	282
8.4 Comparison of weld areas for different weld coupons .....	282
8.5 Comparison of microhardness results for different weld coupons .....	283
8.6 Comparison of EDS results for different weld coupons .....	284
A.1 Ultrasonic Horn Design.....	293
A.2 Ultrasonic Horn Tips .....	294
A.3 Booster Design .....	295

A.4 Anvil Designs .....	296
A.5 Backing Plate Designs .....	297
B.1 Horizontal Metal Cutting Band Saw .....	299
B.2 Computer Numerical Control (CNC) Machine.....	299
B.3 Lathe Machine .....	300
B.4 Steel Holding Device .....	300
B.5 Aluminum Backing Plate .....	300
B.6 Wire Electro-Discharge Machine (WEDM).....	301
B.7 Optical Stereo Microscope .....	301
B.8 Lathe Tool Dynamometer .....	302
B.9 Charge Amplifier .....	300
B.10 Microhardness Tester.....	302
B.11 Scanning Electron Microscope (SEM) .....	303
B.12 Multipurpose X-Ray Diffraction System (XRD) .....	303
B.13 Advanced Optical Microscope .....	304
B.14 Surface Roughness Tester.....	304

# List of Tables

3.1 Properties of horn (D2 steel) and booster (Ti-6Al-4V) materials.....	41
3.2 Results of fatigue and vibro-thermographic analyses .....	50
3.3 Comparison between theoretical and FEM results of booster with horn.....	52
3.4 Material properties of anvil .....	55
3.5 Stereoscopic pictures of anvil tool geometries with specifications (scale in mm) .....	56
3.6 Stereoscopic pictures of weld tip geometries with specifications (scale in mm) .....	58
4.1 Chemical compositions of non-ferrous materials .....	79
4.2 Chemical compositions of ferrous material .....	79
4.3 Physical, mechanical and thermal properties of weld materials .....	80
4.4 Hardness of weld materials for different thickness.....	83
4.5 Surface roughness results for various materials .....	84
5.1 Domain of experiments adopted for USMW of similar thickness Al-Cu weld coupons	92
5.2 Domain of experiments adopted for USMW of dissimilar thickness Al-Cu weld coupons.....	92
5.3 Physical, mechanical and thermal properties of specimens.....	93
5.4 Chemical compositions of specimens.....	94
5.5 $R^2$ and $R_{adj2}$ values for various regression models of TS.....	116
5.6 ANOVA for TS (before elimination of insignificant terms) .....	117
5.7 ANOVA for TS (after elimination of insignificant terms) .....	118
5.8 $R^2$ and $R_{adj2}$ values for various regression models of TP .....	118
5.9 ANOVA for TP (before elimination of insignificant terms) .....	119
5.10 ANOVA for TP (after elimination of insignificant terms) .....	120
5.11 Accuracy testing of all proposed models for prediction of TS.....	127
5.12 Accuracy testing of all proposed models for prediction of TP.....	129
5.13 Experimental domain for specimens used in different surface conditions .....	137
5.14 Overall summary of results obtained from USMW mechanics .....	157
5.15 Effect of acoustic softening parameter ( $\beta$ ) on strength coefficient( $K_S$ ).....	164
6.1 Domain of experiments adopted for USMW of similar thickness Al-Brass weld coupons.....	172
6.2 Domain of experiments adopted for USMW of dissimilar thickness Al-Brass weld coupons.....	172
6.3 Physical, mechanical and thermal properties of specimens.....	173
6.4 Chemical compositions of specimens.....	173
6.5 $R^2$ and $R_{adj2}$ values for various regression models of TS .....	193
6.6 ANOVA for TS (before elimination of insignificant terms) .....	194

6.7 ANOVA for TS (after elimination of insignificant terms).....	194
6.8 $R^2$ and $R_{adj}^2$ values for various regression models of TP .....	195
6.9 ANOVA for TP (before elimination of insignificant terms).....	196
6.10 ANOVA for TP (after elimination of insignificant terms).....	196
6.11 Accuracy testing of all proposed models for prediction of TS .....	201
6.12 Accuracy testing of all proposed models for prediction of TP .....	202
6.13 Experimental domain for specimens used in different surface conditions.....	205
6.14 Overall summary of results obtained from USMW mechanics.....	217
6.15 Effect of acoustic softening parameter ( $\beta$ ) on strength coefficient( $K_S$ ) .....	224
7.1 Domain of experiments adopted for USMW of dissimilar thickness Al-SS weld coupons .....	230
7.2 Physical, mechanical and thermal properties of specimens .....	231
7.3 Chemical compositions of specimens .....	231
7.4 $R^2$ and $R_{adj}^2$ values for various regression models of TS .....	244
7.5 ANOVA for TS (before elimination of insignificant terms).....	245
7.6 ANOVA for TS (after elimination of insignificant terms).....	245
7.7 $R^2$ and $R_{adj}^2$ values for various regression models of TP .....	246
7.8 ANOVA for TP (before elimination of insignificant terms).....	247
7.9 ANOVA for TP (after elimination of insignificant terms).....	247
7.10 Accuracy testing of all proposed models for prediction of TS .....	252
7.11 Accuracy testing of all proposed models for prediction of TP .....	253
7.12 Experimental domain for specimens used in different surface conditions.....	256
7.13 Overall summary of results obtained from USMW mechanics.....	268
7.14 Effect of acoustic softening parameter ( $\beta$ ) on strength coefficient( $K_S$ ) .....	275

# Nomenclature

## List of Symbols

$\{C_e\}$	Element damping matrix
$\{F^C\}_e$	Damping force element vector
$\{F^K\}_e$	Nodal load element vector
$\{K_e\}$	Element stiffness matrix
$\{M_e\}$	Element mass matrix
$\{u\}_e$	Real displacement vector element
$C_d$	Cumulative damage
$F_A$	Force obtained at the knurl surface of anvil
$F_C$	Constraining force
$F_E$	Excitation force for the elongated part
$F_{FR1}$	Frictional force inside the welding spot
$F_{FR2}$	Frictional force outside the welding spot
$F_I$	Inertia force
$f_{pw}$	Frequency of vibration utilised for welding
$F_{PW}$	Weld force due to plastic deformation
$F_{SH}$	Shear force exerted by horn
$K_S$	Strength coefficient
$L$	Length of horn
$L_b$	Length of booster
$N$	Static normal force
$n$	Strain hardening exponent
$P_{total}$	Total power
$Q_{FR1}$	Friction heat inside the weld zone
$Q_{FR2}$	Friction heat outside the weld zone
$Q_{pw}$	Heat of the welding due to plastic deformation
$S_{DZ}$	Area of deformation zone
$S_{FR1}$	Frictional area inside the welding spot
$S_{FR2}$	Frictional area outside the welding spot
$S_H$	Area of horn in contact with workpiece
$S_{PW}$	Weld area due to plastic deformation
$S_w$	Total weld area
$t$	Thickness of workpiece
$T_i$	Weld time in Sec
$V_{avg}$	Average vibration speed

$V_H$	Velocity of horn
$V_s$	Velocity of sound
$W_0$	Initial width of the top part
$Y(T)$	Temperature dependent yield strength
$\beta$	Acoustic softening parameter
$\Delta W$	Change in width
$\varepsilon_p$	Plastic strain
$\vartheta_D$	Deformed volume
$\vartheta_{DZ}$	Volume of deformation zone
$\lambda$	Wavelength of ultrasound waves
$\mu_{s1}$	Static coefficient of friction inside the welding zone
$\mu_{s2}$	Static coefficient of friction outside the welding zone
$\xi_h$	Amplitude of horn
$\xi_{max}$	Maximum amplitude
$\xi_T$	Vibration amplitude of top part
$\Sigma$	Direct stress
$\sigma_N$	Normal stress
$\sigma_y$	Yield stress of the material
$\Phi$	Shear deformed angle
$\tau$	Shear stress

### Abbreviations

ANFIS	Adaptive Neuro fuzzy Inference System
ANN	Artificial Neural Network
ANOVA	Analysis of Variance
CNC	Computer Numerical Control
DOE	Design of Experiment
EDS	Energy Dispersive X-ray Spectroscopy
FEA	Finite Element Analysis
FSW	Friction Stir Welding
SEM	Scanning Electron Microscope
TP	T-Peel Strength
TS	Tensile shear Strength
USMW	Ultrasonic Metal Welding
WP	Weld Pressure
WT	Weld Time
XRD	X-Ray Diffraction

# Chapter 1

## Introduction

### 1.1 Introduction

Sound waves consist of a sequence of compression and rarefaction through which acoustic energy propagate. The frequency of the sound waves is classified into three categories as represented in Fig. 1.1 [1]. The human ear can typically detect the sound frequency range from 20 Hz to 20 kHz which is called the audible range [2]. The upper and lower limits of this range are called ultrasound and infrasound range [3,4]. Nowadays, the applications of ultrasonics have received lots of attention in the manufacturing industries as well as in medical sciences. According to the rate of energy transfer, ultrasonics is divided into two categories such as low and high power ultrasonics. Generally in non-destructive testing and medical diagnostic applications, low power ultrasonics is used whose frequency more than 100 kHz with power intensity is ranging from 0.1 to 0.5 W/cm<sup>2</sup> of power intensity. Similarly, high power ultrasonics found its applications in welding, cutting, drilling operations whose frequency range varies from 20 kHz to 100 kHz with power intensity greater than 100 W/cm<sup>2</sup> [5-7]. Ultrasonic metal welding (USMW) was first demonstrated in the early 1950s when AeroProjects<sup>®</sup> (currently known as Sonobond<sup>®</sup> Corporation) [8] applied low-frequency vibration to obtain cold weld at the resistance spot weld region. But the real and full range of applications of USMW started after the 1960s. First time in 1969, some parts of a car were assembled by using USMW. Since then, this technique has been continuously employed in various sectors such as an automobile, electrical and electronics, manufacturing and aerospace industries [9].

USMW is considered to be one of the novel and innovative techniques which involve the solid state joining process. Recently, USMW draws significant attention as one of the promising methods in the area of joining of dissimilar metals such as plates, sheets, wires, etc. [10]. Moreover, this process is also best suited for joining of soft metals such as copper, aluminium, gold, and silver for various applications [11]. With the advent of advanced alloys, such as titanium and nickel-based super alloys; there is also a need for the suitable welding process. In this regard, conventional fusion welding unable to provide a good joint because it requires melting, diffusion and solidification resulting deterioration of weld quality. Recently, a study has proven that the materials which are considered to be unweldable by resistance spot welding can be achieved good strength using USMW [12].

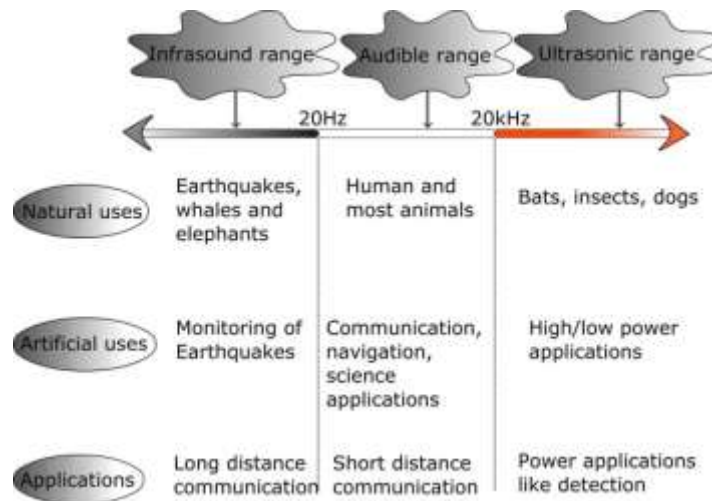


Fig. 1.1 Classifications of sound waves according to the frequency range [1]

Typically, the ultrasonic welding is divided into two categories according to their applications, and these are (i) ultrasonic metal welding, (ii) ultrasonic plastic welding. The significant difference between these two systems is that in case of ultrasonic metal welding, the vibration is parallel to the surface of weld materials and in ultrasonic plastic welding vibration is perpendicular to the surface. However, these two types of systems consist of five standard subsystems, and these are (i) ultrasonic frequency generator, (ii) piezoelectric transducer, (iii) booster, (iv) horn/sonotrode and (v) anvil/fixture. The various components of a typical ultrasonic metal welding system are presented in Fig. 1.2.

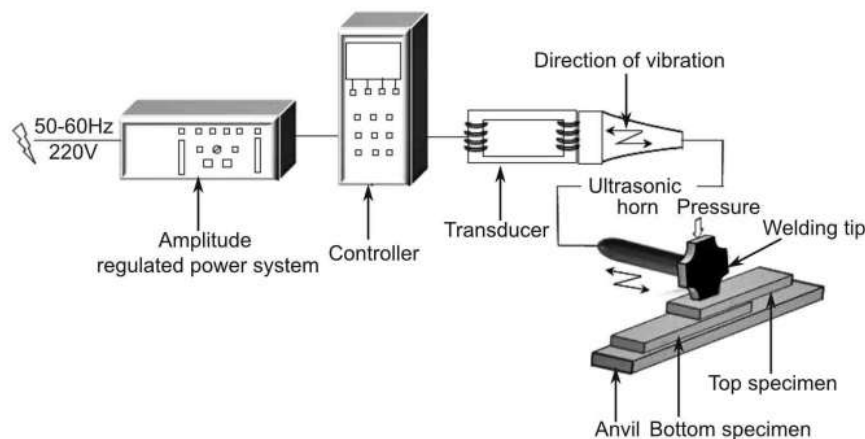


Fig. 1.2 Schematic diagram of a USMW system showing different parts

While, the ultrasonic welding has been used since 1950's, a considerable amount of literature are available regarding the ultrasonic plastic welding and its associated parameters, but there are still many unexplored areas related to ultrasonic metal welding. This is because of an incomplete understanding of mechanics behind the welding and the complicated relationship of controllable parameters to the weld strength. Hence, for a complete understanding of USMW, the design of its components and the effects of processes parameters on the joint strength are investigated for the present work.



## 1.2 Brief Description of USMW Equipment

There are several types of USMW machines used depending on the kind of weld, geometry, and varieties of metals, etc. Typically, all machines employ a transverse mode of vibration to weld metal sheets. Despite the presence of several ultrasonic welding methods like seam, ring, line and torsion, the current research work focuses only on spot welding because of its application in the automobile sector and microelectronic industries. These spot welders are categorised into two configurations namely lateral drive system and wedge reed system. However, these two types of systems have different shape and applications. But, the principle of the deformation in weld area by these vibrational mechanisms remains same [13].

### 1.2.1 Lateral drive spot welding system

This type of welding system is comprised of the ultrasonic frequency generator with a power amplifier, transducer, booster, sonotrode with weldable tips and anvil as shown in Fig. 1.3 [14]. Initially, the 50 Hz frequency of standard alternating current (AC) supply is converted to high-frequency power (15-70 kHz) with the help of ultrasonic frequency generator, and its strength is increased by the power amplifier. The piezoelectric transducer/converter is made up of lead zirconate titanate (PbZnTi) crystals/ ceramic rings. When the voltage with high frequency is applied to these rings [15], a large mechanical displacement is observed. The booster subsequently amplifies the transducer's vibration amplitude depending upon its geometries, and it also serves as mounting for the total welding stack. The horn or mechanical amplifier again increases these values up to that level where it will be sufficient for welding. Another role of the horn is to act as a tool during the welding process. As there is a direct contact between tool and workpiece during the welding, the wear and tear will happen to the horn. Thus, some sonotrodes are designed with replaceable tips. But, most of the sonotrodes are acted as a single unit in order to reduce the energy loss. Moreover, the materials for the horn and booster should be chosen in such a way that these parts can withstand high wear rate, corrosion and fatigue loads. Thus, titanium and tool steels are commonly used as booster and horn materials. In this type of welding system, the horn is placed parallel to the workpiece. Meanwhile, an anvil is used to support the fixture and to hold the bottom specimen firmly. Consequently, a sufficient relative motion between the sheets is observed without any slippage. Therefore, the ultrasonic energy transferred to the weld coupon in a transverse manner. The specimens, usually of thin metal sheets, are overlapped on each other with bottom specimen firmly attached to the anvil surface.

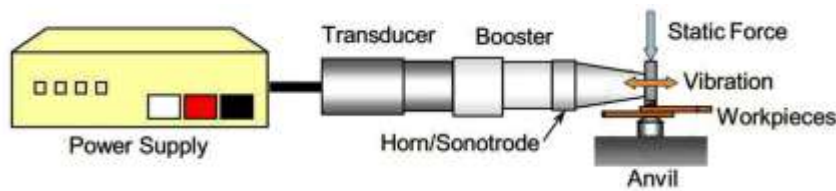


Fig. 1.3 Schematic diagram of lateral drive ultrasonic metal welding system [14]

## 1.2.2 Wedge-reed spot welding system

Like the lateral drive system, the wedge-reed system also consists of five components such as a generator, transducer, wedge, reed and anvil as shown in Fig. 1.4 [14]. In this system, the wedge has the same function as of a booster. The ultrasonic energy is transferred from the transducer to the reed through wedge. The reed vibrates in a bending mode and produces transverse vibrations at the welding tip [16]. Generally, the wedge is attached to the reed by means of welding or brazing to avoid any type of loss during the transfer of vibration energy. However, in some situation, the anvil is also vibrating and resonating out of phase to increase the relative motion between the surfaces [16]. Thus, this system is capable of producing high-quality joints between high strength alloy sheets. Meanwhile, the transducer does not receive any direct resistance from the weld spot rather than it only drives the reed. Thus, the parameters at the weld spot can't be controlled accurately.

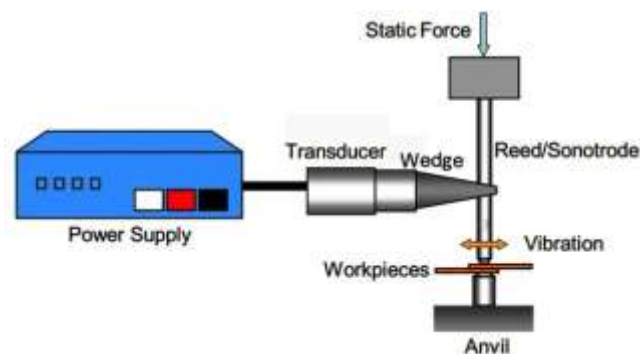


Fig. 1.4 Schematic diagram of wedge-reed ultrasonic metal welding system [14]

Generally, the nature of vibration is same for both lateral drive and wedge reed systems. However, the method in which the vibrations generated is different. In fact, when there is a necessity to weld thicker materials, the wedge reed system will be the favourite one. In the current research, the lateral drive system is used to study the influence of different controllable factors on the joint strength. Meanwhile, these factors can't be controlled in the wedge reed system as the horn is not in direct attachment with the specimen. As the present work includes the joining of thin sheets, high amplitude of vibration is needed with modest clamping force. Therefore, the lateral drive system is chosen for thorough investigation.

### 1.2.3 Ultrasonic vibration assisted other welding processes

Aside from the standard spot welding equipment, ultrasonics can be applied for wire bonding, seam welding, torsion welding and ultrasonic additive manufacturing. Wire bonding, specifically a small scale ultrasonic welding technique, used to connect microelectronic parts. The second type of weld achieved through ultrasonics is the seam weld as shown in Fig. 1.5. It has a rotating lateral drive transducer which is attached to a circular disk type horn for producing the continuous weld. In this kind of system, the anvil may move according to the turning of sonotrode. These types of welding machines find its extensive use in joining of aluminium with copper.

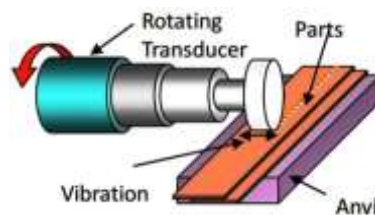


Fig. 1.5 Ultrasonic seam welder [14]

Another means of achieving good ultrasonic weld is the use of a ultrasonic torsional welder as shown in Fig. 1.6. In this type, two ultrasonic transducers are connected to the booster and tooling part produces push-pull or torsional vibration. This kind of welding system can provide a circular pattern type of weld spot on the workpiece. Hence, the nature of the weld produced is same as that of spot and seam welding.

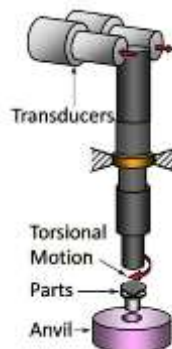


Fig. 1.6 Ultrasonic torsion welder [14]

## 1.3 USMW Principles

Primarily, the normal forces (due to the application of clamping pressure) along with shearing force (due to transverse vibration of parts) are applied to the contacting surface of both materials in a USMW process. The surfaces of the metals may have the oxide coatings as well as the contaminants like moisture and lubricants, which prevent proper metal to metal contact. Furthermore, the surfaces of the specimens have a lot of peaks

and valleys depending upon its roughness. Thus, the initial numbers of contact points depend on the surface roughness, and normal force applied to it as shown in Fig. 1.7 (a). When the ultrasonic vibration is started along with normal force, then the top workpiece moves relative to the bottom workpiece. Due to this relative motion, frictional heat develops, and it causes the plastic deformation and shearing of the interfering asperities. After dispersing the asperities, pure metal to metal contact takes place across the surfaces resulting in the formation of small weld zones (called 'microwelds') [17]. With the course of time, the vibration increases the microweld areas and finally the weld area is completely filled with the weld zones. Fig. 1.7 (d) depicts the final stage of welding.

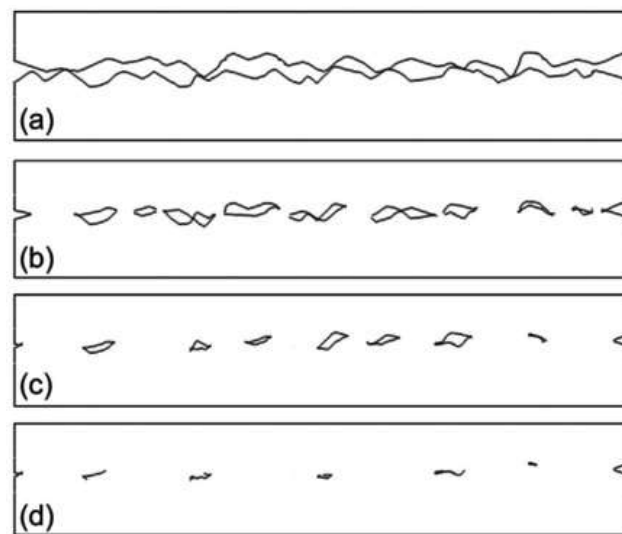


Fig. 1.7 Development of microwelds during the ultrasonic welding (a) initial contact with asperities and (b-d) increase in contact area due to progression in shearing, deformation and yielding of weld zones [14]

The nature of the bond that is developed in between the interface is a solid state type. Thus, the bond achieved is without melting and fusion of the workpieces. Nevertheless, plastic deformation in the weld zone results in the noticeable rise of temperature at varying welding condition. It is well known that the yield points of most metal are sensitive towards the increase of temperature. Hence, the growth in temperature reduces the yield strength of the material significantly and in turn, it further enhances the plastic deformation and flow of materials in the weld zone.

In USMW, the amount of plastic deformation and yielding of the top sheet depend on the process parameters as well as specimen related properties. Process parameters include vibrational amplitude, weld pressure, and weld time. Similarly, specimen parameters consist of thermal conductivity of sheet, hardness, and roughness [13,18,19]. As the USMW is a complex process, the control of process parameters is difficult. Likewise, the thickness of workpiece and weld tip size also determines the quality of the weld. If the material is thick, then high power is required along with large weld tip to transfer the ultrasonic energy efficiently to the weld zone. However, higher force may

hinder the relative motion between the sheets. Thus before finalising the parameter, a lot of trial experiments are required to establish a suitable range.

## 1.4 USMW Applications

There are widespread applications of USMW in many fields and industries such as electrical and electronics industries, automotive, aerospace, medical and consumer goods. Some of the illustrations are shown in Fig. 1.8. Fig. 1.8 (a) shows a miniature air switch (MAS) type terminal which is commonly used in the automotive sector for high current transmission. Fig. 1.8 (b) is the multiple stranded aluminium wires connected to a copper eyelet terminal. Fig. 1.8 (c) shows a heavy duty multi-stranded aluminium and copper connected each other to wire harnesses. Fig. 1.8 (d) displays the joint between a bolt and current carrying conductor using the ultrasonic torsional welder.

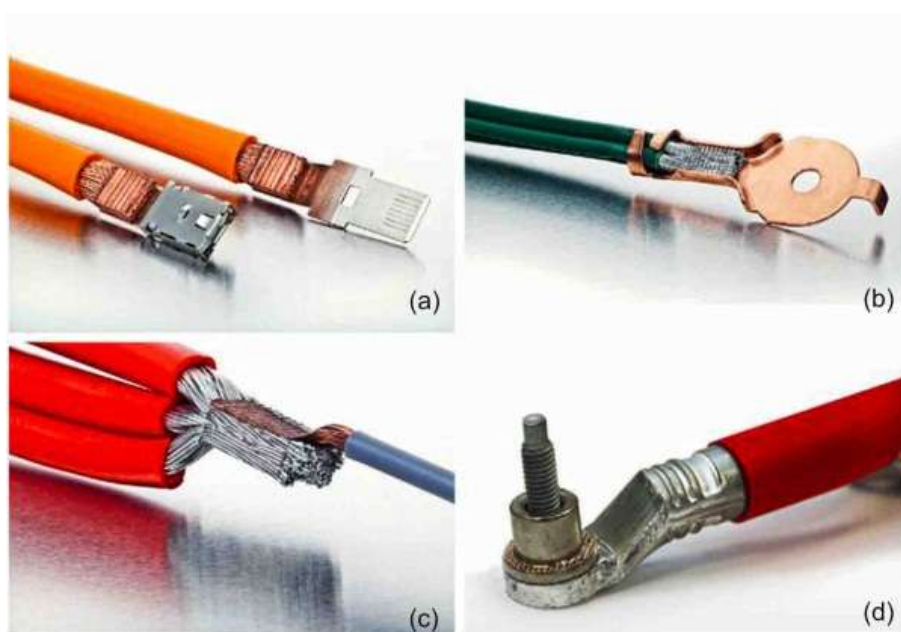


Fig. 1.8 Various applications of USMW (a) MAS type terminals, (b) multiple stranded aluminium wire to copper eyelet, (c) heavy duty copper-aluminium connection, (d) ultrasonic torsion welded bolt to conductor [20]

Likewise, bus bars, terminators, contact assemblies, sensor terminals are all the examples of connections produced by ultrasonic welding, and these are now successfully used in electronics and automotive industries. Moreover, the ultrasonic weld has been extensively used in electrical industries for joining electrical motor coils, field coils, capacitors, and transformers. In fact, the ultrasonic micro bonding is widely used in microelectronics interconnections. USMW is a versatile technique which can be applied in any condition like in water or in vacuum to produce a satisfactory weld [21]. Battery and fuel cell manufacturers also use ultrasonics to make joints between foils to thin copper, nickel or aluminium tabs. Matheny [22] described these type of joints in lithium ion

batteries found extensively in electrical and hybrid vehicles. Packaging industries are also used ultrasonic seam, torsion or spot welding system for sealing purpose. Seam welding is used to seal to cooking pouches and food foils. Similarly, torsion welding system is used to seal cylindrical container which contains reactive and hazardous materials. In addition, it was seen that the conventional welding process like resistance welding consumes 10% of more energy as that of USMW [23,24]. Recently, USMW is tried to join thin sheets of aluminium with other lightweight materials in the structural automotive and aerospace applications [25]. This process is being used to assemble secondary aircraft structures such as helicopter access doors: These doors can sustain loads 5 to 10 times the design load without weld failure in air load tests as described by American welding society [26].

## 1.5 Requirements of Dissimilar Metal Sheets Welding

Ultrasonic metal welding (USMW) is a clean, innovative and emerging solid state technique which can produce a joint between similar or dissimilar metal sheets within very few seconds. In the present research work, the various dissimilar metals have been joined based upon its applications. These importances can be summarized as below:

- The performance of battery electric vehicles (BEVs) depends solely on power and energy transmission. So, to fulfil this objective, dissimilar material joining is necessary. Aluminium (Al) and copper (Cu) materials are desired due to its higher thermal and electrical conductivity, mechanical and corrosion resistance properties. Thus, in this study, AA1100 aluminium alloy and UNS C10100 copper sheets with different thickness are selected for joining purpose.
- Similarly, the major significance of a good quality joint between dissimilar materials like aluminium and brass find its numerous applications in the electrical industries. These materials are utilized extensively in these industries because of its superb electrical and thermal properties, high strength, erosion and fatigue resistances. In the current research work, AA1100 aluminium alloy and UNS C27000 commercial brass sheets are chosen for the investigation.
- Furthermore, increasing demands for weight reductions in aerospace and automobile components have led to an expanding utilization of lightweight metals. So, to lower the weight of automobiles and airplanes, joining of dissimilar thin sheets like aluminum to steel is highly necessary. In the present research work, an attempt has been made to join AA1100 aluminium alloy and SS304 stainless steel sheets.

## 1.6 Objectives of the Present Research

The current research provides the detailed design of the horn and booster, modelling of the process, characterization and testing of specimens produced by a lateral drive ultrasonic welder. The objectives of the current research works can be summarized as below:

- In the recent years, the design issues and related analyses compel the researchers to produce the components by which a good weld can be obtained. Thus, in this study, the ultrasonic spot welding booster and horn are modelled and analysed with sufficient precision. These are designed in such a way that all the components like the transducer, booster and horn will stay in a resonating state, and transmitting the ultrasonic energy to the weld coupon with minimum dissipation.
- Like horn and booster, anvil design also plays a crucial role in getting enough strength and quality for the welded joints. A proper design of the anvil with grooved top surface provides the required friction to the workpiece during the welding time without any slippage. Therefore, various types of anvils are designed and fabricated to get a good joint for the present investigations.
- As the USMW is a complex process, a model is developed on the basis of mechanical considerations. With the support of this model, experimental observations, and numerical simulations have been added to the present study. This model is divided into two parts, namely, the structural part which contains the effects of various types of forces such as shear force, normal force, and frictional forces; and the thermal part which includes the temperature development due to plastic deformation and frictional forces at the interface.
- As stated in the previous section, the materials such as Al, Cu, Br and SS are taken into consideration based upon its applications in industries. Meantime, the ultrasonic welding of all these different combinations of metals depends on the various process parameters like weld pressure, weld time and vibrational amplitude. Thus, these are varied at different levels to get substantial tensile shear and T-peel failure loads.
- In the present research, it is shown that how the artificial intelligence techniques can be applied to get an accurate prediction model for the responses. It is necessary for the future researchers to work with these models to get their actual results.
- In addition, the qualities of the welded joints obtained from the lateral drive ultrasonic machine are characterized by various micro and/or macroscopic analyses of the interfaces. A variety of weld defects in the fractured surfaces are also spotted and analysed.

## 1.7 Thesis Outline

With the knowledge of ultrasonic welding process and its associated parameters and applications (present *Chapter 1*), the present thesis is divided into ten relevant chapters, *Chapter 2* depicts the review of previous literature focused on the dissimilar metal welding with properly designed horns. This review section is divided into several sub-sections such as designing of ultrasonic components, mechanism of solid state welding and USMW, the influence of different materials and its related geometries, effects of various process parameters, thermal and acoustic softening effects and the weld quality analysis. The design and development of the booster, horn and anvil components for the welding experiments are described in *Chapter 3*. The natural frequency of the horn and booster and its associative mode shapes have been revealed by applying the modal analysis module of ANSYS®. Many design criteria such as amplitude distribution, amplitude uniformity at the weld tips, stress distribution and amplification factor for these two components have been investigated. The numerical analysis theories related to these analyzes also have been discussed. As both components are under repeated cyclic stresses, thus fatigue analysis also has been formed. Meanwhile, the heat generation will take place due to this repeated elastic deformation of the materials, and the vibro-thermographic analysis has been carried out to reveal this. Finally, based upon these analyses results, welding components were fabricated such as horn, rigid anvil, and specimen holder and backing plate for efficient transmission of ultrasonic energy to the welding zone and for producing a satisfactory weld. The model for the welding mechanics is addressed in this chapter. The forces beneath the sonotrode which are mainly responsible for shearing and plastic deformation of the material are identified. Meanwhile, the effects of different working conditions on the quality of the joint are determined. Furthermore, it is observed that the friction between the sheets is one of the leading causes of heat generation and subsequently it leads to the plastic deformation. Along with this thermo-mechanical analysis, one other method called acoustic softening analysis is also applied for the accurate prediction of the stress field and plastic deformation and yield stress of the material.

In *Chapter 4*, description about the measuring equipment, materials selection, the process of choosing its dimensions and methods used to find out the different properties are presented. All the dimensions of weld coupons were prepared according to the machine capacity and the preliminary results obtained by varying the coupon length. Furthermore, different properties of the material such as hardness, surface roughness and coefficient of friction between the sheets are investigated as these properties can influence the weld strength and weld quality. Finally, the controllable parameters such as



frequency of vibration, weld pressure, weld time and vibrational amplitude are briefly described. Similarly, the importance of performance measures such as tensile shear strength, T-peel strength, weld area and temperature on the strength of weld and quality are also explained.

In *Chapter 5*, the welding experiments with Al-Cu specimens are extensively described and explained. It is concerned with the study of various welding conditions, i.e., specimens' roughness, anvil design and process parameters, and their effects on the joint strength and quality. Four different sheet thickness combinations of Al-Cu have been selected for the present investigation. Two combinations are comprised of a similar thickness, i.e., 0.3 and 0.45 mm and other two combinations are of the dissimilar thickness, i.e., 0.6mm Al-0.4mm Cu and 0.7mm Al-0.4mm Cu. Experiments have performed using a full factorial design with six repetitions for each test to achieve a good accuracy in results. The tensile shear strength and T-peel strength are found out to study the effects of different process parameters. Subsequently, the thickness combination of highest joint strength (0.7mm Al-0.4mm Cu) is chosen for further analysis. The temperatures developed between the interfaces of sheets and the sonotrode-top part interfaces are calculated not only by using these analytical solutions but also by numerical analysis for the refinement of the results. Furthermore, the numerical simulations have been done on this selected combination of materials to know the effect of acoustic softening. Artificial intelligence technique is also applied to model the whole process. Finally, the interface weld quality of this combination is explained through microhardness study, scanning electron microscope (SEM) with energy dispersive spectroscopy (EDS) investigation and X-ray diffraction (XRD) analysis.

*Chapter 6 and 7* are also revealed the similar analysis as of chapter 6 but for different metal combinations. In *Chapter 7*, Al-Brass is used, and *Chapter 8* includes Al-SS combination.

*Chapter 8* describes the overall comparison of results which are obtained from previous chapters.

Finally, the overall conclusions of the experimental observations and the contributions of the present dissertation drawn during this study are documented in *Chapter 9*. The supplementary data are given in *Appendix*.



## Chapter 2

# Literature Review

## 2.1 Introduction

Ultrasonic welding has been used in the fabrication shop floor over the past twenty years and serving to the manufacturing industries like aviation, medical, microelectronics and much more due to various hurdles faced by the conventional fusion welding processes. It takes very short time (around one second) to weld materials. Thus, it can be used for mass production. But, many times, the welder faced various problems leading to poor weld quality and strength of the joints. In fact, the quality and success of the welding depend on several factors like designing of ultrasonic welding components, a proper understanding of welding mechanics, selection of materials, and control of process parameters. Therefore, the current chapter focuses on the various problems and developments associated with the ultrasonic metal welding (USMW) process. The USMW concept was first introduced in the early 1950s, but its relevant literature came into limelight after 1969. Here, the literature pertaining to available full-text journals/articles are described.

All the reviews will be divided into seven sections those are dealing with various issues associated with USMW as shown in Fig. 2.1. Fig. 2.2 illustrates a clear exploded image describing the percentage of work that has already been done in the corresponding areas (as per the total literature reviewed).

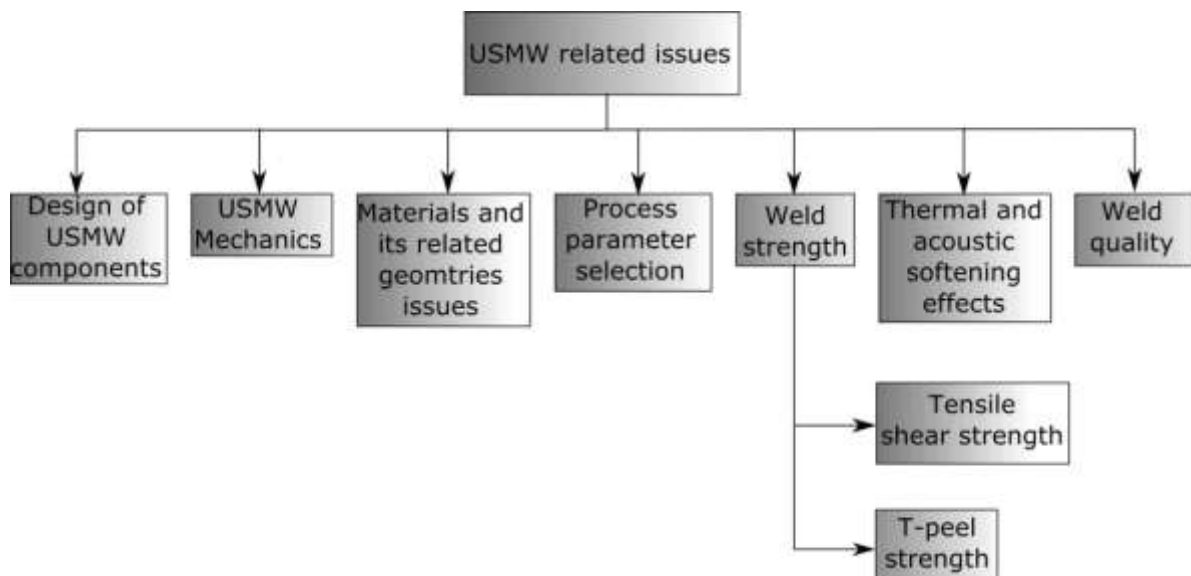


Fig. 2.1 Research issues in USMW

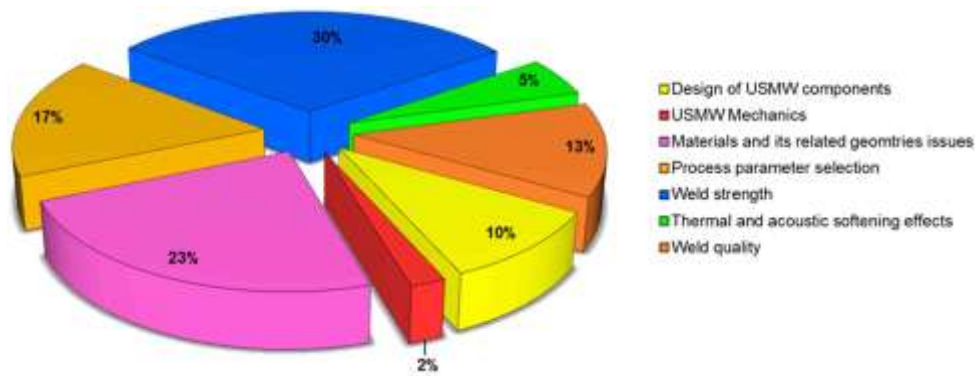


Fig. 2.2 Percentage of literature in the relevant fields surveyed in this work

## 2.2 Ultrasonic Welding System Component Design

The discovery of piezoelectric crystals resulted in a successful implementation in ultrasonics field for various applications. In the subsequent years, the intensity of the acoustic power has been increased to produce high-power acoustics, and it was achieved through the development of components [27,28]. One of the important parts of the ultrasonic welding system is the acoustic horn. It serves mainly two functions such as, to magnify the amplitude of mechanical vibration required for welding and also acts as a tool which is directly in contact with the workpiece. The common principle applied to the horn is that the ultrasound waves are transmitted through it and applied to the welding surface. Thus, the oxide layers or other contaminants on the faying surface are dispersed due to high-frequency vibration and proper metal to metal contact takes place. By that time, the metals get heated due to interatomic vibration and interfacial friction, which promotes the deformation of material. Many researchers are focused on various advantages of USMW and performed numerous experiments to validate their views. Merkulov [29] derived the equations for the horn to compute its resonant length and amplitude gain. The analysis was carried out by taking a non-uniform bar which was excited in a longitudinal vibration mode. This study also demonstrated some of the horn shapes like conical, exponential and catenoidal. But out all of these, catenoidal horn showed the largest amplitude gain. With the support of this study, Nad [30] conducted his ultrasonic machining experiment using different horns like the cylindrical, tapered and exponential type. The modal and harmonic analysis of the horns were done by using finite element analysis. He also showed the effect of different sonotrode shapes on natural frequency, amplification factor, and slenderness ratio. Likewise, Sherrit et al. [31] described a new type of horn design which is superior to other regular horn designs. Generally, resonance frequency depends on the length of the horn and amplitude depends on the different cross-sectional area. For manufacturing of the various horns, it requires reducing its size from larger diameter to

small horn tip diameter, which may be time-consuming. So they suggested a novel horn design by reducing the length of the resonator. Amin et al. [32] did their investigation on various models of the horn, which can affect ultrasonic cutting. They showed different design concept of horns by computer added design procedure and used finite element analysis to validate it. Longitudinal and torsional mode shapes for the ultrasonic exponential horn were given by Lin [33]. When plane wave propagation equation for the exponential horn was analysed with a proper decay constant of the area, then a condition was obtained, in which both mode shapes resonate. This analytical calculation was validated by conducting experiments. Conical, stepped, exponential, gaussian and catenoidal horns are the mostly used horn in many industries. Among all of them, stepped horn has the largest amplification ratio. But the amplification factor for catenoidal horns is higher than conical, exponential and gaussian type. This analysis was also supported by Amza and Drimer [34]. They revealed the effect of mass of various concentrators/horns such as conical, exponential and catenoidal on their longitudinal mode of vibrations. Satyanarayana et al. [35] also performed ultrasonic machining experiments using various types of horn profiles such as exponential, conical and stepped type to know the resonant length, stress and amplification ratio. But, they found the exponential horn has the highest amplification value than other horn profiles. Ensminger [36] also investigated particle velocity, stress, mechanical impedance, and length of a steel conical horn. He designed the horn based on the assumptions that its length was the half-wave length, and operating frequency was 20 kHz. Thus, an amplification of 4.61 was gained. The design and finite element modeling of a stepped horn used for ultrasonic aided electro-discharge machining were proposed by Nanu et al. [37]. In their study, the resonant length of a horn was found out by adjusting the length of the horn and the effect of the radius of curvature on the natural frequency of the horn also revealed. It was found that on increase of radius of curvature and decrease of length, the natural frequency of horn increases. Thus, the correct design is utmost needed in order to get a defect free and good quality joint. Belford [38] performed mathematical analysis with the horn dimensions and showed that the maximum gain could be achieved in case of stepped horn compared to exponential or catenoidal horns. Shu et al. [39] revealed that not only the ultrasonic horns could be used for cutting, drilling or welding operation but also it could be used for embedding and encapsulating metals into joined specimens. The results from this study indicated that the natural frequencies of the designed horns were closer to the ultrasonic generator frequencies and the vibration amplitude of the designed horns also demonstrated a superior performance than the commercially available horns.

Finite element analysis plays a vital role in the analysis of horns. It optimizes the time as well as dimensions for the manufacturing of components through simulation. Woo et

al. [40] conducted a theoretical study on acoustic horns applying high power acoustic power and used FEA to find out the stress and displacement distribution in horns in loading conditions. Adachi et al. [41] reported the modal vibration analysis of the rectangular horns and it was achieved by setting the length of the horn to the half of the wavelength with a longitudinal vibration of 20 kHz. They attempted to get uniform amplitude with reduced Poisson's ratio at the weld tip surface by adding number of slits. The study concluded that frequency of longitudinal mode depends on slit width and thickness of bridge. Similarly, to analyze the performance of the horn, Gourley and Rushton [42] used FEA. They also described the horn characteristics and performance of ultrasonic stack by applying finite element analysis. Roopa Rani and Rudramoorthy [43] investigated various horn profiles numerically for welding of thermoplastic components. They found the stepped horn utilized 75% of energy as compared to 85% for the Bezier horn, and this horn produced more interface temperature than the stepped one. It also observed that Bezier profiled horn developed less stress as compared to the stepped horn due to its smooth curvature at the nodal position. Thus, it can be useful for welding of thicker high-density polyethylene (HDPE) specimens. Another study of high power ultrasonic applications in welding and cutting of thermoplastics was reported by Silva [44]. The numerical analysis was applied to predict the vibration amplitude of wide blade horn, and it was observed that the vibration amplitude was non-uniform along the horn surface. Other numerical studies [45,46] focused on different horn profiles like Bezier and non-traditional B-spline curve with an open uniform knot vector (OUNBS). These improved type of horns had high displacement amplification than the catenoidal horn and lower stress concentration than the stepped horn. Therefore, these studies explored the resonant frequencies, and amplitude magnifications of the horn which dependent upon its shape, length, material, and density.

## 2.3 Bonding Mechanism in USMW

USMW is one of the solid state welding techniques where sonotrode is pressed on the weld specimens, and then the ultrasonic vibration is applied. The part beneath the sonotrode starts to vibrate with the sonotrode motion, resulting a relative movement between the interfaces of sheets [47]. At the beginning stage of the welding, the relative motion is worked as cleaning agent for the intimate surfaces and plastically deforms the asperities present on it [48,49]. Other possible reasons for creating this forming area could be work hardening, generation of heat by friction, diffusion and recrystallization of grains with the increase of time, subsequently these weld areas spread out throughout the weld surface [50,51]. Meantime, microwelds are observed between the adjacent surfaces

where the pure metal to metal contact takes place [52]. Many studies demonstrated the mechanism of joint formation in USMW by observing the morphology of the weld zone related to the friction or diffusion bonding [53]. These studies revealed the microweld areas in which friction exceeds the flow stress level of the material, and thus plastic deformation occurred [54]. Finally, the weld area is completed when the power received by the deformation zone is sufficient. From these studies, it is confirmed that friction plays a key role in USMW.

If the friction between the interfaces is higher than the friction between the sonotrode and top part or between the bottom part and anvil, then the relative motion hinders and the specimens either slides over anvil or the sonotrode loses control over it. Finally, it results in welding of parts either to the sonotrode or anvil tip known as “tip sticking” [55]. Thus, it is desirable to design the sonotrode tip in such a way that there should not be any relative motion between the sonotrode and the part.

Harthron [56] attempted to weld aluminium sheets with the high and low ultrasonic frequency vibrations (20 kHz) and subsonic (30 Hz) vibrations. It was observed that the diffusion and recrystallization did not take place at low frequency as the temperature did not exceed the room temperature. Komiyama et al. [57] performed experiments with pure aluminium using various weld edge textures like trapezoidal or serrated patterns. They found the relative motion in case of serrated patterns was larger than that of trapezoidal edge. Also, the penetration of the serrated patterns is lower than that of trapezoidal patterns. A rise in temperature and severe plastic flow observed for the serrated edge. Again, Sasaki and Hosokawa [58] conducted experiments using aluminium sheets to examine the effect of transitional parameters on the weld microstructure. It has been found that the microstructures around the weld zone were severely deformed due to the temperature rise between sonotrode edge and upper specimen. Thus, the microstructures around the weld tip were severely deformed as the knurls were penetrated into the top sheet. Meantime, there was a stirring phenomenon observed at the weld interface with the increase of weld time and it was due to the plastic deformation. Jahn et al. [59] checked the effects of anvil cap geometry on weld strength and microstructure. It was noticed that wakes and wavy like features at the plastically deformed weld interface influence the solidness of the joints. Meantime, Watanabe et al. [60] also employed two types of weld tips for joining of the A6061 aluminium alloy. The cylindrical weld tip without the knurl pattern showed a good strength than the flat tip with knurl pattern. Because, when the knurl patterns engaged into the top surface then with the advent of time, the indentation size gradually increased with deteriorated strength. Lum et al. [61] presented a model which explained the relationship between the interface microstructure and “weld footprint” formed on the weld zone by the tool edge.

Hetmann and Koehler [62], Hiraishi and Watanabe [63] and Watanabe et al. [64] investigated the effects, thermal conductivity and roughness on the bond strength of Al-Mg alloy, Al-Cu and Al-SUS304 materials. They found the high thermal conductivity combinations materials like Al-Cu showed little bond strength than the low thermal conductivity combinations like Al-SUS304. Bakavos and Prangnell [65] used Al 6111 alloy sheet for the investigation of joining mechanism and microstructure evaluation. They found that under high power ultrasonic wave, good mechanical properties with better shear failure load could be obtained. Similarly, Shakil et al. [66] performed experiments by taking aluminium alloy and stainless steel to assess the effects of clamping pressure and ultrasonic energy on mechanical properties and weld bond quality. Kong et al. [67] proposed a quantitative approach for the representation of weld quality. They suggested the “linear weld density” by dividing the portion of a bonded line to the entire weld. Based on these results, Yang et al. [68] developed an energy analytical model using ultrasonic consolidation technique to find out metal foil deposition on the substrate and also studied the effects of different input factors. As USMW is a cold working process, it could be suitably applied to weld aluminium and steel [69,70]. Furthermore, this process goes through no melting state thus, the generation of brittle IMCs, coarsening of grain, residual stress at heat affected zone and flaws can be prevented. Recently, with the development of high power ultrasonic instruments, many research works are reported on joining of thicker dissimilar materials [65,71]. Haddadi [23] demonstrated that the formation of intermetallic compounds like  $FeAl_3$  and  $Fe_2Al_5$  at the weld interface of aluminium and steel were the primary causes for the reduction in lap shear strength with increase in weld time. In another work, Gunduz et al. [72] tried to weld aluminium with zinc by USMW, and observed that a large amount of intermetallic diffusion and depression in melting point happened due to the presence of high concentration of vacancies during the operation. Zhao et al. [73] reported the formation of  $Al_4Cu_9$  intermetallic layer which is main cause of joint failure. They also uncovered that at lower values of input welding parameters, the joints are partially bonded with dispersed microbonds. But when the weld energy value gradually increased, a swirl like feature was obtained and it led to the mechanical interlocking between the sheets. Meantime, cavity defects and IMCs were also observed at excessively high ultrasonic energies.

The previous studies conclude that the high power ultrasonics can be used as a promising energy efficient solid state welding technique. Furthermore, the quality of the weld depends on friction, interatomic diffusion, and recrystallization at the interface. A number of studies reported that the degree of weld quality depends on nature of the welding surface. If grease or any types of contaminants present on the surface, then it results in low weld strength as a lot of ultrasonic power is required to disperse these



contaminants within a short period of time. In recent time, scanning electron microscopy (SEM) and X-ray diffraction (XRD) analysis have been considered to be extremely useful methods to investigate the quality of the welds by observing the plastically deformed interface.

## 2.4 Materials and Its Geometries

Ultrasonic spot welding allows the joining of similar and dissimilar materials of thinner dimensions. This process may include the dissimilar thickness as well as multiple layer sheets [74]. In this regard, the material properties play a vital role. With this background information and mechanism of the ultrasonic welding, it is necessary to investigate the materials which are amenable to USMW. Thus, “weldability” term came into the picture, and it was first introduced by American Welding Society (AWS). According to AWS, weldability is defined as the ease with which the materials may be joined to meet the service conditions. Over the years, a lot of materials have been considered for their ultrasonic weldability. It primarily depends on the material hardness and crystal structure. Typically, ultrasonic weldability of the material decreases with the increase of hardness. We know that the crystal structure divides the metals into three categories, i.e., face centred cubic (FCC), body centred cubic (BCC) and hexagonal close-packed (HCP). Metals like Al, Cu, Au, Ag and Pt with FCC structure are the most weldable materials. Metals such as Mg, Ti and Zn with HCP structure have the limited weldability. Similarly, metal with BCC structure like Fe, Cr, Mo and W have the weldability lies in between FCC and HCP materials.

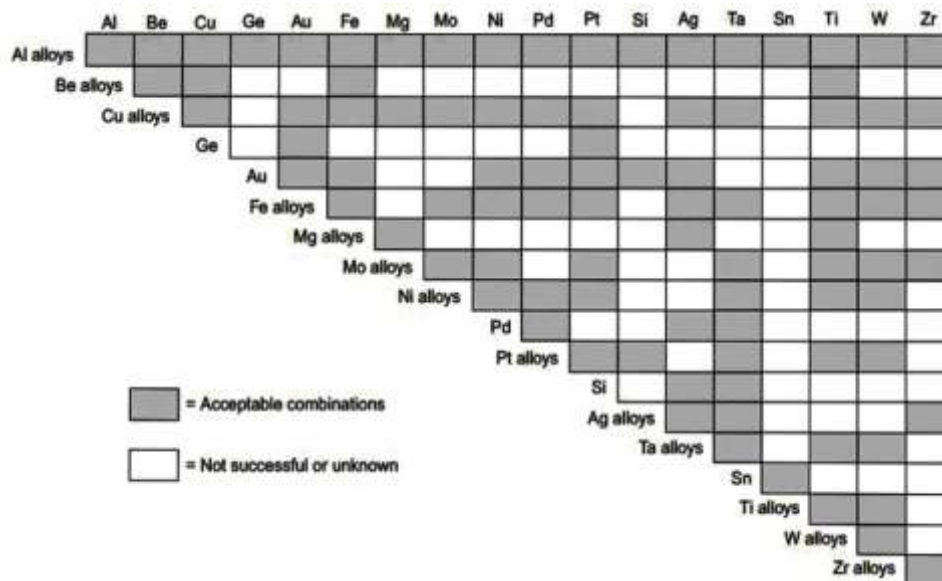


Fig. 2.3 Ultrasonic metal weldability chart [75]

The summary of weldability chart as obtained from experimental observations is presented in Fig. 2.3 [75]. The shaded portions are supposed to represent the combinations those can be welded, and the blank portions represent the combinations those can't be welded or not have been attempted yet. It is observed from the Fig. 2.3 that the aluminium is exceptionally weldable and can be joined to almost all metals. Other easily weldable materials are copper alloys and various precious metals. On the contrary, iron and refractory materials like molybdenum and tungsten can be welded only in case of thin materials [76]. Patel et al. [77] conducted ultrasonic welding experiments using 1.5 mm thick SiCp/2009Al-O and SiCp/2009Al-T6 composites to reveal the welding feasibility of the composites. It was found that microhardness of the weld zone is higher than that of the parent material.

Other than the material properties another important aspect of the material is its dimension. In most of the cases, the specimens are placed in a overlapped manner and parallel to the ultrasonic vibration [13]. In USMW, the ultrasonic energy passes through the top workpiece to the weld spot and due to the friction, the internal heat is generated. The vibrational amplitude of the process has to be adjusted to the thickness of the specimen. The relationship between the losses that occurs during the welding and thickness of the part was given by Wodara [78] as,

$$P_x = P_0 \cdot e^{\frac{k \cdot x}{20}} \quad (2.1)$$

Where,  $P_x$  and  $P_0$  are the alternating acoustic pressure,  $k$  is the absorption coefficient and  $x$  is the thickness.

Similarly, If this dimension of weld specimens are half of the wavelength and weld is made at the centre of the workpiece, then a significant decrease in weld strength can be observed. The wavelength of a material can be found out from the following equation

$$\lambda = \frac{c}{f} = \frac{\sqrt{\frac{E}{\rho}}}{f} \quad (2.2)$$

Where,  $c$  is the sound speed in a rod,  $E$  is the Young's modulus,  $\rho$  is the density and  $f$  is the frequency

From the previous studies, it was observed that the critical length of part was  $(2n + 1)\lambda/4$  ("n" represents the number of modes) where the weld strength clearly decreased [79]. At this length, the sonotrode deforms at the top part heavily without welding. If the length of the top part is  $n\lambda/2$  then the top part is vibrating in resonance with the other components. In this case, a little deformation with very good welding can be achieved.

## 2.5 Process Parameters

There are a number of process parameters those can influence the welding strength, such as frequency of vibration, weld pressure, weld time, and vibrational amplitude. These parameters are regarded as system parameters. Other than these machine parameters another category of parameters are called specimen parameters. They also have an influence on the quality of joint and it includes the specimen hardness, sizes, roughness and the tool textures. A brief description of these parameters is necessary as the correlation between them leads to the quality of the weld joints.

### 2.5.1 Frequency of vibration

In ultrasonic systems, the transducer is designed and tuned to operate at a particular frequency. According to the application, the frequency ranges from 15-300 kHz. But in USMW, typically 20-40 kHz frequency is used for the welding process. The ultrasonic generator is the device which has the capable of amplifying the 50 Hz normal alternating supply current to 20 kHz of vibration and consistently maintaining it during the welding operation using frequency generator, transducer, power amplifier, booster and horn. Meanwhile, the dimensions of the specimens are also selected in such a way that the whole system will vibrate at a resonant frequency. However, a small change in the operating frequency will result in a significant decrease in vibrational amplitude [74]. The shift of the frequency also takes place due to the change in temperature, clamping pressure and/or tool wear. Thus, the modern integrated power controller with automatic feedback circuitry can compensate if there is any shifting in frequency and make the system to resonant at a constant frequency [80].

### 2.5.2 Weld pressure

The weld pressure is a key parameter in USMW. This pressure exerts a normal force on the specimen throughout the welding process. Thus, in some studies, it is also known as the static force. It usually presses the specimens to create an intimate contact between the surfaces and is dependent on the weld tip and anvil geometries. The magnitude of this pressure depends on the material properties and thickness. While adjusting the process parameters, an optimum range of pressure should be defined. Because lower weld pressure can lead to a weak weld and higher values may result in the excessive deformation of the parts, tip sticking and generation of high temperatures [81].

### 2.5.3 Vibrational amplitude

The vibration amplitude is related to the power of the system and the amplification produced by the booster/horn. Thus, it directly reflects the energy delivered to the weld zone. In ultrasonic welding system, amplitude means the axial expansion and contraction of excitation. In the lateral drive system, the amplitude can be controlled by the operator. Originally, this is done with the change in current in the transducer. If the amplitude is set to 100 %, then it means that it uses 100% of system power to produce vibrations [75].

### 2.5.4 Weld time, energy and power

The quality of the weld in USMW also depends on the weld time, which controls the amount of energy and/or power supplied to the joint place. The relationship between the ultrasonic power and weld time varies with the material conditions such as its dimension, properties and surface finish. Fig. 2.4 depicts the basic graph between power and time. The area under this curve represents the energy delivered to the weld surface during the weld time [14]. At “no-loading” condition, USMW system requires a minimum amount of power to maintain the vibration. This power value is directly dependent on the mechanical load [82]. Therefore, an increase in weld pressure and/or mechanical load increases the power level and consequently decreases the weld time to deliver the same amount of energy.

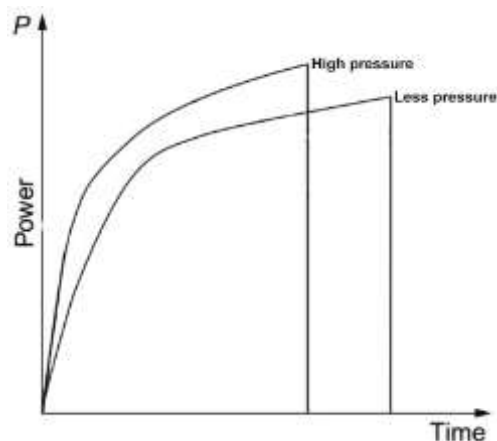


Fig. 2.4 Weld power curve in USMW [14]

Modern USMW uses a close loop feedback control system to monitor the whole process during the welding. In several USMW systems, the ultrasonic power, energy and time are regarded as the independent variable. But, a better approach to control all these parameters is to set a parameter to reach the level of the weld and leave other parameters as the dependent variable. For example, if the welding will be done time control mode, then a particular weld time will be fixed, and the welding will continue until

that time. But the energy or power that will be achieved during weld time can't be controlled. Similarly, this phenomenon is also applied to the energy and power control modes. All these situations make the USMW a complex process in which different process parameters interact among themselves within the very short duration.

## 2.6 Effect of Process Parameters in USMW

There is a necessity to understand the influences of various parameters on the strength of welds that are obtained by the lateral drive system. Many researchers have tried to get a sound joint between dissimilar materials by controlling the process parameters as well as specimen parameters such as weld pressure, weld time, vibrational amplitude, material hardness, roughness, and material dimensions. These studies have shown that USMW generally uses relatively less energy and job deformation as compared to other solid state welding process like friction stir welding (FSW).

In USMW process, pure metal bonding is usually achieved at relatively low temperature ( $<300^{\circ}\text{C}$ ) in very short weld time ( $<1\text{sec}$ ) [83]. Meantime, Park et al. [84] described that USMW requires only about 5 to 10 % of the energy needed for arc welding. Hetrick et al. [85] also demonstrated the ultrasonic welding process as a low heat producing process. For this reason, the issues like part distortion and the degradation of Al alloy property can be eliminated. Kodama [86] performed experiments using soft materials like aluminium, copper, brass and gold using different parameter conditions like specimen roughness, hardness, dimensions, the coefficient of friction and anvil geometry. The results showed that the good strength could be obtained when the amplitude of vibration was reduced with the increase of frequency of vibration. Barnes and Pashby [87] reported that USMW could be used in automotive and aerospace sectors for the joining of lightweight structural components.

Zhang et al. [88] performed various tests taking different ultrasonic energy values to measure the temperature at the weld center and it was concluded that when the peak temperature was above  $500^{\circ}\text{C}$ , the softening of the material took place to enhance the joining of aluminium sheets. De Vries [18] also showed that the temperature generated at the weld interface was of 0.4 to 0.8 times of the melting point of parent material. To support this observation, Siddiq and Ghassemieh [89] explained the effect of both surface and volume softening effects for Al 3003 alloy. It was observed that the coefficients of friction between the sheets were increased with temperature up to a certain limit, and it fell down subsequently.

In this regard, the strong welds can be achieved only after the welding energy exceeds the threshold limit. Therefore, the requisite ultrasonic energy to produce a sound weld is

closely associated with a proper combination of process parameters like vibration amplitude, weld time and clamping force [90]. Al-Sarraf and Lucas [91] reported that the weld quality was highly sensitive towards the combinations of input factors such as clamping force and vibration amplitude. They observed that when the similar materials were taken, then aluminium showed a higher strength than copper. But when the dissimilar combinations were taken with an aluminium sheet on the upper side, then the joint showed a better strength. Seo et al. [92] also determined that the weld strength increases with the increase in vibration amplitude and weld pressure. The results revealed that the weld strength increased with the increase in weld pressure as well as vibration amplitude. Moreover, the maximum weld strength of 87.45 N was obtained at 0.25 sec weld time, 0.20 MPa weld pressure, and 80% vibration amplitude. It was also observed that at a transit section of 5-6mm, the Cu and Ni components were diffused with each other due to high frictional heat between the two sheets. Elangovan et al. [93] conducted experiments with copper sheets by taking Taguchi's design of experiment approach and found that the maximum weld strength depended on process parameters like weld pressure, weld time and vibration amplitude. Although there are not many guidelines presented to specify the quality of the welding, some research studies have been carried out in order to quantify it [94]. It was concluded that for accepting a good quality weld, a well-established parameter combination was needed.

Annoni and Carboni [95] successfully joined AA 6022-T4 aluminium and performed mechanical testing of welded parts for their best use in the practical situation. In this technique, quality welding took place at low temperature, i.e. less than that of melting point of the base material and also at very short period of time. Chen et al. [96] described the same concept and also compared this technique with conventional welding like resistance spot welding (RSW). Watanabe et al. [97] focused on the different application of aluminium and magnesium in the automobile industry. As the magnesium is a light material, they tried to replace the steel. They carried out some welding experiments and investigated the effect of welding parameters on tensile shear strength, microstructure at the welding region and the formation of IMC ( $\text{Fe}_2\text{Al}_5$ ). From their analysis, they concluded that weld strength decreases with high weld pressure and longer welding time. Different types of failure modes are observed during USMW. Daniels [98] carried out a number of experiments using various parameters like weld pressure, weld time, and power in USMW of aluminium to copper. The authors revealed that the weld could be possible between metal to metal and metal to non-metal. They also showed the relationship between specimen thickness, electric power and clamping force. Zhou et al. [99] developed a lobe that contained pull out failure and interfacial failure of the ultrasonic metal welds. Finite element analysis was also employed to predict these failure loads. Similarly, Kim et al.

[100] did the ultrasonic welding experiments by taking materials such as copper and nickel plated copper. They also proposed a quality lobe to categorize the different types of failure, such as nugget, interfacial and button failure modes by conducting T-peel tests.

In ultrasonic consolidation (UC) process, Siddiq and Ghassemieh [101] described the volume and surface softening effects by taking a friction model. It was also validated by performing experiments. Zhu et al. [102] conducted experiments with titanium and aluminum alloy to explain the influence of various parameters like weld pressure and weld times on the mechanical strength, interface microstructure, and microhardness. They concluded that at the end of the weld time, the hardness around the weld zone was increased as compared to the base metal, and some diffusion also appeared across the weld interface. Al-Sarraf and Lucas [103] revealed the design, characterization and test of a lateral drive ultrasonic welding system so that the effective amount of ultrasonic energy could be accumulated in the weld zone. They performed a series of experiments to show the weld quality and the joint strength using these components. Collins et al. [104] did the lap welding experiments by using materials such as aluminium foil and sheet and the relationship among thickness, hardness of the material and the weld strength of the joint was revealed. Tsujino et al. [105] employed two oscillation systems simultaneously in multi-spot ultrasonic welding system for fabrication of a joint followed by measurement of the joint strength.

The other important aspect of any experiment is its statistical design, and it can be developed by using an empirical method. As a matter of fact, the design of experiments was used to conduct experimental campaigns in some papers. These papers not only explore the interdependence among the input parameters but also predict the weld strength of welded joints made by USMW. For instance, Flood [106] used ultrasonic welding to join copper and aluminium by taking different process parameters which affect the weld strength of the materials. This work also illustrated some of its applications in electrical, automobile and electronics industry. Elangovan [107] used a stepped type of horn to carry out experiments using aluminum specimens. They performed experiments as per the response surface methodology (RSM) to develop a second order response model, and this was utilized in GA to find the optimum welding parameters for attaining maximum tensile strength. Likewise, Norouzi et al. [108] modelled and optimized different process parameters associated with ultrasonic welding of acrylonitrile butadiene styrene (ABS) and polymethyl methacrylate (PMMA) using various artificial intelligence (AI) methods. They obtained that artificial neural network (ANN) had better performance than adaptive neuro-fuzzy inference system (ANFIS) and hybrid search (HS) methods and at the same time, genetic algorithm (GA) and particle swarm optimization had the same performance to optimize the process parameters.

In conclusion, it is observed that the various process parameters and specimen related parameters are dependent on the type welding system used for the joining purpose. A large number of literature are available which show the relationship between process parameters like vibration amplitude, weld time, weld pressure and specimen parameters like roughness, hardness and thickness of the sheet on the joint strength. Furthermore, other studies also reported the relationship between the sheet thickness and the power consumption during the welding process. The research work in this thesis is performed using the three process parameters which are used to improve the weld strength and weld quality over a variety of materials.

## **2.7 Numerical and Acoustic Softening Analysis in USMW**

In USMW, the temperature developed is below than the melting point of the base material. A lot of studies have been reported regarding the evolution of temperature through experimental as well as numerical analysis. Elangovan [109] conducted experiments with dissimilar thickness of copper sheets, and the related temperature was found by using a thermocouple and thermal imager. The results obtained from the experimental studies were further validated by finite element analysis (FEA) and finite difference method (FDM). It was observed that the temperature increases with increase in weld time and decrease in specimen thickness. Meantime, the mathematical modelling using FDM method and the FEA method also predicted the similar trend of temperature rise. Likewise, a 3D finite element model was developed by Jedrasiak et al. [110] for the ultrasonic welding of dissimilar materials like AA6111 aluminium alloy to AZ31 magnesium alloy and DC04 low carbon steel. The model successfully predicted the temperature histories for the dissimilar welding combinations and it was observed that heat input was concentrated between the tool and top part and between the workpiece with a uniform spatial distributed manner. Again Elangovan et al. [111] presented a study on temperature and stress distribution during the welding of aluminium to copper. They developed a FEM based model which predicts the temperature during the welding, and it explained the influence of process variables and specimen parameters on the weld behaviour. It also revealed that the temperature developed near to the workpiece was higher than the temperature produced near to the sonotrode because the ultrasonic energy was focused on the sheets during the welding. Chen and Zhang [112] employed numerical analysis of ultrasonic welding process to explore the effect of serrated knurl patterns on the mechanical properties of the interface. The results showed that as the sonotrode vibrates at a very high frequency; the initial geometrical symmetry of the surface was disrupted causing the development of stress, plastic strain and deformation



along the compression direction. Again, Chen and Zhang [113] used a 3D finite element model to study the heat generation and evolution temperature during USMW. The model they developed was quite capable of predicting the heat generation from plastic deformation. It was also observed that the maximum temperature was located at the contact interface of specimens because of a large amount of frictional heat generation and under the serrated edges of sonotrode, a local interface friction and plastic deformation occurred. Thus, the temperature distribution was not symmetric of the whole structure. Konchakova et al. [114] presented a phenomenological modelling of the mechanical properties of the welded structure between metal to CFRP sheets. They pointed out the dependencies of the numerical values of the mechanical behaviour on the interface geometry which were taken as square, elongated rectangle and crossed rectangle. The study also showed that the distribution of damage in the interface of the square geometry was less than the cross rectangle geometry interface.

Acoustic softening is the second source of material softening during USMW. It was first identified by Blaha and Langenecker [115]. They carried out experiments on the zinc mono crystals on which ultrasonic energy of 800 kHz was imposed. It was observed that at a sufficient level of ultrasonic energy, the yield stress of the material reduced. Kirchner et al. [116] also performed several experiments on aluminium alloys and from the quasi-static compression test it was found that a similar type of reduction in the yield stress value under the presence of ultrasonic energy over a broad range of frequencies. Izumi [117] also revealed acoustic softening during the ultrasonic irradiation of copper, aluminium, steel, silver and lead in compression. Acoustic softening of a material depends on the acoustic impedance, melting point, young's modulus and hardenability. It was observed from the above studies that the acoustic softening was more effective with high-value acoustic impedance and Young's modulus and low value of melting point. Domanidis and Gao [118] explored a finite element model to investigate the plastic deformation and stress fields during the ultrasonic welding and used the results to find the optimum process conditions. Their study concluded that the plastic deformation was a relevant feature in the bonding process and the temperature generated during the welding was not only due to the thermal softening but also acoustic softening played a key role in getting an accurate prediction of temperature. Zhang and Li [119] employed thermo-mechanical modelling to study the mechanics of ultrasonic consolidation. It was reported that severe plastic deformation in the bonding region caused a formation of joint during ultrasonic consolidation. A correlation was found between plastic strain from this model and experimentally bonded area.

Plastic deformation and material softening are the two important parts ultrasonic welding process since they bring metal to metal surface so close that bond formation

happens. Both thermal and acoustic softening plays a crucial role to achieve a high temperature which was the sole reason for plastic deformation. But very few kinds of literature are available related to this study.

## 2.8 Research Gaps Identified from the Literature Review

Literature review of this chapter provides information about the significant amount of works those were carried out on the various aspects of USMW process. However, investigation of this process for the dissimilar materials is still to be conducted. On the basis of literature review, following research gaps have been identified:

- Although previous studies attempted to analyze the design characteristics of the ultrasonic tools, there is still a lack of understanding when the extra mass or multifaceted weld tip is used. Furthermore, amplitude uniformity at the weld tip has not received much attention despite the fact that it may affect the joint quality. Likewise, the resonant frequency, mode shape studies, fatigue analysis and vibro-thermographic analysis are not yet been described adequately.
- In the available literature, only theoretical description of the USMW process has only been described for traditional wedge-reed system. However, the detailed mathematical analysis with a thorough explanation of friction inside and outside the weld zone is required. Similarly, there is also a lack of numerical analysis for this thermo-mechanical mechanism with acoustic softening effect.
- A large number of studies have examined the joint strength by considering one or two of the parameters as constant. However, a good result can be obtained by varying these control parameters to study the joint strength and quality. The majority of the investigations are also not considered the effect of dissimilar thickness combinations on the weld strength.
- There is a definite impact of anvil and weld tip surface structure on the joint strength. As the ultrasonic welding includes a complex mechanism, it is necessary to find out the quality of the weld in terms of fracture pattern, wake features, flow behaviour and microhardness at the plastic deformation zone. But, few studies revealed this mechanism with very simple designs.
- Very little analysis is being reported on the effect of various surface conditions on the weld strength. Few lubricants or combination of different lubricants are investigated in USMW process. Hence, a wide range of investigation is required to study the impact of different surface roughness and microhardness of the faying surface on the bond strength.

- It is pertinent to mention that artificial intelligence methods can predict accurate results in comparison to other techniques. But, unfortunately, only one literature was available which showed the prediction results using these techniques in plastic welding. Hence, the focus on artificial intelligence techniques for predicting the weld strength which is much needed for a complex mechanism like USMW.
- The intensive literature review shows that most of the studies have concentrated on the numerical analysis of the component like a horn. According to the author's knowledge, numerical studies behind the mechanism i.e. thermal softening and acoustic softening have not been fully described.

## 2.9 Novelty of the Present Research Objectives and Methodology

The identified research gaps have been filled by the present investigation, and the novelty of the research objectives can be summarized as follow:

- In the present work, the integrated horn and booster have been designed which is capable of welding of thinner metals. A stepped type profile is chosen for these two components to get high amplification and meanwhile a radius of curvature is given at the intersection zone to reduce the stress concentration. The FEM software ANSYS® is used to identify the various vibration characteristics like mode shapes and resonant frequency to ensure that the horn is tuned and vibrate longitudinally.
- Furthermore, as booster and horn are under repeated cyclic loading, the stresses developed in each system also uncovered by using the harmonic analysis. These stresses are again used to explore the effects of cyclic loads by utilizing the fatigue module of ANSYS®.
- There is no much work reported on the design and thermoelastic analysis of a booster and multifaceted horn. Therefore, the computational modeling of these two systems is carried out considering the parts under cyclic loading. As, temperature is also developed in the high-stress region due to thermo-elastic effects, it is captured by a K-type thermocouple and has been validated using multiphysics software COMSOL®.
- Several experiments have been performed to determine the quality and strength of the weld by varying different anvil patterns. In this study, a microstructural observation for the weld zone is presented to fulfil the weld quality characterization. Assessments of weld properties like temperature and microhardness profile for different types of anvil knurl patterns have also been performed.
- A model based on mechanics of USMW is presented to understand the mechanism of the welding process completely. This theoretical analysis is carried out under plastic

deformation criterion and various friction factors inside and outside of the weld zone. Moreover, the results obtained from this study is used in the numerical analysis, and its outcome i.e. temperature is compared with the experimental results.

- The acoustic softening analysis also has been carried out to reveal the material softening in which the static stress of the material is significantly reduced under the influence of ultrasonic energy.
- Artificial intelligence techniques along with the conventional regression analysis are applied to predict the responses like tensile shear and T-peel strength correctly. These results are compared with the experimental values to validate the correctness of these techniques.
- Metallurgical analysis such as scanning electron microscopy (SEM), micro-hardness, energy dispersive X-ray (EDX) and X-ray diffraction (XRD) are conducted for the joints produced under the influence of various process parameters for validating the reasons behind the experimental observations.

The overall methodology of the current research work is illustrated in the form of flow chart as given in Fig. 2.5.

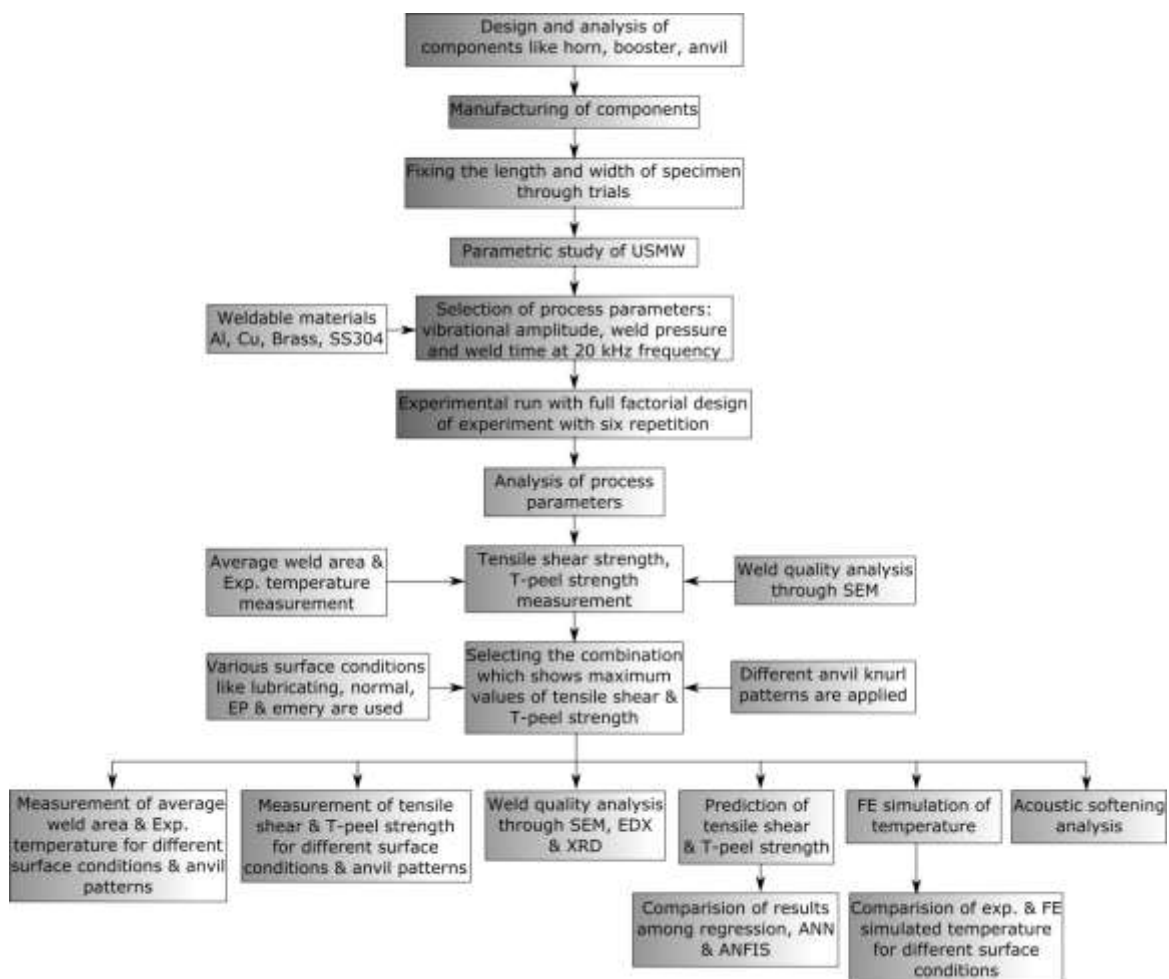


Fig. 2.5 Overall methodology of the current research work

## 2.10 Summary

The present chapter provides an idea about various developments taking place during the past years in the area of ultrasonic metal welding. It clearly describes the major works reported on the responses of process parameters on the weld strength. This chapter is comprised of six major sections which summarize on designing of components, mechanics behind bonding, material and its geometries, selection of process parameters, experimental investigation and numerical and acoustic softening work. The major outcomes of this chapter can be summarized below:

- Despite the invention of USMW 60 years back, many research reports and studies focused only on the designing different horn profiles and analysing the resonant frequency and amplitude of vibration at the weld tip surface during the welding. Meanwhile, the amplitude uniformity at weld tip surface, cyclic stress concentration at the nodal position and vibro-thermographic analysis of both horn and booster components received less attention. Therefore, in this thesis, a design criterion is given for horn and booster and addresses the issues those are raised in the literature study such as modal and harmonic analysis, fatigue analysis and vibro-thermographic analysis.
- With proper design of the tool texture and anvil geometry keeping the machine parameters aside, a good weld can be obtained. Thus, few kinds of literature were discussed only the design and microstructural analysis associated with it. But in the present research work, the relationship between the anvil knurl patterns on the weld strength and the in-depth analysis of microstructures associated with the quality of the weld are revealed.
- Mechanics behind the USMW process is really a complicated one. Thus, previous studies described the process only in a theoretical manner. Furthermore, these studies also showed that the acoustic softening only occurs to ultrasonic consolidation process whilst there is also a significant decrease in the yield strength of the material due to high ultrasonic energy. Hence in this work, an attempt has been made to describe the mechanics of the welding step by step and also considering the acoustic softening phenomenon which has a definite effect on the interface temperature.
- It has been shown in this chapter that many studies attempted to explain the relationship of process parameters like vibrational amplitude, weld pressure and weld time on the tensile shear strength of welded specimens. But these are typically concerned with the welding of wires and cables which are entirely different from welding of thin sheets. However, these studies analyze the effects of process parameters on weld strength at a constant thickness of sheets. Furthermore, the

effects of surface roughness or hardness value have not been adequately investigated in the aforesaid literature. Thus, an attempt has been made in the present study to overcome these obstacles by varying the control parameters and changing the various surface conditions. Meantime, the prediction and numerical analysis have been done to add a technical value to the thesis. Additionally, a detailed microstructural analysis has been performed in the weld cross-sections as well as in the fractured surfaces to reveal the quality of the weld that can be produced by using USMW.

- Considering the identified research gaps, novelty of the present work with adopted methodology is presented.

In the next chapter, the analytical and numerical methods based on modal and harmonic analysis have been elaborated and applied to design the USMW components.

## Chapter 3

# Numerical Analysis on Component Design and Thermo-Mechanical Analysis of USMW

### 3.1 Introduction

Ultrasonic metal welding (USMW) is an advanced joining technology, which is emerging as a potential fabrication process for many industrial applications. The essential components of this equipment are the horn and booster, through which the pressure and high-frequency vibration are applied to create a solid-state weld joint. A good weld can be produced on the contact surfaces by means of a suitable scrubbing motion between the sheets, and this can be possible when the welding system components are properly designed. As the vibration amplitude at the output end of the transducer is very less (in the range of 10 to 30  $\mu\text{m}$ ), welding would not be taken place in this amplitude. So, the majority welding systems employ a booster, which increases the vibration amplitude according to its design shape. It also provides support for mounting of the welding stack. The booster is made up of materials like titanium, monel, and stainless steel which have excellent acoustic properties and high strength. Another important component of this welding system is the acoustic horn. It serves mainly two functions, such as, to further magnify the amplitude of vibration obtained from the booster and also acts as a tool that directly in contact with the workpiece. The common practice is to mount both components (booster and horn) parallel to the direction of vibration through which the ultrasound waves are transmitted and applied to the welding surface in a transverse mode. One of the objectives of the present work is to investigate how these components can be accurately designed and manufactured in order to generate high ultrasonic energy to produce a sound weld. At the same time, an incorrectly designed horn or booster may damage the whole system, because of the mismatching of mechanical impedance. So far, the empirical method has been used to find out the length and other dimensions of these components. But, it is very lengthy, time-consuming process and also accurate result may not be achieved for the intricately shaped horn and booster. Therefore, finite element analysis with proper boundary conditions is preferred to analyse effectively the horn and booster with complex geometries.

### 3.2 Theoretical Design of Horn and Booster

In most of the high-intensity and high-power applications of ultrasonics in manufacturing industries need a horn and booster to provide a greater amplitude of vibration at the output (load) end. These two components act as the tools to concentrate the acoustic waves in a directional radiation pattern. The analysis of this pattern of waves through both of them is very complicated and specific assumptions are required for deriving the design equations even for a solid medium. The most accepted mode of the ultrasonic welding is the longitudinal mode, and it can be analysed by considering a free-free vibration in a non-uniform bar [7] as shown in Fig. 3.1. The assumptions are:

- (i) The wave is propagated in the rod along the axial direction.
- (ii) The walls of these components are so rigid that wave propagation along the lateral direction is neglected.
- (iii) The amplitudes of acoustic pressure remain within the limit of compressibility characteristic for the solid. Therefore, the second order differential terms can be neglected.
- (iv) The bar is tapered in such a way that the presumed plane waves can retain a contact with its walls.

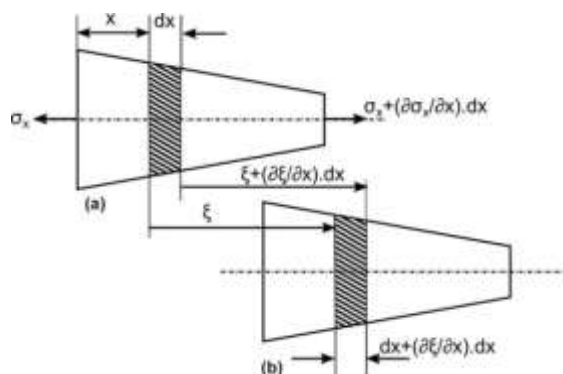


Fig. 3.1 (a) Tapered, axisymmetric and slender bar, (b) Changes in stress distribution after plane wave propagates through it

Let's take an infinitesimally small element on this non-uniform bar of length 'dx'. If  $\xi$  is the displacement at 'x', then at 'x+dx' position, it will be ' $\xi + (\partial \xi / \partial x) dx$ '. It is then evident that the element 'dx' in the new position has changed by an amount ' $(\partial \xi / \partial x) dx$ '. Thus, the strain developed in the strip is,

$$Strain = \frac{\left( \xi + \frac{\partial \xi}{\partial x} dx \right) - \xi}{dx} \quad (3.1)$$

$$Strain = \frac{\partial \xi}{\partial x} \quad (3.2)$$

From Hooke's law of stress-strain relationship



$$\sigma_x = E \cdot \frac{\partial \xi}{\partial x} \quad (3.3)$$

Differentiating Eq. (3.3) w.r.t. x,

$$\frac{\partial \sigma_x}{\partial x} = E \cdot \frac{\partial^2 \xi}{\partial x^2} \quad (3.4)$$

Due to the vibration, an accelerating force is acted on the elementary strip and according to the Newton's law of motion, it can be represented as

$$F_a = m \cdot a \quad (3.5)$$

$$F_a = \rho \times \vartheta \times \frac{\partial^2 \xi}{\partial t^2} \quad (3.6)$$

$$F_a = \rho \times S \times \frac{\partial^2 \xi}{\partial t^2} \cdot dx \text{ (where thickness is unity)} \quad (3.7)$$

Due to the non-uniformity nature of the rod, the constraining force acting on the strip is

$$F_c = F_{final} - F_{initial} \quad (3.8)$$

$$F_c = (\sigma \times S)_{final} - (\sigma \times S)_{initial} \quad (3.9)$$

$$F_c = \left[ \left( \sigma_x + \frac{\partial \sigma_x}{\partial x} \cdot dx \right) \times \left( S + \frac{\partial S}{\partial x} \cdot dx \right) \right] - \sigma_x \times S \quad (3.10)$$

$$F_c = S \times \frac{\partial \sigma_x}{\partial x} \cdot dx + \sigma_x \times \frac{\partial S}{\partial x} \cdot dx + \frac{\partial \sigma_x}{\partial x} \cdot dx \times \frac{\partial S}{\partial x} \cdot dx \quad (3.11)$$

Neglecting  $(dx)^2$  term from the above equation

$$F_c = S \times \frac{\partial \sigma_x}{\partial x} \cdot dx + \sigma_x \times \frac{\partial S}{\partial x} \cdot dx \quad (3.12)$$

To satisfy the equilibrium of that small element, constraining force should be equal to the accelerating force, so by comparing Eq. (3.7) and (3.12)

$$F_c = F_a \quad (3.13)$$

$$S \times \frac{\partial \sigma_x}{\partial x} \cdot dx + \sigma_x \times \frac{\partial S}{\partial x} \cdot dx = \rho \times S \times \frac{\partial^2 \xi}{\partial t^2} \cdot dx \quad (3.14)$$

$$S \times \frac{\partial \sigma_x}{\partial x} + \sigma_x \times \frac{\partial S}{\partial x} = \rho \times S \times \frac{\partial^2 \xi}{\partial t^2} \quad (3.15)$$

Putting the values of Eq. (3.3) and (3.4) in the above equation

$$S \cdot E \cdot \frac{\partial^2 \xi}{\partial x^2} + E \cdot \frac{\partial \xi}{\partial x} \cdot \frac{\partial S}{\partial x} = \rho \times S \times \frac{\partial^2 \xi}{\partial t^2} \quad (3.16)$$

Dividing  $\rho \cdot S$  on both sides of Eq. (3.16)

$$\frac{E}{\rho} \cdot \frac{\partial^2 \xi}{\partial x^2} + \frac{E}{\rho \cdot S} \cdot \frac{\partial \xi}{\partial x} \cdot \frac{\partial S}{\partial x} = \frac{\partial^2 \xi}{\partial t^2} \quad (3.17)$$

Putting  $V_s = \sqrt{\frac{E}{\rho}}$  in Eq. (3.17)

$$\frac{\partial^2 \xi}{\partial x^2} + \frac{1}{S} \cdot \frac{\partial \xi}{\partial x} \cdot \frac{\partial S}{\partial x} = \frac{\rho}{E} \cdot \frac{\partial^2 \xi}{\partial t^2} \quad (3.18)$$

$$\frac{1}{V_s^2} \cdot \frac{\partial^2 \xi}{\partial t^2} + \frac{1}{S} \cdot \frac{\partial \xi}{\partial x} \cdot \frac{\partial S}{\partial x} - \frac{\partial^2 \xi}{\partial x^2} = 0 \quad (3.19)$$

As the both elements undergo harmonic motion, so the displacement equation shown in Eq. (3.19) can be written as

$$\xi = A \cdot \sin(\omega t) + B \cdot \cos(\omega t) \quad (3.20)$$

$$\frac{\partial \xi}{\partial t} = A \cdot \omega \cdot \cos(\omega t) - B \cdot \omega \cdot \sin(\omega t) \quad (3.21)$$

$$\frac{\partial^2 \xi}{\partial t^2} = -\omega^2 [A \cdot \sin(\omega t) + B \cdot \cos(\omega t)] \quad (3.22)$$

$$\frac{\partial^2 \xi}{\partial t^2} = -\omega^2 \cdot \xi \quad (3.23)$$

Putting the value of Eq. (3.23) in Eq. (3.19)

$$\frac{1}{V_s^2} \cdot (-\omega^2 \cdot \xi) - \frac{1}{S} \cdot \frac{\partial \xi}{\partial x} \cdot \frac{\partial S}{\partial x} - \frac{\partial^2 \xi}{\partial x^2} = 0 \quad (3.24)$$

$$\frac{\partial^2 \xi}{\partial x^2} + \frac{1}{S} \cdot \frac{\partial \xi}{\partial x} \cdot \frac{\partial S}{\partial x} + \frac{\omega^2}{V_s^2} \cdot \xi = 0 \quad (3.25)$$

Eq. (3.25) is used to find out the resonant lengths of both axisymmetric horn and booster. Those can be determined by:

$$V_s = \lambda \cdot f \quad (3.26)$$

Normally, the lengths of these parts are the half of the wavelength passing through it. The equations used to find out the resonant length of the different horn, and booster profiles were obtained by Merkulov [120]. The subsequent equations for calculating resonant length and stress can be achieved for a different type of profiles.

**(i) For stepped profile type**

$$L = \frac{\lambda}{2} = \frac{V_s}{2f} \text{ and} \quad (3.27)$$

$$\text{Stress } (S) = \frac{E\omega\xi_m}{V_s} \sin\left(\frac{\omega x}{V_s}\right) \sin(\omega t) \quad (3.28)$$

Stress is maximum at  $x = \frac{l}{2} = \frac{\lambda}{4}$  position

**(ii) For exponential tapered type**

$$L = \frac{V_s}{2f} \sqrt{1 + \left[ \frac{\ln(S_2/S_1)}{2\pi} \right]^2} \text{ and} \quad (3.29)$$

$$\text{Stress } (S) = \frac{E}{\omega} V_0 \left( \frac{\omega}{V_s'} + \frac{\gamma^2 V_s'}{4\omega} \right) e^{\gamma x/2} \cdot \sin\left(\frac{\omega x}{V_s'}\right) \quad (3.30)$$

Maximum stress occurs at  $\frac{dS}{dx} = 0$  and  $\tan \frac{\omega x}{V_s'} = \frac{-2\omega}{\gamma V_s'}$

(iii) For catenoidal type

$$L = \frac{V_s}{2\pi f} \sqrt{\pi^2 + \left[ \cosh^{-1} \frac{r_2}{r_1} \right]^2} \text{ and} \quad (3.31)$$

$$\text{Stress } (S) = \frac{EV_1 \cos K'x}{\omega a \cosh(Kx/a)} \left( \tanh \frac{Kx}{a} + aK' \tan K'x \right) \quad (3.32)$$

At the point of maximum stress,  $\frac{dS}{dx} = 0$ , from which  $\frac{1}{s} \frac{dS}{dx} = \frac{2x}{x^2+b^2}$

The one-dimensional propagation of the longitudinal wave in the bar can be analysed by the Eq. (3.18). Thus, it can be expressed as

$$\frac{\partial^2 \xi}{\partial x^2} = \frac{\rho}{E} \cdot \frac{\partial^2 \xi}{\partial t^2} \quad (3.33)$$

The solution to the above second order differential equation depends on two variables.

$$\xi(x, t) = \xi(x) \cdot \xi(t) \quad (3.34)$$

The left-hand side of Eq. (3.33) is independent of x whereas the right-hand side is independent of t. Thus, the simplified equation can be derived further:

$$\frac{\partial^2 \xi}{\partial x^2} + \left( \frac{\omega}{V_s} \right)^2 \cdot \xi = 0 \quad (3.35)$$

$$\frac{\partial^2 \xi}{\partial t^2} + \omega^2 \cdot \xi = 0 \quad (3.36)$$

According to Eq. (3.34), the general solution can be presented as

$$\xi(x) = A \cdot \sin \left( \frac{\omega}{V_s} \right) x + B \cdot \cos \left( \frac{\omega}{V_s} \right) x \quad (3.37)$$

$$\xi(t) = C \cdot \sin(\omega t) + D \cdot \cos(\omega t) \quad (3.38)$$

where, A, B, C, D are constants. So, the overall solution becomes

$$\xi(x, t) = \left[ A \cdot \sin \left( \frac{\omega}{V_s} \right) x + B \cdot \cos \left( \frac{\omega}{V_s} \right) x \right] \cdot [C \cdot \sin(\omega t) + D \cdot \cos(\omega t)] \quad (3.39)$$

The natural frequency of both components can be found from Eq. (3.39) by putting the boundary conditions for the free-free bar. It can be written as

$$f_n = \frac{n_m}{2L} \sqrt{\frac{E}{\rho}} \quad (3.40)$$

The performance measure of the horn is the amplification ratio/gain and is given by

$$\frac{\xi_1}{\xi_2} = \frac{V_1}{V_2} = \frac{S_2}{S_1} = \left( \frac{D_2}{D_1} \right)^2 \quad (3.41)$$

From all the design profiles of horn and booster, the stepped profile offers high amplification ratio as compared to exponential and conical profiles [121]. Finite element method is a suitable route to design and to model these ultrasonic components more accurately and efficiently.

### 3.3 Background Theories for Numerical Design of Booster and Horn

Out of different numerical methods, finite element method (FEM) can be utilized to analyse different types of horn and booster geometries and can solve a practical problem with required boundary conditions, which is tough to derive using conventional methods by means of differential equations [32]. For the present investigation, commercially available finite element programs ANSYS® and COMSOL® are used to find out the resonant frequencies, safe working stresses, the temperatures at high-stress regions and nodal displacement of an acoustic horn and booster with the required dimensions. Meanwhile, when a structure is actuated by a dynamic loading, it is sensible to assume its variable response. In such cases, the dynamic analysis may have to be executed to determine both varying loads and responses. Thus, to investigate the effect of cyclic loading on both components, the dynamic analysis is conducted in this study. All the structural dynamics problems can be based on the D'Alembert's principle that gives the time-dependent response of every nodal point in the structure by including the "inertia force" and "damping force" term in the equation. Therefore, the general equation of motion can be presented by [122],

$$[M].\left\{\frac{\partial^2 \xi}{\partial t^2}\right\} + [C].\left\{\frac{\partial \xi}{\partial t}\right\} + [K].\{\xi\} = \{F\} \quad (3.42)$$

The first step of the dynamic analysis is achieved by performing the *modal analysis*. This analysis is necessary to obtain the natural frequencies and appropriate mode shapes of the horn and booster in such a way that, they will be in a resonating state with other systems. Meanwhile, it is assumed that the materials used for both elements have little damping properties and, therefore, the equation of motion for an un-damped system can be written as

$$[M].\left\{\frac{\partial^2 \xi}{\partial t^2}\right\} + [K].\{\xi\} = \{0\} \quad (3.43)$$

For a free-free vibrated linear system, it is assumed that each node has a sinusoidal function of the peak amplitude of that node, and the displacement vector can be written as

$$\{\xi\} = \{A\} \sin(\omega t) \quad (3.44)$$

The velocity vector can be written as

$$\{\dot{\xi}\} = \{A\} \cdot \omega \cdot \cos(\omega t) \quad (3.45)$$

Similarly, the acceleration vector can be expressed as

$$\{\ddot{\xi}\} = -\{A\} \cdot \omega^2 \cdot \sin(\omega t) \quad (3.46)$$

Substituting the values of Eqs. (3.44) and (3.46) in Eq. (3.43)

$$[M].[-\{A\}.\omega^2.\sin(\omega t)] + [K].[\{A\}\sin(\omega t)] = \{0\} \quad (3.47)$$

$$\sin(\omega t) [-[M].\{A\}.\omega^2 + [K].\{A\}] = \{0\} \quad (3.48)$$

The different modal properties of both the elements can be determined from the above equation. The Eigenvalue equation and can be represented as

$$([K].\lambda_E[M])\{A\} = \{0\} \quad (3.49)$$

It is important to note that the total numbers of Eigenvalues or natural frequencies are equal to the total number of degrees of freedom in the model, and each of it corresponds to an Eigenvector or mode shape. It is worth noting that, usually the first few Eigenvalues of the model are preferred. Since the FEM gives an approximate solution to the problem, the higher Eigen values and vectors are inaccurate.

The second step of the dynamic analysis is the *harmonic analysis* that is required to find out the prolonged cyclic response of both the elements under periodic loading. This analysis is also known as frequency response analysis. It solves the D'Alembert's principle shown in Eq. (3.42) for linear structures undergoing steady-state vibrations. It is assumed that all the points/ nodes are moving with the same known frequency. But, due to the presence of damping, the phase shift may occur. The nodal displacements of in-phase particles are given by

$$\{\xi\} = \{\xi_{max}\}e^{i\omega t} \quad (3.50)$$

The velocity is given by

$$\{\dot{\xi}\} = \{\xi_{max}\}i\omega.e^{i\omega t} \quad (3.51)$$

The acceleration can be written as

$$\{\ddot{\xi}\} = -\{\xi_{max}\}\omega^2.e^{i\omega t} \quad (3.52)$$

Likewise, the force can be defined as

$$\{F\} = \{F_e\}e^{i\omega t} \quad (3.53)$$

Putting the values of Eqs. (3.50) to (3.53) in Eq. (3.42)

$$[M].-\{\xi_{max}\}\omega^2.e^{i\omega t} + [C].\{\xi_{max}\}i\omega.e^{i\omega t} + [K].\{\xi_{max}\}e^{i\omega t} = \{F_0\}.e^{i\omega t} \quad (3.54)$$

$$(-\omega^2.[M] + i\omega.[C] + [K])\{\xi_{max}\} = \{F_0\} \quad (3.55)$$

The inertia and static loads on the nodes of each element can be computed. The values for these two loads are represented as

*For inertia loads*

$$\{F^m\}_o = (2\pi\omega)^2[M_e].\{\xi\}_e \quad (3.56)$$

*For static loads*

$$\{F^K\}_o = -[K_e].\{\xi\}_e \quad (3.57)$$

The third step is the *fatigue analysis* of both horn and booster. The objective of this study is to characterize the capability of material to persist the cyclic loads as it may experience during its lifetime. Since, ultrasonic vibration occurs at 20000 cycles/sec, the component that bears this load over a year, leads to a high cycle fatigue (HCF). However,

the fatigue loading that causes the maximum damage can't be easily seen. To keep up the trail of loading occurrences for a particular node, the maximum stress intensity range is calculated by "rain flow" or "range counting method." These stress differences and intensity are calculated as

$$\{\sigma\}_{i,j} = \{\sigma\}_i - \{\sigma\}_j \quad (3.58)$$

The stress intensity is calculated on the basis of  $\{\sigma\}_{i,j}$  and it is represented as

$$\sigma_I(i,j) = \text{Max}(|\sigma_1 - \sigma_2|, |\sigma_2 - \sigma_3|, |\sigma_3 - \sigma_1|) \quad (3.59)$$

The interim maximum alternating shear stress is calculated and represented as

$$\sigma_{i,j}^d = \frac{\sigma_I(i,j)}{2} \quad (3.60)$$

Eventually, the maximum alternating shear stress is calculated as

$$\sigma_{i,j}^c = K_e \cdot \sigma_{i,j}^d \quad (3.61)$$

The rise in temperature due to the fatigue loading on both the components is the concluding analysis. It is based on the principle that when a solid is subjected to elastic cyclic stresses, then the material is heated due to alternate expansion and compression. But, when the alternating pressure is released, then it comes back to its initial shape and temperature. By utilizing the Galerkin technique of finite element analysis, the governing equation can be represented as

$$[C].\{T\} + [K].\{T\} = \{Q\} \quad (3.62)$$

### 3.4 FEM Application Strategy

Finite element analysis (FEA) is one such promising numerical method that can be used to solve complex problems. In the ultrasonic field, FEA has been applied to determine the vibrational characteristics of the modelled tools prior to its application in the manufacturing industries [121]. It uses a mesh of elements to connect the nodes and also used for modelling of the structure. It requires the material properties along with the loading conditions for the simulation purpose and the results those have been found out can be compared with the analytical results. The FEA software ANSYS® has been opted to determine the natural frequencies and corresponding mode shapes of the model [123]. In general, there are three mode shapes are observed during the analysis of horn and booster such as bending, torsion, and longitudinal modes. Fig. 3.2 shows these shapes after FE simulation of the rod with a uniform cross-section area as an illustration.

The present study explains the design, modeling, and fabrication of the ultrasonic spot welding components like a horn, booster, and anvil for a lateral drive system. The horn and booster are the major components that are responsible for transferring the ultrasonic energy to the weld zone [124]. Thus, these components are necessary to build a welding

system that will produce high-quality joints and in this regard, FEA is very much useful. The aim of this analysis is to get a tuned horn and booster at a particular frequency with low-stress concentration and high magnification. Subsequently, these components are manufactured.

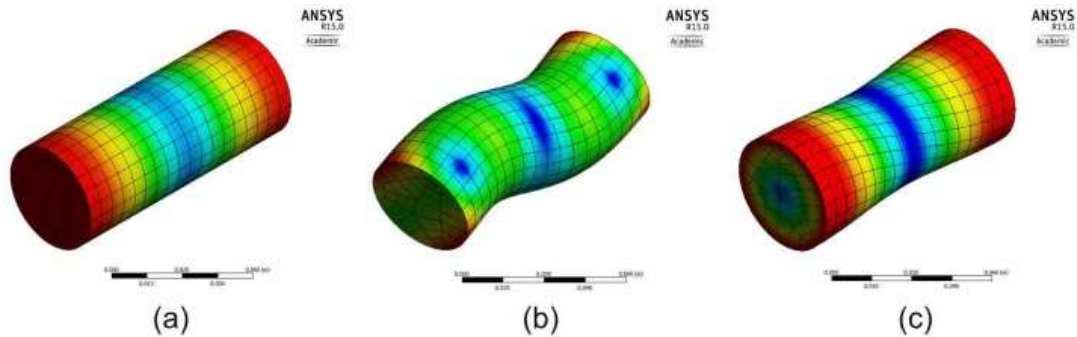


Fig. 3.2 Classifications of mode shapes with contours (a) longitudinal mode, (b) bending mode, (c) torsional mode

### 3.4.1 Modal analysis

In the present study, the ultrasonic generator produces 20 kHz of longitudinal frequency. To ensure a required performance from the welding horn, it is necessary to isolate the longitudinal mode frequency from other modes. Notably, much attention is given to design the horn. Because the horn acts as a tool, and it wears very fast as comparable to the booster. Thus, a horn with multi weldable tips is designed with high wear resistance and low acoustic loss material [125]. Initially, the lengths of both components are calculated theoretically from Eq. (3.27) using particular material's properties as shown in Table 3.1 [126]. For this study, D2 steel and titanium (Ti-6Al-4V) are used for horn and booster materials respectively for 20 kHz frequency, and their theoretical lengths are found to be 130 mm and 126.8 mm respectively. These components are designed to be half of the wavelength to match the frequency of the ultrasonic generator. Modifying the dimensions of input and output working surfaces can lead to the change in vibration amplitude. So the performance of the ultrasonic system is measured by its amplification ratio/gain as described in Eq. (3.41). It represents the capability of the system to weld high thickness materials. The dimensions of the input and output ends are fixed by the size of the booster and the particular weld tip size. The input and output diameters of the horn are 44 and 35 mm and for the booster, these are 55 and 44 mm respectively. The spot-welding horn with the booster is presented in Fig. 3.3.

Table 3.1 Properties of horn (D2 steel) and booster (Ti-6Al-4V) materials

Property	Units	D2 steel	Ti-6Al-4V
Density ( $\rho$ )	Kg/m <sup>3</sup>	7670	4430
Young's modulus (E)	GPa	210	114
Poisson's ratio ( $\nu$ )		0.3	0.33
Velocity of sound (C)	m/sec	5232	5072

The supports which hold the horn and booster are called support rings/flanges. These are attached at the nodal sections and should have larger diameters than the horn and booster. Otherwise, there will be a damping of amplitude in the latter stage [32]. Another advantage of designing these integral components are to apply the clamping force perpendicular to the weld specimens. The details are given in *Appendix A*. In the present analysis; the welding tip is designed as an integral part of USMW system to eliminate the stress concentration, increase the ultrasonic energy intensity at the welding zone and reduce the slippage between the contact surfaces of horn tip and upper specimen [127]. The weld tip surface has knurled patterns to engage into the specimens effectively. The dimensions of the knurl patterns are comparably less than the area of the weld tip. The welding tip and its associated knurl pattern dimensions are represented in *Appendix A*. For carrying out FE simulation; it is required to choose judiciously element type, real constant, material properties, geometry, meshing, boundary conditions, etc. [128]. As it is a 3D analysis, the solid187 element has been selected, which has the ability to analyze irregular shapes of both components and it also has the better compatibility to metal deformation [123]. It can also be applied to the curved boundary with plasticity, creeping, expansion, large deformation, and even a body with failure. In FEM, a variety of mesh techniques exists to mesh models of different topology. The horn and booster which are being investigated are discretized by a mesh of simple and uniform hexahedral elements connected by a number of nodes, as seen in Fig. 3.4. These elements have been chosen because of its accuracy in measuring higher-stress gradients than triangular elements. In this study, a mesh independence test has been performed for getting desired, reliable and accurate longitudinal mode of frequency and it is calculated for a different number of elements as shown in Fig. 3.5. A sensible amount of elements (i.e. 97368 for horn and 53135 for the booster) are selected keeping in view of computational time, the convergence of the tuned mode and accuracy of the result. It shows that the present model is sufficiently accurate to solve the problems of frequency domain for these two components. Thus, it provides the confidence to the welder for determination of natural frequencies and mode shapes.

Modal analysis by means of the Block Lanczos method is used to determine the natural frequencies and mode shapes of the acoustic horn and booster. It is a linear analysis and any non-linearities such as plasticity and contact elements are ignored as those effects are insignificant. It ensures the rigidity of the whole structure. Lower the natural frequency, lesser the rigidity of these components. By proper design, the horn will resonate with other parts of the system in the range of 19.5-20.5 kHz using Eq. (3.49). There may be the possibility of getting more than one natural frequencies and



mode shapes within this range. Thus, different mode shapes are observed like longitudinal, bending and torsional. But, the first and longitudinal or axial mode shape is always favoured. It has two reasons: firstly the transducer produces mechanical vibration in the longitudinal direction and secondly when mode 2 and 3 are superimposed with the main longitudinal mode of ultrasonic vibration then it causes a bending mode. Thus, this is an undesirable phenomenon which can jeopardize the advantages of ultrasonic vibration such as poor welding operation. Fig. 3.6 depicts the natural longitudinal mode of vibration.

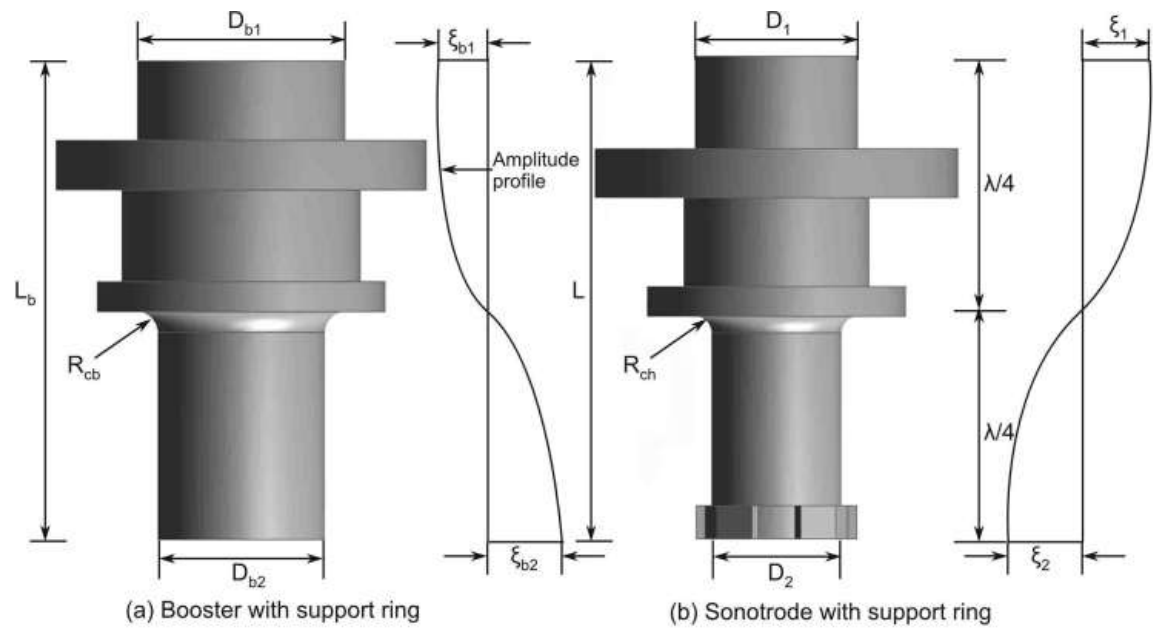


Fig. 3.3 Modeled booster and horn with amplitude profiling

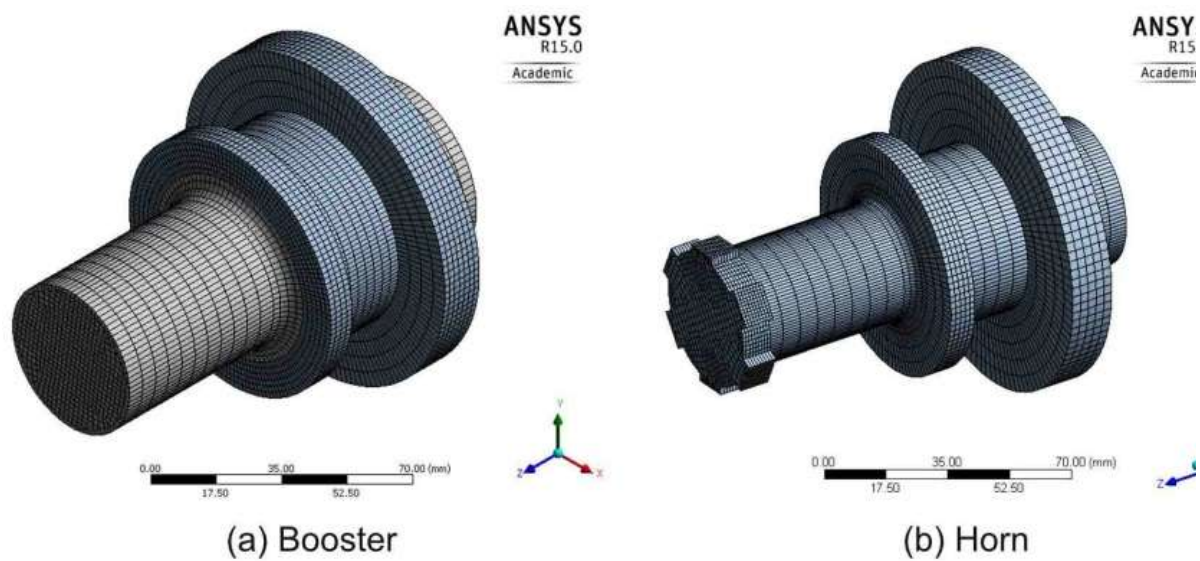


Fig. 3.4 Meshed 3D models for finite element analysis

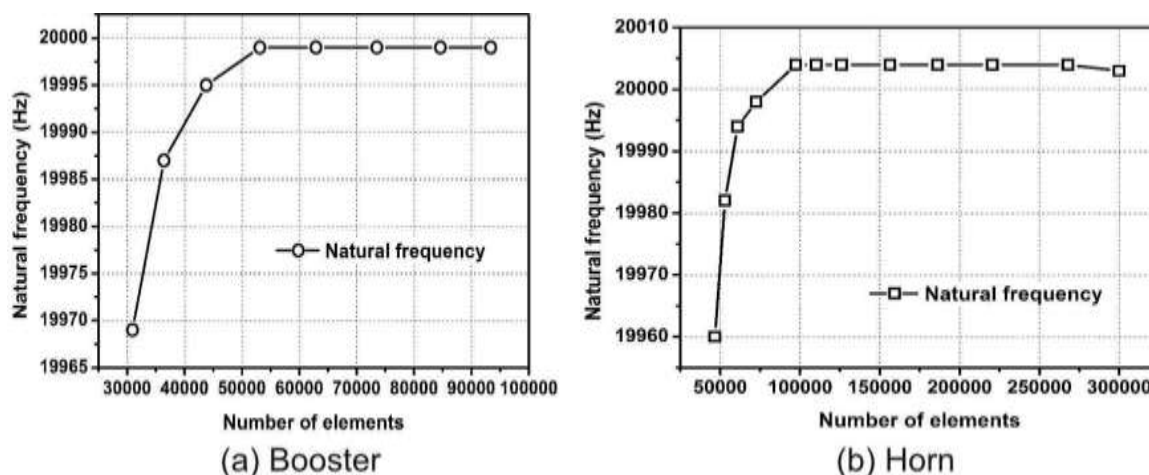


Fig. 3.5 Mesh independence test of natural frequency for different numbers of elements

A number of trial runs have been done with respect to shortening of length and adding radius of curvature at the nodal plane of the components so that; the frequency of the axial mode should match the machine frequency, and the stress concentration would be as low as possible. Firstly, from the modal analysis, the natural frequencies of horn and booster are uncovered by adjusting the length of both parts. Subsequently, they are shortened gradually by 0.5 mm keeping all other dimensions constant to get the desired 20 kHz frequency. During these analyses, bending, torsional and longitudinal mode shapes are obtained. As stated above, these mode shapes are the unwanted phenomena, and they are gradually disappearing when the total length of the booster and horn are set to 125.4 mm and 126.8 mm respectively. The various lengths of both components with first longitudinal vibration mode are shown in Fig. 3.7. It is observed that the natural frequencies of both the parts modeled by FEA approaches to the operating frequency of the system, after shortening of the length.

The radius of curvatures ( $R_{cb}$  and  $R_{ch}$ ) also has been changed to encounter the danger of stress concentration, which is applied to the junction of the big and small cross-section for both the components. Fig. 3.8 shows the effect of changing of  $R$  on the natural frequency. It has been observed that with increasing  $R$ , the natural frequency also increases. When the  $R$  values are 4.5 and 5.5 mm, then the 20004 Hz and 19999 Hz frequencies are obtained for horn and booster respectively. Hence, it is observed that the natural frequencies of the horns modelled by FEA approaches to the operating frequency of the system.

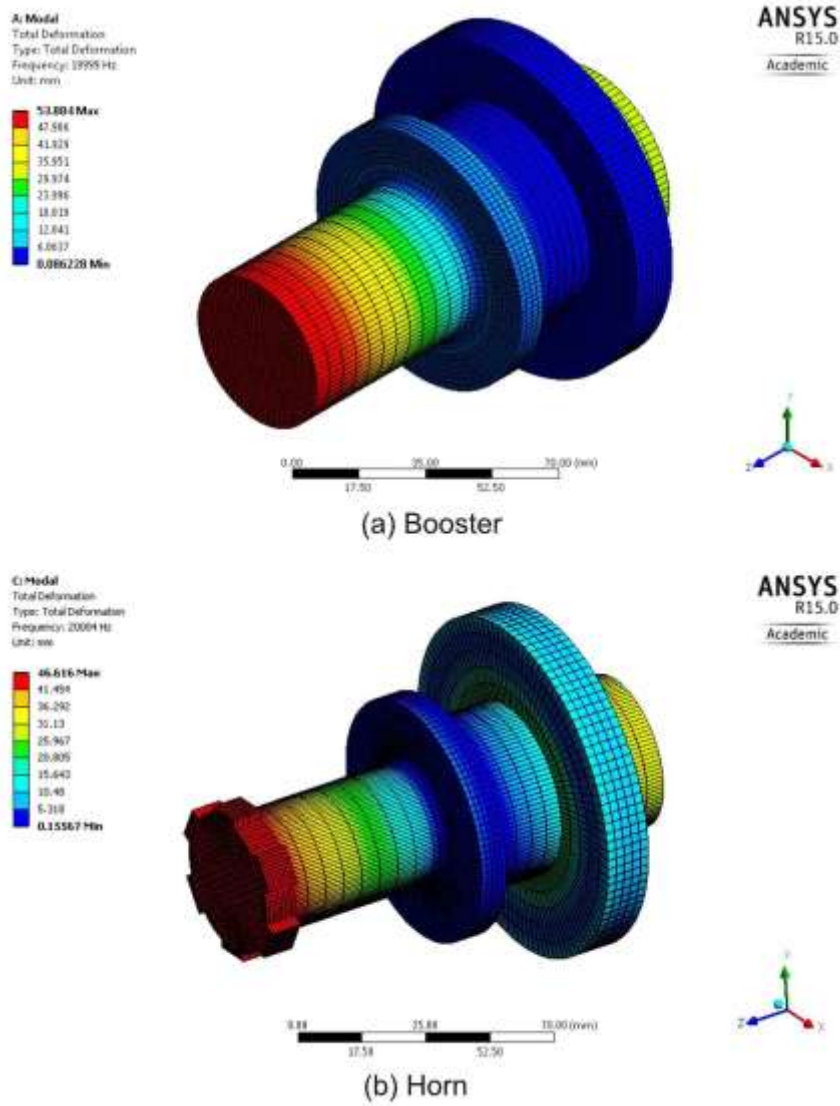


Fig. 3.6 Natural frequencies from modal analysis

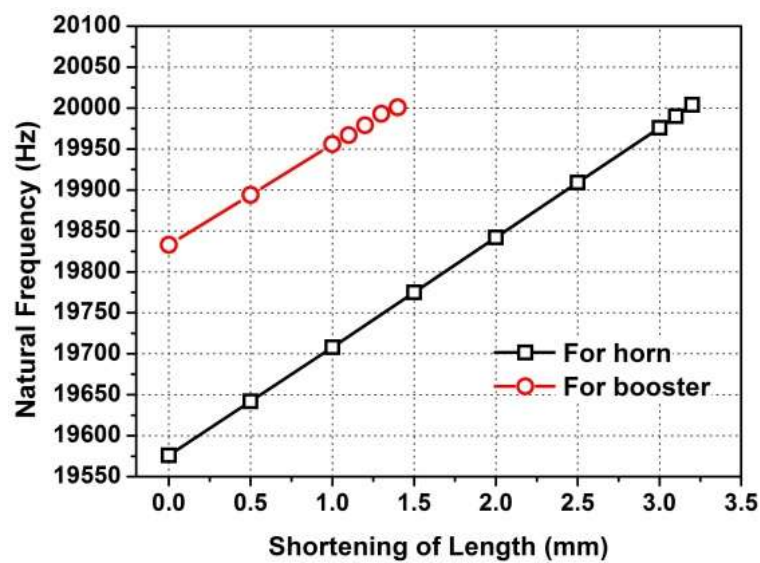


Fig. 3.7 Variation of natural frequencies with shortening of lengths from theoretical ones

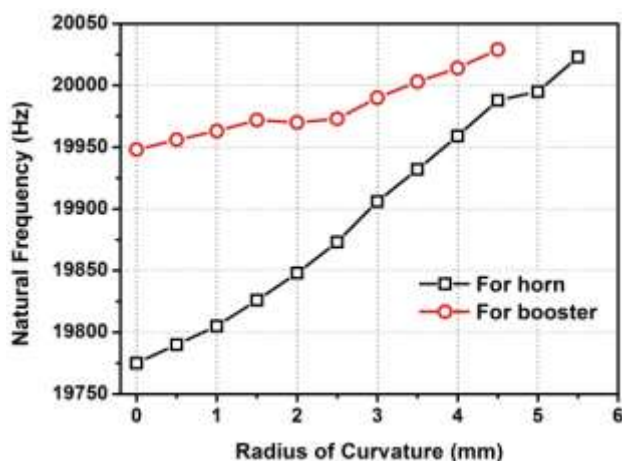


Fig. 3.8 Variation of natural frequencies with radius of curvatures

### 3.4.2 Frequency response analysis

Frequency/harmonic response analysis is a technique used to determine the steady-state response of a linear structure to loads that may vary sinusoidally with time. It involves time history processor, which shows the stresses at different positions of the parts, and displacement of nodes at the booster output end as well as at the free end of the horn. Meanwhile, the analysis has been carried out without considering the damping effect due to the modest damping capacity of horn and booster materials. Therefore, the damping term in Eq. (3.55) is neglected. In the present experimental setup, the ultrasonic generator can produce a maximum amplitude of  $30\ \mu\text{m}$  as per its specifications. By using Eq. (3.41), the amplification factor for both the components is determined as 1.5. Thus, the theoretical output amplitude of the booster and horn is modified to  $45\ \mu\text{m}$  and  $67.5\ \mu\text{m}$  for the first longitudinal vibration frequency. The results obtained from the modal analysis are taken as the input for the harmonic analysis. The graphical representation of amplitude distribution is displayed in Fig. 3.9. The working amplitudes of the booster output end and tool tip are found as  $47.35\ \mu\text{m}$  and  $68.86\ \mu\text{m}$  respectively when the forced frequency matches with the first longitudinal natural frequency of both the parts.

The nodal planes are located at the midsection of the horn and booster which represent a good agreement with the theoretical principles (Fig. 3.10). The present analysis also reveals stresses at different positions of the horn and booster for the frequency given by modal analysis. The stress plots for both components are shown in Fig. 3.11. It indicates that both parts experienced a sinusoidal waveform at the same frequency as the input. According to the stress profile, it is increasing with time up to the nodal position and then gradually fades away. Therefore, the values of stress are found to be minimal at both the free ends, which also satisfy the theoretical principles.

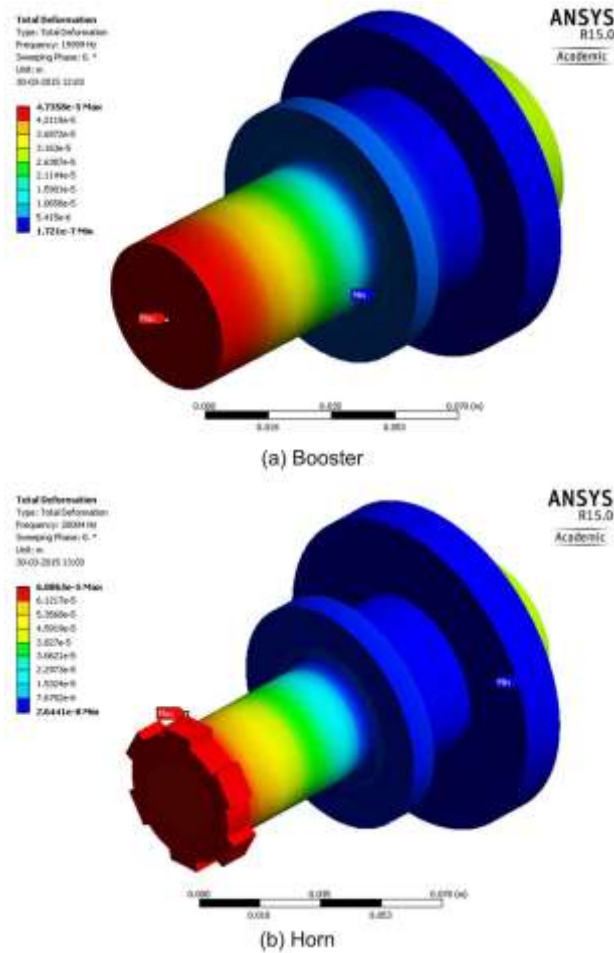


Fig. 3.9 Harmonic analysis of the components showing amplitude distribution

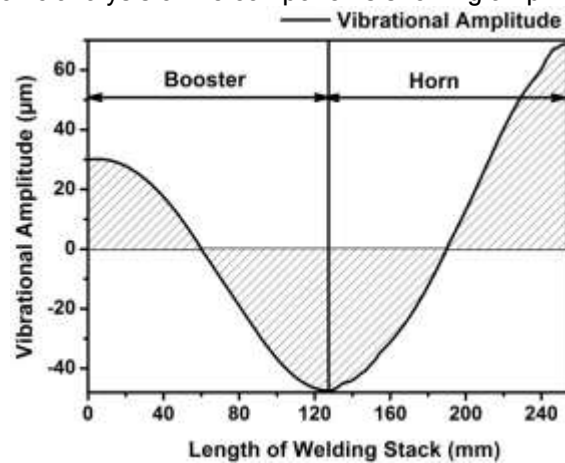


Fig. 3.10 Amplitude variation plot with respect to length of both parts

After the application of the loading condition connected with the longitudinal mode of vibration, the stress of the horn can be analyzed using Von Mises criteria [129]. Fig. 3.12 shows the Von Mises stress distribution along the length of the welding stack. The contour plots represent that it increases with the gradual increase in the length, and becomes maximum at the abruptly changing sections. The maximum stresses observed in this analysis are 196.67 MPa and 576.6 MPa for booster and horn respectively. In this study, the maximum stresses of the horn and booster design are significantly lower than

the yield strength of the D2 steel. Hence, the ultrasonic welding booster and horn can operate within safe operating conditions in terms of stress levels.

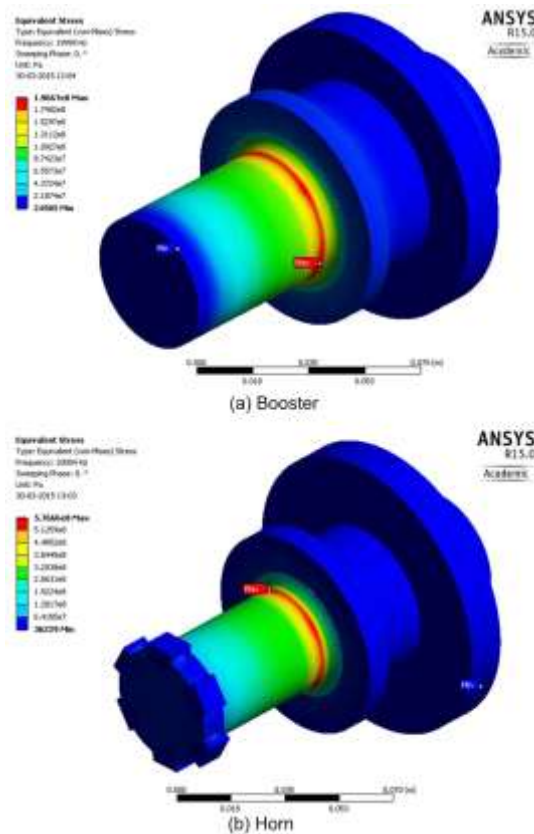


Fig. 3.11 Von Mises stress distributions for both components

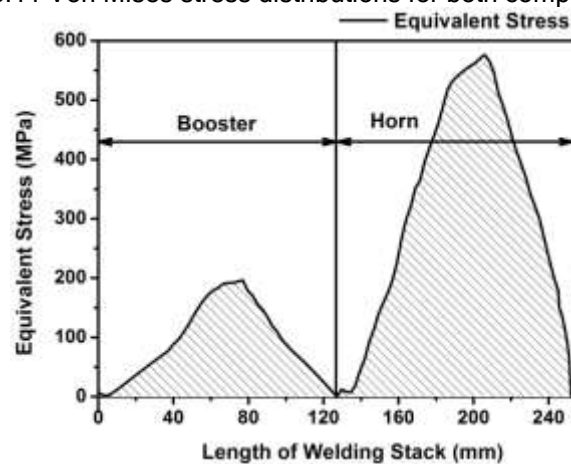


Fig. 3.12 Stress variation plot with respect to length of both parts

### 3.4.3 Horn amplitude uniformity

Amplitude uniformity is defined as the variation between the minimum and maximum amplitude at the weld tip surface of the horn [130]. In USMW, the quality of the joint depends on the uniformity of amplitude. Fig. 3.13 reveals the normalized amplitude (ratio of vibrational amplitudes at different points on the weld tip to the maximum amplitude

observed on the weld tip) of the weld tip surface. From this figure, about 99.8 % of uniformity in amplitude is obtained.

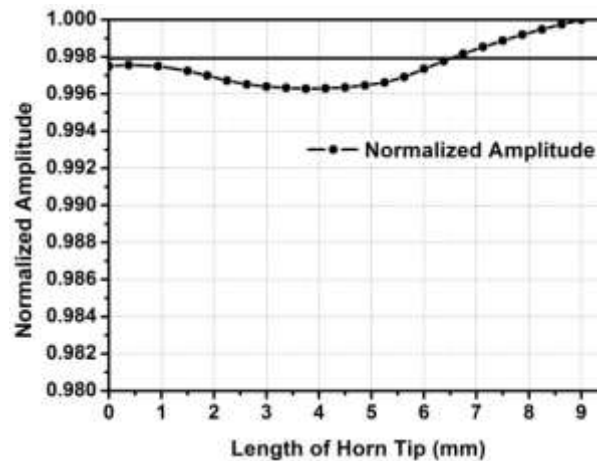


Fig. 3.13 Variation of FE simulated normalized amplitude of horn tip with horn tip length excited at 20.04 kHz

#### 3.4.4 Fatigue analysis of components

According to ASTM [131], fatigue is defined as the phenomenon associated with the gradual and the localized development of permanent changes within the structural body due to the application of repeated stress or strain. In the present context, the horn and booster are subjected to a cyclic loading of 20000 Cycles/Sec. It is expected that the components are working ten hours per day at a rate of producing six welds per minute. Hence, in a year, more than  $10^5$  welds are produced expecting the components are in working condition throughout the year which gives a situation of high cycle fatigue (HCF). Thus, it affects the total life of the tools. Meantime, it is very hard to point out the initiation and proliferation of cracks. It is based on the S-N (stress-cycle) curve. The relevant horn and booster material data are obtained from military handbook [132]. In a conventional USMW operation, the maximum and minimum stress levels are changed or varied according to the loading and unloading conditions. Thus, these type problems are solved by ANSYS<sup>®</sup> fatigue module with non-constant amplitude loading conditions. At the top, middle and bottom parts of the horn and booster have different dimensions, so these parts are experiencing different stress values during the typical welding time of 1 sec and for the remaining 59 sec, these parts are not undergoing any load (as in static state). In this study, the equivalent stress values obtained from harmonic analysis during this welding time are taken as the maximum input values to the fatigue analysis and Gerber hypothesis is preferred to find out mean stress effects as it is quite suitable for ductile material and can consider its -ve and +ve values. To calculate the total amount of fatigue damage, the cumulative damage calculations need to be done by using Miner rule, and it

states that if this value is equal to 1, then the system will fail [133]. It is represented in Fig. 3.14 and mathematically it can be expressed as

$$Cumulative\ damage\ (C_d) = \frac{Design\ life\ (N_i)}{Available\ life\ (N_f)} \quad (3.63)$$

It is observed that, at the top and bottom regions of the booster and horn, the cumulative damages are 0.142 and 0.218 respectively, which are well underneath the limit. However, cumulative damages of 1.175 and 1.111 are found in the nodal regions, where the stresses are high, suggesting possibility of failures of both parts at given working frequencies and amplitudes. The results are summarized in Table 3.2.

Table 3.2 Results of fatigue and vibro-thermographic analyses

Components	Cumulative damage			Temperature at the middle zone from COMSOL® in °C	Temperature at the middle zone from thermocouple in °C
	Top	Bottom	Middle		
Horn (D2 steel)	0.218	0.218	1.111	63.5	64.85
Booster (Ti-6Al-4V)	0.142	0.142	1.175	49.8	50.24

### 3.4.5 Vibro-thermographic analysis of components

During fatigue loading, the components are under repeated elastic cyclic stresses, and the ultrasonic wave propagates through them. For this reason, the heat generation will take place due to elastic deformation of the material. But, when the pressure is released, then it comes back to its actual shape and initial temperature as per the principle of vibro-thermographic analysis [134]. In order to simulate the temperature rise in the specimen, the Dulong-Petit law of the heat transfer equation is used, and it is represented as

$$\rho \cdot C_p \cdot \frac{\partial T}{\partial t} - \nabla(K \cdot \nabla T) = Q_h \quad (3.64)$$

In this study, the 3D modelled horn and booster is considered for the vibro-thermographic analysis; and the gradual elevation of temperature in those vibrating components is simulated by COMSOL® Multiphysics software with proper boundary conditions. Input amplitudes of 30 μm and 45 μm are provided on the top surface of the booster and horn respectively with an excitation frequency of 20 kHz. The heat source in Eq. (3.64) can also be written as [132].

$$Q_h = \frac{1}{2} \omega \cdot \eta \cdot Real[\varepsilon : Conj(C : \varepsilon)] \quad (3.65)$$

Where,  $\omega$  is the angular frequency,  $\eta$  is the isotropic loss factor/ damping coefficient,  $\varepsilon$  is the strain tensor and  $C$  is the elasticity tensor.

In the above expression, the isotropic loss factors are varied from 0.001 to 0.008 for both systems. These factors are calculated until the error between the simulated values and experimental results are reached a minimum value. At the same time, the initial temperature is assumed as 293.15 K with a thermal insulation condition applied to the



surface where the load is applied. Other than these two ends, all other boundaries are subject to a convective cooling condition, and the corresponding convective heat transfer coefficient is taken as  $5 \text{ W/m}^2\cdot\text{K}$  [135]. The predicted temperatures achieved from this analysis are shown in Fig. 3.15.

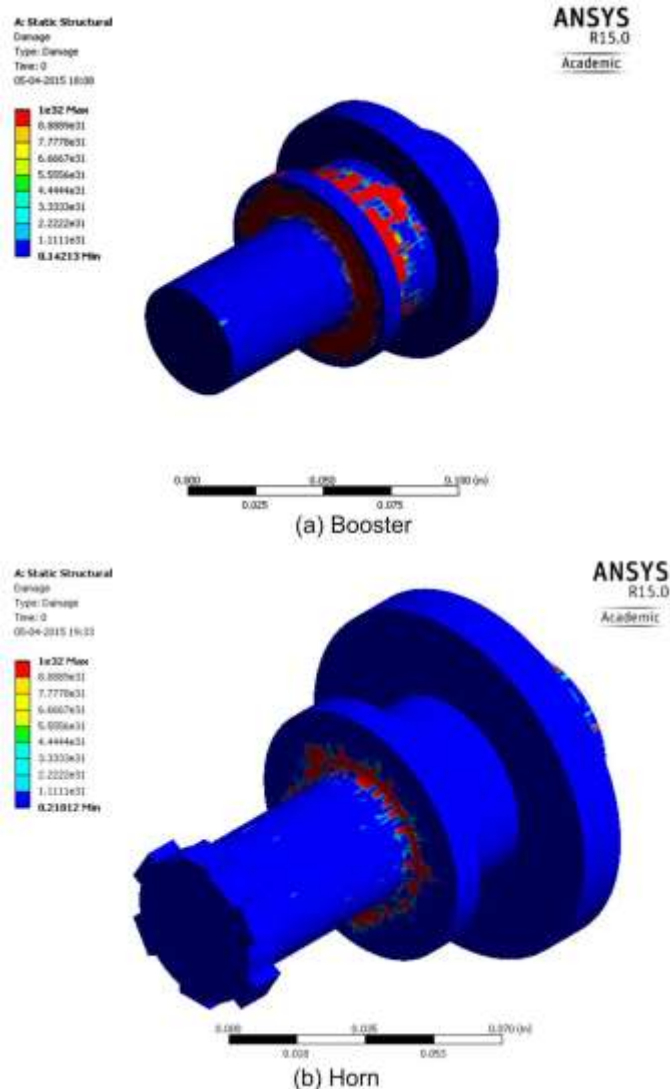


Fig. 3.14 Cumulative damage calculation from fatigue analysis

Meanwhile, the vibro-thermographic analyses results of the different parts are compared with the temperature values got experimentally using thermocouples (Table 3.2). It is shown that the D2 steel horn has a higher temperature of  $63.5^\circ\text{C}$  at the nodal region followed by the titanium booster. It is because of high internal damping takes place within the horn, which causes the decrease in elastic modulus and density of the material. At the same time, the stress produced in the booster is much below than the horn and the internal damping coefficient is lesser as compared to the horn. For this reason; the vibrations can be easily transmitted through it to the horn for the effective welding of thin metal sheets. Meantime, the errors of 2.08% and 0.87% are obtained for horn and booster while comparing the experimental temperature values with the simulated results.

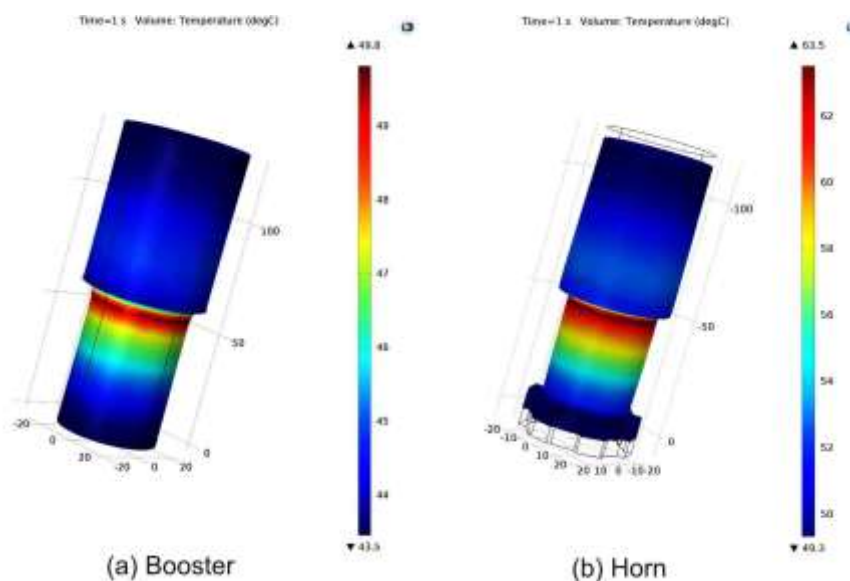


Fig. 3.15 Predicted temperatures from vibro-thermographic analysis

### 3.4.6 Simultaneous simulation of both components

Designing of the welding stack (composed of horn and the booster) is really a challenging task because the high-frequency vibration should precisely occur at the welding tip and the amplitude should be maximized at the welding tip. In this analysis, both of these components have been investigated simultaneously instead of considering separately. From the harmonic analysis, it has been observed that the input amplitude is modified by 1.509 times for the booster, and again it is amplified by 1.5 times for the horn to create a good weld between the sheets. Thus, at the end of horn 67.92  $\mu\text{m}$  amplitude is obtained and this value is quite close to the theoretical result. Also at the nodal position of the booster and horn, i.e. at 65.4 mm and 192.2 mm, the amplitude becomes zero, and the Von Mises stresses turn out to be 187.7 MPa and 563.08 MPa respectively. These variations in amplitude and stresses with the length of welding stack are given Fig. 3.16. The summary of the results are given in Table 3.3, and it signifies that there are 1.11 % and 2.52 % errors in the length calculation of both systems. Similarly, 0.61 % error is obtained for both systems while calculating the magnification ratio.

Table 3.3 Comparison between theoretical and FEM results of booster with horn

Sl No.	Factors	Theoretical calculated horn	Theoretical calculated booster	FEM Analysed horn	FEM Analysed booster	% error in horn	% error in booster
1	Frequency (kHz)	20	20	20	20	0	0
2	Total length (mm)	130	126.8	126.8	125.4	2.52	1.11
3	Diameter ratio	1.25:1	1.25:1	1.25:1	1.25:1	0	0
4	Magnification factor	1.5	1.5	1.5	1.509	0.61	0.61

## **3.5 Manufacturing of Various Horns and A Booster**

These two parts are fabricated using the computer numerically controlled (CNC) machine for the practical tests. A working sketch of the components can be seen from *Appendix A*, are manufactured by Telsonic® industries, Switzerland. Fig. 3.17 depicts the various types of horns and booster those were used not only for welding but also for other ultrasonic assisted manufacturing processes working at 20.04 kHz.

## **3.6 Design of Sonotrode Tip and Anvil**

The design of ultrasonic tooling plays a significant role in the determination of quality and strength of the welding. The ultrasonic tooling consists of sonotrode tip and anvil. For effective transmission of ultrasonic energy to the welding surface, the ultrasonic vibration is applied to the horn tip initially and at the same time, the anvil is kept as a static one. With proper design of the tool texture and anvil geometry keeping the machine parameters aside, a good weld can be obtained. Thus, the weld tip needs to be made up of materials those have good fatigue strength, wear resistance, corrosion properties and it should not be readily bonded with the workpiece (pre-welding or tip sticking) [81].

Therefore, to avoid the tip sticking phenomenon, the patterns are engraved on the tip surface where the welding happens between aluminum with other high strength materials [136]. Although, the tool textures are not well described for the welding of high thickness advanced alloys, a knurl pattern of approximately  $\frac{1}{2}$  of the specimen thickness has been observed in one of the EWI project [137]. Normally, the tip length should be 50 to 100 times of the workpiece thickness [138] because the tangential forces at the weld zone become more uniform on increasing the length of the tip. Similarly, a good anvil design provides proper friction between the weld coupons and avoids slippage between the sonotrode and top part. It also acts as a rigid support to the substrate. As this component is not ultrasonically driven and comparatively large surface area than the weld tip, a less aggressive knurl pattern can be used [138].

### **3.6.1 Material selection**

Significant amount of literature are reviewed for the tool materials that are likely implemented for a broad range of materials, industries and welding technologies [136]. The following materials are used for making the anvil:

*AISI Type 304 Stainless steel:* Austenitic 18Cr-8Ni-2Mn stainless steel with face-centered cubic structure. It is broadly used in industries because of its high wear resistance, excellent corrosion resistance, and superior hardness properties.

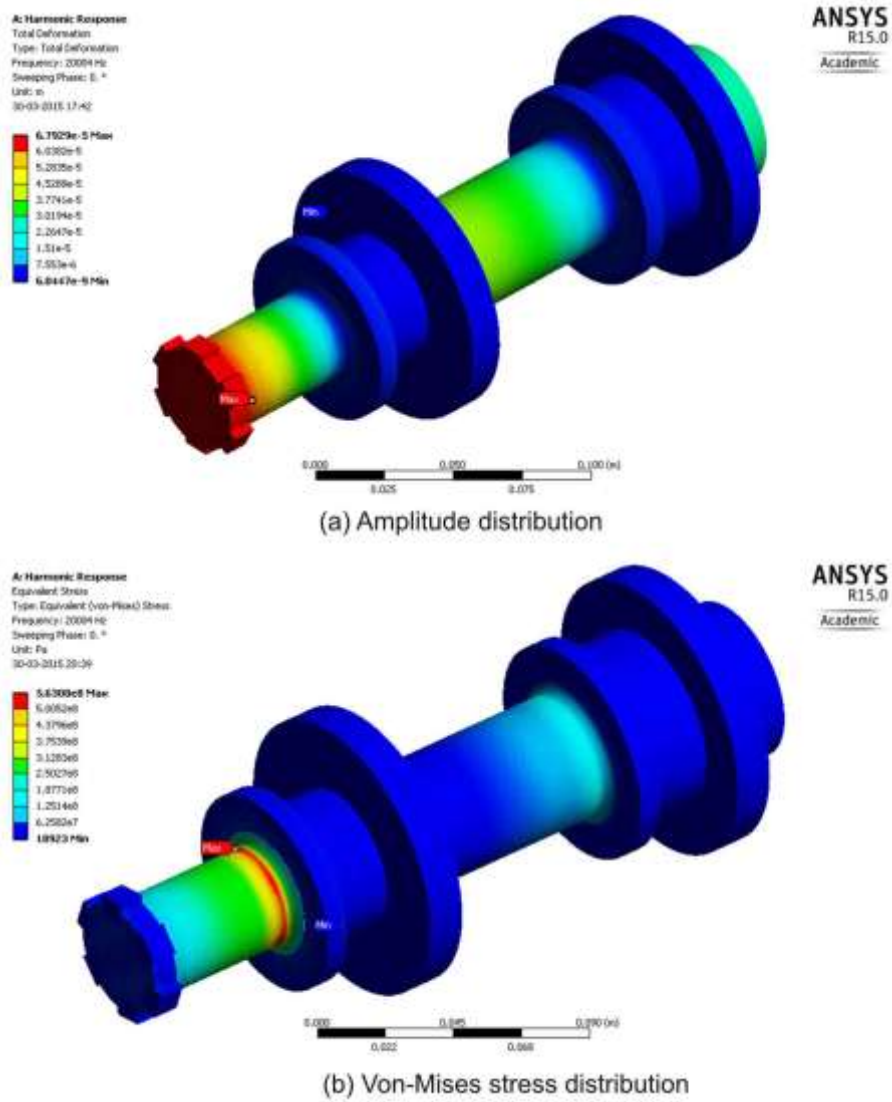


Fig. 3.16 Simulated results of amplitude and stress distributions for booster with horn



Fig. 3.17 Manufactured various spot welding horns and booster

*D2 steel*: Martensitic 12Cr-0.8Mo-0.8V tool steel with body-centered cubic structure. It has the properties like high wear resistance, good toughness value, great high-temperature deformation resistance and superior fracture property under high loads and also softening at elevated temperature.

An explanation is necessary regarding the material properties of the anvil because that may affect the ultrasonic weldability. In the present study, increasing the amount of nickel content in the stainless steel improves the fatigue strength, corrosion resistance and high-temperature strength at the elevated temperature and excessive stress surroundings [139]. In the presence of oxygen, the addition of chromium content in the stainless steel creates an environment for the formation of a continuous passive film to protect from corrosion. The addition of manganese also increases the hardenability and counteracts the brittleness due to the presence of sulfur. Likewise, D2 steel is the second type of tool material that can be easily machined using conventional techniques, less expensive and relatively available than the stainless steel. The alloying elements present in it are chromium, molybdenum, tungsten, and vanadium and these elements make possible for these alloys to resist severe service conditions [140]. It is important to note that all the relevant properties like hardenability, creep strength, corrosion resistance and wear resistance of the tool are enhanced by the addition of vanadium and molybdenum. Meanwhile, it should be noticed that no single tool possesses all the desired properties, therefore for joining a particular combination of materials; the anvil material should be chosen judiciously to achieve a good joint. Some more relevant information about the properties of these materials is summarized in Table 3.4. These mechanical and physical properties with the chemical compositions were obtained from the material test reports provided by the manufacturer, Matweb [126] and ASM handbooks [139].

Table 3.4 Material properties of anvil

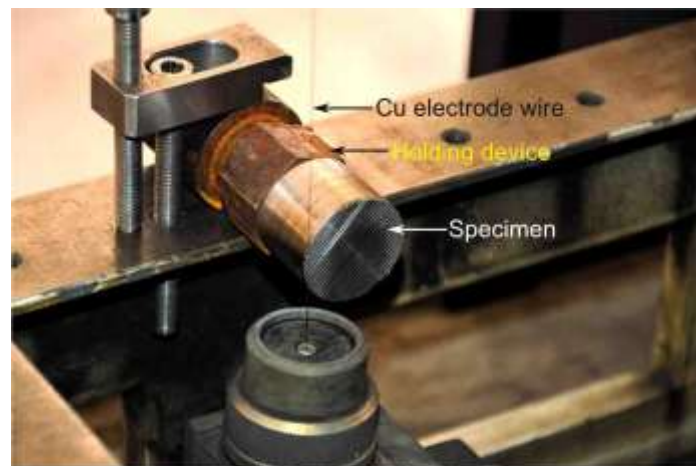
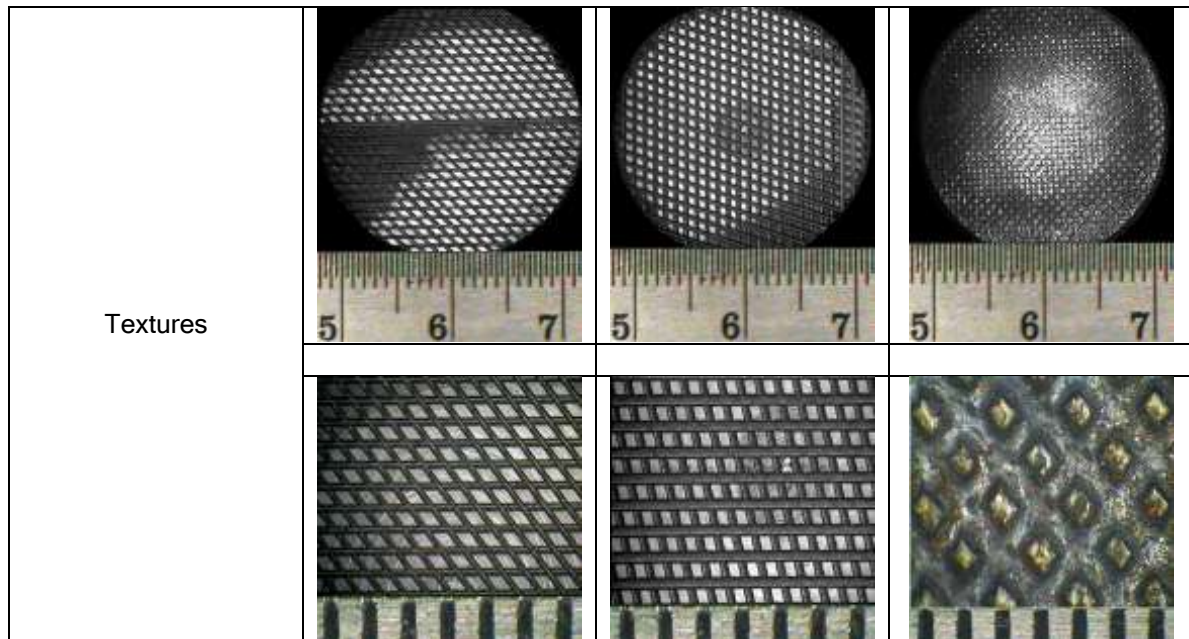
Property	Units	D2 steel	SS 304
Common name		AISI type D2 tool steel	AISI type 304 Stainless steel
Hardness	HV	220	161.4
Density ( $\rho$ )	Kg/m <sup>3</sup>	7670	8000
Young's modulus (E)	GPa	210	193
Yield strength	MPa	1650	215
Ultimate tensile strength	MPa	1916	505
Compositions	wt %	1.55C, 18Cr, 0.4Mn, 0.3Si, 0.8Mo, 0.8V, Fe (Bal)	0.08C, 18Cr, 2Mn, 8Ni, 0.045P, 1.0Si, 0.03S, Fe (Bal)
Applications		Tools requiring very high wear resistance with moderate toughness (shock-resistance)	Cooking equipment, cooling coils, cryogenic vessels, food processing equipment, hospital surgical equipment, nuclear vessels

### 3.6.2 Equipment employed for anvil development

Fabrication of anvil is necessary to perform experiments, and this work has been accomplished by the exact design of anvil shown in *Appendix A*. This design is made according to the specification of ultrasonic welding machine. As the weld tips are an integral part of the horn, the knurl patterns present on it were made while the horn was manufactured. At the same time, the D2 steel anvil was also made by the Telsonic® industries. The present study describes the machines used for developing the SS 304 anvil. A long rod of SS 304 cut into two pieces by using a power saw equipped with a bi-metal blade (*Appendix B*). Sufficient tolerances were given at the time of cutting in order to avoid any discrepancies in dimensional accuracy. For reducing the diameter of the SS 304 bar to 32.0 mm, carbide tipped tool with a 3 jaw chuck lathe (*Appendix B*) was employed for turning purpose and facing was also done to reduce the length to 25.6 mm. After the tools had been in proper dimension and shape, these were made stepped using a computer numerical control (CNC) milling machine shown in *Appendix B*. Thus, the top part of the anvil surface was machined to the diameter of 14.8 mm for a 2.0 mm depth. This was machined according to the base plate dimensions represented in *Appendix A*. In fact; the base plate was acting as a connecting component between anvil and force dynamometer. For attaching the anvil to the base plate, the drilling was done with 6.9 mm diameter by a 7.0 mm high-speed steel (HSS) end mill cutter up to a depth of 12.0 mm. This drilled hole was internally threaded using an 8.0 mm HSS taper. Finally, the surface textures were made by the wire EDM machine (*Appendix B*) according to the specifications given in Table 3.5. As per the given values, a program was written in G codes with space coordinates and fed into the machine for cutting purpose. In this machine there was no holding device to hold the specimen so, to overcome this; a holding device was made from a scrap mild steel piece shown in *Appendix B*. During the cutting, a depth of cut of 0.6 mm was given with the angles. Fig. 3.18 represents the stages of creating knurl patterns using wire EDM machine. Different anvil textures and weld tip designs are shown in Table 3.5 and Table 3.6.

Table 3.5 Stereoscopic pictures of anvil tool geometries with specifications (scale in mm)

Anvil cap no.	1	2	3
Material	SS 304	SS 304	D2 steel
Cutting width (mm)	0.55	0.55	0.55
Non cutting width (mm)	1	1	0.65
Angle(degrees)	75	45	75
Shape	Parallelogram	Parallelogram	Truncated pyramid













(a) Status: M/C off



(b) Status: M/C on

Fig. 3.18 Stages of cutting operation on the surface of anvil using wire EDM

Table 3.6 Stereoscopic pictures of weld tip geometries with specifications (scale in mm)

Weld tip no. with specifications	Textures	
<p>Tip 1, Truncated pyramid type knurls with cutting width of 0.1 mm and non-cutting width of 0.4 mm at 90° angle</p>		
<p>Tip 2, Truncated pyramid type knurls with cutting width of 0.1 mm and non-cutting width of 0.17 mm at 45° angle</p>		
<p>Tip 3, Truncated pyramid groove type knurls with cutting width of 0.17 and 0.1 mm with non-cutting width of 0.45 and 0.5 mm at 50° angle</p>		
<p>Tip 4, Truncated pyramid type knurls with cutting width of 0.1 mm and non-cutting width of 0.3 mm at 45° angle</p>		
<p>Tip 5, Truncated pyramid groove type knurls with cutting width of 0.15 mm and non-cutting width of 0.3 mm at 45° angle</p>		





### 3.7 Introduction to Thermo-Mechanical Analysis of USMW

USMW uses high-frequency vibration, usually of 20 kHz or above with clamping pressure to provide friction like motion between the two metal surfaces. During this motion, the impurities and oxide layers deform present on it disappear and create a suitable environment for metal-to-metal contact. As this is a solid state welding process, the bonding occurs below the melting point of the base material, and it is due to frictional heating, interatomic diffusion, and mechanical interlocking. The greatest advantages of this process are the absence of liquid-solid transformations, no atmospheric contamination, and nature-friendliness, which can't be seen in other competing processes like resistance spot welding. In addition, the ultrasonic spot welding is the favoured technique for aluminium and its alloys while comparing the joint strengths with other techniques under quasi-static and dynamic loading [85]. The sonotrode is one of the parts of a system that directly touches the upper surface of the specimen and vibrates parallel to the plane of the weld interface and perpendicular to the axis of clamping force application. Consequently, the vibratory energy is transmitted to the weld spot. Initially, these micro weld spots are elliptical in shape, and gradually the size of weld spots increase over the course of time to form a continuous weld joint as shown in Fig. 3.19.

In this section, the mechanics behind the ultrasonic welding process is described. The primary objective of this work is to investigate a process model that will predict the forces like shear force ( $F_{SH}$ ) and static normal force ( $N$ ) at the weld interface during the welding, and it will also give an idea to the welder to predict the unfavorable condition, which will not produce any sound weld. The assumptions are:

- (i) Only top and bottom layer/surfaces experience plastic deformation when yield condition is met for the top part.
- (ii) The compressive stress on the top part is constant and uniform. This is given by  $N/S_H$  or  $S_{DZ}$ .
- (iii) Additionally, it has been found experimentally that the area in which welding occurs does not go beyond the horn area. This means  $S_W \leq S_H$  for all the conditions.

- (iv) The elongated part of the top workpiece is treated as the elastic rod excited at the face which in contact with the welded part.
- (v) The bottom workpiece is rigid and fixed as the anvil and hence the forces act on the lower surfaces of the bottom workpiece and anvil surfaces is of equal amount and in opposite direction.

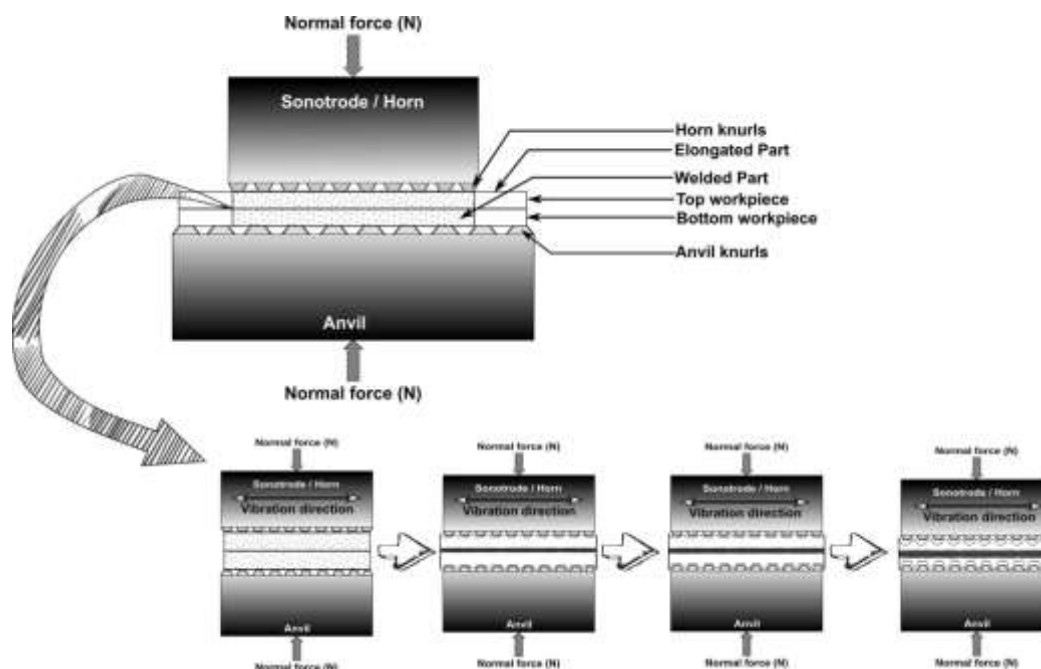


Fig. 3.19 Detailed schematic presentation of weld area growth with time

From Fig. 3.20, the equilibrium of forces for the top part can be written as

$$m \times \ddot{\xi}_{max} = F_{SH} - F_{PW} - F_{FR1} - F_{FR2} - F_E \quad (3.66)$$

Thus, to determine the forces which are described in Eq. (3.66), *structural analysis* of the welding is carried out.

### 3.8 Structural Analysis

When the knurl patterns of the sonotrode and anvil are engaged into the specimens, it results in a complex local stress pattern produced in it due to the sharp peaks. Thus, the elastic-plastic deformation takes place under the peaks and valleys of knurls. However, this complex pattern of stresses will die out at some distance from the sonotrode penetration. Thus, the knurling effect on the stress field will be no longer available. But for the determination of shear force of the horn, a layer of the top workpiece which is just under the sonotrode knurl is taken for investigation. It is assumed that the stress field is uniform in this layer as shown in Fig. 3.21. There are two elements considered in this layer. The element “A” is under the knurl and “B” represents the element that is present in

between the two knurls where the friction takes place. In the present analysis the element “A” is considered as the zone where the actual weld is taken place.

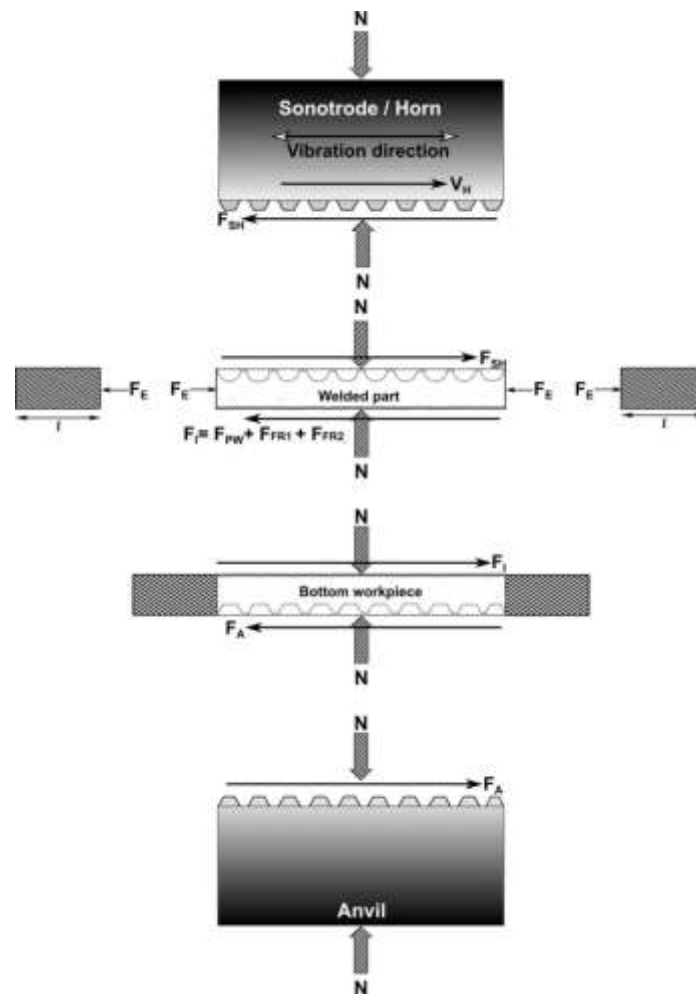


Fig. 3.20 Detailed analysis of forces acting on individual components during the welding [18]

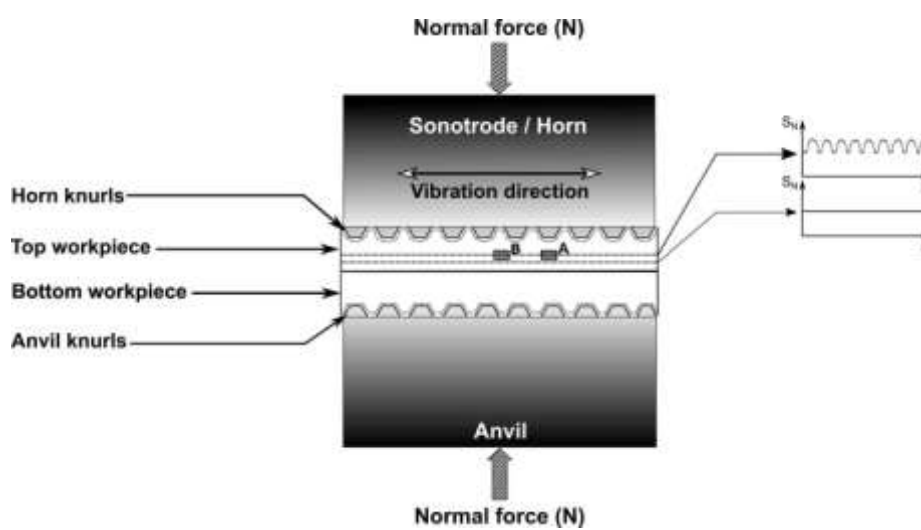


Fig. 3.21 Stress distribution under the knurls pattern during [18]

### 3.8.1 Shear force exerted by horn

However, the element "A" is subjected to plastic deformation during the welding because of the synergetic effects of the combined compressive and shearing stresses. The shearing and compressive forces that are acting on this element are presented in Fig. 3.22. The limits of the shear stress can be found out by applying principal stress condition and Tresca's yield criteria.

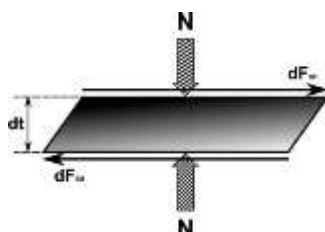


Fig. 3.22 Small element of top workpiece under the sonotrode knurl

**(i) Principal stress condition:**

Let's take an inclined plane of a uniform stressed rectangular component, whose thickness is unity. The shear stresses on this plane are equal ( $\tau_{xy} = \tau_{yx}$ ). For better clarification, a 3D element is taken to represent the principal stresses, and it is shown in Fig. 3.23.

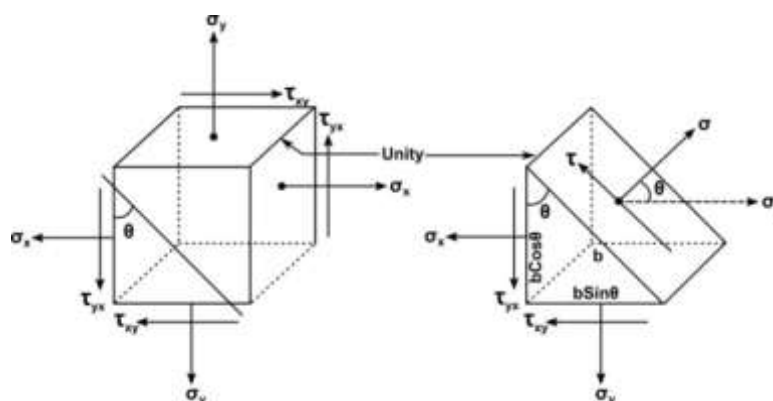


Fig. 3.23 A 3D element for representation of principal stress

Considering equilibrium of forces in x-direction

$$\sigma \cdot \cos \theta \cdot b \cdot (1) - \sigma_x \cdot b \cdot \cos \theta \cdot (1) - \tau_{xy} \cdot b \cdot \sin \theta \cdot (1) = 0 \quad (3.67)$$

$$(\sigma - \sigma_x) = \tau_{xy} \cdot \tan \theta \quad (3.68)$$

Similarly considering equilibrium of forces in y-direction

$$\sigma \cdot \sin \theta \cdot b \cdot (1) - \sigma_y \cdot b \cdot \sin \theta \cdot (1) - \tau_{yx} \cdot b \cdot \cos \theta \cdot (1) = 0 \quad (3.69)$$

$$(\sigma - \sigma_y) = \tau_{yx} \cdot \cot \theta \quad (3.70)$$

Multiplying Eq. (3.68) and (3.70)

$$(\sigma - \sigma_x)(\sigma - \sigma_y) = \tau_{xy} \cdot \tau_{yx} \cdot \tan \theta \cdot \cot \theta \quad (3.71)$$

$$(\sigma - \sigma_x)(\sigma - \sigma_y) = \tau_{xy}^2 \quad (3.72)$$

Eq. (3.72) is a quadratic equation and its solutions are

$$\sigma_1 = \left(\frac{\sigma_x + \sigma_y}{2}\right) + \frac{1}{2}\sqrt{(\sigma_x - \sigma_y)^2 + 4\tau_{xy}^2} \quad (3.73)$$

$$\sigma_2 = \left(\frac{\sigma_x + \sigma_y}{2}\right) - \frac{1}{2}\sqrt{(\sigma_x - \sigma_y)^2 + 4\tau_{xy}^2} \quad (3.74)$$

In ultrasonic welding, as the forces are acting on the surface vertically thus,  $\sigma_x = 0$ . Then, the above two equations can be reduced to

$$\sigma_1 = \left(\frac{\sigma_y}{2}\right) + \frac{1}{2}\sqrt{(\sigma_y)^2 + 4\tau_{xy}^2} \quad (3.75)$$

$$\sigma_2 = \left(\frac{\sigma_y}{2}\right) - \frac{1}{2}\sqrt{(\sigma_y)^2 + 4\tau_{xy}^2} \quad (3.76)$$

**(ii) Tresca's yield criteria:**

According to this criteria, the yield will take place when the maximum value of  $|\sigma_1 - \sigma_2|, |\sigma_2 - \sigma_3|, |\sigma_3 - \sigma_1| = 2K$  or  $Y$ . Thus from Eq. (3.75) and (3.76)

$$|\sigma_1 - \sigma_2| = 2\sqrt{\left(\frac{\sigma_y}{2}\right)^2 + \tau_{xy}^2} \quad (3.77)$$

$$|\sigma_2 - \sigma_3| = \frac{\sigma_y}{2} - 2\sqrt{\left(\frac{\sigma_y}{2}\right)^2 + \tau_{xy}^2} \quad (3.78)$$

$$|\sigma_3 - \sigma_1| = -\frac{\sigma_y}{2} - 2\sqrt{\left(\frac{\sigma_y}{2}\right)^2 + \tau_{xy}^2} \quad (3.79)$$

Out of the above three equations, Eq. (3.77) will give the maximum value. So

$$|\sigma_1 - \sigma_2| = 2K \text{ or } Y \quad (3.80)$$

$$2\sqrt{\left(\frac{\sigma_y}{2}\right)^2 + \tau_{xy}^2} = Y \quad (3.81)$$

$$\tau_{xy} = \sqrt{\frac{Y^2}{4} - \left(\frac{\sigma_y}{2}\right)^2} \quad (3.82)$$

This  $\tau_{xy}$  is responsible for the plastic deformation in the volume inside the weld zone. Thus, for the small element shown in Fig. 3.22, the shear stress is

$$\tau_s = \frac{dF_{SH}}{dS} \quad (3.83)$$

$$\int dF_{SH} = \int \tau_s \cdot dS \quad (3.84)$$

$$F_{SH} = \sqrt{\frac{Y(T)^2}{4} - \left(\frac{N/S_H}{2}\right)^2} \times S_H \quad (3.85)$$

Cases:

- (i) If  $F_{SH} < \tau_S \times S_H$ : Top workpiece will only vibrate and no relative motion is observed between the horn and workpiece.
- (ii) If  $F_{SH} = \tau_S \times S_H$ : Top workpiece will move relative to the motion of the horn and therefore extrusion and yielding occurs in the top part.

It is worth noting that the stresses and plastic deformation occur just below the sonotrode tip when it satisfies the second case. In USMW, *sublayer plastic deformation and atomic adhesion* are the two major criteria for joining.

### 3.8.2 Shear force at weld interface

In order to calculate the shear force at the weld interface, the problem is divided into two parts

- (A) Forces related to the dynamics of the top workpiece
- (B) Interface forces between the workpieces

Both of these problems will be analyzed separately in the following sections.

#### (A) Forces related to the dynamics of the top workpiece

*Case 1: Both workpieces have the same dimensions as horn*

The Fig. 3.24 shows the parts isolated from the sonotrode and anvil with normal and shear forces acting on both. In this case, both top and bottom workpieces are treated as rigid and have similar dimension as of horn. Due to the rigidity property of the material, elastic deformation due to shear is negligible. It is believed that the movement of the horn will produce an oscillating force on the workpieces. As these parts have the same dimension as of horn tip, the resonance effect of larger parts is neglected in this case.

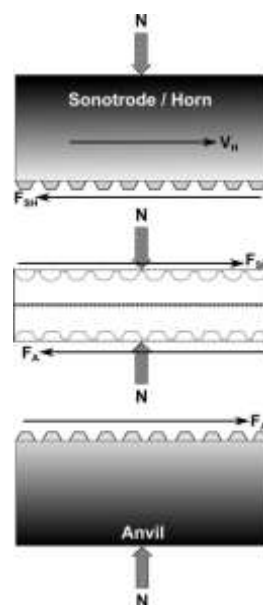


Fig. 3.24 Free body diagram of workpieces, horn, and anvil [18]

During the welding, it has been noticed that initially friction happens due to ultrasonic vibration. Thus, some amount of heat is produced, and it leads to a formation of thin film of plastic deformation as shown in Fig. 3.25. In this figure, the two parts are separated from each other to show the interface force  $F_I$ .

As the horn moves with some amplitude, the top workpiece is also moving with the same amplitude. As the motion is oscillatory in nature thus, the amplitude of top part can be written as

$$\xi_T(t) = \xi_h \cos(\omega t) \quad (3.86)$$

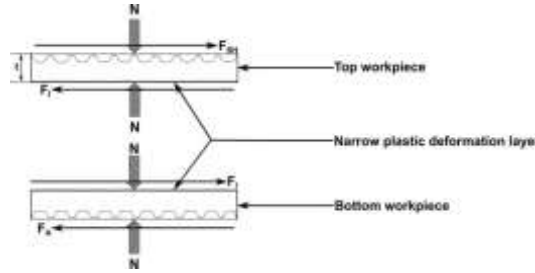


Fig. 3.25 Free body diagram of both top and bottom workpieces [18]

Similarly, the acceleration of top workpiece is also same as the acceleration of the horn and can be presented as

$$\frac{d^2 \xi_T}{dt^2} = -\omega^2 \cdot \xi_h \cdot \cos(\omega t) \quad (3.87)$$

Therefore, at the maximum amplitude, the deformation of the top workpiece is maximum due to the high relative motion. Thus,  $F_{SH}$  and  $F_I$  forces are also maximum at this point, and the net force acting at the maximum deflection condition is

$$m \cdot \ddot{\xi}_{max} = F_{SH} - F_I \quad (3.88)$$

$$\rho \cdot S_h \cdot t \cdot (\omega^2 \xi_h) = F_{SH} - F_I \quad (3.89)$$

In all the cases, the bottom part is assumed to be rigid and fixed to the anvil. So, there is no relative motion between the anvil and bottom workpiece. Thus, the forces developed here are also same.

$$F_A = F_I \quad (3.90)$$

*Case II: Both workpieces have different dimensions as horn*

It is very rare that the workpieces have the same dimension as the horn tip size. When the top workpiece is extended in both longitudinal and lateral direction, then the rigid part assumption to the top surface is no longer valid. It is due to the fact that the extended part will vibrate elastically, and the anti-resonance condition is developed. Therefore, the top part is divided into two zones (a) rigid zone and (b) elongated zone. These two regions are schematically represented in Fig. 3.26.

As previously described, the rigid top part will move according to the movement of the horn. Thus, the elongated part will also get excited with horn velocity and frequency.

Therefore, it is a case of forced vibration, and the elongated part is treated as a rod to find the excitation force ( $F_E$ ). Here the welding happens only in the rigid zone so, the net force on it will be

$$m \cdot \ddot{\xi}_{max} = F_{SH} - F_I - F_E \quad (3.91)$$

The one-dimensional governing equation for a vibrated top part can be written as

$$\frac{\partial^2 U}{\partial x^2} = \frac{1}{C^2} \frac{\partial^2 U}{\partial t^2} \quad (3.92)$$

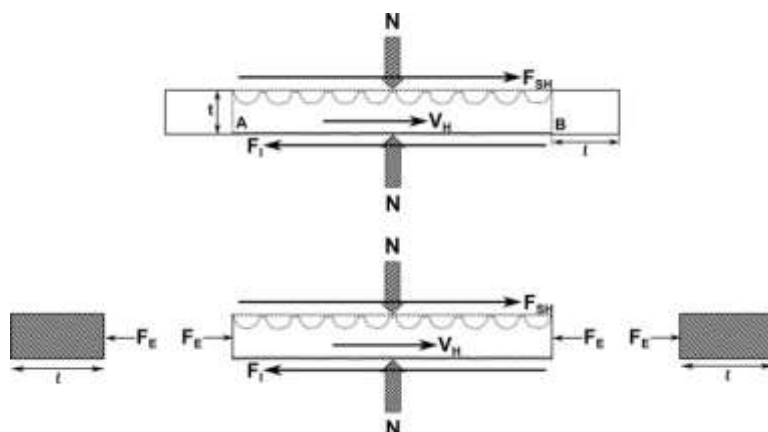


Fig. 3.26 Free body diagram of welded part with it's forced vibrated elongated part [18]

The solutions to the above equation can be represented as

$$U(x, t) = \left[ A \cos\left(\frac{\omega}{C}\right)x + B \sin\left(\frac{\omega}{C}\right)x \right] [C \cos \omega t + D \sin \omega t] \quad (3.93)$$

To determine the constants A, B, C, D, the boundary conditions are applied.

(i) When time( $t$ ) = 0, initial displacement  $u(x,0)=0$ . Thus, Eq. (3.93) can be written as

$$U(x, 0) = \left[ A \cos\left(\frac{\omega}{C}\right)x + B \sin\left(\frac{\omega}{C}\right)x \right] [C \cdot 1] = 0 \quad (3.94)$$

In this case,

$$\left[ A \cos\left(\frac{\omega}{C}\right)x + B \sin\left(\frac{\omega}{C}\right)x \right] \neq 0$$

So

$$C = 0 \quad (3.95)$$

(ii) At this point, the velocity also becomes zero i.e.  $\dot{U}(x, 0) = 0$ . Thus Eq. (3.93) can be written as

$$\frac{\partial}{\partial t} \left[ \left[ A \cos\left(\frac{\omega}{C}\right)x + B \sin\left(\frac{\omega}{C}\right)x \right] [C \cos \omega t + D \sin \omega t] \right] = 0 \quad (3.96)$$

$$\left[ A \cos\left(\frac{\omega}{C}\right)x + B \sin\left(\frac{\omega}{C}\right)x \right] D \cdot \omega \cdot \cos \omega t = 0 \quad (3.97)$$

In this case,  $D \cdot \omega \neq 0$ , thus

$$\cos \omega t = 0 \text{ and } \omega t = \frac{\pi}{2} \quad (3.98)$$

After putting the values of Eq. (3.95) and (3.98) in Eq. (3.93), then



$$U(x, t) = \left[ A \cos\left(\frac{\omega}{C}x\right) + B \sin\left(\frac{\omega}{C}x\right) \right] \times D \quad (3.99)$$

(iii) At the initial starting point i.e.  $U(0, t) = \xi_h$ . Thus Eq. (3.100) can be expressed as

$$U(0, t) = [A \times 1 + B \times 0] \times D \quad (3.100)$$

$$AD = \xi_h \quad (3.101)$$

(iv) The deformation at the end of the rod is also zero. Thus,

$$\frac{\partial U}{\partial x}(l, t) = 0 \quad (3.102)$$

$$\frac{\partial}{\partial x} \left[ A \cos\left(\frac{\omega}{C}x\right) + B \sin\left(\frac{\omega}{C}x\right) \right] \times D = 0 \quad (3.103)$$

$$\frac{-A\omega}{C} D \sin\left(\frac{\omega}{C}x\right) + BD \cdot \frac{\omega}{C} \cdot \cos\left(\frac{\omega}{C}x\right) = 0 \quad (3.104)$$

At the end of the rod, when  $x=l$ . So, Eq. (3.105) becomes

$$\frac{-A\omega}{C} D \sin\left(\frac{\omega}{C}l\right) = -BD \cdot \frac{\omega}{C} \cdot \cos\left(\frac{\omega}{C}l\right) \quad (3.105)$$

$$BD = \xi_h \cdot \tan\left(\frac{\omega l}{C}\right) \quad (3.106)$$

After finding out all the constants, the final equation can be written as

$$U = \left[ A \cos\left(\frac{\omega}{C}x\right) + B \sin\left(\frac{\omega}{C}x\right) \right] \times D \quad (3.107)$$

$$U = \left[ \xi_h \cdot \cos\left(\frac{\omega}{C}x\right) + \xi_h \cdot \tan\left(\frac{\omega l}{C}\right) \cdot \sin\left(\frac{\omega}{C}x\right) \right] \quad (3.108)$$

The excitation force for the elongated part can be presented as

$$F_E = \sigma \times S \quad (3.109)$$

$$F_E = S_H \times E \times \frac{\partial U}{\partial x} \quad (3.110)$$

After putting the values of U from Eq. (3.108)

$$F_E = S_H \times E \times \left[ \frac{\partial}{\partial x} \left[ \xi_h \cdot \cos\left(\frac{\omega}{C}x\right) + \xi_h \cdot \tan\left(\frac{\omega l}{C}\right) \cdot \sin\left(\frac{\omega}{C}x\right) \right] \right] \quad (3.111)$$

$$F_E = S_H \times E \times \left[ -\xi_h \cdot \left(\frac{\omega}{C}\right) \cdot \sin\left(\frac{\omega}{C}x\right) + \xi_h \cdot \left(\frac{\omega}{C}\right) \cdot \tan\left(\frac{\omega l}{C}\right) \cdot \cos\left(\frac{\omega}{C}x\right) \right] \quad (3.112)$$

But, the exciting force at the starting point of elongated part i.e.  $x=0$  is given by

$$F_E = S_H \times E \times \xi_h \cdot \left(\frac{\omega}{C}\right) \cdot \tan\left(\frac{\omega l}{C}\right) \quad (3.113)$$

Now Eq. (3.91) can be written as

$$m \cdot \ddot{\xi}_{max} = F_{SH} - F_I - F_E \quad (3.114)$$

$$F_{SH} = m \cdot \ddot{\xi}_{max} + F_I + F_E \quad (3.115)$$

$$m \cdot \ddot{\xi}_{max} + F_I + F_E = \sqrt{\frac{Y(T)^2}{4} - \left(\frac{N/S_H}\right)^2} \times S_H \quad (3.116)$$

This equation represents that the yielding and plastic deformation will occur only if the LHS is equal to the RHS of the equation. Eq. (3.116) also, can be represented as

$$F_I = \sqrt{\frac{Y(T)^2}{4} - \left(\frac{N/S_H}{2}\right)^2} \times S_H - m \cdot \ddot{\xi}_{max} - F_E \quad (3.117)$$

In the Eq. (3.117), the first term of the RHS side has limited value, and it depends mainly only on normal force and temperature. The second term is a constant term for a particular material and geometry. Therefore, if the third term will be high (anti-resonance condition) then,  $F_I$  will be very less. Hence, the welding couldn't take place rather than extrusion and yielding will occur.

**(B) Interface forces between the workpieces**

Initially, the surfaces of the specimens are covered with the contaminants and asperities, and the normal force of horn is not alone sufficient to disperse these unwanted materials. Thus, these contaminants still provide resistance to make a bond between the surfaces. But, during the welding, these unwanted materials in contact will plastically deform due to the shearing action of horn and friction between the sheets. Therefore, a substantial heat is developed which is responsible for lowering the yield strength of the top part. Practically, when the welding process starts, metal to metal adhesion occurs in the form of small microbonds and these areas grow with the increase of time. Finally, the weld area entirely covered with the deformed material. Considering a small element of the area where metals are in contact with each other and welding occurs as shown in Fig. 3.27.

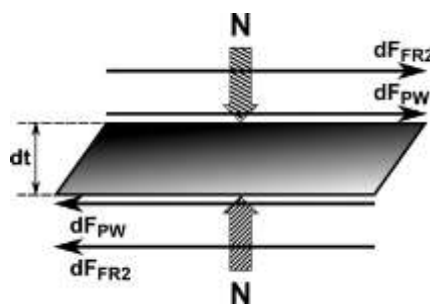


Fig. 3.27 A small element of weld area subjected to both plastic deformation and friction

From Fig. 3.27, the yield stress value is given by

$$\tau_s = \frac{dF_{PW}}{dS} \quad (3.118)$$

$$\int dF_{PW} = \int \tau_s \times dS \quad (3.119)$$

From Eq. (3.82),  $\tau_s$  can be written as

$$F_{PW} = \sqrt{\frac{Y(T)^2}{4} - \left(\frac{N/S_H}{2}\right)^2} \times S_{PW}(t) \quad (3.120)$$

Experimentally, it was found that when the normal force is high, the growth of weld area is also very high. So, the maximum error may occur. Typically, the weld area is

$$S_{PW} = \frac{S_H \text{ or } S_{DZ}}{2} \quad (3.121)$$

When the total interface force is concerned, then it is divided into two categories

- (i) Force responsible for plastic deformation ( $F_{PW}$ )
- (ii) Total frictional force ( $F_{FR}$ )

Total frictional force is the net force developed inside the weld zone and also outside the weld zone. Mathematically, it can be expressed as

$$F_I = F_{PW} + F_{FR1} + F_{FR2} \quad (3.122)$$

The frictional force inside the weld zone is given by

$$F_{FR1} = \mu_{S1} \times \sigma_N \times S_{FR1} \quad (3.123)$$

The frictional force outside the weld zone is given by

$$F_{FR2} = \mu_{S2} \times \sigma_N \times S_{FR2} \quad (3.124)$$

Now Eq. (3.66) can be presented as

$$m \times \ddot{\xi}_{max} = F_{SH} - F_{PW} - F_{FR1} - F_{FR2} - F_E$$

Putting the value of Eq. (3.90) in the above equation

$$\rho \cdot S_h \cdot t \cdot (\omega^2 \xi_h) = F_{SH} - F_{PW} - F_{FR1} - F_{FR2} - F_E \quad (3.125)$$

$$\rho \cdot S_h \cdot t \cdot (\omega^2 \xi_h) + F_{PW} + F_{FR1} + F_{FR2} + F_E = \sqrt{\frac{Y(T)^2}{4} - \left(\frac{N/S_H}{2}\right)^2} \times S_H \quad (3.126)$$

In Eq. (3.126), if LHS is not smaller than the RHS, then yielding will happen during the welding and consequently tip sticking and extrusion phenomena occur which is the unfavorable condition of the welding process.

### 3.8.3 Significance of forces

$F_{SH}$ : Determines the yielding and extrusion of top workpiece beneath the horn. Thus, the value of  $F_{SH}$  should be less than or equal to shear stress

$F_E$ : Determines the resonance or anti-resonance of the top workpiece. If it is high then, the anti-resonance condition occurs.

$F_{PW}$ : This force required for the welding due to plastic deformation inside the weld spot.

$F_{FR1}$ : This force is needed for the welding due to friction occurs inside the weld spot.

$F_{FR2}$ : This force is necessary to find out the friction that occurs outside the weld spot.

### 3.9 Thermal Analysis

During USMW, a significant heat is deliberated at the weld zone due to the plastic deformation as well as friction. Thus, it significantly affects the material properties. The ultimate aim of this analysis to generate an equation that will give a well-approximated result of acoustical power dissipated to the weld spot. In order to cope up with the experimental condition, it is realized that the heat developed during the welding process can be divided into two categories such as

- (i) Heat generation inside the welding spot.
- (ii) Heat generation outside the welding spot.

#### 3.9.1 Heat generation inside the welding spot

In this zone, small microbonds are initially developed and gradually these are increased with the increase in weld time. These deformation islands or microbonds occur randomly at the beginning of the welding. Because the top workpiece (aluminium) has the high thermal conductivity for which the temperature will radiate fastly from this zone. It is assumed that the areas of all microbonds are same and also dissipate the same amount of power. Thus, it is given by:

$$\frac{\text{Total power } (P_{Total})}{\text{Volume of deformation zone } (\vartheta_{DZ})} = \frac{\sum P_i}{\vartheta_{DZ}} \quad (3.127)$$

$$\frac{P_{Total}}{\vartheta_{DZ}} = \frac{\int dp}{\vartheta_{DZ}} \quad (3.128)$$

Firstly, it is considered that the heat generated in the weld zone is due to the plastic deformation of the material. A layer under shearing action is shown in Fig. 3.28.

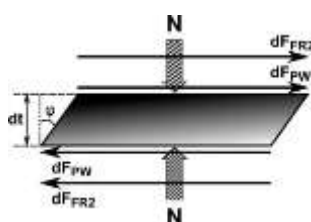


Fig. 3.28 Small element under shear strain for heat generation

The workdone by this deformed volume for a particular period of time is equal to the shear angle change within that time. Mathematically,

$$\frac{d\Delta w}{\Delta T_i} \times \frac{1}{d\vartheta} = \tau_s \times \frac{\Delta \xi_T}{dT_i} \times \frac{1}{\Delta T_i} \quad (3.129)$$

In Eq. (3.130)

$$\frac{\Delta w}{\Delta T_i} = \text{Power } (P)$$

$$\frac{\Delta \xi_T}{\Delta T_i} = \text{Velocity } (V_{avg}) \quad (3.130)$$

Thus, Eq. (3.130) can be expressed as

$$\frac{dP}{d\vartheta} = \tau_S \times \frac{V_{avg}}{dT_i} \quad (3.131)$$

As the ultrasonic wave is believed to be sinusoidal in nature and it passes through the weld thus, the total time is divided into four sections as shown in the Fig. 3.29.

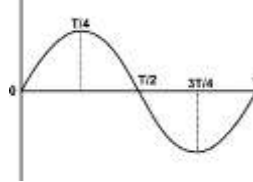


Fig. 3.29 Sinusoidal ultrasonic wave

Hence Eq. (3.130) can be written as

$$V_{avg} = \frac{\int_0^{T_i} \Delta \xi_T}{\int_0^{T_i} \Delta T_i} \quad (3.132)$$

From Eq. (3.86),  $\xi_T$  can be written as

$$V_{avg} = \frac{1}{(T_i - 0)} \times \int_0^{T_i} |\xi_h \times \omega \times \cos \omega T_i| \cdot dT_i \quad (3.133)$$

$$V_{avg} = \frac{1}{(T_i)} \times \xi_h \times \omega \times \frac{1}{\omega} \times \left[ [\sin \omega T_i]_0^{T_i/4} - [\sin \omega T_i]_{T_i/4}^{T_i/2} - [\sin \omega T_i]_{T_i/2}^{3T_i/4} + [\sin \omega T_i]_{3T_i/4}^{T_i} \right] \quad (3.134)$$

$$V_{avg} = 4 \times \xi_h \times f_{PW} \quad (3.135)$$

Putting the values of Eq. (3.135) in Eq. (3.131)

$$\frac{dP}{d\vartheta} = \tau_S \times \frac{4 \times \xi_h \times f_{PW}}{dT_i} \quad (3.136)$$

$$\frac{dP}{dS \times dx} = \tau_S \times \frac{4 \times \xi_h \times f_{PW}}{dx} \quad (3.137)$$

$$\int dP = \int \tau_S \times 4 \times \xi_h \times f_{PW} \times dS \quad (3.138)$$

Putting the value of Eq. (3.138) in Eq. (3.128)

$$\frac{P_{Total}}{\vartheta_{DZ}} = \frac{\int dp}{\vartheta_{DZ}} \quad (3.139)$$

$$\frac{P_{Total}}{\vartheta_{DZ}} = \frac{\int \tau_S \times 4 \times \xi_h \times f_{PW} \times dS}{\vartheta_{DZ}} \quad (3.140)$$

$$\frac{P_{Total}}{S_{DZ} \times dt} = \frac{\int \tau_S \times 4 \times \xi_h \times f_{PW} \times dS}{S_{DZ} \times dt} \quad (3.141)$$

$$\dot{q}_{PW} = \frac{P_{Total}}{S_{DZ}} = \frac{4 \times \xi_h \times f_{PW} \times F_{PW}(t)}{S_{DZ} \times dt} \quad (3.142)$$

Eq. (3.142) represents the amount of acoustic power that is deliberated due to plastic deformation and it is nothing but the heat produced at the weld zone.

Similarly, another source of heat inside the weld spot is the friction. Hence, it can be presented as

$$\frac{P_{FR1}}{S_{FR1}} = \frac{F_{FR1} \times V_{avg}}{S_{FR1}} \quad (3.143)$$

$$\dot{q}_{FR1} = \frac{\mu_{S1} \times N \times 4 \times \xi_h \times f_{PW}}{S_{FR1}} \quad (3.144)$$

### 3.9.2 Heat generation outside the welding spot

Similarly to the above case, the heat generation outside the weld spot is only due to the friction. So, the heat can be expressed as

$$\frac{P_{FR2}}{S_{FR2}} = \frac{F_{FR2} \times V_{avg}}{S_{FR2}} \quad (3.145)$$

$$\dot{q}_{FR2} = \frac{\mu_{S2} \times N \times 4 \times \xi_h \times f_{PW}}{S_{FR2}} \quad (3.146)$$

In Eq. (3.146)  $S_{FR2}$  can be calculated as

$$S_{FR2} = S_H - S_{PW} \quad (3.147)$$

Schematically this area can be observed from the following figure

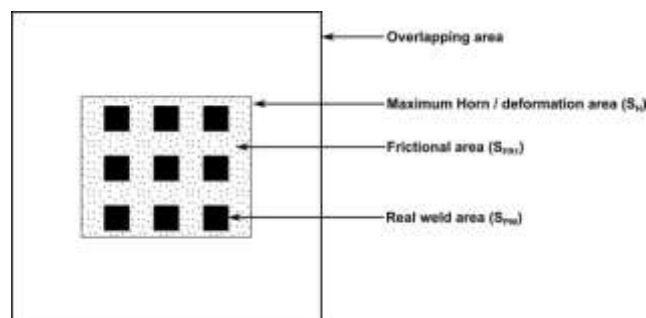


Fig. 3.30 Schematic diagram of different areas

## 3.10 Acoustic Softening Analysis

Acoustic softening is the second reason for material softening in which the static stress of the material is significantly reduced under the influence of ultrasonic energy. It was first observed by Langenecker [141]. It is different from material to material, and mainly depends on acoustic impedance, melting point, Young's modulus and hardenability of the material. The majority of previous investigations are based on the thermo-mechanical analysis of the welding mechanics, but no one has taken the acoustic softening effect into account. Without the knowledge of it, the accurate stress field and plastic deformation cannot be modelled. The objective of the present analysis is to develop a method to

quantify the acoustic softening to characterize it under the broad range of process parameters, geometries and materials.

### 3.10.1 Preparation of material model

In the subsequent experiments, AA 1100 aluminium alloy is used as one of the weld material which is usually placed on the top during the welding process. Hence, a material model is necessary to find the relationship between acoustic softening, thermal softening and strain hardening. Hockett [142] observed the strain hardening behaviour of AA1100 material with respect to the thermal softening. He presented the stress-strain relationship at a particular temperature in the plastic region by using the power law equation shown below.

$$\sigma_y = K_S \times \varepsilon_p^n \quad (3.148)$$

In this equation, the constants like  $K_S$  and  $n$  at different temperatures were found out by Hockett [142]. The intermediate values are calculated by using linear interpolation, and it is represented in Fig. 3.31.

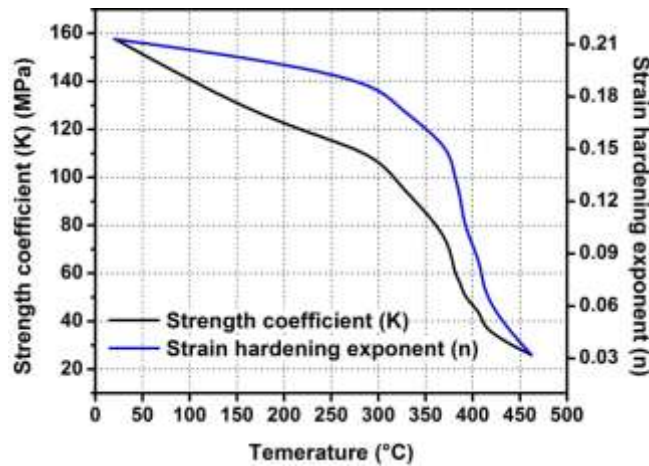


Fig. 3.31 Variation in power law constants with respect to temperature for AA1100

In the present analysis, the power law model given by Hockett is slightly modified by adding an acoustic softening parameter ( $\beta$ ). The range of this newly added term varies from zero to one. If  $\beta=1$ , then it is believed that the acoustic softening has no impact on the material deformation and the material is deformed normally. But when the  $\beta=0$ , then it implies that the ultrasonic energy deforms the material sufficiently. The following shows the power law equation with acoustic softening parameter.

$$\sigma_y = \beta \times K_S \times \varepsilon_p^n \quad (3.149)$$

It is assumed that the effect of parameter “ $n$ ” on the yield strength of the material is negligible and  $K_S$  is the important term which mostly affects the yield strength ( $\sigma_y$ ) of the material. Thus, the acoustic softening parameter linearly affects the  $K_S$  term.

### 3.10.2 Acoustic softening term calculation

To quantify the acoustic softening in the sheets during USMW process, the  $\beta$  is decreased from one to zero until the error between modelling result (i.e. increase in sheet width) and experimental result is minimized. For clear understanding, a contour plot of modelled sheet deformation is demonstrated in Fig. 3.32.

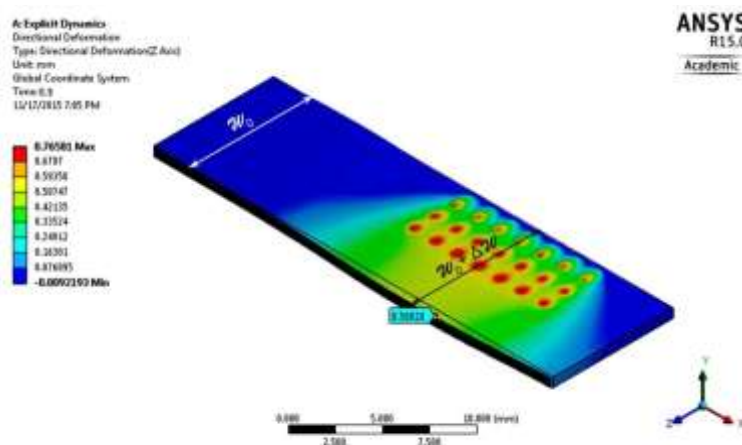


Fig. 3.32 Contour plot of sheet with initial sheet width and deformed sheet dimension

## 3.11 Summary

The present chapter provides an idea about the detailed theoretical as well as numerical analyses of the components, which leads to manufacture them correctly and precisely. This chapter also highlights the detailed analysis of the model associated with the welding mechanics and it is believed that the properties of the materials change significantly with the elevated temperatures. These detailed analyses along with the manufacturing are summarized below:

- A lateral-drive ultrasonic metal spot welding system and its related components have been addressed and designed by employing FE simulation. Based on the assumptions of free-free vibrated non-uniform bar, the theoretical calculations have been discussed for finding out the resonant lengths. The modelling of D2 steel horn and titanium booster has been achieved by employing FEA.
- The natural frequency of the horn and booster and its associative mode shapes have been revealed by applying the modal analysis module of ANSYS®. The performance of these components has been obtained by tuning the horn at the longitudinal mode by shortening the length and adding radius of curvature to the nodal sections. Finally, from this analysis, the lengths of booster and horn are attained as 125.4 mm and 126.8 mm with a radius of curvatures of 5.5 mm and 4.5 mm respectively. It is



observed that the simulated natural frequencies of 19999 Hz and 20004 Hz for both the components are quite close to the operating frequency of the system.

- The numerical theories related to these analyses also have been discussed. The locations of the high-stress region, the amplitude of the welding tip with gain have been examined by driving the transducer with a longitudinal mode of frequency at an amplitude of 30  $\mu\text{m}$ . Von Mises stresses have also been calculated to obtain the safe working condition of these components. The maximum stresses observed in this analysis are 196.67 MPa and 576.6 MPa for booster and horn. These results are found to be lower than the yield point of the horn and booster material. Meantime, the values of stresses are found to be very low at both the free ends, which also satisfy the theoretical principles.
- As these components were subjected to a cyclic loading of 20000 cycles/sec, the permanent changes were occurred within the structural body due to the application of repeated stress or strain. From the Miner's rule, it is observed that cumulative damages of 1.175 and 1.111 are obtained at the nodal section, suggesting the possibility of failures at the given working condition.
- Meanwhile, the heat generation will take place due to repeated elastic deformation of the materials, and it is observed that the D2 steel horn has a higher temperature at the nodal region followed by the titanium booster. The temperatures obtained from the simulation, and experimental results are found to be close to each other and errors of 2.08 % and 0.87 % are noticed for horn and booster respectively.
- For better accuracy in design, both of these components have been investigated simultaneously instead of taking individual one. It is spotted that there are 1.11 % and 2.52 % errors in the length calculation of both systems. Similarly, 0.61 % error is obtained while calculating the magnification ratio of both the components.
- Welding components were also fabricated such as horn, rigid anvil, specimen-holder and backing plate for effective transmission of ultrasonic energy to the welding zone and for producing a satisfactory weld.
- The complex mechanism behind the USMW has been addressed and modelled analytically. The forces beneath the sonotrode which are primarily responsible for shearing and plastic deformation of the material are identified. By doing so, the effects of different welding conditions on the quality of the joint can be determined.
- Meantime, if the top part dimension is large, then it produces an anti-resonance effect. Therefore, a good welding can't be achieved. But by controlling the size of the top sheet and the force related to the extended part, a healthy joint can be obtained.
- Furthermore, it is observed that the friction between the sheets is one of the causes for heat generation and subsequently it leads to the plastic deformation. Along with

this thermo-mechanical analysis, the acoustic softening analysis is also applied for accurate prediction of stress field, plastic deformation and yield stress of the material.

- The temperatures developed between the interfaces of sheets and the sonotrode-top part interfaces are calculated not only by using these analytical solutions but also by numerical analysis for the exactness of the results. A flow chart is shown in Fig. 3.33 summarizing all the steps those are followed in the thermo-mechanical and acoustic softening analysis.

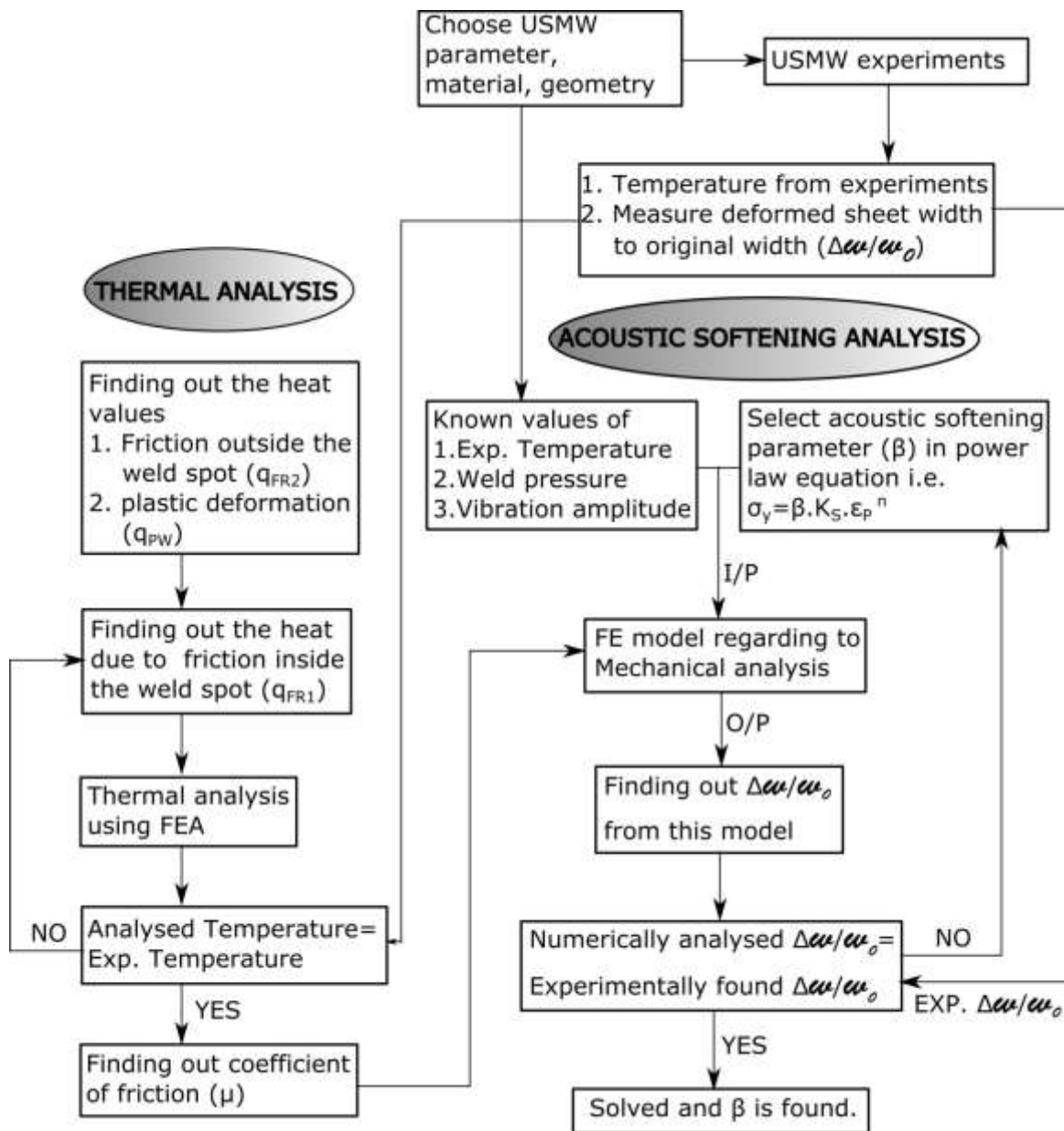


Fig. 3.33 Flow chart representing the thermo-mechanical model to quantify acoustic softening

## Chapter 4

# Experimentation and Planning for Experimental, Numerical and Metallurgical Investigations on USMW

### 4.1 Introduction

This chapter discusses the equipment and materials used during the present investigation for ultrasonic spot welding of dissimilar metals. Although many types of equipment involved in this process, the discussion will be brief and limited to the important ones. Initially, a brief description of the ultrasonic metal welding (USMW) machine and its different controllable and fixed parameters is provided. The mechanical properties, i.e. Young's modulus, modulus of elasticity and ultimate tensile strength of the weld metals such as aluminium, copper, brass and stainless steel are found out by using a universal testing machine. The dimensions and thickness of these weld materials are selected according to the experimental trials, as the incorrect dimensions may lead to poor weld strength. Similarly, the hardness and surface roughness of the sheets are investigated, as these properties affect the joint strength and quality. The process parameters and its ranges those can be set in the machine to join thin metal sheets are also briefly illustrated.

### 4.2 Ultrasonic Metal Welding Equipment

All the spot welding experiments have been performed with a Telsonic<sup>®</sup> lateral drive welding machine at a constant power of 3 kW and a frequency of 20 kHz. The designed and analyzed stepped horn with multifaceted weldable tips and a stepped booster are fabricated from D2 steel and titanium at Telsonic<sup>®</sup> industries, Switzerland using computer numerical control (CNC) and laser cutting machines. These two components are tuned in such a way that all the parts are in a resonating state and draw minimum power at no load condition. It may be noted that for various applications like wire splicing, tube sealing, solar panels assembly and joining of battery foils; different ultrasonic welding tips are required. In the present study, thin sheets are welded, thus; the stepped type horn with flat welding tip of size 11 mm×9 mm and a rigid anvil with identical spaced and parallel knurl patterns are implemented for the experiments. Fig. 4.2 shows the principal set up for ultrasonic welding machine.

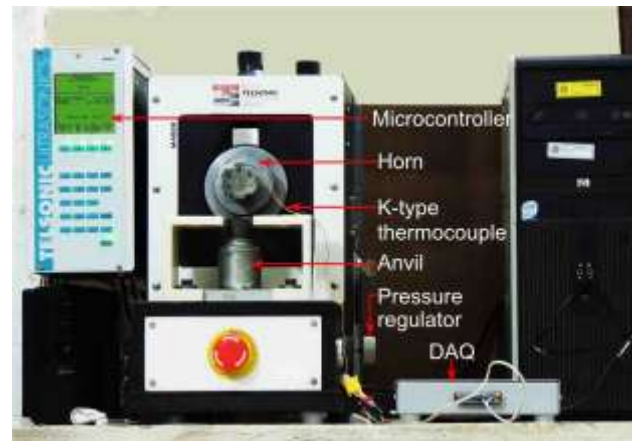


Fig. 4.1 USMW machine setup

The ultrasonic welding machine is typically consisted of six subsystems (i) generator, in which 50 Hz electrical energy is converted to a frequency of 20 kHz, (ii) piezoelectric transducer/ converter, which is producing mechanical vibration of 20 kHz frequency from the high-frequency electrical energy, (iii) booster, which enhances the amplitude of vibration, (iv) horn/sonotrode/concentrator, which amplifies the amplitude of vibration required for welding, (v) anvil, that provides the rigid support to the workpiece during the welding. The schematic diagram of these systems is shown in Fig. 4.2.

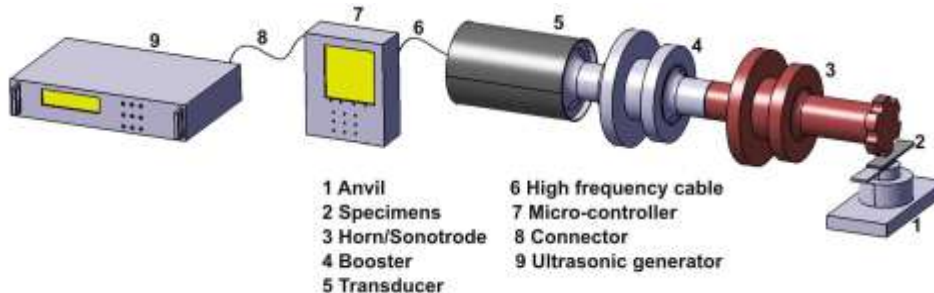


Fig. 4.2 Schematic diagram of different parts

### 4.3 Universal Tensile Test Machine

The calibrated testing machine INSTRON®1195 is used to extract the mechanical properties as well as the strength of the weld for all types of weld materials such as aluminium, copper, brass and stainless steel. This machine is equipped with 2 kN load cell that can record the tensile load and displacement of the stretched specimen. This process can yield accurate stress results but due to the presence of relative stiffness between the machine and the samples, the measurement values of strain are erroneous. Thus, to avoid such type of results, the strain is measured by an extensometer. An extensometer is a device that can measure the extension of the workpiece longitudinally when the material is pulled by an external load [143]. In the present analysis, a calibrated

extensometer (model: AC-07-1040) is used to measure the extension. Fig. 4.3 (a) presents the total tensile test machine setup and Fig. 4.3 (b) shows the extensometer set up on the tensile test machine.

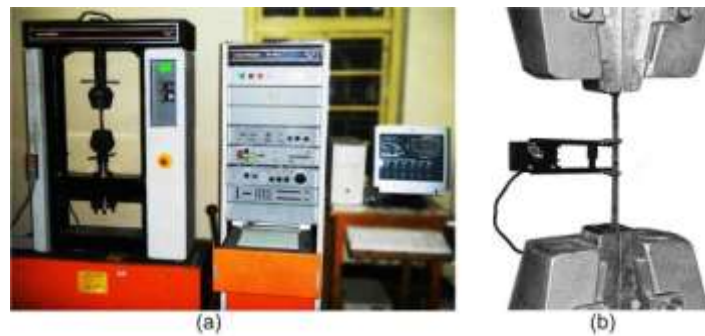


Fig. 4.3 (a) INSTRON® 1195 universal testing machine, (b) Extensometer set-up on universal testing machine

## 4.4 Weld Materials for USMW

The ultimate objectives of various sectors like automotive, aircraft, railway transportation, medical, microelectronics, etc., are to reduce the weight and energy consumption by introducing new and innovative techniques. To attain these goals, lightweight and high strength materials such as aluminium, stainless steel, titanium, magnesium, copper alloys are necessary. Out of these, aluminium is widely utilized as a part of making fuel cell components in the battery, connecting semiconductor devices, transistors, diodes and furthermore in aerospace industry [8,26]. Therefore, the present work includes aluminium (AA1100), copper (UNS C10100), brass (UNS C27000) and stainless steel (SS 304) as the weld materials and having the chemical composition shown in Table 4.1 and Table 4.2 [126] provided by the supplier.

Table 4.1 Chemical compositions of non-ferrous materials

Materials	Chemical components (%)								
	Al	Cu	Mn	Zn	Si	Fe	Zn	Pb	Others
AA1100	99	0.05-0.20	0.05	0.10	0.3	0.3	-	-	0.3
UNS C10100	-	99.99	-	-	-	-	-	-	-
UNS C27000	-	63-68.5	-	-	-	0.070	31.3-37	0.10	-

Table 4.2 Chemical compositions of ferrous material

Materials	Chemical components (%)							
	Fe	Ni	Cr	Mn	Si	C	P	S
SS 304	66-74	8-10.5	18-20	2	1.0	0.08	0.04	0.03

### 4.4.1 Mechanical properties extraction

The mechanical properties of the specimens used in USMW experiments are found out according to the standard test methods for tension testing of metallic materials i.e. ASTM

E8M standard [144]. The dog bone shape materials carefully cut without any burrs, notches or rough edge surfaces that may affect the result. The gauge length of the specimen for the test is 36 mm with 26 mm grip at each side. The detailed dimensions are represented in Fig. 4.4. In the experiments, each test is carried out six times to get an accurate result. The strain rate during the testing is set at 2 mm/min to avoid any type of dynamic effects on the workpiece. The extensometer attached to the specimen recorded the data and transferred to the controller, where it is processed by the machine to give the relationship between load and displacement. Finally, these data are converted to the stress-strain diagram for finding out Young’s modulus, ultimate tensile strength (UTS) and yield strength (YS) of the material. The average of these data for the weld materials is tabulated in Table 4.3 with the physical and thermal property values [126]. The extracted mechanical properties of the material are further used for the finite element modelling of the welded samples.

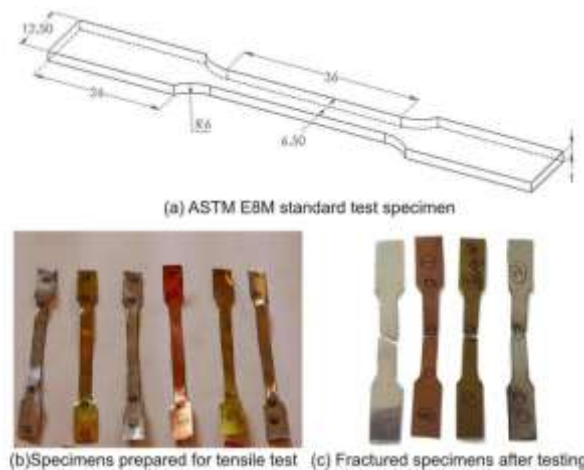


Fig. 4.4 Dog bone specimens before and after tensile testing

Table 4.3 Physical, mechanical and thermal properties of weld materials

Properties	Unit	Materials			
		AA1100	UNS C10100	UNS C27000	SS 304
Density	kg/m <sup>3</sup>	2710	8940	8470	8000
Young’s modulus	Pa	68.9E9	115E9	105E9	193E9
Poisson’s ratio		0.33	0.31	0.3	0.29
Ultimate tensile strength	Pa	135.5E6	302.1E6	420.4E6	858.1E6
Yield strength	Pa	115.2E6	251.5E6	336.1E6	649.4E6
Co-efficient of thermal expansion	°C <sup>-1</sup>	23.6E-6	17E-6	20.3E-6	17.3E-6
Thermal conductivity	W/m°C	220	391	116	16.2
Specific heat	J/kg°C	904	385	380	500
Melting point	°C	660	1085	930	1455

#### 4.4.2 Yield strength variation with temperature

The temperature dependent yield strength has been obtained from the standard reference [145], because in USMW, plastic deformation and yielding occur at elevated

temperatures. As the boundary condition of the USMW is very complex, and the yield strength is associated with the temperature rise at the weld interface and as well as the sonotrode-top part interface. Thus, a linear approximation procedure is used for the temperature dependent yield strength to find out the satisfactory result as shown in Fig. 4.5.

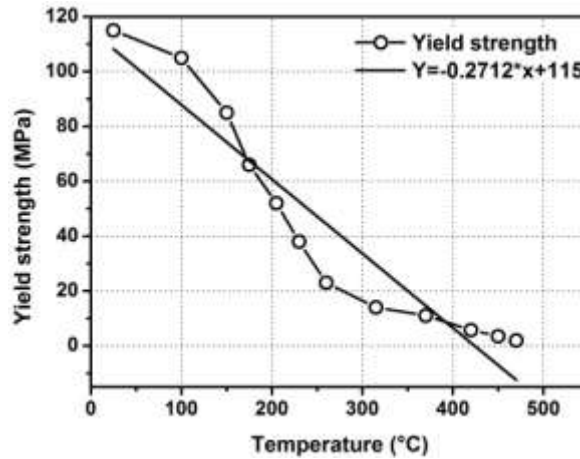


Fig. 4.5 Linear approximation of yield strength with temperature

### 4.4.3 Weld coupon thickness

Ultrasonic metal welding depends on the amount of relative motion takes place at the interfaces of materials. Meanwhile, the ultrasonic energy produced by the generator is applied to the top workpiece through the horn, and ultimately it propagates to the weld zone for producing severe plastic deformation. During this propagation, some energy may loss due to interatomic friction, and it results in dissipation of heat. In the present work, 0.3 mm, 0.45 mm, 0.6 mm and 0.7 mm thick aluminium, 0.3 mm, 0.4 mm, 0.45 mm thick copper and brass, 0.1 and 0.2 mm thick SS 304 materials are selected keeping an eye on the generator capacity. The lateral drive welding system used in the experimental work has the maximum power of 3 kW, and it can be capable of welding the thinner materials. Most of the previous literature [84,91] confirm that the thickness of the upper specimen has a significant effect on the weld strength rather than the thickness of the lower specimen because the top specimen is more subjected to the impact of ultrasonic energy.

### 4.4.4 Weld coupon length

From the previous studies, it is clear that the length of weld coupon significantly affects the weld strength and quality of the joint because the waves of vibration from the long and wide specimens are reflected back in an anti-phase manner [86]. Thus, the influence of specimen size on the weld strength was verified experimentally. Initially, the specimens

are prepared according to the ASTM standard with a 20 mm overlap. Fig. 4.6(a) illustrates the coupon dimensions along with extension length. Fig. 4.6(b) represents the various dimensions of specimens used for verification purpose.

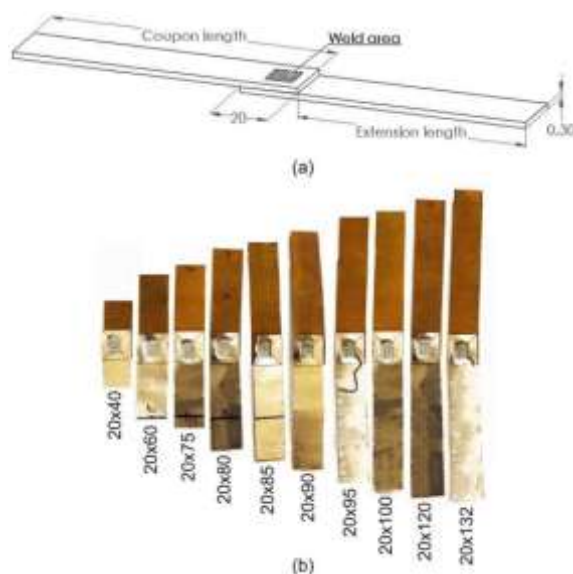


Fig. 4.6 (a) Schematic diagram showing extension length, (b) lap welded samples of different dimensions

The weld joints are produced with the same Telsonic® lateral drive ultrasonic welder and for each coupon extension length six samples are tested. The results with standard deviation bars are shown in Fig. 4.7 for the 0.3 mm aluminium (AA1100) alloy and copper (UNS C10100) with different power levels and coupon lengths as an illustration.

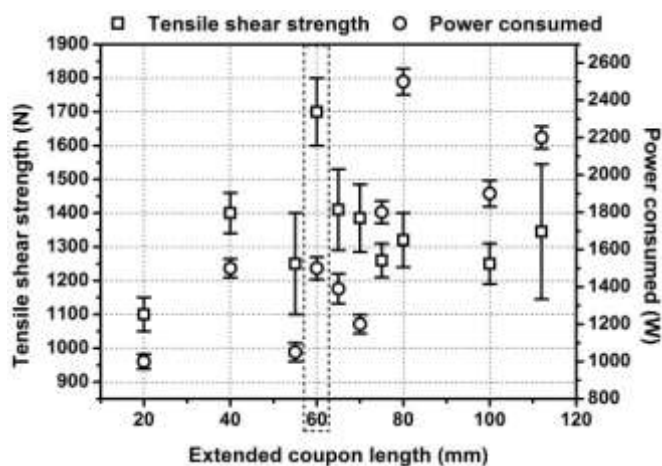


Fig. 4.7 Effect of extension length on tensile shear strength and power consumed

The results obtained from this study are in agreement with DeVries [18] who used 2.5-kW Sonobond® wedge-reed system to weld 1-mm thick aluminium 6061 T-6 alloy. It can be observed from the above figure that 20 mm width and 80 mm length (marked in box), good weld strength with moderate amount power is consumed. Therefore, this coupon length also minimizes the number of materials which will be used in the subsequent experiments.



### 4.4.5 Sheet hardness

In USMW, sheet hardness has a vital role in deciding the weldability. That means, with the increase of hardness; the weldability of the material decreases [56], and it requires more ultrasonic energy to be plastically deformed. The hardness of the sheets was measured by Vaiseshika® 7005 Vickers hardness tester (see Appendix B) with a 100 gm load and 15 sec dwell time. It uses a square pyramid-shaped diamond indenter, which is pressed into the test material. The Vickers hardness is measured by using the Eq. (4.1). During the measurement, each test was repeated six times to get accurate results presented in Table 4.4.

$$HV = \frac{1.8544F}{d^2} \tag{4.1}$$

where F is the load applied in kgf and d is the average length of both diagonals in mm.

Table 4.4 Hardness of weld materials for different thickness

Properties	Materials											
	AA1100				UNS C10100			CuZn37			SS 304	
Thickness (mm)	0.3	0.45	0.6	0.7	0.3	0.4	0.45	0.3	0.4	0.45	0.1	0.2
Hardness (HV)	43	45	46	48	60	67	72	99	100	102	130	141

### 4.4.6 Sheet roughness

The roughness of the all the specimens used for USMW is measured by Zeiss Handysurf® E-35B surface roughness tester (see Appendix B) because the surface roughness is considered as one of the crucial parameters for heat generation between the surfaces [64]. With this measuring instrument, the substrates on the working surface were measured through the average surface roughness (R<sub>a</sub>) term. The roughness of the specimen is measured by taking an arithmetic height of surface irregularities from its mean line over an evaluation length of 4 mm shown in Fig. 4.8.

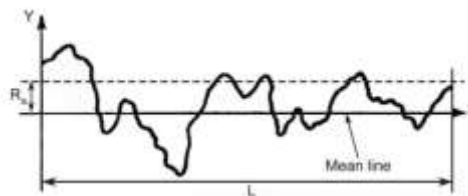


Fig. 4.8 Surface roughness profile showing R<sub>a</sub>

The measuring speed of the probe is 0.3 mm/Sec and Eq. (4.2) is used to determine R<sub>a</sub> value [146].

$$R_a = \frac{1}{L} \int_0^L |y| dx \tag{4.2}$$

For a particular sheet, six readings have been taken in the parallel and perpendicular direction in different areas of different thickness materials. These results are summarized in Table 4.5.

#### 4.4.7 Co-efficient of friction determination

The materials used in the subsequent experiments are divided into four categories based on their surface conditions:

- Lubricated surface (A)
- Normally cleaned surface (B)
- Electrolytic polished surface (C)
- Emery paper (P120 grit) polished surface (D)

Table 4.5 Surface roughness results for various materials

Properties	Materials											
	AA1100				UNS C10100			CuZn37			SS 304	
Thickness (mm)	0.3	0.45	0.6	0.7	0.3	0.4	0.45	0.3	0.4	0.45	0.1	0.2
R <sub>a</sub> in parallel (µm)	0.1	0.2	0.5	0.6	0.1	0.2	0.2	0.1	0.1	0.2	0.2	0.13
R <sub>a</sub> in perpendicular (µm)	0.4	0.5	0.7	0.8	0.13	0.2	0.3	0.2	0.2	0.23	0.2	0.25
Surface Condition	A	B	C	D	A	B	C	D	A	B	C	D

To know the static coefficient of friction of each surface, a setup is established consisting of a weight and a scale. Initially, each set of aluminium-copper, aluminium-brass, and aluminium-stainless steel are mounted on the table, and the scale is attached to the top aluminium sheet only. Subsequently, a load is placed on the top sheet, and it is further increased by 50 grams. This setup is represented in Fig. 4.9.

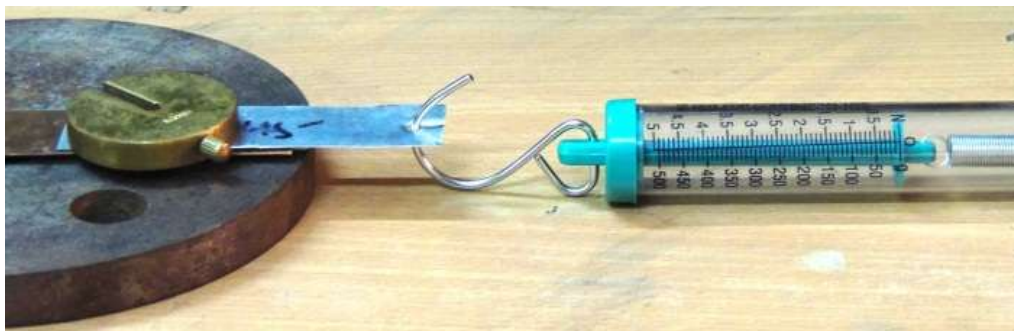


Fig. 4.9 Static coefficient of friction determination setup

Finally, a displacement is given to the scale which held parallel to the plane of the sheets. The linear approximations of the static coefficient of frictions between various pairs are shown in Fig. 4.10.

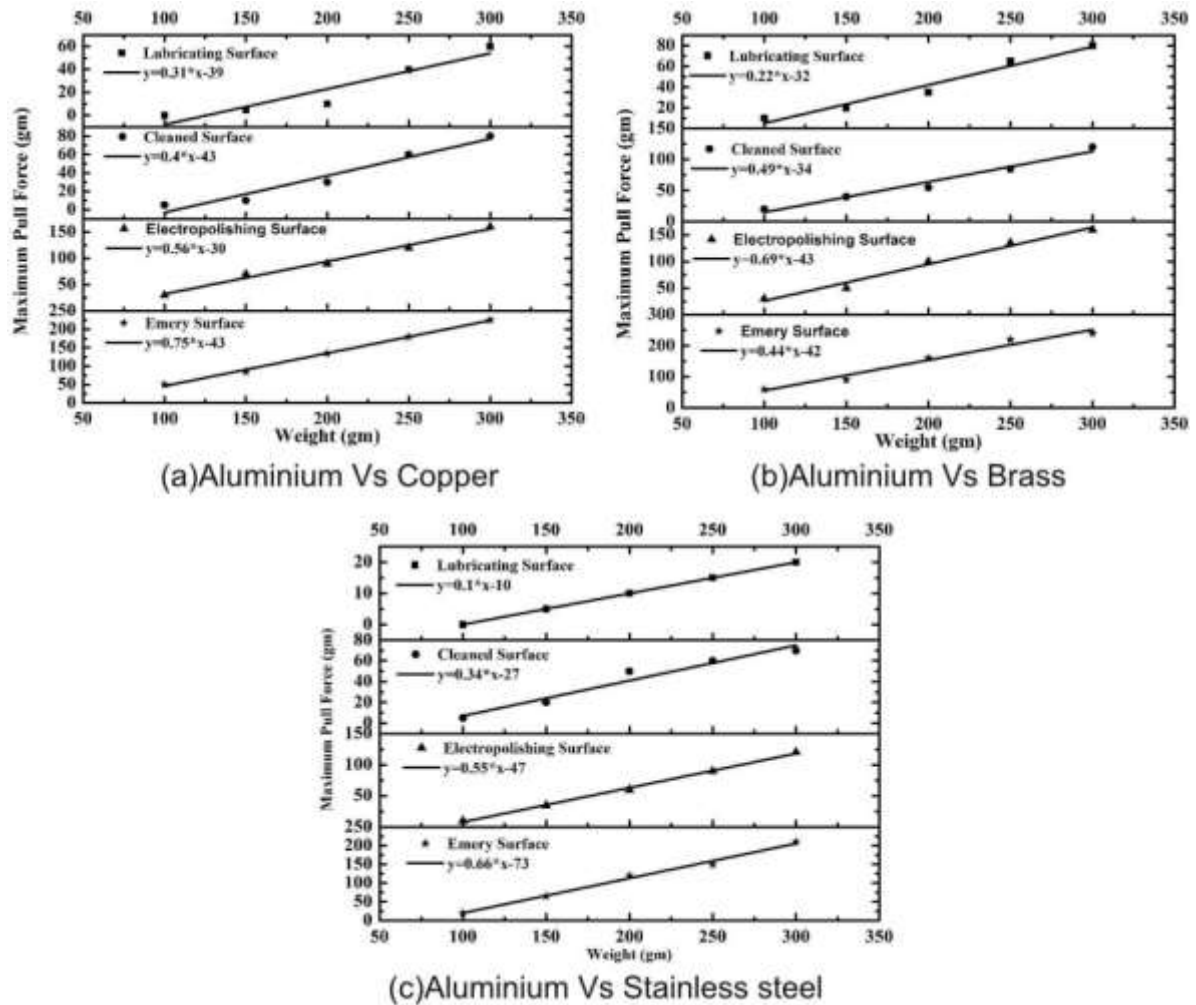


Fig. 4.10 Coefficient of friction for different materials with various surface conditions

## 4.5 USMW Parameters

During the investigation, the influence of different welding parameters on the response have been observed, and it includes

- *Vibrational frequency (f)*: Normally varies between 19.5 to 20.5 kHz. During the operation, all the components like a transducer, booster and horn are in resonating state.
- *Vibrational amplitude ( $\xi_h$ )*: The  $\xi_h$  ranges between 47 and 68  $\mu\text{m}$ . The direction of vibration of weld tip is perpendicular to the surface of material.
- *Weld pressure (WP)*: The WP varies from 0.14 to 0.44 MPa depending on the thickness of the workpiece.
- *Weld time (WT)*: Normally, it ranges from 0.18 Sec to 1 Sec depending upon thickness and hardness of the material.

## 4.6 Performance Measures in USMW

The various performance measures or responses have been studied during the experiments. These are:

- *Tensile shear strength (TS)*: The tensile shear strength includes the breakage of weld that is taken place between the overlapped sheets. In this test, the direction of application of tensile force is parallel to the plane of the weld coupons as shown in Fig. 4.11 (a). In the subsequent section, the results demonstrate that the tensile shear strength of the weld is higher than the strength of parent material.
- *T-peel strength (TP)*: The second method of testing the joints produced by the ultrasonic welding is to pull the specimen perpendicular to the weld surface shown in Fig. 4.11 (b). Normally, the breaking force values measured in this test is 20 to 40 % of the tensile shear strength [56].
- *Weld area (WA)*: Due to the presence of serrations on the horn and anvil surfaces, several point/line contacts have been made between these sheets. At these points, small micro bonds initially develop, and when input parameter values are increased, the micro bond areas are also gradually increased and are saturated finally. So, it is tough to measure this kind of area which, is known as “real weld area.” Meanwhile, an average or general weld area is calculated by the multiplication of one micro bond area with no. of points present on the horn tip.
- *Interface temperature (T)*: Usually, the temperature is measured by inserting thermocouples near the weld spot. The deciding factors for determining the temperature are ultrasonic power, weld time, material properties, thermal conductivity and geometry of the workpiece. The temperature observed in the weld zone is normally 0.3 to 0.9 times of the temperature of the material having the lowest melting point.

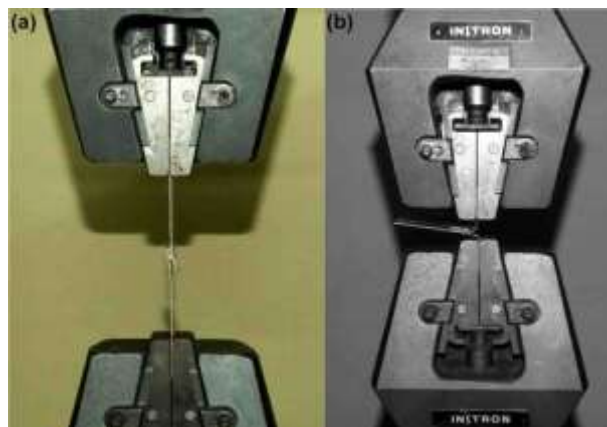


Fig. 4.11 (a) Lap-shear coupon test fixture, (b) T-peel coupon test fixture

## **4.7 Summary**

The equipment and the materials (going to be used in the subsequent experiments) are described in this chapter briefly, and emphasises are given on the following points:

- The mechanical properties of all the weld metals were extracted at 2 mm/min crosshead speed by using a universal testing machine fitted with an extensometer.
- All the dimensions of weld coupons are prepared according to the machine capacity, and the preliminary results are obtained by varying the coupon length. From this study, it has been finalized that 20 mm × 80 mm weld coupons can be used in the experiments as it shows good weld strength and consumes moderate amount power.
- Furthermore, different properties of the material such as hardness, surface roughness and coefficient of friction between the sheets are investigated as they have the ability to influence the weld strength as well as weld quality.
- Finally, the controllable parameters such as frequency of vibration, weld pressure, weld time and vibrational amplitude are briefly described.
- Similarly, the importance of performance measurements such as tensile shear strength, T-peel strength, weld area and temperature on the strength of weld and quality are also explained.



## Chapter 5

# Experimental and Numerical Investigations on Al-Cu Weld Coupons

## 5.1 Introduction

In modern day industrial scenario, there is often the need to join dissimilar materials due to their technical and beneficial advantages. Copper and aluminium are the two common materials used in electric power industries for power transmission because of their high electrical and thermal conductivity. These materials also have a broad range of applications in joining of battery tabs in hybrid and electric vehicles and microelectronics circuits. Welding of these materials has now indeed turned out to be an emerging area of research. Many pioneers have already worked in this field to investigate the welding and weldability aspects of these materials, thereby, retaining both productivities as well as product quality. Unfortunately, these soft and lightweight metals face a lot of hurdles during homogeneous or heterogeneous joining by traditional fusion welding processes. This is because of the vast difference in chemical, mechanical and physical properties, and the production of bulk and brittle intermetallic compounds (IMCs). Thus, average weld strength with a high degree of distortion [73] is observed. Due to these persisting difficulties, the alternative welding techniques like resistance spot welding (RSW), friction stir welding (FSW) and ultrasonic metal welding (USMW) have received a lot of attention. Although FSW is found to be relatively better than traditional welding technique, it faces difficulties while meeting challenges of electronic industries. It also showed poor weld strength with IMCs at the weld interface [147]. This leads to the importance of USMW, which is just another type of solid state welding process where the coalescence has been obtained by applying high-frequency vibration and a moderate amount of pressure. In the meantime, this technique also uses relatively less energy and less job deformation as compared to FSW. In this context, the current study mainly attempts to investigate the effects of process parameters on getting the maximum weld strength and at the same time, to reduce the formation of cracks due to over welding.

## 5.2 Problem Definition

Most of the previous studies were concentrated on the effect of one process parameter i.e. weld energy on the joint strength and temperature generated during the welding. Whilst, it also has been found out that lesser attention has been given to the welding of

different thickness Al-Cu combination with the variation of various control parameters. Therefore, the present work highlights the effects of various machine parameters such as weld pressure, weld time and vibration amplitude on different performance indicators like tensile shear strength and T-peel strength along with the average weld area and interface temperature in the welding of these materials. Based on the maximum value of tensile shear failure load and T-peel failure load results from the experiments, the optimum specimen thickness combination has been chosen. Subsequently, on that particular combination, the different anvil patterns, as well as different surface conditions, have applied on it to study their effects on the responses. Meantime, assessments of weld properties like average weld area; temperature and metallurgical analysis of these conditions have also been performed. Likewise, to establish a predictive model for the welding process, three prediction techniques such as regression analysis, artificial neural network (ANN) and adaptive neuro-fuzzy inference system (ANFIS) have applied to it. Moreover, the numerical analysis has also been performed for modelling and validating of the experimental results.

## 5.3 Experimentation

In the present work, a series of experiments have been carried out to collect the responses like tensile shear failure load, T-peel failure load, weld area and interface temperature during the welding of Al-Cu metal sheets of different thickness.

### 5.3.1 Design of experiment

A lateral drive ultrasonic metal welder (Telsonic® Ultrasonics, Switzerland, model: M4000, as shown in Fig. 4.1) with a flat weld tip of size 11 mm × 9 mm is used in the present analyses. It has parallel serrations present on the weld tip to provide adequate gripping of the lapped sheets. The maximum power available from this spot welder is 3 kW with a pre-set frequency of 20 kHz. The welding experiments are performed using time control mode, and the peak amplitude of 68 μm is obtained during the unloading condition. The power and ultrasonic energy are automatically tuned with the change of weld time. Fig. 5.1 illustrates a schematic diagram consisting of weld materials, anvil, and horn with positions of thermocouples attached to the bottom sheet.

The ultrasonic vibration is applied perpendicular to the length of the sheets with the motion of the lower specimen restricted by the anvil, and the top specimen vibrate with the sonotrode. The dimensions, material properties and efficiency of transmitting the ultrasonic energy of the workpiece materials determine the power requirement for achieving a good weld. Thus, a lot of screening test have been performed carefully to



choose the process parameters for welding. The detailed experimental domains are presented in Table 5.1 and

Table 5.2. To investigate the effects of process parameters on the responses, the full factorial design of experiment is chosen. Meanwhile, for better accuracy of results six numbers of replicates have been taken for each test condition. Thus, a total of 504 samples is prepared and out of which 252 samples are used for tensile shear tests and 252 samples for T-peel tests.

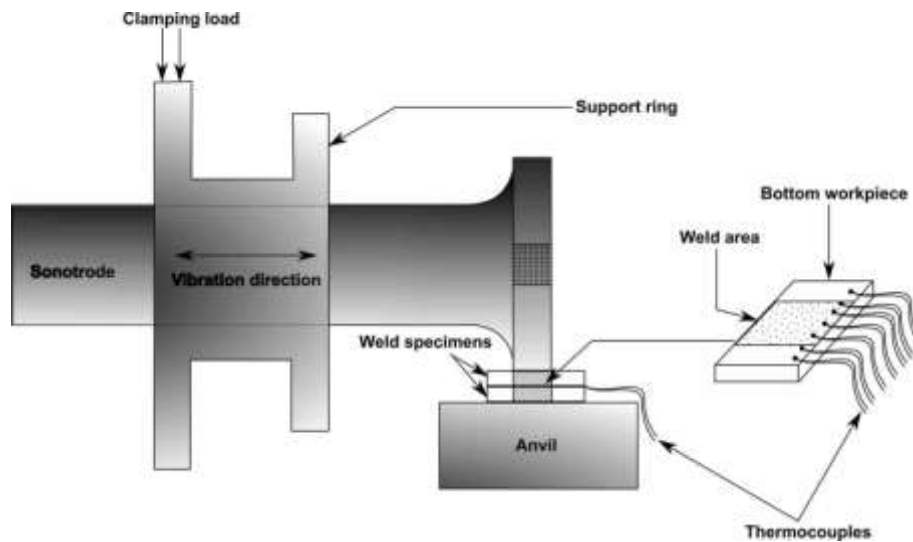


Fig. 5.1 Schematic diagram of ultrasonic weld system with thermocouples attached to the specimen

### 5.3.2 Workpiece and tool material

Ultrasonic spot welds are created between the commercially available extruded sheets of AA1100 aluminum and UNS C10100 copper with different thickness. In the subsequent experiments, aluminium sheets of thickness 0.3, 0.45, 0.6 and 0.7 mm are taken. Likewise, the thickness of copper specimens is also varied in 0.3, 0.4 and 0.45 mm. These sheets are sheared into rectangular 80 mm length  $\times$  20 mm wide test specimens. The configuration is shown in Fig. 5.2. The coupon lengths are taken as parallel to the rolling direction of sheets. There is no further treatment of weld surfaces to change its surface roughness. The weld coupons are overlapped for 20 mm along its length and formed an overlap area of  $20 \times 20 \text{ mm}^2$  for the lap welding (Fig. 5.3).

The weld spots are positioned just at the center of the overlapped region. The surfaces of the specimens have been cleaned with acetone in order to deprive of grease and other asperities present on it. As the AA1100 samples are softer than UNS C10100 samples, thus Al sheets were placed on the Cu sheets. Table 5.3 represents the mechanical, thermal and physical properties and Table 5.4 shows the chemical compositions of specimens used in this study.

Table 5.1 Domain of experiments adopted for USMW of similar thickness Al-Cu weld coupons

Thickness	0.3Al Vs 0.3Cu							0.45Al Vs 0.45Cu						
Factors	Level 1	Level 2	Level 3	Level 4	Level 5	Level 6	Level 7	Level 1	Level 2	Level 3	Level 4	Level 5	Level 6	Level 7
Amplitude ( $\mu\text{m}$ )	47	54	60	68	...	...	...	47	54	60	68	...	...	...
Weld pressure (MPa)	0.14	0.24	0.32	...	...	...	...	0.26	0.34	0.42	...	...	...	...
Weld time (Sec)	0.18	0.2	0.22	0.23	0.24	0.25	0.26	0.26	0.28	0.3	0.34	0.36	0.38	0.41

Table 5.2 Domain of experiments adopted for USMW of dissimilar thickness Al-Cu weld coupons

Thickness	0.6Al Vs 0.4Cu							0.7Al Vs 0.4Cu						
Factors	Level 1	Level 2	Level 3	Level 4	Level 5	Level 6	Level 7	Level 1	Level 2	Level 3	Level 4	Level 5	Level 6	Level 7
Amplitude ( $\mu\text{m}$ )	47	54	60	68	...	...	...	47	54	60	68	...	...	...
Weld pressure (MPa)	0.22	0.26	0.28	...	...	...	...	0.34	0.38	0.42	...	...	...	...
Weld time (Sec)	0.4	0.5	0.6	0.7	0.85	0.9	1	0.5	0.6	0.7	0.75	0.8	0.85	0.9

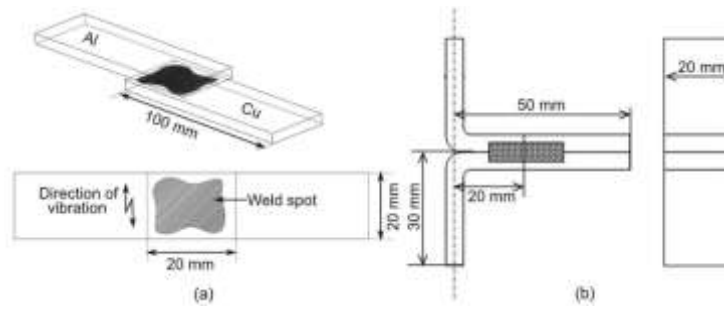


Fig. 5.2 Schematic diagrams of weld coupons (a) for tensile shear test, (b) T-peel test



Fig. 5.3 Welded samples

### 5.3.3 Welding performance evaluation characteristics

The optimum weld strength of the joint has been determined by tensile shear tests, and T-peel tests carried out by INSTRON<sup>®</sup> 1195 universal tensile tester with a 20 kN load cell at a crosshead speed of 2 mm/min (Fig. 4.3). During these testing of materials, the spacers were used at the extreme ends in order to keep the ultrasonically welded specimens aligned and also to avoid any type of sheet bending and nugget rotation. In the present analysis, weld area is taken as an additional response. The weld area is observed by an optical stereo microscope (Radical Instrument<sup>®</sup> with 25X magnification) shown in Appendix B, and the grabbed image is analysed as well as its dimensions are quantified by Image J<sup>®</sup> software.

Table 5.3 Physical, mechanical and thermal properties of specimens

Properties	Unit	AA1100	UNS C10100
Density	Kg/m <sup>3</sup>	2710	8940
Young's modulus	GPa	68.9	115
Poisson's ratio		0.33	0.31
UTS	MPa	135.5	302.1
YS	MPa	115.2	251.5
Coefficient of thermal expansion	°C <sup>-1</sup>	$23.6 \times 10^{-6}$	$17 \times 10^{-6}$
Thermal conductivity	W/m°C	220	391
Specific heat	J/Kg°C	904	385

Table 5.4 Chemical compositions of specimens

Component Elements Symbol	Composition (%) in AA1100	Composition (%) in UNS C10100
Al	99	...
Cu	≤0.05-0.20	99.99
Mn	0.05	...
Zn	0.10	...
Si	0.3	...
Fe	0.3	...
Others	≤0.3	...

## 5.4 Results and Discussion

### 5.4.1 0.3 mm Al-Cu and 0.45 mm Al-Cu similar thickness weld coupons

The first set of experimental runs has been performed using aluminium and copper specimens having a similar thickness (Al on top). The amount of ultrasonic energy delivered to the welding spot is directly proportional to the control parameters like weld pressure, weld time and vibrational amplitude. Therefore, to get a perfect joint, a certain range of these parameters are necessary because the insufficient value of these parameters can lead to the weak weld; whereas the excessive value of these parameters will result in cracks around the weld zone. The effects of these control parameters on the performance measures are described in the subsequent sections.

#### 5.4.1.1 Influence of process parameters on tensile shear and T-peel failure load

After completion of the weld between Al-Cu specimens by USMW, the weld coupons are debonded by a universal tensile test machine. The weld strength results of the debonded specimens are determined from the ultimate failure load. The present study considers two types of weld strengths such as tensile shear failure load and T-peel failure load for the evaluation of the joints produced by USMW. These tensile shear strength and T-peel strength as a function of weld pressure and weld time at various amplitudes are demonstrated in Fig. 5.4 and Fig. 5.5 for aluminium and copper specimens of 0.3 mm and 0.45 mm thicknesses respectively. In those figures, the solid lines represent tensile shear failure loads, and dotted lines show T-peel failure loads. From the analysis of debonded weld samples, it is observed that these two strengths of various welds first increase and afterwards diminish with an increase in weld time. It is believed that prolonged weld time

can cause cracks around the weld spot [148]. Meanwhile, an increase in weld pressure also increases these weld strengths and approaches maximum at a particular value of weld pressure. After this point, these strengths decrease due to suppression of relative motion between sheets at the excessive amount of weld pressure. Furthermore, there is an increase of weld strength when the vibration amplitude increases. Rising in amplitude means that the scrubbing action between faying surfaces also increases and resulting in a better bonding strength [97]. These results show a similar nature as demonstrated by Zhao et al. [73]. They observed that the tensile shear strength increased with the increase in weld energy, and optimum strength was achieved at 1000 J. However; this optimum strength was further declined with the increase in weld energy.

It can be observed from the Fig. 5.4 that the highest value of tensile shear failure load and T-peel failure loads for the 0.3Al-0.3Cu are recorded as 329.53 N and 120.8 N respectively at the weld pressure of 0.24 MPa, a weld time of 0.23 sec and amplitude of 47  $\mu\text{m}$ . These values are elevated further with the increase in vibration amplitude such as 54  $\mu\text{m}$ , 60  $\mu\text{m}$ , and 68  $\mu\text{m}$ , resulting in higher tensile shear failure loads of around 345.8 N, 422.4 N and 482.65 N respectively. Likewise, the T-peel failure loads of around 129.35 N, 135.53 N and 141.32 N are also obtained at 54  $\mu\text{m}$ , 60  $\mu\text{m}$  and 68  $\mu\text{m}$  of vibration amplitude. The reasons for these types of outcomes are similar as described before.

It is clear from the Fig. 5.5 that the tensile shear and T-peel failure loads of the 0.45Al-0.45Cu exhibits the similar type profile as of the 0.3Al-0.3Cu. In this case, the ranges of the welding conditions are slightly changed to get a desired joint strength. By continuously increasing the weld pressure, it can be observed that the tensile shear and T-peel failure loads begin to increase up to 470.85 N and 175.5 N at 47  $\mu\text{m}$  respectively and with weld pressure of 0.34 MPa and of 0.34 sec weld time. However, these weld strengths dropped with the increase in weld time and weld pressure. The overall tensile shear failure loads exhibit higher values of 513.65 N, 531.45 N and 564.6 N respectively when the vibration amplitude values are increased to 54  $\mu\text{m}$ , 60  $\mu\text{m}$ , and 68  $\mu\text{m}$ . Similarly, T-peel failure loads are calculated to be around 182.83 N, 187.17 N and 193.52 N at these three amplitude settings i.e. 54  $\mu\text{m}$ , 60  $\mu\text{m}$  and 68  $\mu\text{m}$  respectively. It is noticed that when the thickness of the weld materials increases then more amount of ultrasonic energy is required to remove the oxide film present on the surface, and a satisfactory weld can be achieved. Meantime, the amount of ultrasonic energy also depends on the weld time and weld pressure. If these two values are beyond a certain limit, then “over welding” happens and cracks with tip sticking occurs due to dislocating the molecular bonds formed between the mating surfaces.

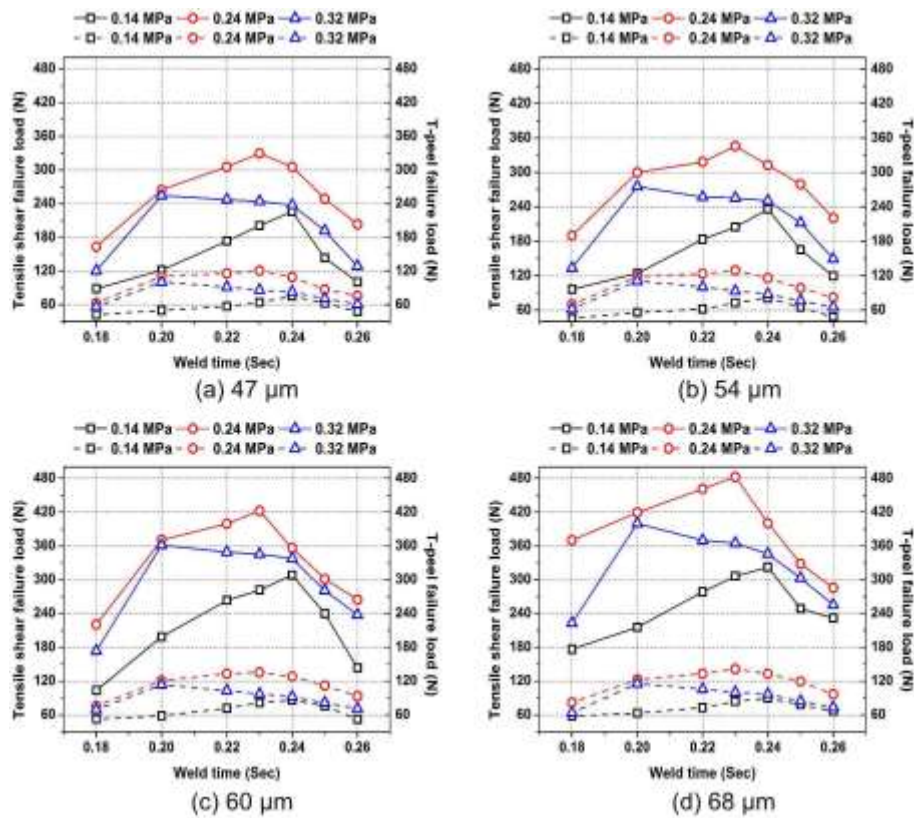


Fig. 5.4 Tensile shear and T-peel failure loads of 0.3Al-0.3Cu weld coupons for different vibration amplitudes

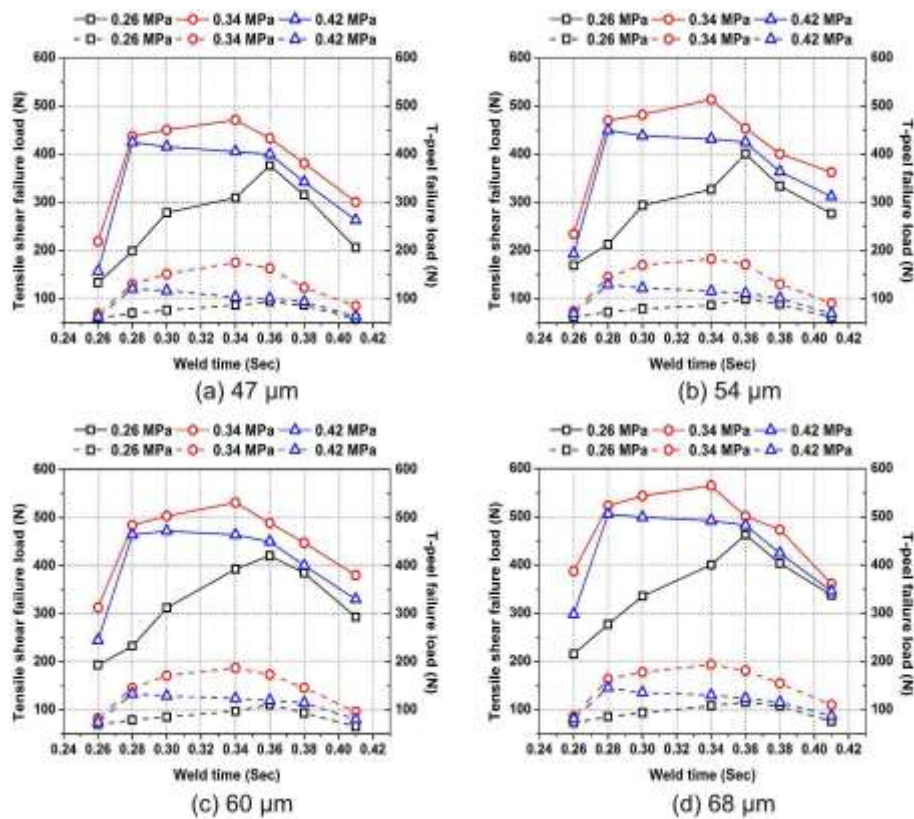


Fig. 5.5 Tensile shear and T-peel failure loads of 0.45Al-0.45Cu weld coupons for different vibration amplitudes

## 5.4.1.2 Influence of process parameters on weld area

Initially, when the metal to metal contact takes place during the welding, small microbonds are developed and gradually increased with the weld time and vibration amplitude. Because, with the increase of these parameters, more temperature is generated at the weld region, these micro bond areas are gradually saturated and appeared in elliptical forms. Meanwhile, it is tough to measure the weld area for each sample after completion of the weld. Thus, an average is calculated by multiplying the area of one weld spot with the number of indented spots appeared on the aluminium material by sonotrode.

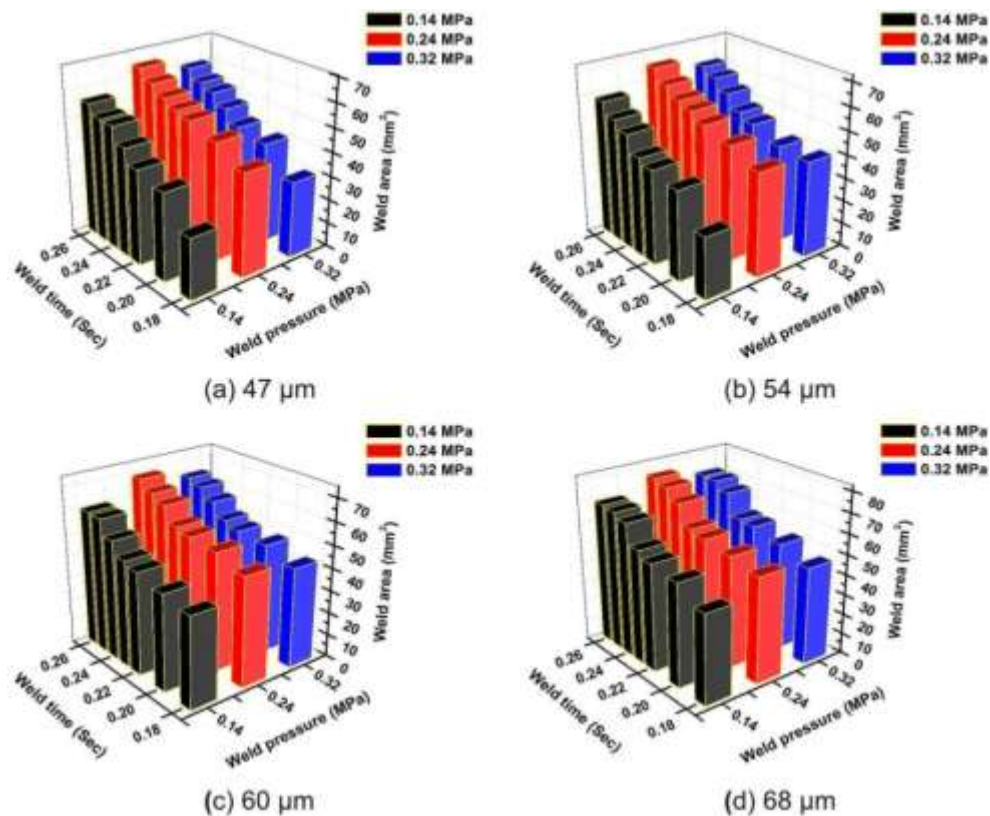


Fig. 5.6 Weld areas of 0.3Al-0.3Cu weld coupons for different vibration amplitudes

Fig. 5.6 depicts a comparison result of the weld areas with respect to various process parameters. From the 0.3Al-0.3Cu experimental sets, it is noticed that the weld area begins to grow and attains a maximum value of 65.39 mm<sup>2</sup> due to increase in weld time from 0.18 to 0.26 sec at a vibration amplitude of 47 μm and a moderate amount of weld pressure of 0.24 MPa. Likewise, the weld area values are also increased with vibration amplitude, i.e., at 54 μm, 60 μm, and 68 μm, weld area were around 67.23 mm<sup>2</sup>, 69.15 mm<sup>2</sup> and 76.62 mm<sup>2</sup> respectively. This is expected because an increase in amplitude can cause higher plastic deformation in the mating surfaces which lead to the distribution of microbonds more and maximize the quality of the weld.

Fig. 5.7 illustrates the graph between different process parameters with weld area for the weld coupons of 0.45Al-0.45Cu. Similar to previous analysis, here the tests are also conducted using four amplitude settings comprising of 47  $\mu\text{m}$ , 54  $\mu\text{m}$ , 60  $\mu\text{m}$  and 68  $\mu\text{m}$ . The weld area begins to rise and reaches the peak value of 67.19  $\text{mm}^2$  at maximum weld time of 0.41 sec, weld pressure of 0.34 MPa and 47  $\mu\text{m}$  of vibration amplitude. Likewise, the weld area exhibit higher values of 69.63  $\text{mm}^2$ , 72.52  $\text{mm}^2$  and 79.19  $\text{mm}^2$  respectively when the vibration amplitude values are increased to 54  $\mu\text{m}$ , 60  $\mu\text{m}$ , and 68  $\mu\text{m}$  respectively. The weld area is also influenced by the increase of the thickness of the metal sheets, and greater weld areas are noticed in the case of higher thickness material.

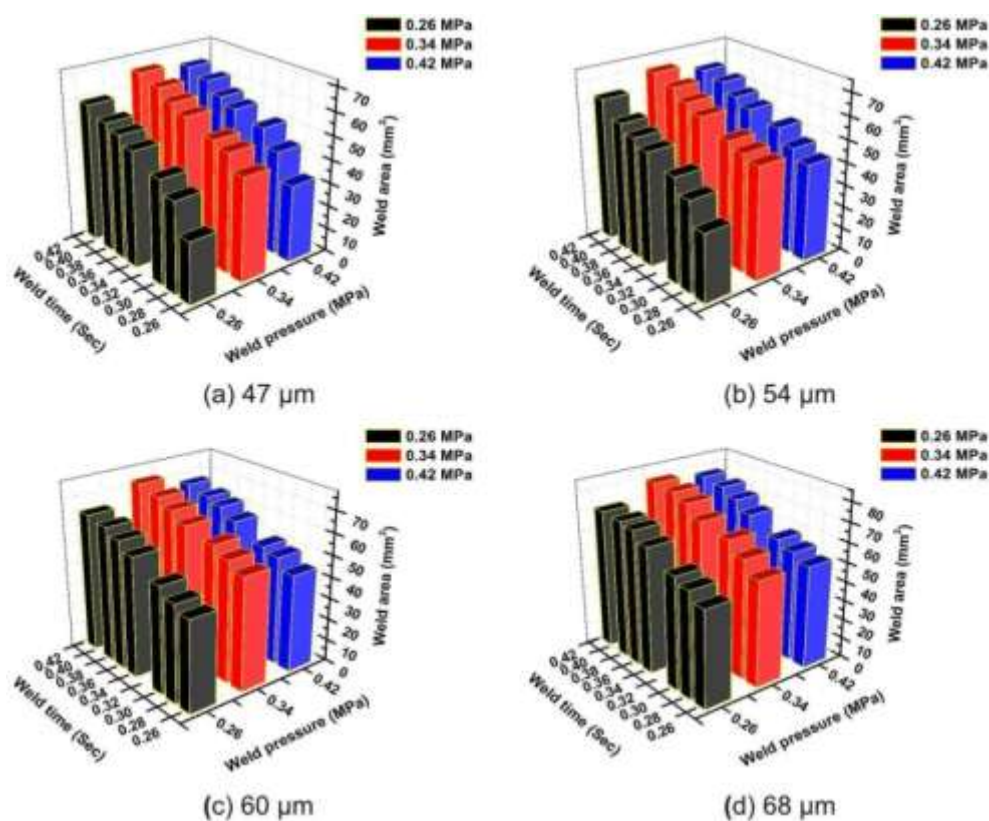


Fig. 5.7 Weld areas of 0.45Al-0.45Cu weld coupons for different vibration amplitudes

#### 5.4.1.3 Effect on weld interface temperatures by process parameters

The interface temperature at the weld zone of 0.3Al-0.3Cu is measured by K-type thermocouples to provide information about the roots of plastic deformation during the welding process. The full experimental set-up for thermal measurements with positions of thermocouples is shown in Fig. 5.1. The temperatures are recorded and the profiles for 0.3Al-0.3Cu sheets with respect to weld time are illustrated in Fig. 5.8.

It can be noticed that the temperatures rise very quickly up to 0.2 sec for all the vibration amplitudes and subsequently the increasing rates gradually slow down. The maximum temperature of 270.42  $^{\circ}\text{C}$  is observed at the weld time of 0.26 sec, weld



pressure of 0.24 MPa and vibration amplitude of 47  $\mu\text{m}$ . However, this interface temperature value is increased to 287.83  $^{\circ}\text{C}$ , 305.15  $^{\circ}\text{C}$  and 313.23  $^{\circ}\text{C}$  with the increase in vibration amplitude to 54  $\mu\text{m}$ , 60  $\mu\text{m}$ , and 68  $\mu\text{m}$  respectively. It can be observed that most of the frictional works are performed at the weld interface, and this is originated from the scrubbing motion of the sheets. Thus, increasing in amplitude value means the increasing the degree of scrubbing motion and finally, it leads to rising in temperature. In support of this experimental results, Elangovan et al. [111] modelled and predicted the temperatures at the weld zone. They showed that the temperature obtained at the weld zone was nearly 100  $^{\circ}\text{C}$  higher than the edge of the sheet. In the present analysis, as the temperatures obtained were above 250  $^{\circ}\text{C}$ , this can result in appreciably reducing the yield strength of the material and enhancing the probability of intermetallic compound formation.

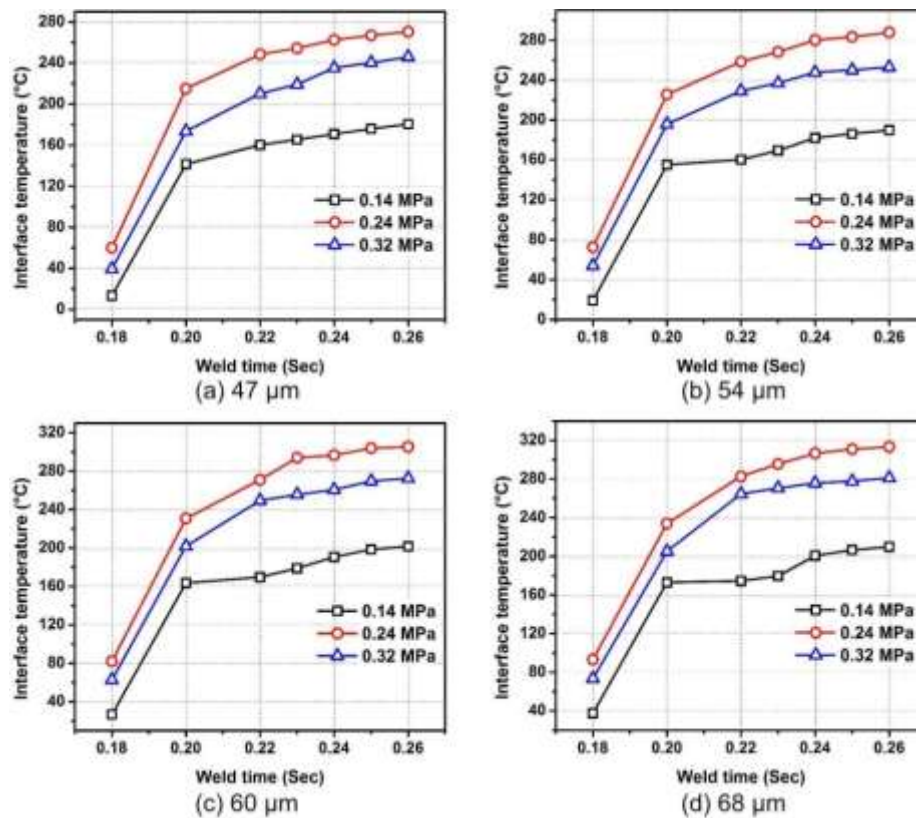


Fig. 5.8 Weld interface temperatures for 0.3Al-0.3Cu weld coupons at different vibration amplitudes

Furthermore, another attempt has been made to measure the interface temperatures of 0.45Al-0.45Cu samples during the welding. The temperature data are depicted in Fig. 5.9. As like before, the peak temperature increased swiftly up to 0.28 sec and then its rate gradually reduced. The maximum interfacial temperature reached around 292.78  $^{\circ}\text{C}$  at the weld time of 0.41 sec, weld pressure of 0.34 MPa and vibration amplitude of 47  $\mu\text{m}$ . However, this interface temperature value is increased to 303.83  $^{\circ}\text{C}$ , 314.39  $^{\circ}\text{C}$  and

328.98 °C with the increase in vibration amplitude to 54  $\mu\text{m}$ , 60  $\mu\text{m}$ , and 68  $\mu\text{m}$  respectively. In fact, the peak temperature obtained in 0.45Al-0.45Cu is higher than the 0.3Al-0.3Cu because the large amount of energy is used in the thicker material to get desired strength.

One noticeable feature that can be observed from the temperature profile is that the heating rate decreases with the increase in weld time. At the initial stage of welding, more amount of ultrasonic energy is delivered to the weld zone as the ultrasonic power and contact resistance are high. But, with the passing of weld time, weld joint gets time to dissipate heat by conduction and convection with a decrease of frictional heat due to sticking. Hence, the temperature rising rate is reduced.

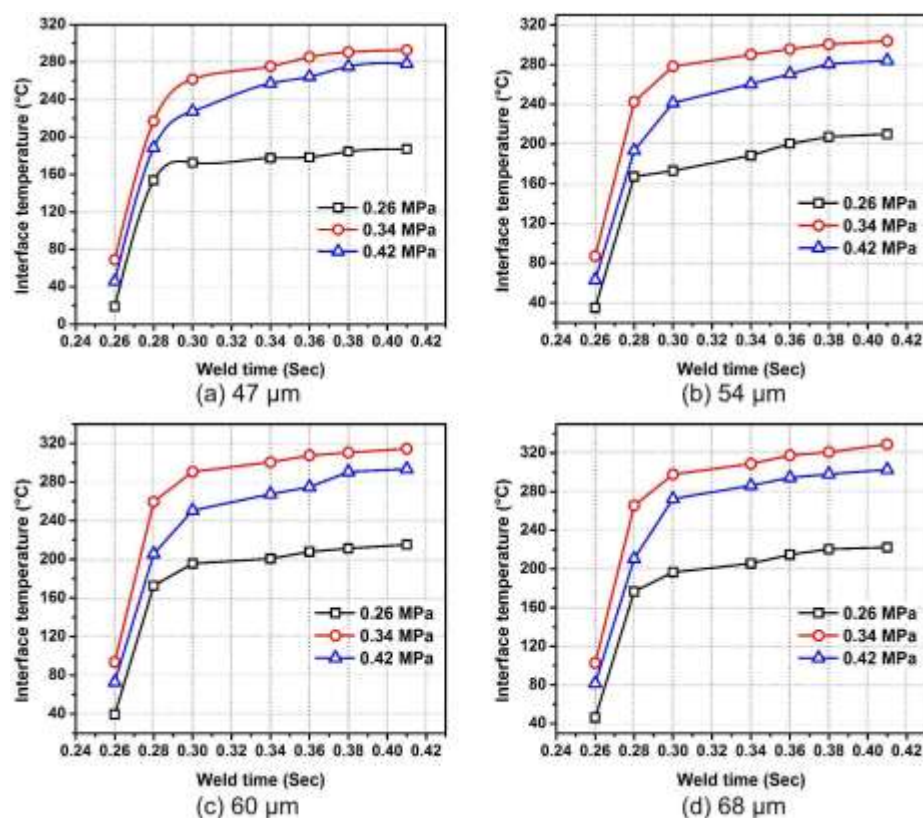


Fig. 5.9 Weld interface temperatures for 0.45Al-0.45Cu weld coupons at different vibration amplitudes

#### 5.4.1.4 Microscopic investigations on weld quality

It is seen that the quality of welding depends on the material properties, process parameters, and thickness of the workpiece. Thus, for the present metallurgical analysis of 0.3Al-0.3Cu and 0.45Al-0.45Cu, three kinds of test specimens are selected based on the both tensile shear and T-peel failure loads occurring at the highest vibration amplitude of 68  $\mu\text{m}$ . The reason behind selecting this vibration amplitude is that in this condition, not only the highest tensile shear and T-peel failure loads are noticed, but also it is believed

that sufficient amount of plastic deformation also occurred. Therefore, to reveal the solid state diffusion between the weld surfaces, scanning electron microscopy (SEM) images along the cross-sections of “under weld,” “good weld” and “over weld” conditions have been taken and shown in Fig. 5.10. In the case of “under welding” condition, the gap between the two weld surfaces is spotted and no microbonds are found. The reason behind this phenomenon is that if the welding pressure is too low, then weld energy can't transfer to the workpiece causing low slippage between the specimens. Moreover, with less welding time, the atomic bonding will not be perfect which results in a bad weld strength. But in “good welding” condition, the weld interface is tightly packed with microbonds and thus, the bond density is high in this case. With the increase of weld time and at a moderate amount of weld pressure, the status of ultrasonic energy is improved and thus the plastic flow is increased at the interface. So the weld strength increases. However, higher weld time can produce oxide layer and crack, decreasing the weld strength. This condition is treated as “over welding” condition.

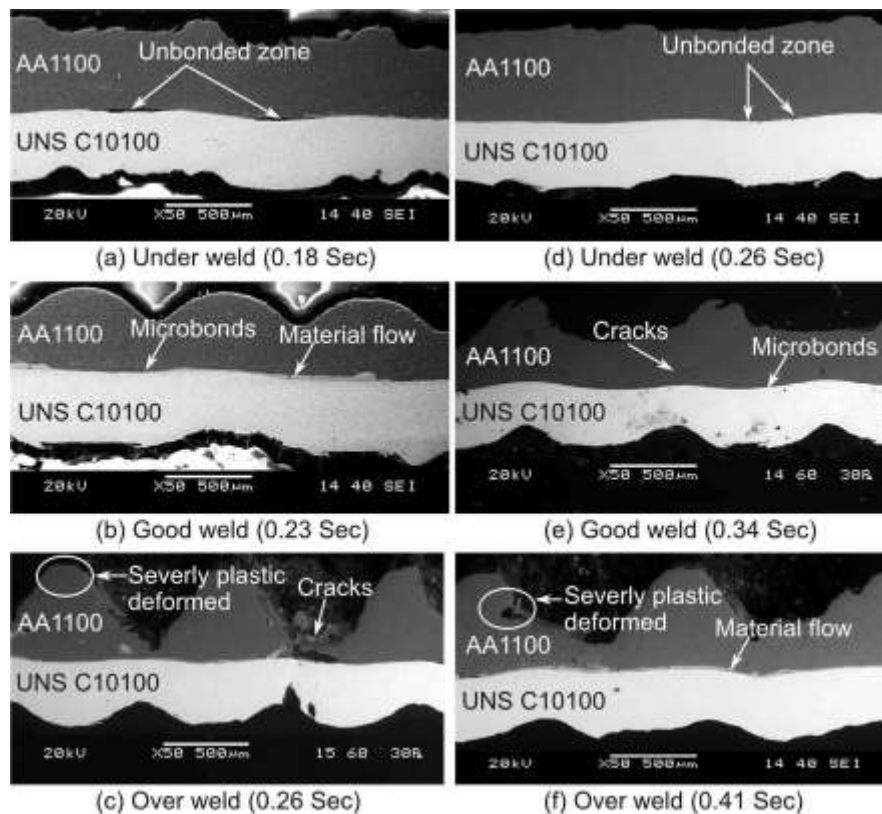


Fig. 5.10 SEM micrographs of weld cross-sections for (a)-(c) 0.3Al-0.3Cu joints and (d)-(f) 0.45Al-0.45Cu joints

#### 5.4.2 0.6Al-0.4Cu and 0.7Al-0.4Cu dissimilar thickness weld coupons

The second set of experimental runs has been performed using aluminium and copper specimens having dissimilar thickness. As already stated, the amount of ultrasonic energy

delivered to the welding spot is directly proportional to the process parameters like weld pressure, weld time and vibrational amplitude. The welds are made starting from the low energy levels to high energy levels resulting an increase of strength up to a certain limit of ultrasonic energy. Further increase in energy results in a reduction in strength and formation of cracks. Thus, the control of process parameters is essential for getting a sound weld joint. In the forthcoming sections, the effects of these controlling parameters on the various aspects of weld attributes will be described along with microstructural analysis.

#### 5.4.2.1 Influence of process parameters on tensile shear and T-peel failure load

In the previous section, it has already been discussed that the tensile shear and T-peel strength of the weld coupons are measured using a universal testing machine. The ultimate failure load from these analyses shows that it is a function of weld pressure, weld time and vibration amplitude. Fig. 5.11 and Fig. 5.12 represent the tensile shear strength and T-peel failure loads for 0.6Al-0.4Cu and 0.7Al-0.4Cu specimens at various amplitudes respectively. In those figures, the solid lines represent tensile shear failure loads, and dotted lines show T-peel failure loads. In both of these experiment sets, one common feature is noticed i.e. the nature of the graph profile. It is observed that these strengths increase with the rise in weld time and vibration amplitude with a moderate amount of weld pressure and finally, it reached the peak point. But, afterwards, these strengths gradually decreased due to excessive weld time resulting formation of cracks around the weld spot. Furthermore, it is worthwhile to state that the weldability of the joined specimens decreases with the increase in mass or thickness of the sheet which is in contact with the sonotrode tip [149]. Therefore, the increase in thickness can reduce the desired effects of solid state weld technique over any other conventional welding process. However, using a high capacity generator can produce more ultrasonic power and consequently it can reduce the limitation and enable the thicker samples to be welded. Nevertheless, the relationship between weld pressure and vibration amplitude must be matched with each other because a low weld pressure can't produce a good weld and a high pressure can hinder the relative motion between the intimate surfaces of sheets. Meanwhile, the increase in excitation of sonotrode results in the rise of vibration amplitude, but at the same time, it is also too difficult to support the weld specimens at the same position when a high-frequency vibration is applied to it. However, if the sonotrode confers low amplitude of vibration then, the relative motion between the two samples will not be adequate to disperse oxide layer present on the weld surface. Thus, it can be stated that for obtaining a good quality joint, a sufficient level of energy is required in a

very less time. Excessive ultrasonic energy can cause tip sticking or severe fatigue fractures in the specimens.

Fig. 5.11 (a) represents the relationship between tensile shear failure load and weld pressure when the weld time is varied from 0.4 to 1 sec at 47  $\mu\text{m}$  vibration amplitude. On increasing weld time from 0.4 to 0.7 sec tensile shear strength tends to grow gradually. However, it constantly reduces between 0.7 to 1 sec weld time. This may be due to the formation of the oxide layer at the weld interface preventing atomic bonding. The maximum tensile shear and T-peel failure loads of 784.38 N and 210.87 N were noticed at 0.7 Sec weld times and at 0.26 MPa weld pressure. Fig. 5.11 (b) illustrates the variation of welding strength with weld pressure as weld time varies from 0.4 sec to 1 sec keeping vibration amplitude at 54  $\mu\text{m}$ . At the weld pressure of 0.26 MPa and a weld time of 0.7 sec, maximum tensile shear failure load and T-peel failure load of 823 N and 212.13 N are achieved. Similarly, at vibration amplitude of 60  $\mu\text{m}$  (Fig. 5.11 (c)), due to higher relative motion between two sheets, tensile shear failure load and T-peel failure loads of 893.5 N and 220.29 N are achieved in 0.7 sec. Moreover, in the case of 68  $\mu\text{m}$  (Fig. 5.11 (d)), tensile shear failure load and T-peel failure loads of 953.8 N and 235.85 N are observed in 0.7 sec, which are the highest values among all the cases.

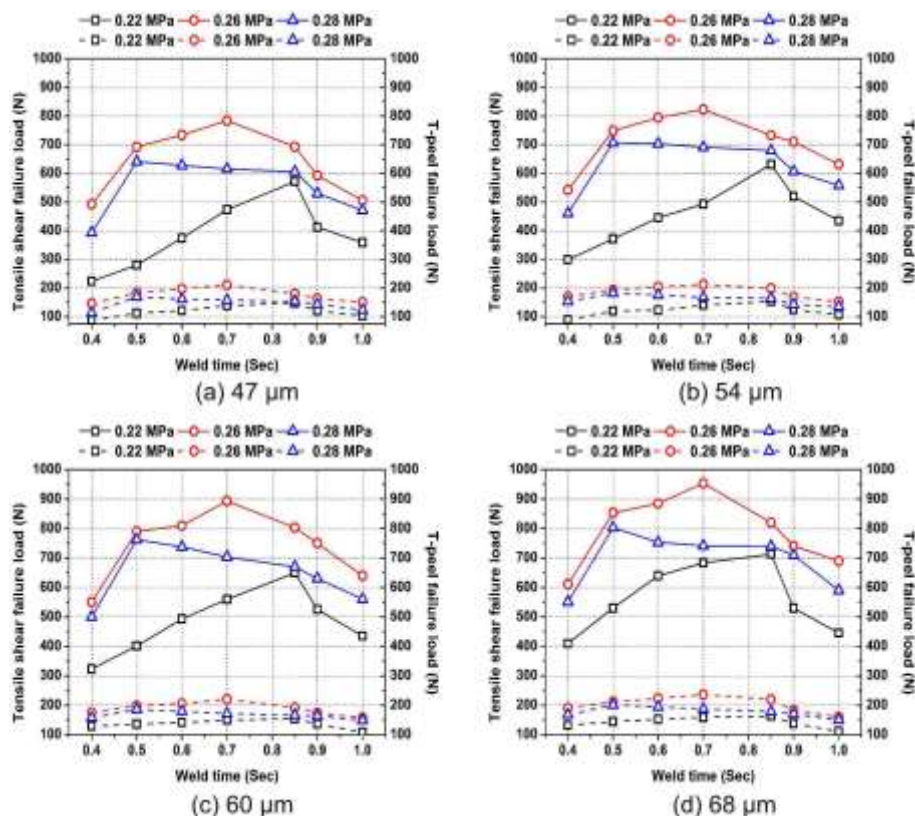


Fig. 5.11 Tensile shear and T-peel failure loads of 0.6Al-0.4Cu weld coupons for different vibration amplitudes

Fig. 5.12 (a) to (d) show the tensile shear and T-peel test results with respect to various parameter conditions. These figures clearly signify that the maximum tensile

shear failure load and T-peel failure loads of 1048 N and 232.92 N have achieved with a weld pressure of 0.38 MPa, a weld time of 0.75 sec and vibration amplitude of 47  $\mu\text{m}$ . After 0.75 sec, these failure loads tends to decrease because the cracks are formed around the weld zone of aluminium sheet. For the lower clamping pressure like 0.34 MPa, the oxide layer may not be broken at the short welding period of time, and thus, the formation of micro bonds may not happen. For high clamping force like 0.42 MPa, the strength decreases even if the welding time is high. The reason for this behaviour is the occurring of the interfacial lock at the weld interface and the heat which is generated due to it, breaks the bonds [56]. These natures of the weld pressure and weld time remain same for 54  $\mu\text{m}$ , 60  $\mu\text{m}$ , and 68  $\mu\text{m}$  amplitude. Moreover, tensile shear failure load and T-peel failure loads values are raised further with the increase in vibration amplitude such as 54  $\mu\text{m}$ , 60  $\mu\text{m}$ , and 68  $\mu\text{m}$ , resulting in higher tensile shear failure loads of around 1258 N, 1351 N and 1512 N respectively. Likewise, the T-peel failure loads of around 262.17 N, 270.53 N and 280.83 N are also obtained at 54  $\mu\text{m}$ , 60  $\mu\text{m}$  and 68  $\mu\text{m}$  of vibration amplitude respectively.

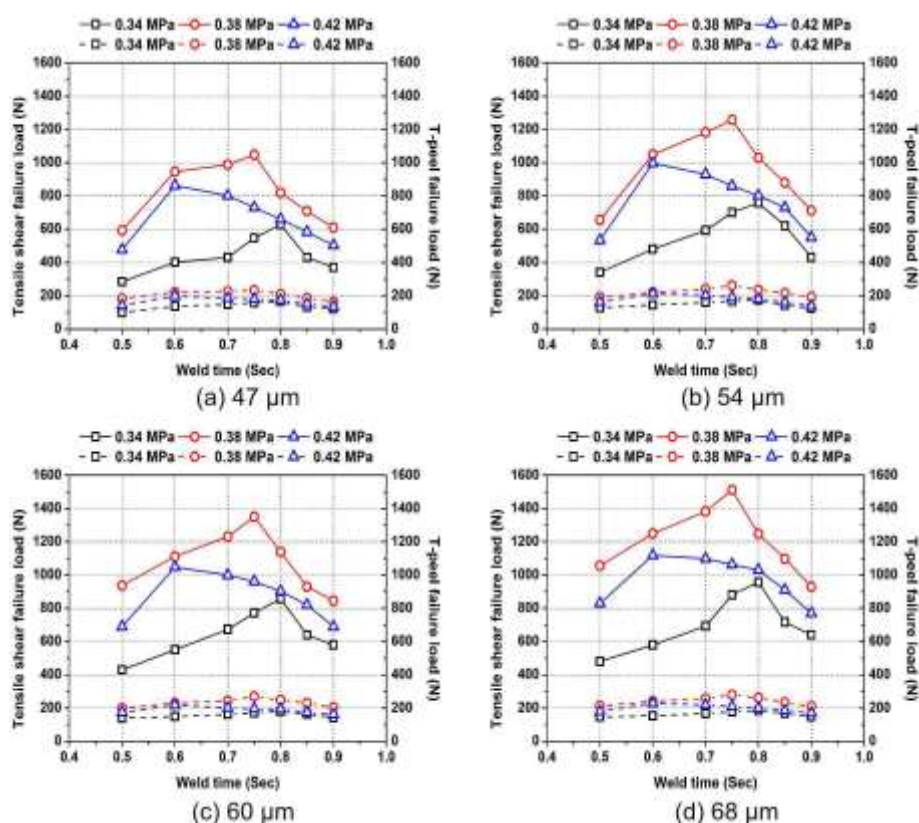


Fig. 5.12 Tensile shear and T-peel failure loads of 0.7Al-0.4Cu weld coupons for different vibration amplitudes

#### 5.4.2.2 Influence of process parameters on weld area

A comparison of the weld areas is shown in Fig. 5.13 for 0.6Al-0.4Cu. The experiments are conducted using four different vibration amplitudes of 47  $\mu\text{m}$ , 54  $\mu\text{m}$ , 60  $\mu\text{m}$  and 68

$\mu\text{m}$  and the relevant average weld areas are measured. Initially, the weld area is continued to increase, and the peak value of  $68.49 \text{ mm}^2$  is obtained at 1 sec of weld time, 0.26 MPa of weld pressure and  $47 \mu\text{m}$  of vibration amplitude. Likewise, the weld areas noticed at  $54 \mu\text{m}$ ,  $60 \mu\text{m}$  and  $68 \mu\text{m}$  are  $70.54 \text{ mm}^2$ ,  $74.57 \text{ mm}^2$ , and  $81.23 \text{ mm}^2$  respectively.

Fig. 5.14 represents the graph between different process parameters with weld area for the weld coupons of 0.7Al-0.4Cu. As like before, the tests are conducted using the above said four settings. The weld area begins to rise and reaches the peak value of  $69.23 \text{ mm}^2$  at maximum weld time of 0.9 sec, weld pressure of 0.38 Mpa and  $47 \mu\text{m}$  of vibration amplitude. Likewise, the weld area exhibit higher values of  $71.42 \text{ mm}^2$ ,  $77.63 \text{ mm}^2$ , and  $84.52 \text{ mm}^2$  respectively when the vibration amplitude values are increased to  $54 \mu\text{m}$ ,  $60 \mu\text{m}$ , and  $68 \mu\text{m}$ . Furthermore, the weld area obtained in this material thickness combination is higher than the 0.6Al-0.4Cu weld coupons.

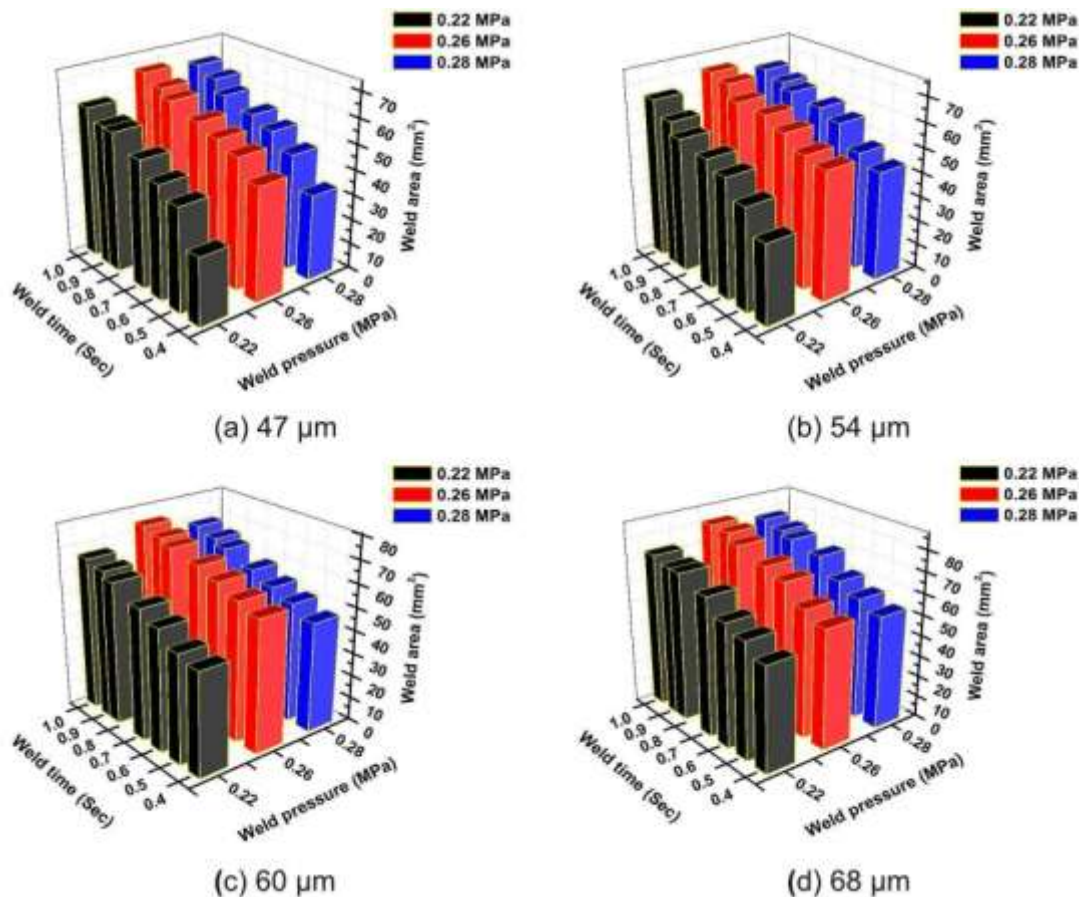


Fig. 5.13 Weld areas of 0.6Al-0.4Cu weld coupons for different vibration amplitudes

#### 5.4.2.3 Effect on weld interface temperatures by process parameters

As the thermal conductivity of the aluminium is lower than copper, the interface temperature rises suddenly, and it is the reason for high plastic deformation of the aluminium material. Therefore, the temperature measurements of 0.6Al-0.4Cu weld

specimens are performed and presented in Fig. 5.15. USMW performs in a fraction of time, it is hard to gather a large amount of data regarding temperature [150]. To investigate the trend of temperature rise in the weld coupon, 0.1 mm diameter K-type thermocouple is implanted near to this area. The curves show that, as the welding time increases, the temperature rises very quickly and reaches a maximum value of 340.69 °C at 68  $\mu\text{m}$  of vibration amplitude, followed by 329.66 °C at 60  $\mu\text{m}$ , 322.04 °C at 54  $\mu\text{m}$  and 310.83 °C at 47  $\mu\text{m}$ . All these temperature values are observed at 0.26 MPa of weld pressure and 1 sec of weld time.

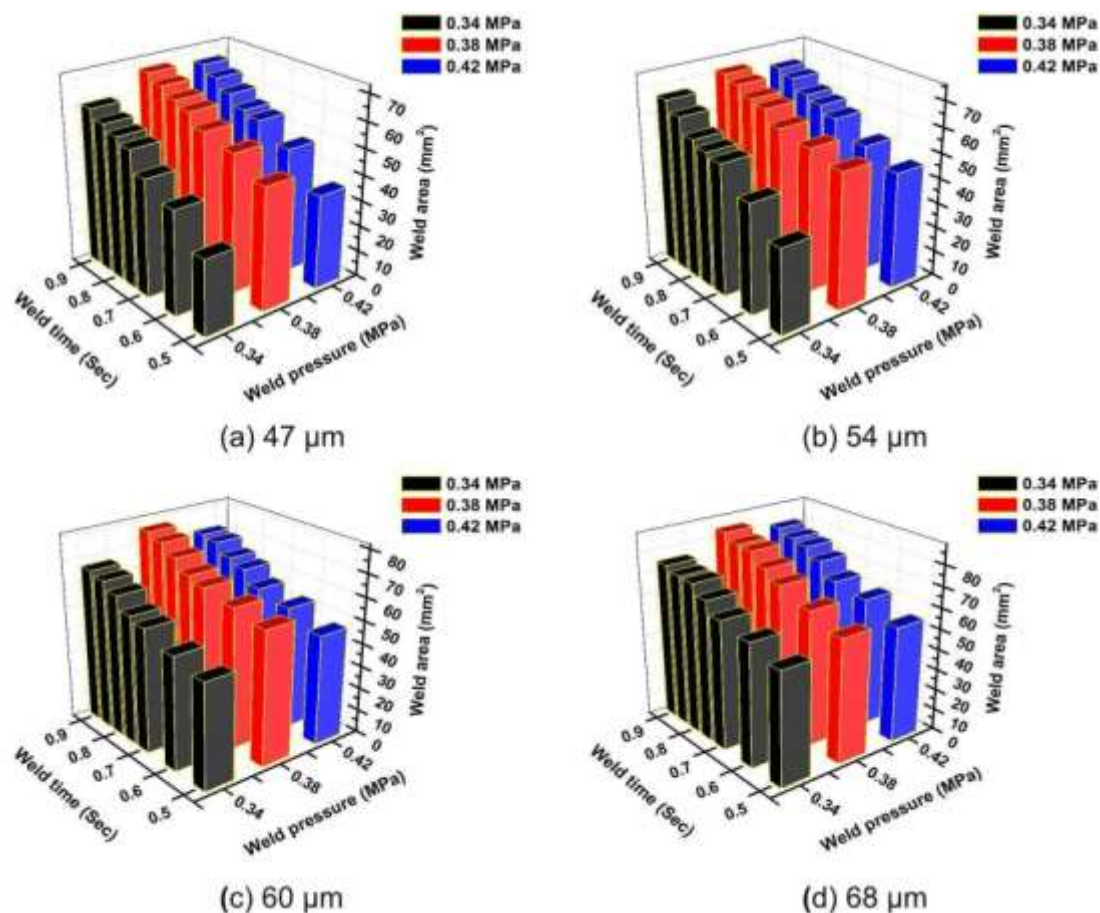


Fig. 5.14 Weld areas of 0.7Al-0.4Cu weld coupons for different vibration amplitudes

Furthermore, an attempt has been taken to measure the interface temperatures of 0.7Al-0.4Cu samples during the welding. The temperature data are depicted in Fig. 5.16. As like before, the maximum interfacial temperature reached around 317.07 °C at the weld time of 0.9 Sec, weld pressure of 0.38 MPa and vibration amplitude of 47  $\mu\text{m}$ . However, this interface temperature value rise to 329.37°C, 342.19 C and 350.35°C with the increase in vibration amplitude of 54  $\mu\text{m}$ , 60  $\mu\text{m}$ , and 68  $\mu\text{m}$  respectively. In fact, the peak temperature obtained in 0.7Al-0.4Cu is higher than the 0.6Al-0.4Cu because the large amount of energy is used in higher thickness material to get desired strength.



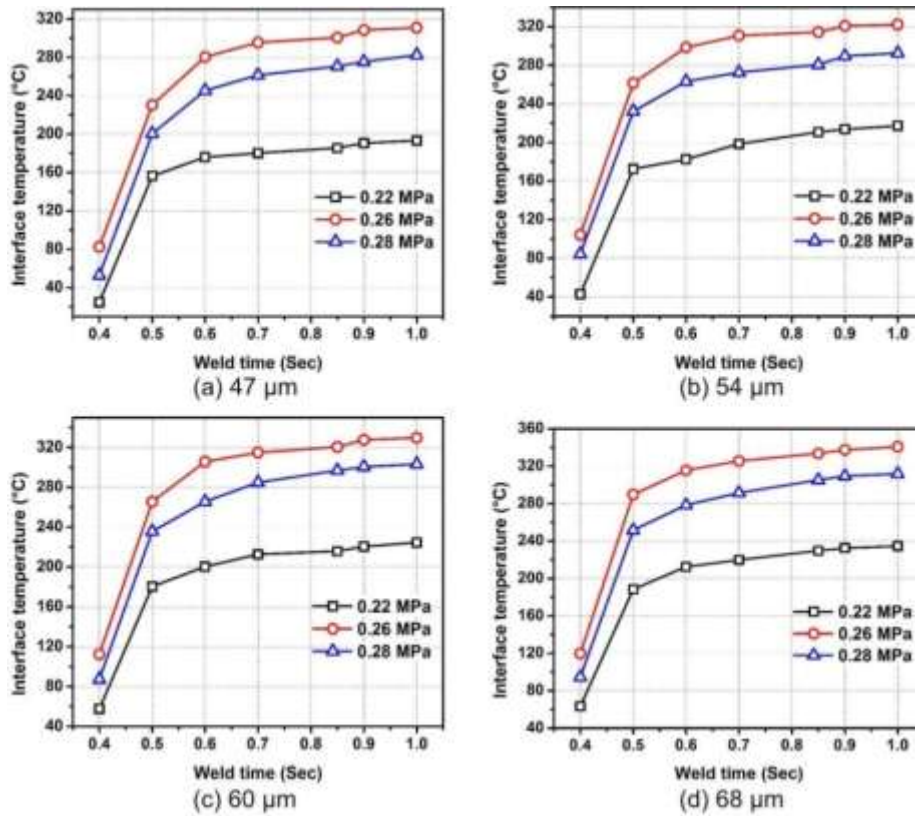


Fig. 5.15 Weld interface temperatures for 0.6Al-0.4Cu weld coupons at different vibration amplitudes

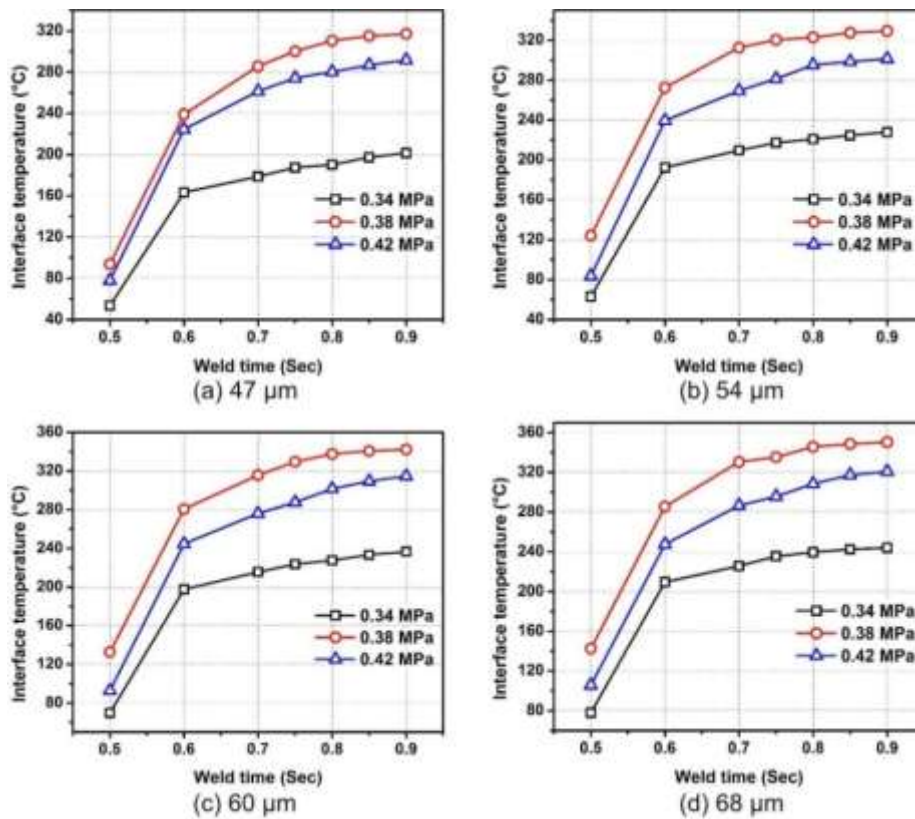


Fig. 5.16 Weld interface temperatures for 0.7Al-0.4Cu weld coupons at different vibration amplitudes

#### 5.4.2.4 Microscopic investigations on weld quality

The characteristics of a good weld include highly dense interfacial bonds with no gaps. It can be obtained from bond density attribute, and it includes features like micro-bonding, unbonded region, and swirls like pattern. SEM images along the cross-sections of “under”, “good” and “over” weld conditions using 0.6Al-0.4Cu and 0.7Al-0.4Cu specimens are shown in Fig. 5.17. In under weld condition, there is a gap between two materials and no micro bonds are found in this condition and in good condition, the welding interface is tightly packed with micro bonds. The bond density is high in good weld condition. But in over weld condition, there is no uniformity of aluminium material at the welding zone. In this condition, as the temperature increases, the sheets get to be more ductile and subsequently profound distortion or extrusion will happen in the top sheet by the sonotrode tip which is otherwise called sticking.

#### 5.4.3 Weld quality determination for 0.7Al-0.4Cu weld coupons

It is seen that the quality of welding depends on the material properties, input process parameters and thickness of the workpiece. If the welding pressure is too low, then weld energy can't transfer to the workpiece causing less rubbing between the specimens. With the increase of weld pressure, the ultrasonic energy is improved resulting higher interatomic diffusion and plastic flow at the interface [91]. So, the weld strength increases. Similarly, the weld time also plays a vital role. With less welding time, the atomic bonding will not be perfect which results in poor weld strength. However, higher weld time can produce oxide layer and cracks, decreasing the weld strength. Also, the strength of the weld depends on the correct vibration amplitude for particular values of weld pressure and time. Therefore, out of the existing sets of the experiment, 0.7Al-0.4Cu has been selected because; it provides the maximum tensile shear and T-peel failure loads for the weld joint. Meanwhile, the weld attributes like bond density, post weld thickness, microhardness distributions, fractographic and X-ray diffraction (XRD) analyses of weld surfaces which influence the performance of the weld are discussed in the subsequent sections.

##### 5.4.3.1 Microhardness distribution in weld zone

According to the principle of USMW, the welding between sheets occurs due to plastic deformation at an elevated temperature. In this study, the microscopic and microhardness analyses are explained in detail to reveal the microstructural changes during the USMW process. In this process, two types of features noticed and they are initial work hardening

of the weld specimen followed by softening due to the generation of high temperature on the increase of weld time.

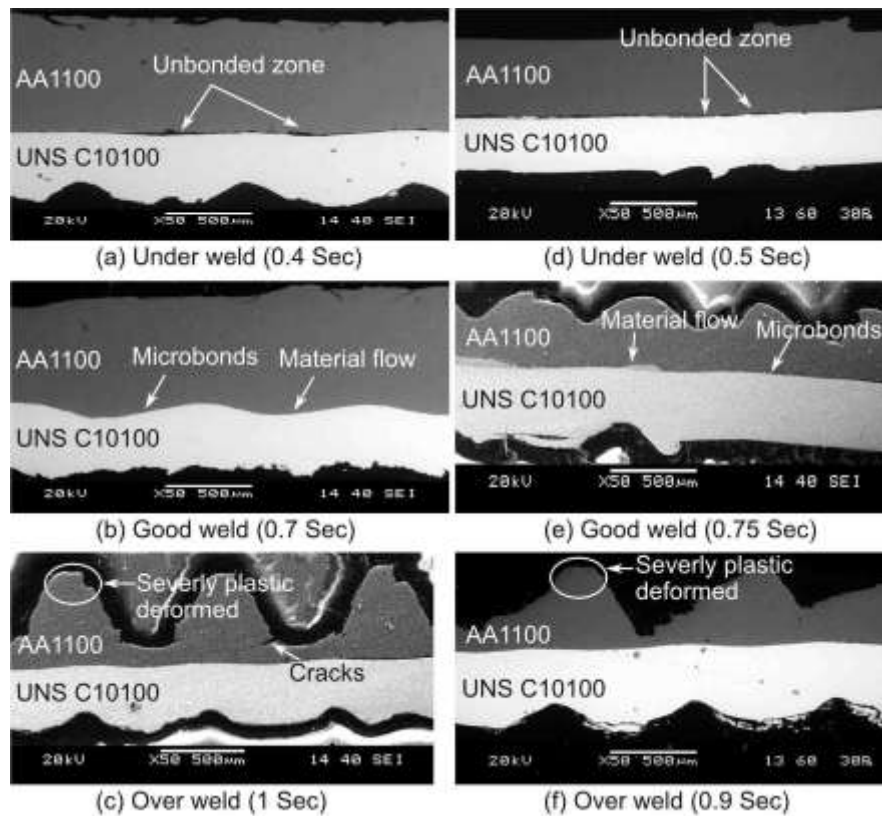


Fig. 5.17 SEM micrographs of weld cross-sections for (a)-(c) 0.6Al-0.4Cu joints and (d)-(f) 0.7Al-0.4Cu joints

When the ultrasonic vibration starts, the weld interface experiences a shear force due to the friction, and thus plastic deformation happens. Due to it, the initial grain size of the parent material elongate, and they are noticed only in the initial stage. As the time increases further, then the new crystal structures are formed, and the formerly elongated grains are disappeared. The newly formed crystal structures are of finer size and same lattice structure as of the undeformed grains of parent material. This recrystallization process is due to the input of ultrasonic energy to the weld area continuously. However, if welding is continued further, then the grains begin to grow, and consequently, material softening happens. The microscopic observation of grains around the weld interface with respect to various weld times is shown in Fig. 5.18.

Thus, the microhardness measurements on the cross-sections of previously described “under”, “good” and “over” weld samples are taken in order to prove the work hardening and softening during the welding process. It is believed that the peaks under the sonotrode knurl experiences severe plastic deformation and thus it is expected that high strain rate occurs in this zone. The Vickers hardness results are plotted against the weld time and shown in Fig. 5.19. From this figure, it was observed that at the starting stage of USMW, the hardness shows 57% higher results than the hardness of the parent materials

and it is due to severe cold working at the interface. Meanwhile, when the weld time is increased further, then the hardness value is drastically reduced and even lower than the parent material. This type of phenomena is not only observed in USMW but also seen in other welding process like friction stir welding. The results demonstrate that the USMW shows a significant material softening at the weld zone due to the dislocation of atoms and coarsening of grains [151].

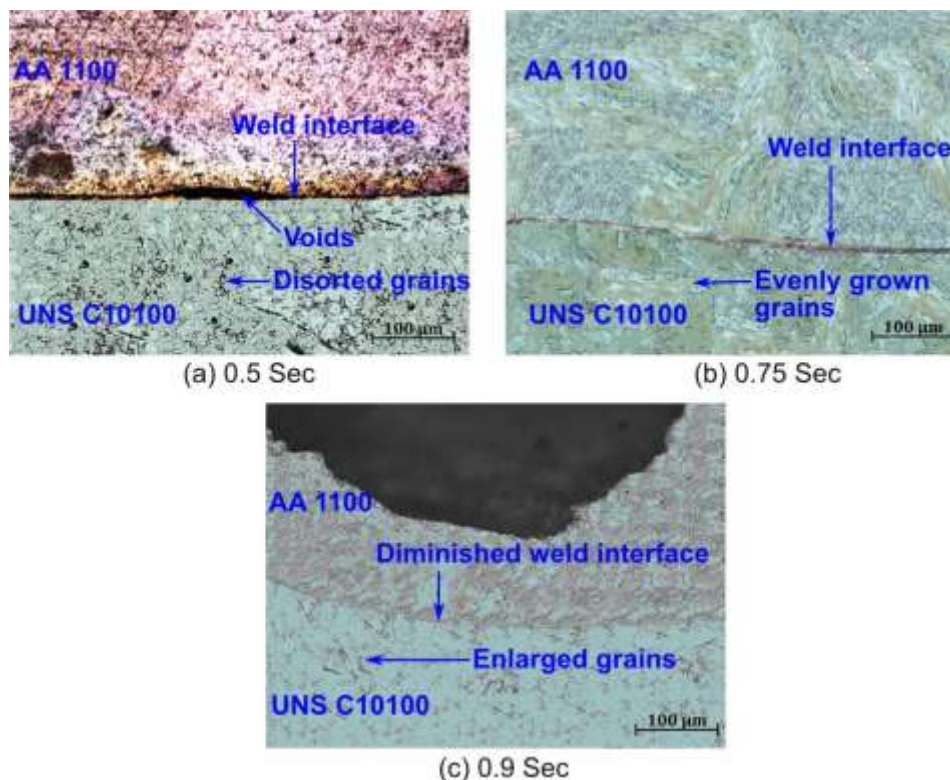


Fig. 5.18 Optical microscopic images of 0.7Al-0.4Cu weld specimens with increase in weld time

The hardness variations along the weld interface in a horizontal manner with respect to various weld times is shown in Fig. 5.20. These weld times are selected based on “under”, “good” and “over” weld condition. For the short welding time, the microhardness under the peak of sonotrode is higher than the crest position. It is due to the fact that the plastic deformation starts from the centre of peak position and gradually proceeds towards the crest position as the welding proceeds. Thus, the crest region is not much work hardened as comparable to the peak position. Furthermore, at short welding time, there is a much fluctuation in hardness value but when the welding time increases; the fluctuation is diminished showing material softening behaviour. In the meantime, the hardness value is also lowered at the highest weld time.

In order to complete the 2D mapping analysis of microhardness results, the measurements are also taken in the vertical direction of the weld cross-section. Thus, Fig. 5.21 reveals the variations of hardness with time at various locations below the crest zone. This vertical measurement showed that the hardness value is very high in the

surface region for shorter welding time, and it is drastically reduced towards weld interface due to material softening. But for higher welding times, there is an extraneous amount of cold work hardening at the surface region of crest zone. Thus, there is less difference observed between the surface and interface zone.

The summarized results of this analysis are the materials which are under high ultrasonic energy experiences instant work hardening followed by softening. The process is more or less similar to annealed process, where the cold worked materials regain its strain-free grains through recrystallization and grain growth through the application of heat.

#### 5.4.3.2 Fractographic analysis of weld surface

In the lap shear test of weld samples, various failure modes are observed like an interfacial failure, nugget pull-out failure, base metal failure, etc. Considering the good weld condition where the tensile shear and T-peel failure loads are maximum, the sample joined at 0.75 sec of weld time, 0.38 MPa of weld pressure and 68  $\mu\text{m}$  of vibration amplitude is analysed using SEM.

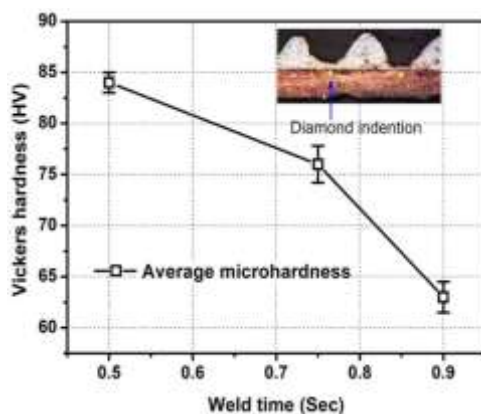


Fig. 5.19 Average microhardness of peaks beneath sonotrode tip for different weld times

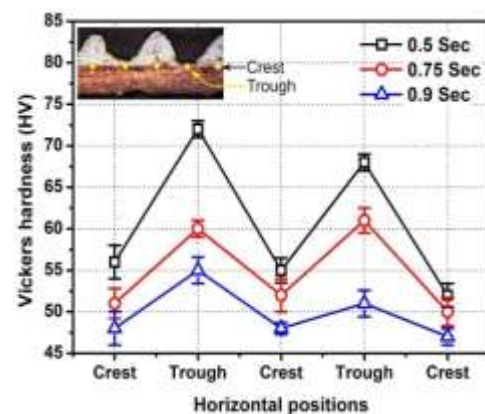


Fig. 5.20 Hardness distribution along the horizontal direction for 0.7Al-0.4Cu weld samples

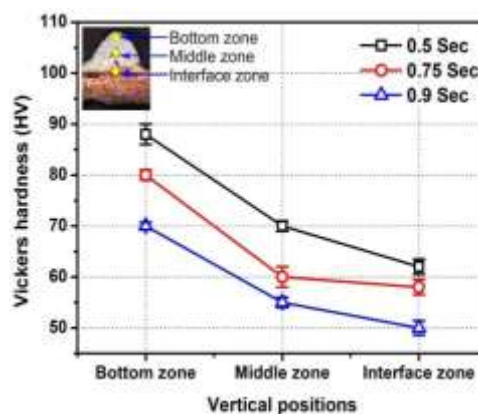


Fig. 5.21 Hardness distribution along the vertical direction for 0.7Al-0.4Cu weld samples

The nine grooves on the sonotrode tip make the top surface of sheets non-uniform, and this surface is entirely composed of peaks and valleys as seen in Fig. 5.22. Fig. 5.23 (a) and (b) depicts the overall fractured surfaces of Al side and Cu side respectively where the fracture happened at the periphery of the weld spot. To understand the tensile shear fractography fully, there are four notable features found on the fractured surfaces and these are divided into four types (i) Al-containing zone, (ii) Cu-enriched zone, (iii) vertical pressure lines, and (iv) squeezed out eutectic mushy liquid. The fracture surface of the Al side is shown in Fig. 5.23 (a). It is observed that due to the lower hardness of Al than Cu, it is severely deformed, and thus less Cu is located on it. But as the Cu is harder than Al, so it undergoes less deformation, and there is no improvement of weld area which affects the weld quality. It is represented in Fig. 5.23 (b). Fig. 5.23 (c) and (d) represents the magnified images of Al side and Cu side respectively where the vertical lines can be clearly observed. These lines are created when the teeth of evenly engraved sonotrode tip pressed the two sheets for the firmly gripping purpose.

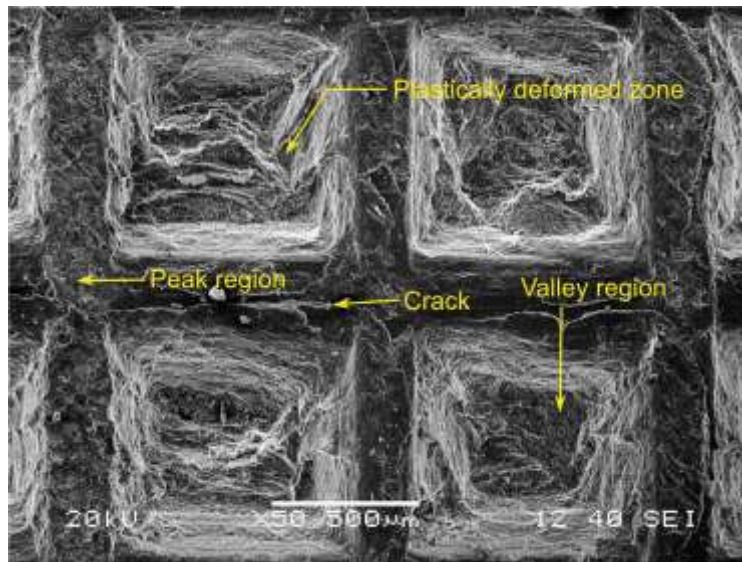


Fig. 5.22 Typical SEM image of top surface of Al sheet under sonotrode tip showing peak and valley regions

It is believed that the valley of the vertical pressure lines in the interface caused plastic deformation and forms a relatively stronger bond. Meanwhile, a squeezed out eutectic mushy liquid is observed at the edge of the weld spots confirming the localised melting during USMW process. As previously described, the temperature generated in this stage was 335.26 °C, and this temperature was sufficient enough to increase the flowability of the specimen. Thus, it increased the real bonding area and maximized the weld strength. Fig. 5.23 (e)-(h) illustrate higher magnification image of the spots specified on Al and Cu fractured surfaces. In these figures, the predominant feature noticed i.e. parallel scrubbing lines, and along with this feature one another feature noticed i.e. dimple fractured region. Parallel scrubbing lines represent the scrubbing action between the

sheets which occurs during the welding process, and the dimple fractured region signifies the zone where the real welding has happened. These type of similarly fractured features also appear after the typical shear failure tests as described by Truog [152].

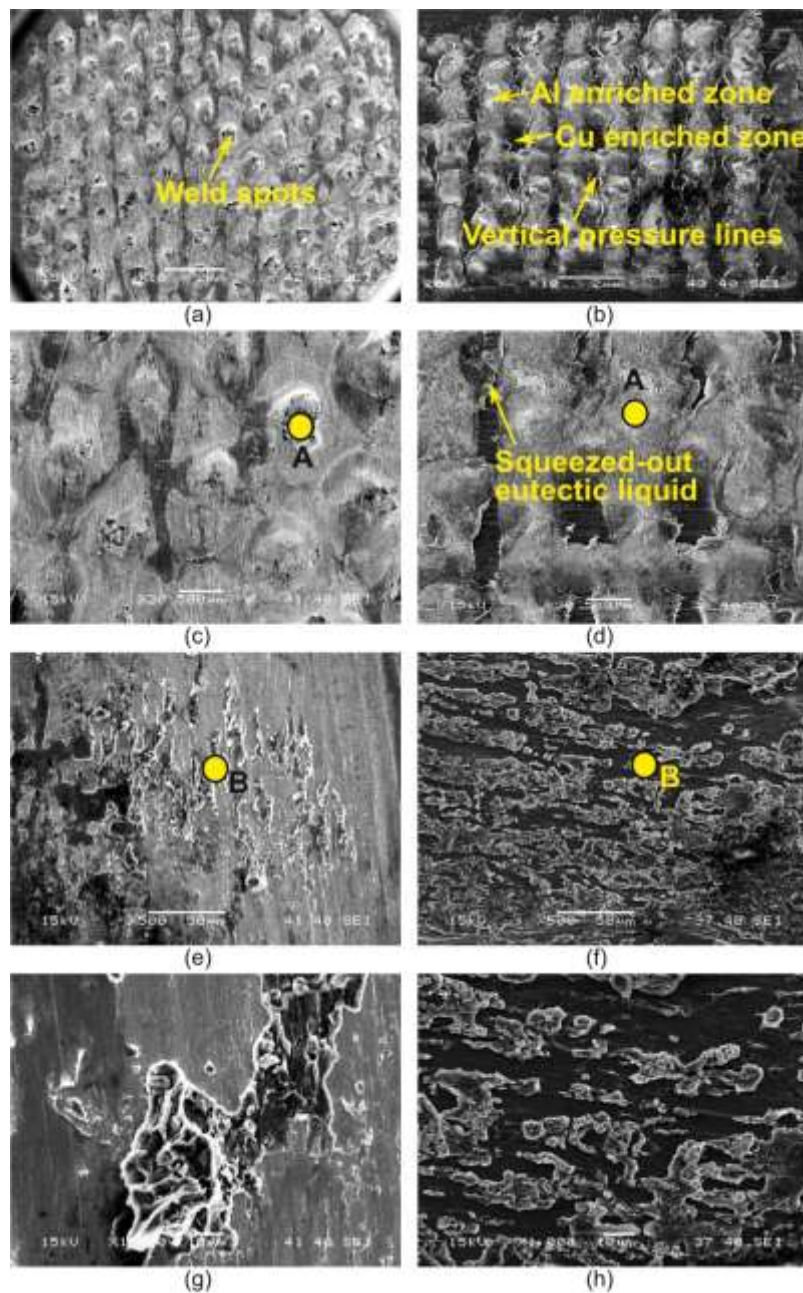


Fig. 5.23 Overall fractured surface SEM images of tensile shear failed samples (a) Al side and (b) Cu side; (c) magnified image of (a) showing weld spots; (d) magnified image of (b) indicating squeezed-out eutectic liquid feature; (e) and (f) magnified pictures of spot A denoted in (c) and (d); (g) and (h) higher magnification images of spot B indicated in (e) and (f)

#### 5.4.3.3 Scanning electron microscopy (SEM) with EDS investigation of fractured surface

Generally, energy dispersive spectroscopy (EDS) analysis has been used for the quantitative analysis. Hence, EDS results along with SEM images have been obtained

from the fractured surfaces of good weld condition. Fig. 5.24 (a) illustrates a little amount of Cu i.e. 32.4 (wt %) presents on the fracture surface of Al side. Fig. 5.24 (b) also confirms a 77.22 (wt %) of Al is deposited on the Cu surface. These results reveal that, as Al is a softer material than copper, its weld surface is more quickly deformed plastically during ultrasonic welding. So, most of the fracture occurs on the low strength Al side during testing. The SEM micrograph with the backscattered electrons (BSE) mode of the weld cross-section is also taken to reveal the amount of diffusion across the interface, and it is selected for the good weld sample. The high magnification SEM figure with EDS mapping is shown in Fig. 5.25 (a). The line scan result unveils that there is no continuous intermetallic compound (IMC) layer formed at the weld interface due to quick process and low-temperature generation as compared with other welding processes. The diffusion interlayer thickness is observed as about 1.5  $\mu\text{m}$  from Fig. 5.25 (b). Normally, the possible chances of formation of IMC in between Al and Cu may be AlCu, Al<sub>2</sub>Cu and Al<sub>4</sub>Cu<sub>9</sub>. The chemical compositions (wt %) from EDS analysis is 66.67Al-33.33Cu. Therefore, it suggests that the dominant element present in this IMC is probably Al<sub>2</sub>Cu according to the Al-Cu phase diagram [153].

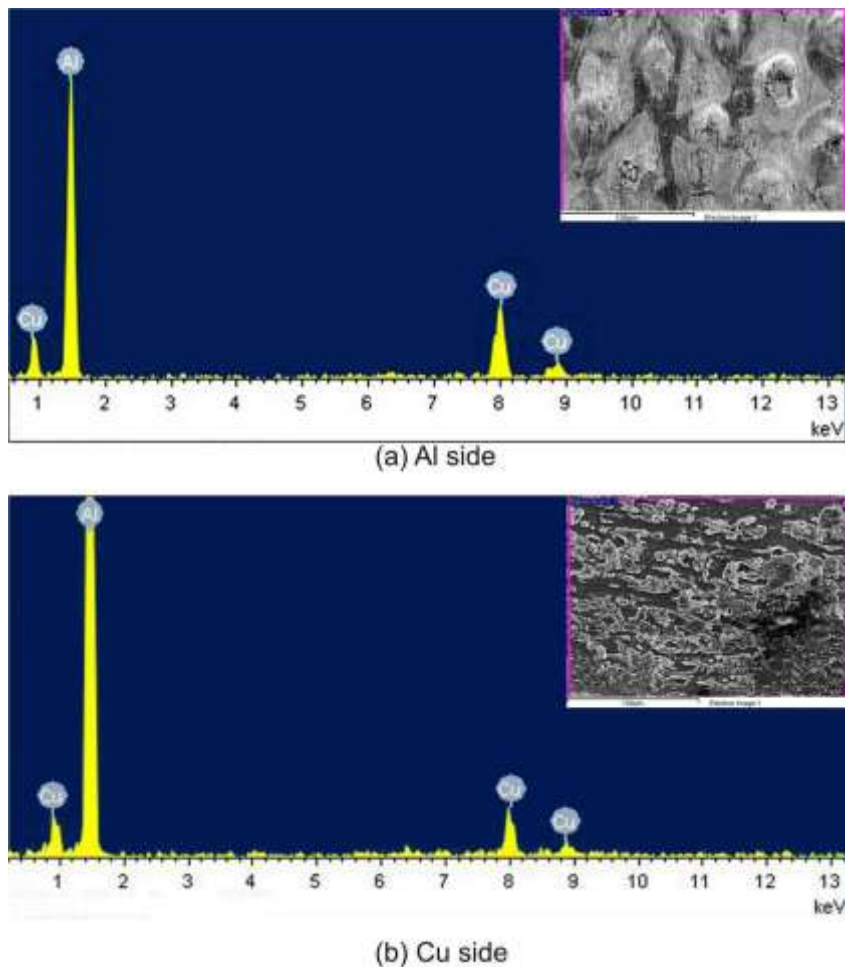


Fig. 5.24 EDS analysis of fractured surfaces of good weld sample



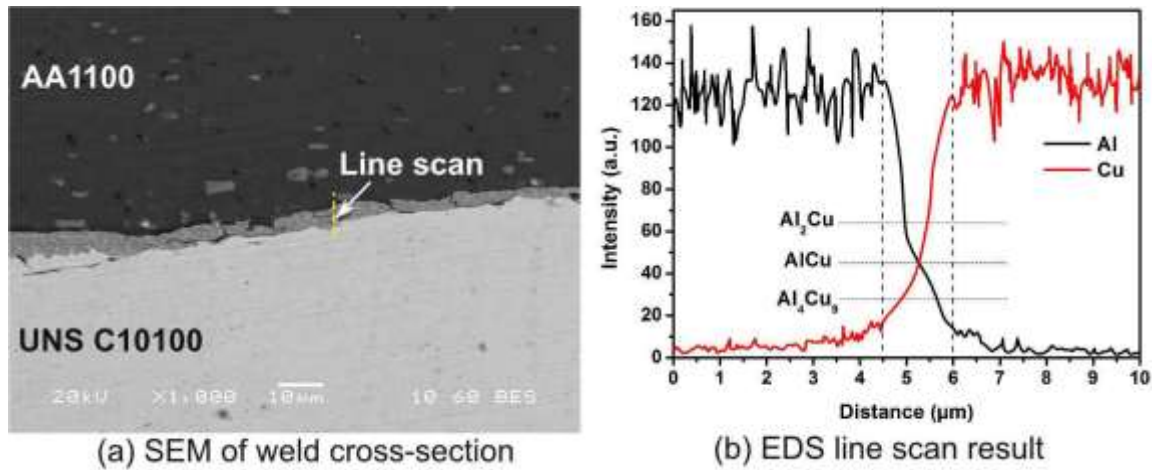


Fig. 5.25 (a) High magnification SEM image and (b) EDS line analysis of weld interface for good weld joint

#### 5.4.3.4 X-ray diffraction (XRD) analysis of fractured surface

The purpose of performing X-ray diffraction (XRD) analysis is to validate the results; those are already obtained in SEM and EDS analyses. Thus, the XRD analysis has been carried out on the fractured surfaces of Al and Cu, which are previously described as the good weld samples. Fig. 5.26 (a) and (b) depicts the peak intensities of various compounds with respect to diffraction angle  $2\theta$ . This graph confirms the EDS analysis result that there exists only one intermetallic compound (IMC) and it is  $\text{Al}_2\text{Cu}$ . The other compounds observed are the Al on Cu fracture surface and Cu on Al fractured surface. A similar type of results also reported by other researchers [155, 156] in USMW and also similar types of report by Xue et al. [156] while performing friction stir welding of A6061 aluminium alloy with copper sheet.

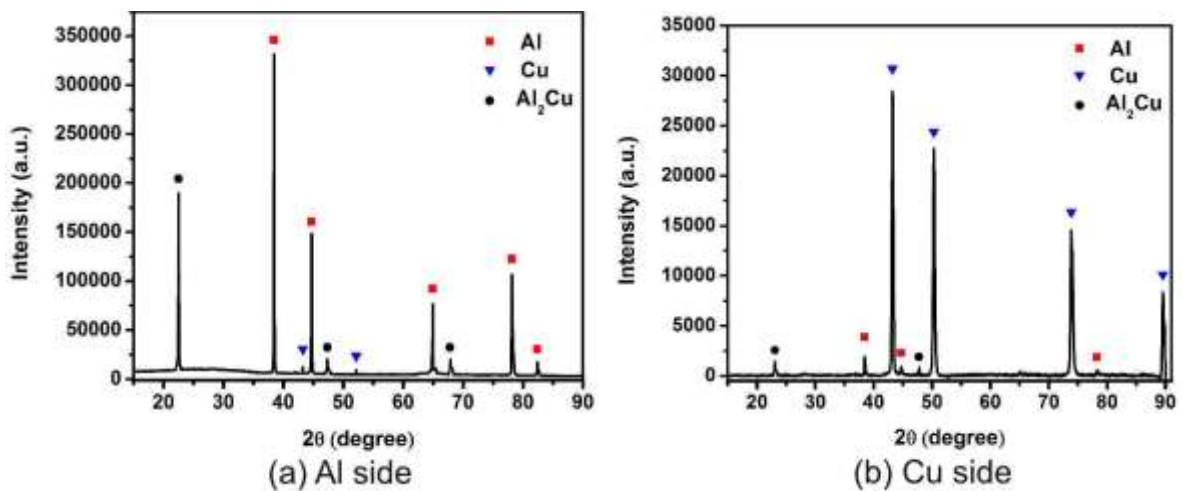


Fig. 5.26 XRD results showing the presence various elements on (a) Al fractured surface, (b) Cu fractured surface

#### 5.4.4 Prediction of responses for 0.7Al-0.4Cu weld coupons

To meet the demands of today's competitive and dynamic market, manufacturing processes should be automated. Unfortunately, due to lack of knowledge about the physics of real world problems, those can't be adequately mathematically modeled. One of such example is statistical regression analysis. This traditional technique can be executed based on the experimental data collected by using the full factorial design of experiment [157]. However, this method is carried out according to responses, and it is not capable of capturing all the dynamics of the process. Thus, soft computing method like artificial neural network (ANN) has become a practical and powerful approach to solve the very complex problems. This approach is well-known to find out the non-linear relationship between input and output. It works like distributed information processing structure in the brain [158]. For this approach, the objective of the current research is to urge predictive models between multiple inputs and a single output. A comparative study based on regression, ANN and adaptive neuro-fuzzy inference system (ANFIS) approaches are also represented.

##### 5.4.4.1 Prediction of responses by regression analysis

The ultimate aim of a welder is to select his process parameters for a desired quality of the product/weld joint. To correlate the ultrasonic welding parameters like weld pressure (WP), weld time (WT) and vibration amplitude (A) to the final objective of the weld joint i.e. tensile shear failure load (TS) and T-peel failure load (TP), regression analysis is conducted. An empirical model is proposed for the TS of the weld joint. Meanwhile, the coefficient of determination ( $R^2$ ) and adjusted  $R^2$ -statistic ( $R_{adj}^2$ ) are determined and compared in Table 5.5 for the various models. It is observed that second order polynomial model is best suited for the current problem, where  $R^2=91.73\%$  means, this model can be able to explain the response up to 91.73%.  $R_{adj}^2=90.83\%$  represents the number of predictors those can express the significance of relationship between the input variables and responses. Thus, the second order polynomial regression model is preferred for further analysis in this study.

Table 5.5  $R^2$  and  $R_{adj}^2$  values for various regression models of TS

Degree of model	$R^2$ (%)	$R_{adj}^2$ (%)
Linear	33.60	31.11
Linear+interaction	35.72	30.71
Quadratic	91.73	90.83

Analysis of variance (ANOVA) is typically used to check the adequacy of the developed regression model, where its columns represent the sum of square error (SS), the degree of freedom (DF), mean square error (MS), F-statistic and P-values.

Table 5.6 summarizes the ANOVA for tensile shear failure load (TS). The last column of ANOVA table represents P-values, and these values are generally used for the checking of the significance of input factors on the response. These values are determined with a 95% of confidence level. Thus, the factors having P-values more than 0.05 are treated as the insignificant terms and represented in “\*” symbol. Therefore, these insignificant terms are eliminated from the table by the backward stepwise model fitting process.

Table 6.7 depicts the ANOVA table after elimination with rest of the terms. After elimination, the  $R^2$  and  $R_{adj}^2$  values are 91.47% and 90.81% respectively. Thus these two values obtained here are below than the values obtained in full quadratic model (i.e. 91.73% and 90.83%) unveiling the significance of relationship between the responses and the input variables after elimination of terms like  $A \times WP$ ,  $A \times WT$  and  $A^2$ . Eq. (5.1) depicts the TS model in the un-coded unit.

$$TS = -35769.52 + 15.50 \times A + 1.58 \times WP + 15205.48 \times WT - 8820.70 \times WP \times WT - 1.96 \times 10^5 \times WP^2 - 8414.21 \times WT^2 \quad (5.1)$$

Table 5.6 ANOVA table for TS (before elimination of insignificant terms)

Source	Sum of Squares	DF	Mean Square	F-Value	p-value
Model	5.37E+06	9	5.96E+05	91.22	< 0.0001
A-Amplitude	8140.21	1	8140.21	1.25	0.2681
B-Weld pressure	1.88E+06	1	1.88E+06	287.63	< 0.0001
C-Weld time	9.92E+05	1	9.92E+05	151.75	< 0.0001
AB	4939.4	1	4939.4	0.76	0.3875*
AC	151.71	1	151.71	0.023	0.8793*
BC	1.19E+05	1	1.19E+05	18.17	< 0.0001
$A^2$	9997.27	1	9997.27	1.53	0.2201*
$B^2$	1.84E+06	1	1.84E+06	281.41	< 0.0001
$C^2$	1.43E+06	1	1.43E+06	218.39	< 0.0001
Residual Error	4.84E+05	74	6536.7		
Total Error	5.85E+06	83			
$R^2=91.73\%$ , $R_{adj}^2=90.83\%$					

Table 5.7 ANOVA table for TS (after elimination of insignificant terms)

Source	Sum of Squares	DF	Mean Square	F-Value	p-value
Model	5.35E+06	6	8.92E+05	137.68	< 0.0001
A-Amplitude	1.21E+06	1	1.21E+06	186.02	< 0.0001
B-Weld pressure	2.02E+06	1	2.02E+06	311.33	< 0.0001
C-Weld time	1.20E+06	1	1.20E+06	185.51	< 0.0001
BC	1.19E+05	1	1.19E+05	18.34	< 0.0001
B <sup>2</sup>	1.84E+06	1	1.84E+06	283.96	< 0.0001
C <sup>2</sup>	1.43E+06	1	1.43E+06	220.37	< 0.0001
Residual Error	4.99E+05	77	6477.97		
Total Error	5.85E+06	83			
R <sup>2</sup> =91.47%, R <sup>2</sup> <sub>adj</sub> = 90.81%					

Fig. 5.27 (a) reveals the normal probability plot for TS to check the deviation of data from normality. From this plot, it can be noticed that all the residuals are situated near to the straight line except two data points. These encircled outliers exhibit significant deviation from the mean line because of the presence of measurement error in the testing results. Residual versus fitted values plot in Fig. 5.27 (b) represents the relatively constant variance, and non-linear relationship also exists as no outlier data exist. In addition, the residual versus run order illustrates that there is no unusual type of structure present in the data and are scattered randomly around zero (Fig. 5.27 (c)). Histogram plot in Fig. 5.27 (d) explores the symmetry of residuals on both the sides of zero mean line. This plot is in the form of Gaussian distribution and no outliers present in the data set.

Likewise, for T-peel failure load (TP), R<sup>2</sup> and R<sup>2</sup><sub>adj</sub> are reviewed and compared in Table 5.8 for choosing the degree of regression model. It can be clearly noticed that the quadratic model has the highest R<sup>2</sup> and R<sup>2</sup><sub>adj</sub> values of 94.08% and 93.36% among all the models. Thus, this model is selected for further analysis due to the reason as described before. Table 5.9 represents the ANOVA table for T-peel failure load with all terms. The terms whose P-values greater than 0.05 are treated as insignificant terms and are marked with “\*”.

Table 5.8 R<sup>2</sup> and R<sup>2</sup><sub>adj</sub> values for various regression models of TP

Degree of model	R <sup>2</sup> (%)	R <sup>2</sup> <sub>adj</sub> (%)
Linear	20.56	17.59
Linear+interaction	22.55	16.52
Quadratic	94.08	93.36

Later on, these parameters are removed from the table through the backward elimination process. The modified table after removal is shown in Table 5.10 which consists of only significant terms and their F and P-values. This table indicates the two

interaction terms like  $A \times WP$  and  $A \times WT$  with one square term  $A^2$  are insignificant. Meanwhile,  $R^2$  and  $R_{adj}^2$  values found in this table are 93.77% and 93.29% respectively. These values are less than that of the values obtained from full quadratic model. Eq. (5.2) represents the TP model in un-coded unit.

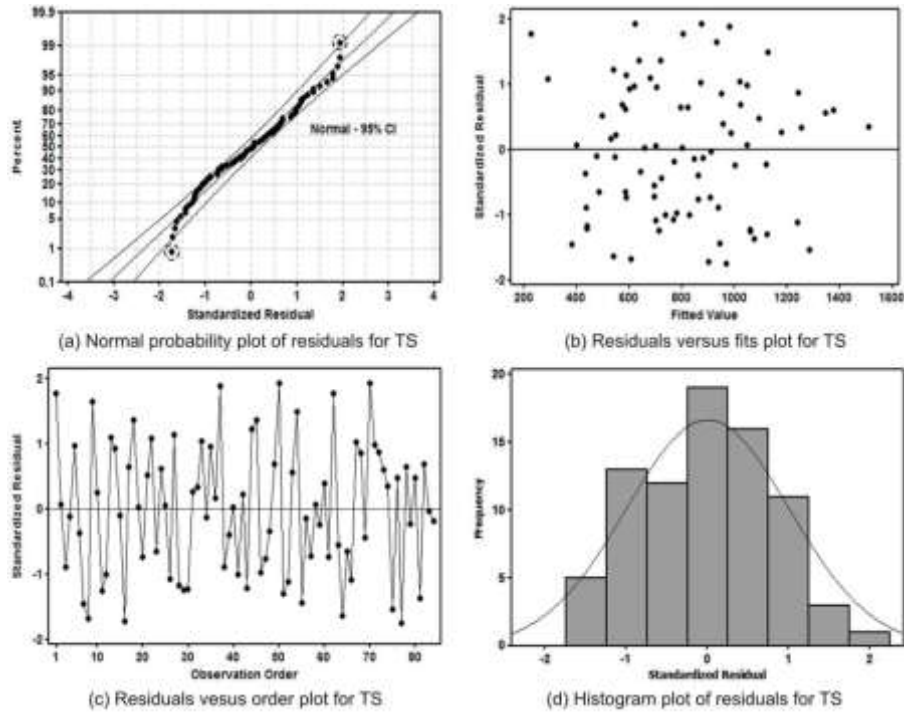


Fig. 5.27 Various residual plots for TS

$$TP = -6120.13 + 1.56 \times A + 28797.48 \times WP + 2074.62 \times WT - 1241.14 \times WP \times WT - 36192.07 \times WP^2 - 1147.73 \times WT^2 \quad (5.2)$$

Table 5.9 ANOVA table for TP (before elimination of insignificant terms)

Source	Sum of Squares	DF	Mean Square	F-Value	p-value
Model	1.18E+05	9	1.31E+04	130.57	< 0.0001
A-Amplitude	1.23E+02	1	1.23E+02	1.23	0.2712
B-Weld pressure	6.26E+04	1	6.26E+04	625.09	< 0.0001
C-Weld time	1.78E+04	1	1.78E+04	178.08	< 0.0001
AB	7.68E+01	1	7.68E+01	0.77	0.384*
AC	5.71E+01	1	5.71E+01	0.57	0.4525*
BC	2.35E+03	1	2352.03	23.5	< 0.0001
$A^2$	2.45E+02	1	245.29	2.45	0.1217*
$B^2$	62594.15	1	62594.15	625.51	< 0.0001
$C^2$	26561.44	1	26561.44	265.43	< 0.0001
Residual Error	7405.15	74	100.07		
Total Error	1.25E+05	83			
$R^2=94.08\%$ , $R_{adj}^2=93.36\%$					

Table 5.10 ANOVA table for TP (after elimination of insignificant terms)

Source	Sum of Squares	DF	Mean Square	F-Value	p-value
Model	1.17E+05	6	19535.39	193.24	< 0.0001
A-Amplitude	12254.2	1	12254.2	121.22	< 0.0001
B-Weld pressure	66632.17	1	66632.17	659.11	< 0.0001
C-Weld time	22371.17	1	22371.17	221.29	< 0.0001
BC	2352.03	1	2352.03	23.27	< 0.0001
B <sup>2</sup>	62594.15	1	62594.15	619.17	< 0.0001
C <sup>2</sup>	26561.44	1	26561.44	262.74	< 0.0001
Residual Error	7784.27	77	101.09		
Total Error	1.25E+05	83			
R <sup>2</sup> =93.77%, R <sup>2</sup> <sub>adj</sub> = 93.29%					

The residual plot of TP is presented in Fig. 5.28. From these graphs, it is confirmed that the model describes the adequacy of results. Normal probability in Fig. 5.28 (a) illustrates the normal distribution of data points those are influencing the response. It can be seen from this figure that all the residuals are normally distributed with 95% of confidence interval. Residual versus fitted values in Fig. 5.28 (b) shows the symmetry in the distribution of residues within  $\pm 2$ . Residual versus order of observations specify that there is no significant effect on the response due to randomness in run order (Fig. 5.28 (c)). Histogram depicts that data are not skewed and evenly distributed on both sides of zero mean value (Fig. 5.28 (d)).

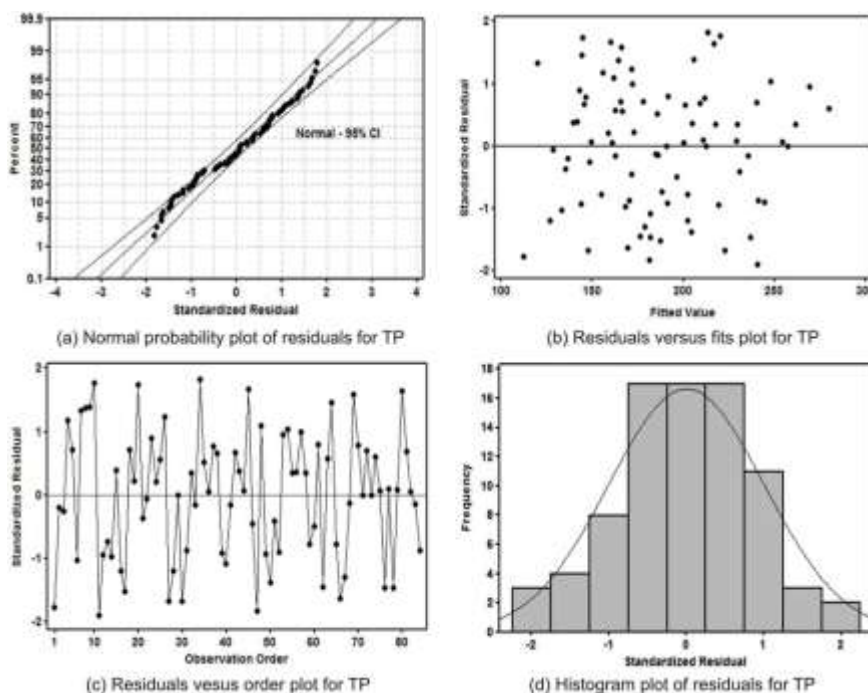


Fig. 5.28 Various residual plots for TP

#### 5.4.4.2 Prediction of responses by ANN approach

A multi-layer feed forward network (MLNN) with three input neurons, one hidden layer, and one output neuron has been selected for the current analysis. The neurons between the layers are connected by links called as synaptic weights. For the update of these weights to minimize the error between predicted and experimental value, back propagation (BP) method is used. This technique has a unique learning principle known as delta rule to minimize the sum of squared error. Fig. 5.29 depicts the schematic diagram of multi-layer perceptron network. In this network, the input layer receives signals from three parameters (i.e. A, WP, and WT) and passes this information to the network for further processing. The hidden layer utilizes a logistic sigmoid transfer function which normalizes the input data and transformed within the range from zero to one. Typically, BP learning uses the gradient descent algorithm to minimize the MSE between the predicted and target data.

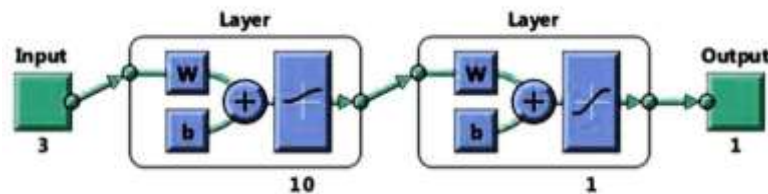


Fig. 5.29 Schematic illustration of multi-layer feed forward neural network

But, one major problem with this basic algorithm is the prolonged learning time [159]. Therefore, the fastest converging training algorithm such as Levenberg- Marquardt back propagation algorithm (LMBP) is used in this study. Weights are initialized by a particular seed value and the learning factors like learning rate, and momentum factor is set as 0.05 and 0.7 respectively. The experimental data set is randomly divided into three subsets. The first subset is the training set which consists of 70% of total data, the second subset is the testing set composed of 15% of total data, and finally, 15% of total data are selected randomly for validating purpose. The training set is utilized to calculate the gradient and optimize the weight factors. For this, several iterations have been performed to minimize the MSE and freeze the weights. The remaining testing set is used to find out the prediction error (to check the adequacy and correctness of the model) on the unknown data set.

It should be noted that the neurons in the hidden layer are treated as the computational measures that perform non-linear mapping interface between external inputs and outputs. Empirically, one layer is sufficient in MLNN because, in these types of networks, the number of neurons has a predominant role than the number of layers [160]. Determination of the correct number of hidden neurons is a critical task in the design of the neural network. A large number of neurons provide too much of flexibility which may

cause overfitting of data. Similarly, less number of neurons restricts the network to be learned effectively. Thus, the performance is degraded [161]. However, there are various methods [162] available for choosing the correct number of hidden layer neurons but in this study simple trial and error process is followed on the basis of least MSE of the testing data set. These data are recorded after a maximum number of epochs at which the MSE is converged, and it is plotted against the number of nodes in the hidden layer for TS and TP in Fig. 5.30. The plot shows that there is an optimal number of neuron where the least MSE of testing is obtained as provided by Tsai and Wang [160]. Thus, the number of neurons in the hidden layer for TS and TP is set as 10. Now these models are ready to predict the validation of input data and also for the comparison purpose.

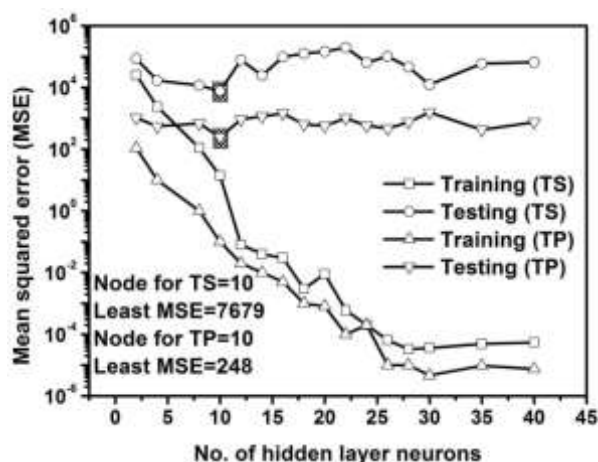


Fig. 5.30 Optimal number of hidden neurons for TS and TP in ANN model

The MSE variation with a number of iterations plots for TS and TP with 10 number of hidden neurons are illustrated in Fig. 5.31. It can be observed from the plot that the MSE converges and attains a stabilized value after 1000 epochs for TS and 2000 epochs for TP. The best MSE for TS and TP are  $3.1 \times 10^{-3}$  and  $1.1 \times 10^{-3}$ , and these are achieved at 1067 and 2000 epochs respectively.

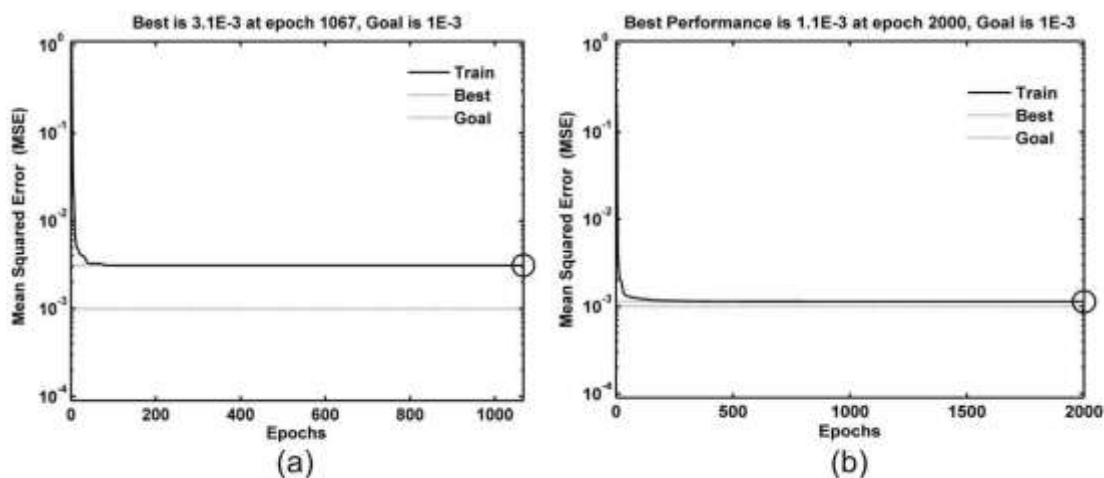


Fig. 5.31 MSE variation with number of iterations for (a) TS and (b) TP



#### 5.4.4.3 Prediction of responses by fuzzy neural network

Nowadays researchers have applied various hybrid intelligent techniques like ANN with fuzzy logic called adaptive neuro-fuzzy inference system (ANFIS) for the prediction of responses to the welding process. Conventional mathematical procedures are not suitable to describe a poorly defined system with full of uncertainty. Thus, the motivation for this hybridization is to solve a complicated mathematical relationship among various dynamic process variables. ANFIS is an advanced fuzzy inference system (FIS) with learning capacity like ANN. Due to this fact, neural network training algorithm can make a change in this FIS structure and fine tunes the predicted output [163]. This fuzzy modelling was first explored by Takagi and Sugeno [164]. It decreases significant computational efforts like in the conventional feed forward neural network algorithm and found numerous applications in the control sector [165]. Thus, this type of fuzzy reasoning is adopted for the current study. It also provides mapping of input -output relationship through “learning” and “fine tuning” procedures of the neural network and fuzzy inference. Fig. 5.32 illustrates a simple ANFIS architecture comprising of 3 inputs, membership functions (MFs), a fuzzy rule base and a single output. This structure uses the “If-then” rules for the encoding purpose. Thus, it can be suitable to handle any higher order problems efficiently [166].

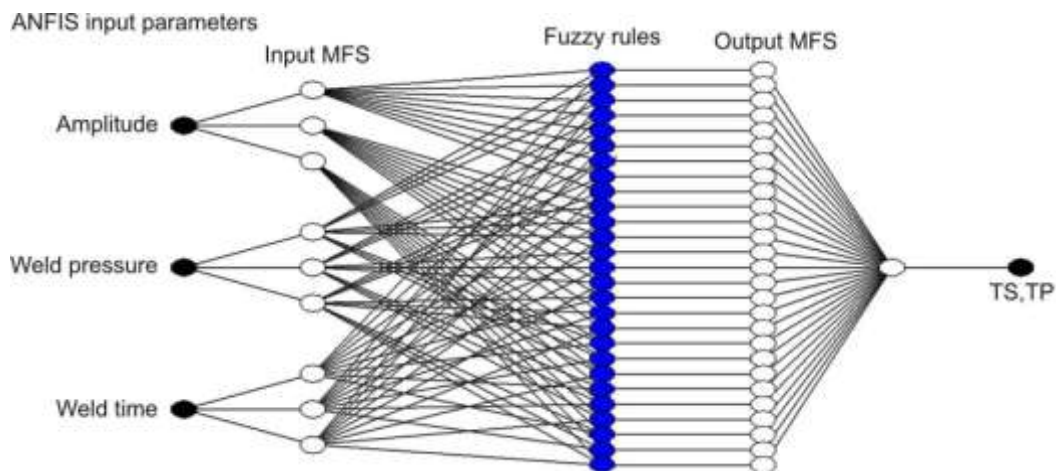


Fig. 5.32 Schematic illustration of a typical ANFIS architecture

Fig. 5.33 displays a sample graphical representation of bell type MFs for each input parameters like amplitude, weld pressure and weld time with their linguistic terms used in this study. Usually, the layers of this structure are divided into two parts, i.e., premise and consequent parts. These parts in this inference system are composed of 5 layers on the basis of its operation, and they are (i) fuzzification, (ii) rule base, (iii) normalising, (iv) defuzzification, (v) output. Each layer consists of several nodes which are described by various functions. The output of these nodes is treated as the input signals for the present

nodes. The nodes displayed in boxes are known as the adaptive nodes, and these are adjustable in nature.

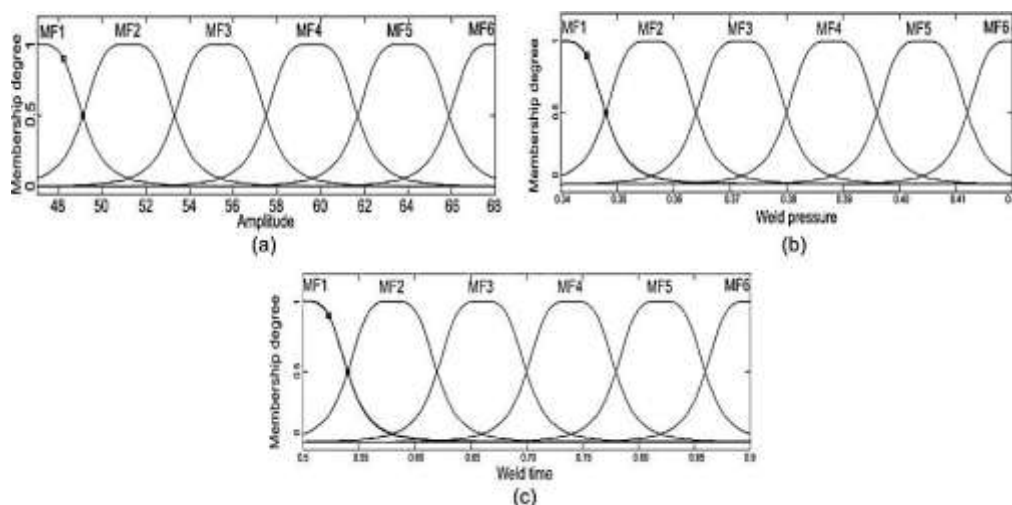


Fig. 5.33 A demonstration of bell type MFs for each input parameters in USMW process

At the same time, the circled nodes are the fixed nodes and describe that the parameters are fixed in the system [165, 166]. The major advantage of ANFIS is the expression of parameters in the fuzzy linguistic terms and it is chosen by the designer. However, the learning method works in an exact way as that of the neural network. The numbers of membership functions play a vital role in getting least MSE and to find out the best number of MF, simple trial and error method is followed. MSE with respect to the number of MFs for responses like TS, TP is illustrated in Fig. 5.34.

It can infer from this figure that the 4 number of MFs are sufficient to get the least MSE. Even if the MFs are increased, the result is not changed much. But the network gets more complicated as the number of rules is increased. Meanwhile, the parameters associated with MFs are tuned using a hybrid system of back propagation and least square method [169]. This Takagi-Sugeno ANFIS modelling was accomplished by MATLAB 2014b using bell type MFs to fuzzify the input parameters. Fig. 5.35 shows the fuzzy reasoning procedure for a single order Takagi-Sugeno fuzzy inference system. It is an approximate reasoning method from which the conclusions of fuzzy if-then rules are deduced. At last, the output is expressed in terms of linear equation or constant with a similar weighted average formula.

#### 5.4.4.4 Overall comparison of prediction techniques results for model validation

For checking the efficiency and correctness of the proposed models, a set of 20 experimental data is chosen randomised from the total number of experiments and these are not also used in training as well as testing purpose. If these developed models pass the validation process successfully, it can be said that these models are not only useful

for model building in a particular range of parameters using the same experimental condition but also these models can well execute and predict the responses.

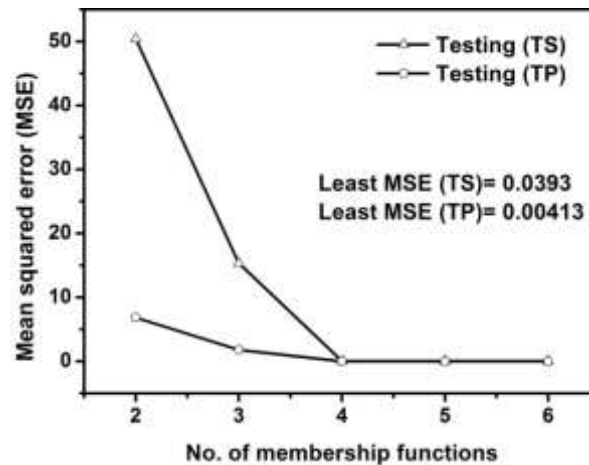


Fig. 5.34 Optimal number of MFs for TS and TP in ANFIS model

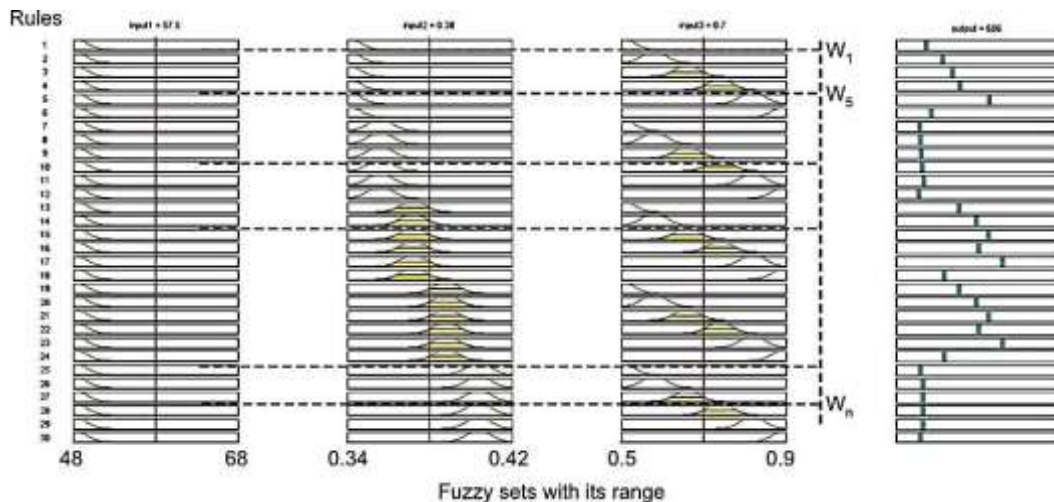


Fig. 5.35 Graphical representation of fuzzy reasoning procedure of ANFIS controller using MATLAB

Fig. 5.36 depicts the graph obtained from residuals for these 20 experimental input parameter conditions. These residuals are calculated by taking the difference between experimental and predicted values of TS for regression, ANN and ANFIS model. It can be observed from the figure that the residuals for regression vary from -5.03 to 5.49 and for ANN, it ranges from -4.94 to 4.95. But for ANFIS, it ranges from -1.04 to 0.84 which is the minimum variation among all models. Thus, it can be outlined that the ANFIS is the best model which can accurately predict the experimental TS with a little deviation. Likewise, the residual values for TP are represented in Fig. 5.37. It can be inferred from the figure that the regression, ANN, and ANFIS residual values are varied from -5.54 to 4.41, -4.44 to 4.34 and -0.95 to 0.52 respectively. Again ANFIS model approximate better results than the ANN and regression model results for TP.

To demonstrate the highest level of accuracy among the proposed predictive models, the parity graphs are plotted between the experimental and predicted values for TS, and it is shown in Fig. 5.38. This graph represents the data those are obtained in training, testing and validation process. It can be seen from the figure that there is an excellent fit between predicted and experimental values in all the cases. These 3 models are able to give the TS results very accurately except 2 or 3 outliers in regression modelling. Meantime, it should be noted that more the values closer towards the line, that model is more accurate. Conclusively, it can be inferred that both ANN and ANFIS are more accurate than the regression model. The  $R^2$  values for regression, ANN and ANFIS are obtained as 91.47%, 98.30% and 99.98% respectively. Therefore, these models can be ranked as ANFIS, ANN and regression in terms of accuracy for predicting TS.

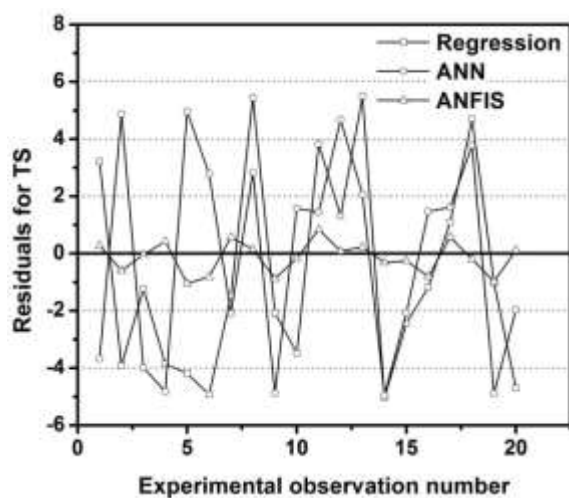


Fig. 5.36 Error profile of validation data on TS for different models

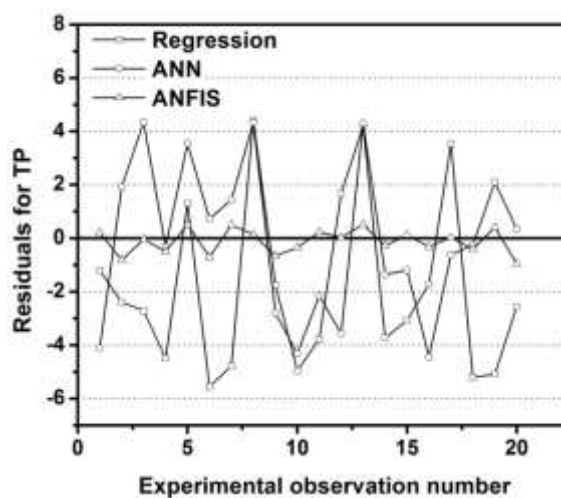


Fig. 5.37 Error profile of validation data on TP for different models

Likewise, Fig. 5.39 illustrates the parity plot for TP. From this graph, all models show an excellent fit between predicted and experimental values. Among all the models, the predicted values of ANFIS models are closer to the line than the values obtained in ANN and regression modelling. Thus, it can be said that ANFIS is more accurate than other two techniques with an  $R^2$  value of 99.79%. Eventually, the ANN modelling has given comparatively accurate result than regression modelling with  $R^2$  values of 99.36% and 93.77% respectively. Hence, in this case also, ANFIS has occupied the first position followed by ANN and regression based on the accuracy of predicting the TP.

Absolute error is one of the powerful statistical tools to demonstrate the performance of the proposed models. It can be calculated as per the following equation:

$$\% \text{ Absolute error} = \frac{|\text{Expt. value} - \text{Pred. value}|}{\text{Expt. value}} \times 100 \quad (5.3)$$

In this case, the new data set considered those are not taken before to develop or test the model. These values along with experimental and residuals are listed in Table 5.11

and Table 5.12. The average absolute error is calculated by taking an average of all the absolute error values. Thus, these values of TS are obtained as 0.47%, 0.48% and 0.07% for regression, ANN and ANFIS respectively. Likewise, the average absolute errors of TP are noticed as 1.89%, 1.44% and 0.22% for regression, ANN and ANFIS respectively.

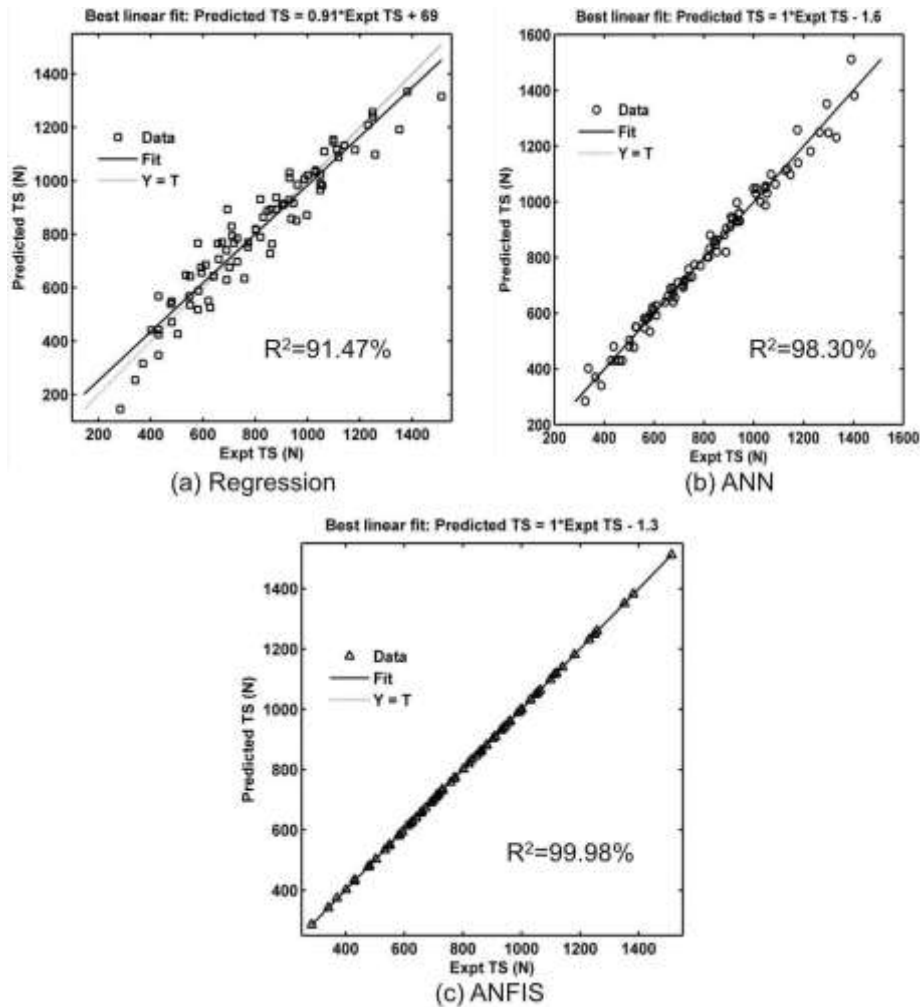


Fig. 5.38 Comparison of various model predicted values with experimental results for TS

Table 5.11 Accuracy testing of all proposed models for prediction of TS

Run No	Input parameters			Exp. TS	Residuals for TS			% Absolute error for TS		
	A	WP	WT		Regression	ANN	ANFIS	Regression	ANN	ANFIS
1	47	0.34	0.5	283.87	3.21	-3.66	0.28	1.13	1.29	0.09
2	47	0.34	0.6	401.82	-3.91	4.87	-0.59	0.97	1.21	0.14
10	47	0.38	0.7	988.17	-1.22	-3.98	-0.03	0.12	0.40	0.00
18	47	0.42	0.75	730.59	-3.85	-4.81	0.41	0.52	0.65	0.05
19	47	0.42	0.8	660.19	-4.18	4.95	-1.04	0.63	0.75	0.15
23	54	0.34	0.6	480.33	-4.92	2.788	-0.80	1.02	0.58	0.16
29	54	0.38	0.5	656.12	-1.48	-2.09	0.57	0.22	0.31	0.08

32	54	0.38	0.75	1258	5.43	2.83	0.14	0.43	0.22	0.01
35	54	0.38	0.9	712.02	-2.07	-4.88	-0.87	0.29	0.68	0.12
44	60	0.34	0.6	550.8	-3.47	1.58	-0.16	0.63	0.28	0.03
46	60	0.34	0.75	773.19	3.82	1.44	0.84	0.49	0.18	0.10
47	60	0.34	0.8	856.9	1.31	4.67	0.08	0.15	0.66	0.00
49	60	0.34	0.9	580.3	5.49	2.06	0.22	0.94	0.35	0.03
51	60	0.38	0.6	1112.39	-5.03	-4.94	-0.31	0.45	0.44	0.02
59	60	0.42	0.7	1000.53	-2.44	-2.06	-0.25	0.24	0.20	0.02
65	68	0.34	0.6	580.12	-1.17	1.46	-0.80	0.20	0.25	0.13
68	68	0.34	0.8	957.7	1.09	1.61	0.57	0.11	0.16	0.05
71	68	0.38	0.5	1056.35	4.70	3.78	-0.19	0.44	0.35	0.01
77	68	0.38	0.9	930.12	-1.01	-4.88	-0.98	0.10	0.52	0.10
80	68	0.42	0.7	1098.3	-4.69	-1.96	0.11	0.42	0.17	0.01
Average absolute error (%)								0.47	0.48	0.07

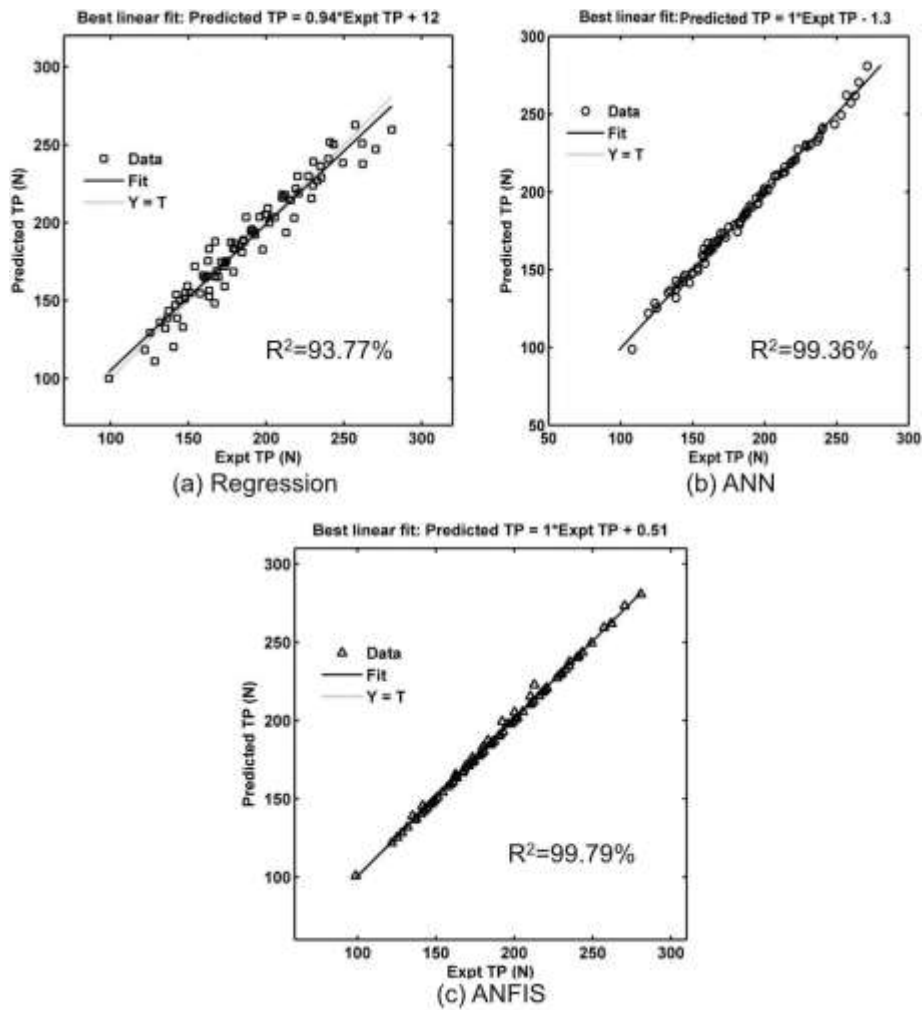


Fig. 5.39 Comparison of various model predicted values with experimental results for TP

Table 5.12 Accuracy testing of all proposed models for prediction of TP

Run No	Input parameters			Exp. TS	Residuals for TS			% Absolute error for TS		
	A	WP	WT		Regression	ANN	ANFIS	Regression	ANN	ANFIS
1	47	0.34	0.5	98.82	-1.20	-4.11	0.20	1.21	4.16	0.21
2	47	0.34	0.6	136.63	-2.39	1.92	-0.81	1.75	1.40	0.59
10	47	0.38	0.7	227.17	-2.71	4.34	-0.03	1.19	1.91	0.01
18	47	0.42	0.75	178.83	-4.49	-0.31	-0.49	2.51	0.17	0.27
19	47	0.42	0.8	173.35	1.31	3.54	0.52	0.75	2.04	0.30
23	54	0.34	0.6	144.42	-5.54	0.72	-0.69	3.84	0.50	0.48
29	54	0.38	0.5	190.92	-4.78	1.43	0.49	2.50	0.75	0.25
32	54	0.38	0.75	262.17	4.41	4.33	0.14	1.68	1.65	0.05
35	54	0.38	0.9	192.37	-1.75	-2.79	-0.66	0.91	1.45	0.34
44	60	0.34	0.6	149.39	-4.95	-4.31	-0.35	3.31	2.88	0.23
46	60	0.34	0.75	171.04	-3.77	-2.14	0.23	2.20	1.25	0.13
47	60	0.34	0.8	179.16	1.66	-3.56	0.02	0.93	1.99	0.01
49	60	0.34	0.9	142.83	4.20	4.30	0.51	2.94	3.01	0.36
51	60	0.38	0.6	230.39	-3.73	-1.35	-0.27	1.61	0.58	0.12
59	60	0.42	0.7	201.13	-3.06	-1.19	0.11	1.52	0.59	0.05
65	68	0.34	0.6	154.14	-1.71	-4.44	-0.31	1.11	2.88	0.20
68	68	0.34	0.8	184.53	3.53	-0.61	0.03	1.91	0.33	0.01
71	68	0.38	0.5	212.39	-5.20	-0.24	-0.40	2.44	0.11	0.19
77	68	0.38	0.9	210.92	-5.09	2.10	0.40	2.41	0.99	0.19
80	68	0.42	0.7	219.15	-2.55	0.34	-0.95	1.16	0.15	0.43
Average absolute error (%)								1.89	1.44	0.22

#### 5.4.5 Impact of various anvil designs for 0.7Al-0.4Cu weld coupons

Most of the literature of USMW are concentrated on the effects of the different process parameters on the weld strength and temperature generated during the welding. As the ultrasonic welding includes a complex mechanism, thus it is necessary to find out the quality of the weld in terms of fracture pattern, wake features, flow behaviour and microhardness at the plastic deformation zone. The design of ultrasonic tooling plays a significant role in the determination of quality and strength of the welding. A good design of this part provides proper friction between the weld coupons and avoids slippage between the sonotrode and top part. Therefore, this study is aimed at examining the weld strengths, effects of welding parameters and weld quality characteristics using three different types of anvils (as described in section 3.6.2).

A lot of screening test are performed carefully to choose the process parameters for welding. To compare the effects of various anvil geometries, all the experiments have been done by applying a constant clamping pressure of 0.38 MPa with a highest vibration amplitude of 68  $\mu\text{m}$ . In this study, only the variable factor is taken as weld time. Therefore, the effects of this parameter on the weld strength are investigated for different anvils.

#### 5.4.5.1 Effect of weld time on tensile shear and T-peel failure loads

For a welder, it is important to yield excellent quality of welding by taking suitable process parameters and proper design of anvil surface patterns. The specifications of anvil knurl patterns are given in Table 3.5. The tensile shear and T-peel failure load curves as a function of weld time for these three anvil patterns are shown in Fig. 5.40. It is observed that these two strengths increase with weld time up to 0.75 sec, after this value, these strengths gradually decrease due to severe plastic deformation and cracking around the weld zone. In the tensile shear tests, the welds are generally fractured at the weld interface for the weld time less than 0.6 sec. It may be due to the improper mixing of metal at plastic deformation zone. But, when the weld time is 0.7 or 0.75 sec then, the fracture occurs at the periphery of the weld zone, and also partial tearing of aluminum sheets are observed. Thus, it is treated as a good weld condition and in this zone, the sufficient amount of heat generation and plastic deformation occurs. After the 0.75 sec, the nugget pullout failure occurs due to the formation of cracks in the weld zone.

Furthermore, there is a trend of increasing tensile shear and T-peel strength with increasing of non-cutting width and angle of the knurls. The surfaces of copper have not been deformed plastically when the smaller non-cutting width type knurl is used. For instance, in between anvil 1 and anvil 3, the angle of the knurl is same but the non-cutting width is different. Another reason for lowering the both strengths is the geometrical shape of the knurls.

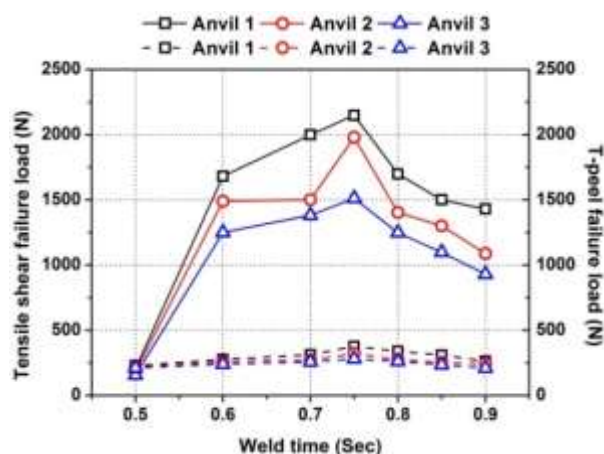


Fig. 5.40 Tensile shear and T-peel failure loads of 0.7Al-0.4Cu weld coupons with weld time for various anvil patterns



For the present study, flat type knurls are engraved on anvil 1 & 2, and on anvil 3, pyramidal type knurls are created. These results show a similar nature as demonstrated by Jahn et al. [59]. They found that the weld size and strength increases with increase in weld energy. It was also shown that aluminum metal was not sufficiently plastically deformed at the low energy to fill the grooves between the knurls. Thus, it has been experimentally found for anvil 3 that there is an insufficient plastic deformation occurred because its shape and it prevents the further indentation of the horn tip to the top surface of the aluminum sheet. On the other hand, a larger area of contact and the appropriate angle of anvil 1 make the material flow freely and to allow the horn tips to indent further. In addition, the part sticking to the sonotrode seldom occurs while using anvil 1. Thus, anvil 1 produced a greater failure load than anvil 2 and 3.

The highest tensile shear strength of 2148.4 N and T-peel strength of 376.88 N are obtained for anvil 1 at 68  $\mu\text{m}$  amplitude. The more strength values at higher amplitude are attributed to the larger frictional heat that gives rise to more plastic deformation at the interface layer. But at the highest weld time of 0.9 sec, relatively lesser failure loads are obtained due to gradual softening and thinning of the material. Therefore, it can be considered as over weld condition.

#### 5.4.5.2 Effect of weld time on weld area

Morphological observations of the weld surface revealed that the various geometries of anvils yield different weld spots. As it is tough to measure the dimension of these spots, a systematic method has been followed to quantify these dimensions with the help of Image J<sup>®</sup> software package. The weld area is illustrated in Fig. 5.41 as a function of weld time for different anvils.

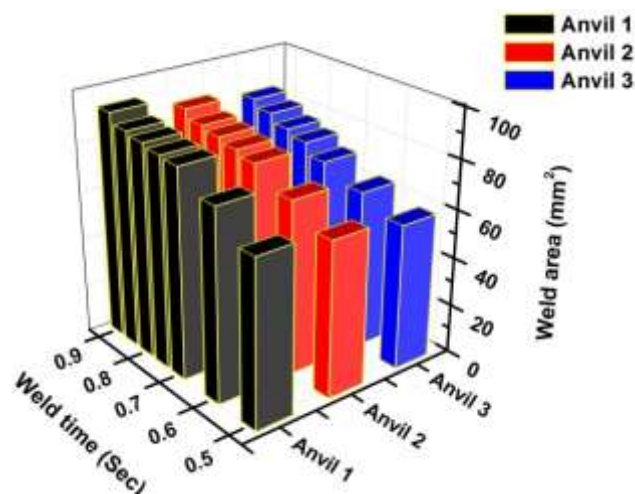


Fig. 5.41 Weld area as a function of weld time of 0.7Al-0.4Cu weld coupons for different anvil patterns

The weld area increases with weld time in all the welding condition. For the same weld time, weld area increases with the physical size of the sonotrode knurls, i.e. for anvil 1. At low weld time and low vibration amplitude, the aluminium sheet has not been adequately deformed plastically and only friction presents in between the weld coupons. On the contrary, at high vibration amplitude and weld time, the growth of the micro bonds will be more and thus, it results in the production of larger weld spot size. The angle of the knurls also plays a significant role for a generation of higher weld area with less friction as evidenced by SEM photographs present in Fig. 5.42. In Fig. 5.42 (a), the plastic deformations have shown around the knurl patterns of anvil 1 and in Fig. 5.42 (b), the plastic deformations have also been observed around the knurl pattern, but these patterns also pose ductile fractures for anvil 2. Likewise, Fig. 5.42 (c) depicts the severe plastic deformation with fracture patterns near to the weld spot. It can be observed from this figure that due to the anvil 3 knurl pattern, the surface of the copper specimen suffers the maximum deformation and a lot of fractures are also observed. Thus, it is believed that the lowest failure loads are obtained due to this reason.

#### 5.4.5.3 Effect of weld time on interface temperatures

The temperatures achieved in the weld zone by a number of K-type thermocouples at various amplitudes and weld times for respective anvil patterns are represented in Fig. 5.43. However, when the horn tip and anvil tip teeth crunch into the aluminum and copper sheets, heat has been developed between the sheets due to high-frequency rubbing action and plastic deformation at the overlapped zone. A maximum temperature of 406.71°C is measured when the anvil 1 used 68  $\mu\text{m}$  amplitude and 0.9 sec of weld time. This temperature is equal to the 61 % of the melting point of the aluminum sheet. These results show a similar trend as reported by Chen et al. [96], who obtained 400 °C at the weld surface while joining of aluminum automotive sheet. Similarly, a temperature of 382.65 °C and 350.35 °C have been achieved for anvil 2 and anvil 3 respectively at 68  $\mu\text{m}$  amplitude and 0.9 sec of weld time.

These temperature measurements also revealed the relationship between the production of heat and weld strength of the samples. At a particular ultrasonic frequency, the higher amplitude and weld time led to a faster increase in temperature and thus the material is softened. The softening means the yield strength of the material decreases and plastic deformation capacity increases. The above effects are the possible reasons for rapid micro joining and accelerate the welding mechanism by plastic work. It is clear that a speedier and higher temperature rise accomplished at an elevated amount of welding time and amplitude correspond to a higher degree of softness and better plastic deformability.

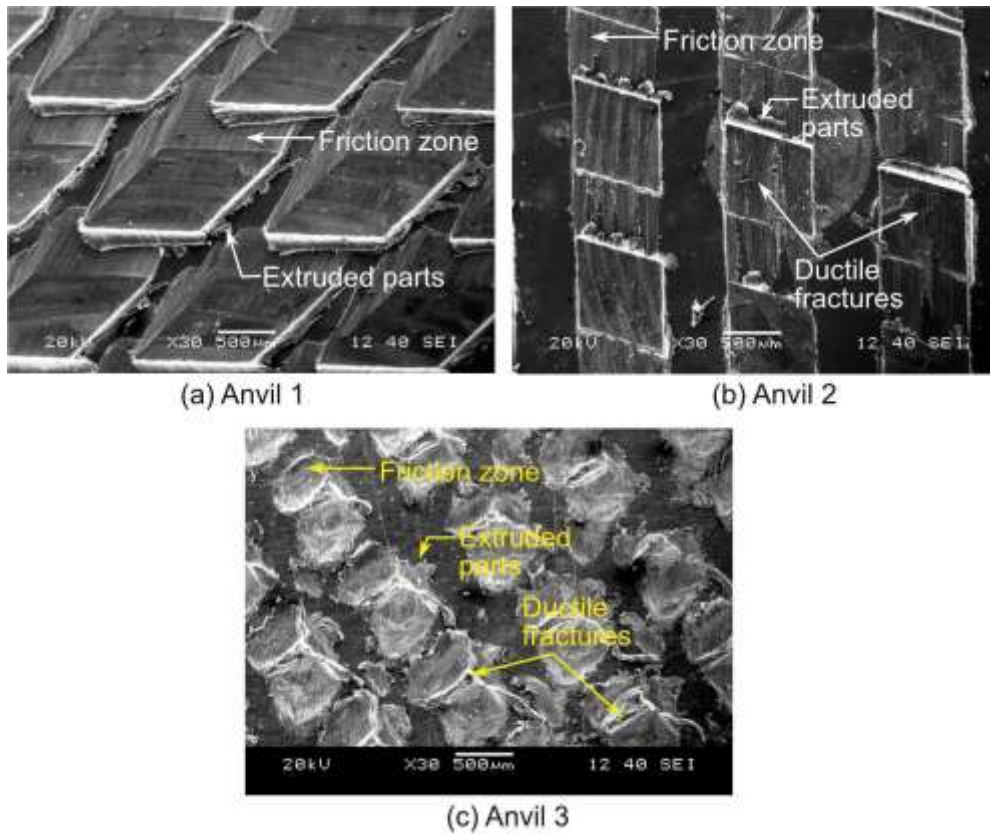


Fig. 5.42 SEM photographs of impressions on copper sheet by anvils a) for anvil 1, b) for anvil 2, (c) for anvil 3

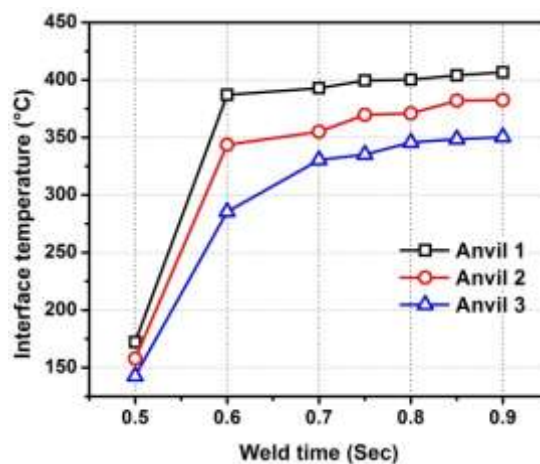


Fig. 5.43 Temperatures measured at weld interface with time of 0.7Al-0.4Cu weld coupons for different anvil patterns

#### 5.4.5.4 Weld quality assessment

When the USMW process starts, the weld interface encounters the shear forces due to high-frequency vibration and causes extensive plastic deformation. This deformation caused the changes in microstructure and formed a recrystallized microstructure along the weld interface [94]. This microstructural change is directly reflected in the mechanical

strength of welded materials. Vickers microhardness estimations are made on the cleaned weld interfaces of anvil 1 to confirm the hardening and softening in the welded materials. Anvil 1 is selected as it gives maximum weld strength in terms of tensile shear and T-peel failure loads at the previously described parameter combinations. In this study, the microhardness is measured in two ways i.e. in horizontal and vertical direction. The hardness distributions along the horizontal direction of weld surface are demonstrated in Fig. 5.44.

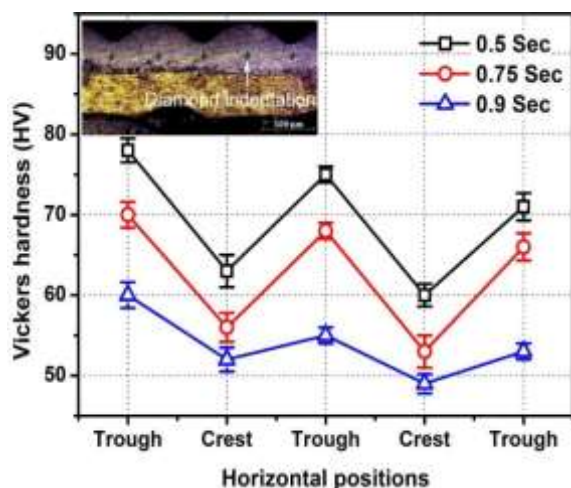


Fig. 5.44 Hardness distribution along the horizontal direction for anvil 1

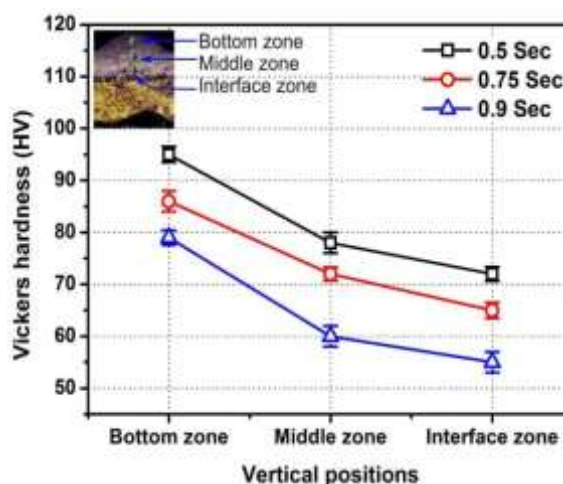


Fig. 5.45 Hardness distribution along the vertical direction for anvil 1

For low weld time, hardness values under the tip of the sonotrode or at the trough position are higher than the hardness at the crest locations. It is because the plastic deformation starts at the peak position and gradually disperses as the welding proceeds. Therefore, the area at the trough position is much work hardened than the crest position. However, as the weld time increases, the hardness value decreases due to softening of the material. The hardness measurements are also taken in the vertical positions to demonstrate the plastic behavior of materials. Fig. 5.45 illustrates the hardness value in the vertical direction. From this figure, it has been observed that in the bottom zone; the hardness value is maximum for the lowest welding time of 0.5 sec, and the middle region experiences a lower hardness value as compared to the bottom surface. Thus, the atoms at the interface got the higher ultrasonic energy that reveals instantaneous work hardening and then softening due to the continuous rise in temperature.

The joint strength of the weldment can be determined by the various physical attributes [170]. These weld characteristics are bond density, post weld thickness and thermo-mechanically affected zone (TMAZ). As this study only focuses on the various dimensional effects of the anvil on weld strength, therefore bond density and bond thickness are taken into consideration. Bond density for different weld times is estimated by taking the proportion of projected region to the entire welded interface region. Then, a decent weld should have thick interfacial bonds without any voids, and these can be

observed from microstructural analysis of the weld interface. There are numerous ideas available to describe the formation of weld in USMW. It includes concepts like metallurgical adhesion which are originated from plastic deformation [88], local heating [171] and mechanical interlocking [172]. As mechanical interlocking and metallurgical adhesion play a predominant role, in the present work, cross-sectional views are examined thoroughly. Three distinct phases are identified during the welding process along the weld cross-section, and they are (i) development of micro bonds, (ii) convoluted wakes like features and (iii) flow of Al material to the Cu side. As the joint strengths produced by anvil 1 are better than anvil 2 and 3, thus it is taken under metallurgical observation. The bond thickness is a vital physical attribute to assess the weld performance. SEM images of under weld, good weld and over weld are shown in Fig. 5.46 for anvil 1. For clear understanding, the black dotted box marked off each figure is zoomed. In under weld condition, the voids are clearly observed as it has been done under a low weld time of 0.5 sec and also at 68  $\mu\text{m}$  vibration amplitude. On the contrary, a dense bonding region can be shown in good weld condition and as well as in over weld condition. As the good weld condition shows a higher strength than the over weld condition, indicates that the bond density feature alone cannot adequately describe the effect of dense micro bonds on weld strength. But, in Fig. 5.46 (b), one can observe the plastic flow of aluminum material to the copper surface due to the accumulation of intensified ultrasonic energy. This also depends on the extensive deformation produced by the anvil knurl pattern.

For the weld time of 0.75 Sec, the three anvils show a continuous weld interface line as shown in Fig. 5.47. As it is a good weld condition for each anvil, the voids are not seen on the weld line, and penetration of both weld and anvil tip can be observed. Surface extrusion and plastic deformation at the weld periphery of anvil 1 are found to be largest among all other anvils. Thus, it is one of the reasons for getting higher strength by using anvil 1. There are two types of wake features observed in the morphological analysis of the weld joints. As the sufficient plastic deformation occurs at anvil 1, the finer wakes are found in the means of convoluted profile than other anvils. A sinusoidal pattern of the interface has also been noticed which bears resemblance with anvil tip knurls. Therefore, this feature has tried to find a correlation between interface morphology and geometry of knurl pattern. It has been spotted that the troughs and crests of the wavy interface are transient and change with the weld time and amplitude. So, a consistent relationship between the wake features and anvil knurl does not exist.

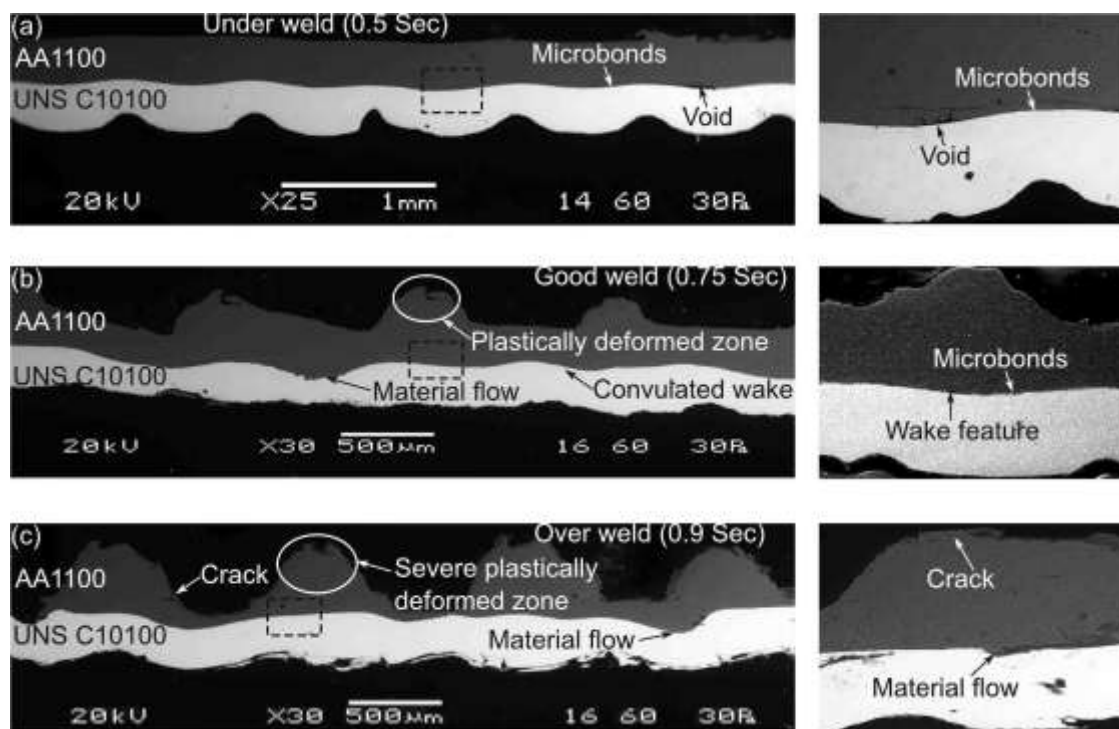


Fig. 5.46 SEM images of different weld conditions a) under weld, b) good weld, c) over weld

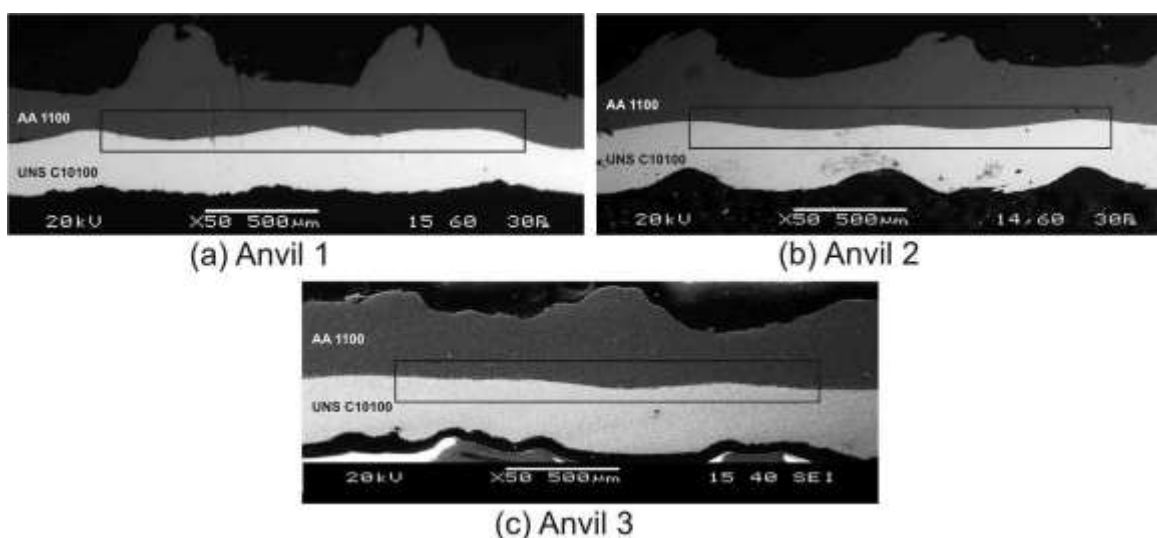


Fig. 5.47 SEM images revealing wake features for various anvils (a) anvil 1, (b) anvil 2, (c) anvil 3

#### 5.4.6 Impact of different surface conditions for 0.7Al-0.4Cu weld coupons

From the previous literature, it can be concluded that vibration energy and weld time are the two key factors for the formation of joints between dissimilar materials in USMW. At the same time, the size and growth of the IMC layer also determine the weld strength. However, there are still many points related to the surface conditions of the weld interface, but they are not adequately defined and explained. The aim of the present study is to weld Al and Cu using ultrasonic welding method and to investigate the effects of

various welding conditions on the tensile shear and T-peel failure loads of the joint. Furthermore, the impact of different surface roughness and microhardness of the faying surface on the bond strength are also studied. The microstructural analysis of the welded zone is also analysed in details. The detailed experimental domain is presented in Table 5.13. During the experiment, the weld energy is transferred to the faying surface and is controlled by changing the weld time while other two parameters are kept constant.

Table 5.13 Experimental domain for specimens used in different surface conditions

Parameters	Terms	Domain of experiment
Amplitude ( $\mu\text{m}$ )	A	68
Weld pressure (MPa)	P	0.38
Weld time (sec)	T	0.5-0.9
Frequency (kHz)	f	20

In this study, four surface conditions like lubricated, normal, electrolytic polished (EP) and emery polished are considered. For the lubricating condition, ethanol has been dropped onto the bottom specimen and the gap is ultimately filled by it due to the capillary effect. The specific purpose of using it on the faying surface is to reduce the coefficient of friction of Al alloys during the welding process [173]. Similarly for the electrolytically polished condition, a solution of perchloric acid and ethanol has been used to increase the surface roughness of both sheets. After EP, the average surface roughness was about  $0.9 \mu\text{m}$  for AA1100, and those of UNS C10100 was about  $0.77 \mu\text{m}$ . The surface condition of the weld samples is also modified by P400 SiC emery paper. The polishing has been done along the rolling direction of sheets. After it, the surface roughness of  $1.6 \mu\text{m}$  and  $0.98 \mu\text{m}$  were obtained for AA1100 and UNS C10100 sheet respectively.

#### 5.4.6.1 Influence of weld time on tensile shear and T-peel failure loads

From the trial experiments, it has been found that when the welding pressure is above  $0.38 \text{ MPa}$ , the weld samples are stuck to the welding tip and consequently the cracks are formed. So in this study, the maximum vibration amplitude of  $68 \mu\text{m}$  and weld pressure of  $0.38 \text{ MPa}$  are kept constant and weld time is treated as the variable. Fig. 5.48 shows the relationship between tensile shear and T-peel failure loads with the variation of weld time for four different conditions. Firstly, when the ethanol is added to the faying surface, the increase in these two failure loads remains relatively constant up to  $0.7 \text{ sec}$  of weld time. This is because at the initial stage of welding, complete lubrication is not achieved due to infiltration of ethanol and as it has an alkyl group. Moreover, it efficiently prevents any direct contact between the faying surfaces. Subsequently, these loads increased sharply up to the weld time of  $0.85 \text{ sec}$ , and maximum values of  $1550.48 \text{ N}$  and  $370.46 \text{ N}$  are obtained for the tensile shear and T-peel failure loads respectively. The probable reason

for this phenomenon can be explained as that when the weld time increases; friction amplitude rises and adhesive wear took place due to evaporation of ethanol and direct metal to metal contact occurs. That created a suitable environment for plastic deformation of the Al sheet. After reaching the threshold limit, these failure loads decreased due to excessive weld time and cracks are seen at the periphery of the weld zone. For the normal condition case, both tensile shear and T-peel failure loads showed a maximum load of 1512 N and 280.83 N respectively at 0.75 sec. Afterwards, the loads gradually decrease with weld time as explained earlier. This trend showed a similar behaviour reported by Annoni and Carboni [95]. Similarly for the EP and emery polished surface conditions, there is a sharp increase in these failure loads initially, and its values are less than that of the normal state, but more than the lubricating (with ethanol) surfaces. This is due the fact that at the beginning phase of welding, the EP and emery possessed a higher surface roughness values as compared to others. Thus, during the welding, wide scratch marks are noticed with the occurrence of material softening. In EP condition, maximum tensile shear failure load of 1193.79 N and T-peel failure load of 247.81 N are observed. Those maximum values are obtained at the weld time of 0.75 Sec, which is identical to the normal condition. Likewise, maximum loads of 1070.29 N and 229.65 N are observed at 0.7 sec for tensile shear and T-peel conditions in emery paper polished case.

#### 5.4.6.2 Relationship between welding time and weld interface temperatures

The temperature at the weld interface is measured to support the plastic deformation during the welding process. Fig. 5.49 shows the interface temperature behaviour during the ethanol adhesion as well as polished with an electrolytic solution and emery paper. Firstly, the ethanol application at the faying zone made the temperature not to increase suddenly.

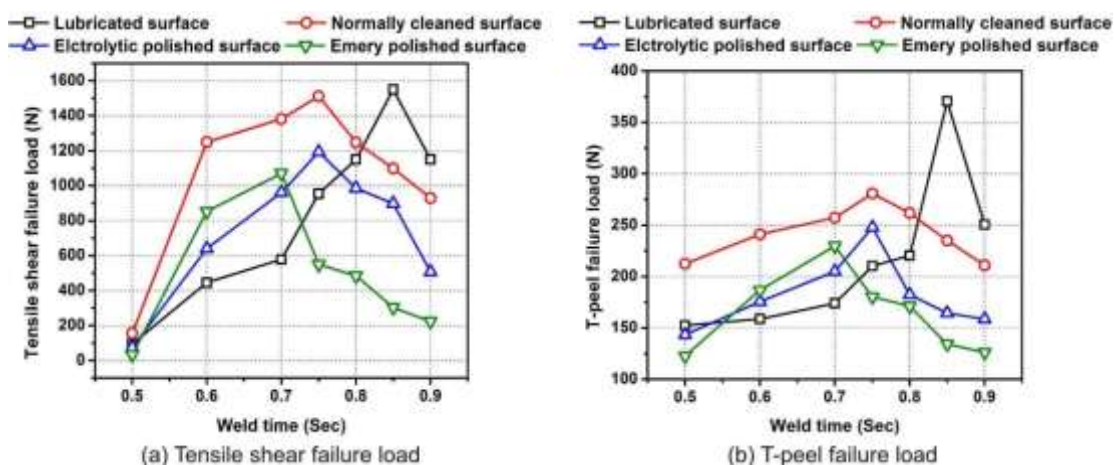


Fig. 5.48 Tensile shear and T-peel failure loads of 0.7Al-0.4Cu weld coupons for different surface conditions (a) Tensile shear failure load; (b) T-peel failure load



This is because of the strong interface stirring phenomenon that has taken place up to a weld time of 0.7 Sec. But after that, as the weld time increase, the temperature is also increased and created a suitable environment for plastic flow. Due to it, the oxide film presents over the surfaces ruptured, and pure metal to metal contact has taken place. The maximum temperature of 375°C is obtained. In normally cleaned condition, 350°C is observed as the highest temperature at the end of 0.9 Sec. This temperature is below than the temperature produced by ethanol adhesion. This suggested that appropriate frictional force is essential to boost the heat generation by friction during the welding. During this investigation, the surface roughness of the weld samples is also modified by polishing with an electrolytic solution as well as emery paper. As the surface roughness of emery paper is more than that of electrolytically polished one, the initial temperature rise is also very high for the emery paper polished surface. But gradually when the time increased the rise of temperature is not uniform, and finally a maximum temperature of 295°C is obtained for emery condition as comparable to 319°C of EP condition. The reason for lowering the heat generation is that the relative motion between the sheets got obstructed due to high surface roughness. These results showed the same nature as observed by Watanabe et al. [64].

#### **5.4.6.3 Measurement of weld interface microhardness**

It was studied that, there was no formation of the large heat affected zone (HAZ) in USMW as compared with fusion welding process [173]. In order to prove this, the hardness distribution in the weld zone as well as in the base material is found out experimentally. Fig. 5.50 represents the Vickers microhardness distribution of the joint interface in a longitudinal direction. The readings are taken at a clamping pressure of 0.38 MPa, vibrational amplitude of 68  $\mu\text{m}$  and weld time of 0.9 sec. Because, at the end of weld time, it is assumed that the materials are sufficiently softened. It is worth noting that, the average hardness of the joint under these four conditions is HV88.55. But this hardness value is higher than that of the AA1100-UNS C10100 joint made by other welding processes like FSW (HV42.15) and friction welding (HV64.5) [174,175]. In all the cases, grain refining has taken place due to severe plastic deformation, and consequently, the hardness value is increased. The hardness of the joint produced by lubricating condition showed the maximum hardness than other conditions. Because in this condition, the temperature generation is maximum and it created a suitable environment for plastic deformation. It is also observed that the tensile shear and T-peel failure loads are also maximum in this condition. Thus, it can be assumed that failure loads are directly related to the microhardness [95].

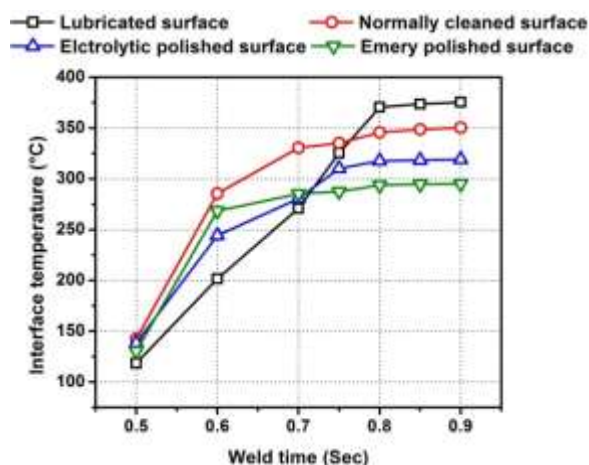


Fig. 5.49 Interface temperatures of welded specimens at various surface conditions

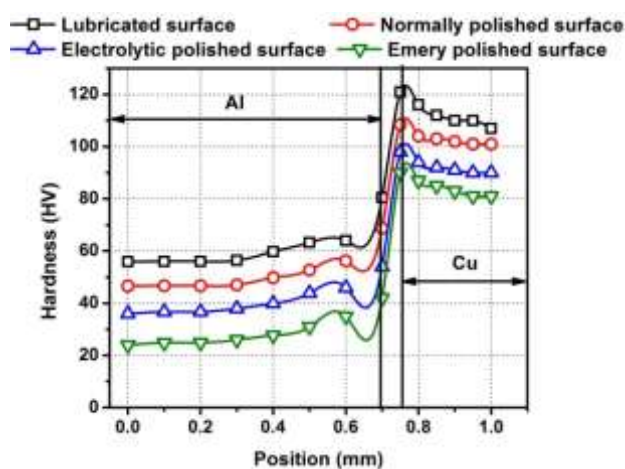


Fig. 5.50 Microhardness distribution across the 0.7Al-0.4Cu interface for different surface conditions

#### 5.4.6.4 Analysis of fractured surfaces

The fractured surface analysis has been done in order to investigate the plastic flow behaviour and appearance of different regions. It is carried out at a welding pressure of 0.38 MPa, the vibration amplitude of 68  $\mu\text{m}$  and weld time of 0.9 sec. Fig. 5.51 shows the SEM micrographs of the fractured surface for the lubricating condition. Fig. 5.51 (a) reveals a low magnification photograph of the bottom surface of top specimen in which four regions are clearly visible i.e. welded region (WR), base material (BM), dimple (D) and fine dimple (FD). In it, the black circled region is the weld zone and magnified image of it is shown in Fig. 5.51 (b). The darker flat region is the BM where no welding has not taken place and the grey looked like region is the WR where the actual weld has happened. This is to say; a substantial plastic deformation is observed at the WR due to the high temperature of 375°C, and thus, it facilitates the rupture of the oxide film. Due to it, grain refinement has also taken place, and it forms fine irregularities called as D and FD. After peeling out from Cu specimen, some cracks and micro cracks are also

observed. Similarly, Fig. 5.51 (c) represents the fractured surface of the bottom specimen and Fig. 5.51 (d) is the magnified image of the black circled region in it. Due to the ethanol adhesion, an island type of irregularities is scattered on Cu surface. This weld island (WI), also sometimes referred as nucleation sites. This feature has been observed as convex in shape, and it is thought to be the first stage of welding where this region is in a state of transition to D region.

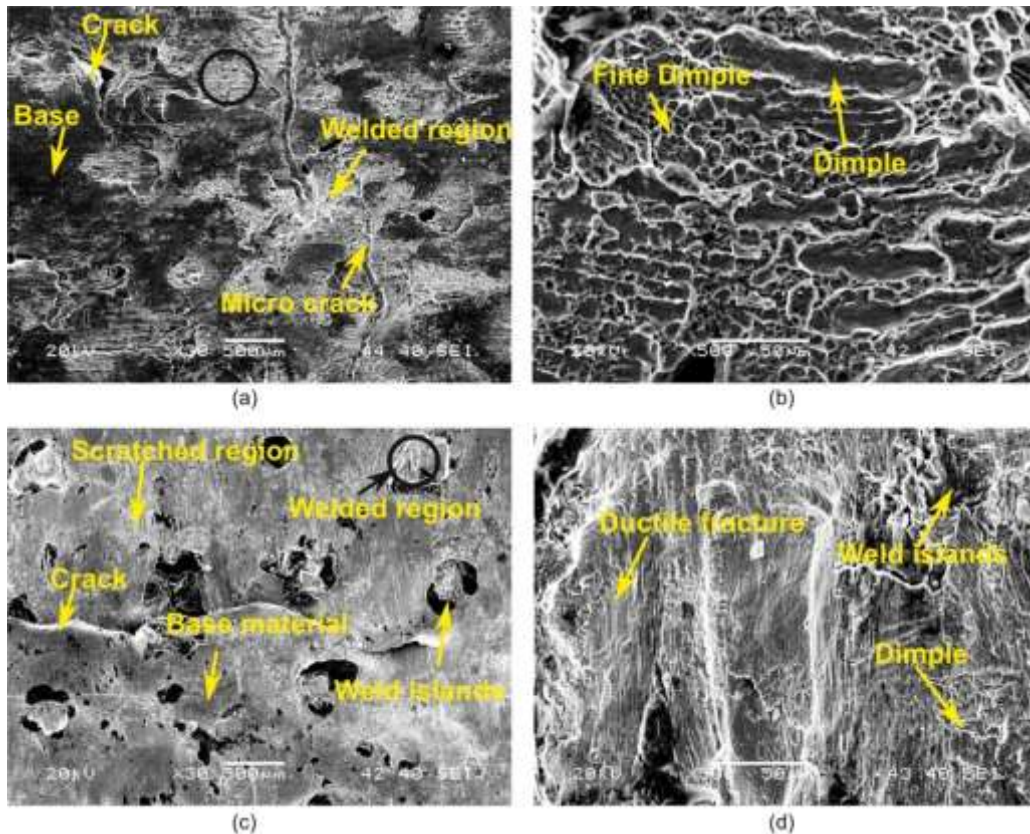


Fig. 5.51 Fractured surfaces of ultrasonically welded specimens in lubricating surface condition (a) Al side surface with 30X zoom; (b) Magnified image of a; (c) Cu side surface with 30X zoom; (d) Magnified image of c

The SEM micrograph for the normal condition is represented in Fig. 5.52. As the Al is softer material than Cu, thus it is more plastically deformed, and it can be seen from Fig. 5.52 (a) and (c). In both of these cases, the black looked like region represents the WR. From Fig. 5.52 (a), the weld spots observed on the bottom surface of the Al sheet appear to be mirror images of the knurl patterns of horn tip those are penetrated into Al material. However, the size of these weld spots and fractured surfaces vary according to different loading conditions and knurl patterns. But in this surface condition, one other type of region is observed and that is called scratched region (SR). In this region, only friction between the sheets happens and no welding has taken place. Fig. 5.52 (b) represents the faying surface of Cu material and Fig. 5.52(d) is the magnified image of black circled zone. In these photographs, the vertically fractured patterns are found inside the welding spot, indicating a ductile fracture. Due to heavy plastic deformation, crack is also formed

just around the welding spot in Al as well as Cu material. Since Cu is harder than Al; it is less amenable to plastic deformation. Therefore, WI and abraded regions are seen more than D region.

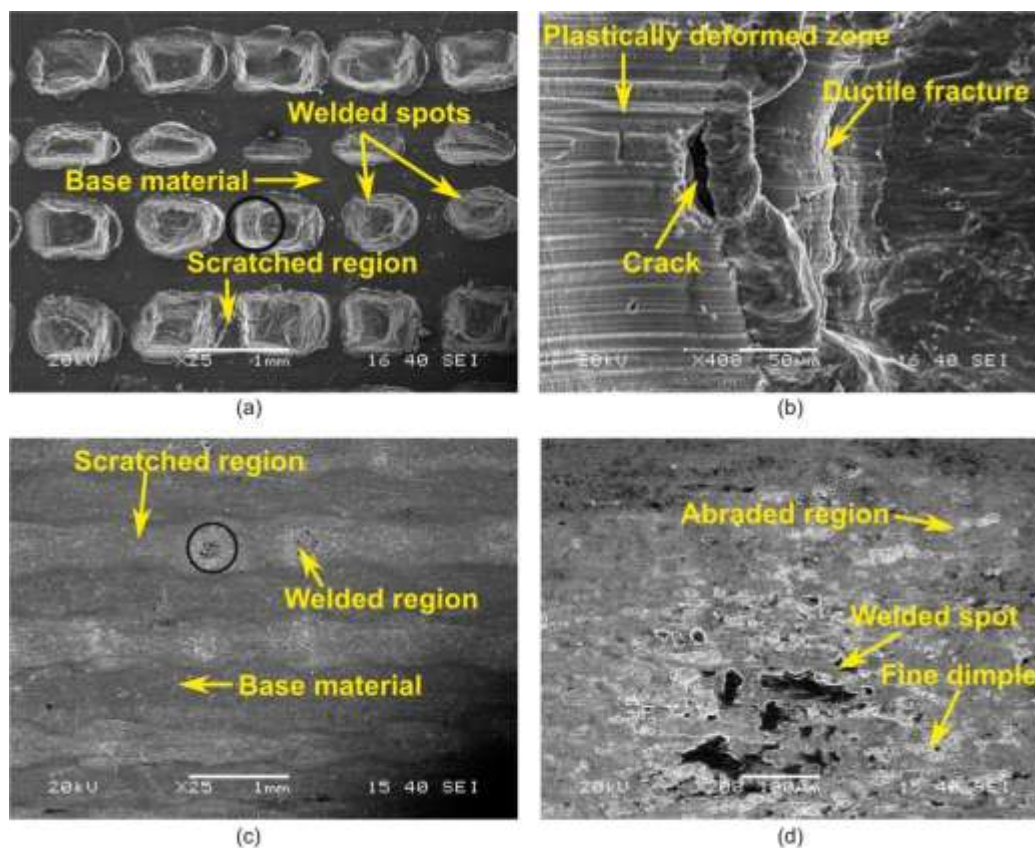


Fig. 5.52 Fractured surfaces of ultrasonically welded specimens in normal surface condition (a) Al side surface with 25X zoom; (b) Magnified image of a; (c) Cu side surface with 25X zoom; (d) Magnified image of c

In EP condition, as the surface roughness is modified by the electrolytic polishing, more scattered regions have been observed in Fig. 5.53 (a) and (c). The black spotted region is the EP region where no welding has taken place. Thus, ductile fracture with FD has been observed and can be seen from Fig. 5.53 (b). In comparison with this figure, less plastically deformed zone is noticed in Fig. 5.53 (d).

Similarly in emery polished condition, the surface peaks formed by polishing are readily crushed and become flat during the welding. Fig. 5.54 (a) and (c) show the surfaces in which the scratched region becomes more prevalent than the welded area. This is because of high surface roughness, which enhanced friction between the sheets and due to it, the relative motion between the sheets disappeared. It can also be seen from Fig. 5.54 (b) that, due to the softness of the Al material, ductile fractures happen with some D and FD regions. But, as Cu is harder than Al, they are less acquiescent to an extension. Thus, there is no increase of weld area. It can be clearly observed from Fig. 5.54 (d). These results, therefore, demonstrate that surface roughness of the material plays a vital role in deciding the joint strength in USMW.

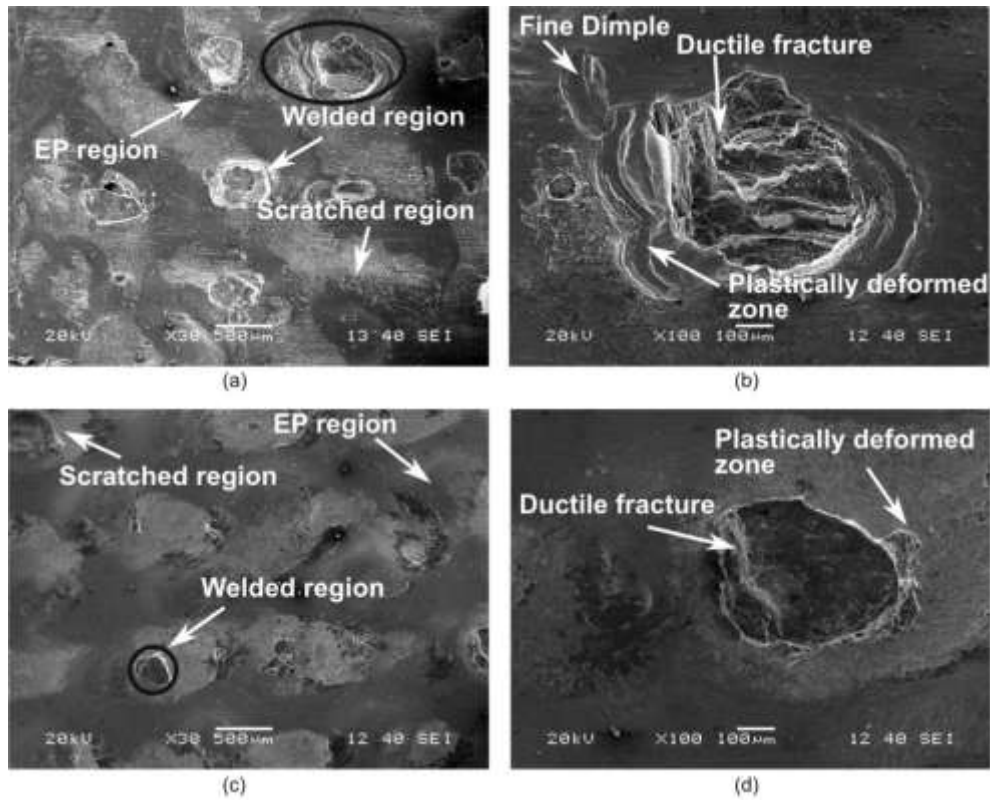


Fig. 5.53 Fractured surfaces of ultrasonically welded specimens in EP surface condition (a) Al side surface with 30X zoom; (b) Magnified image of a; (c) Cu side surface with 30X zoom; (d) Magnified image of c

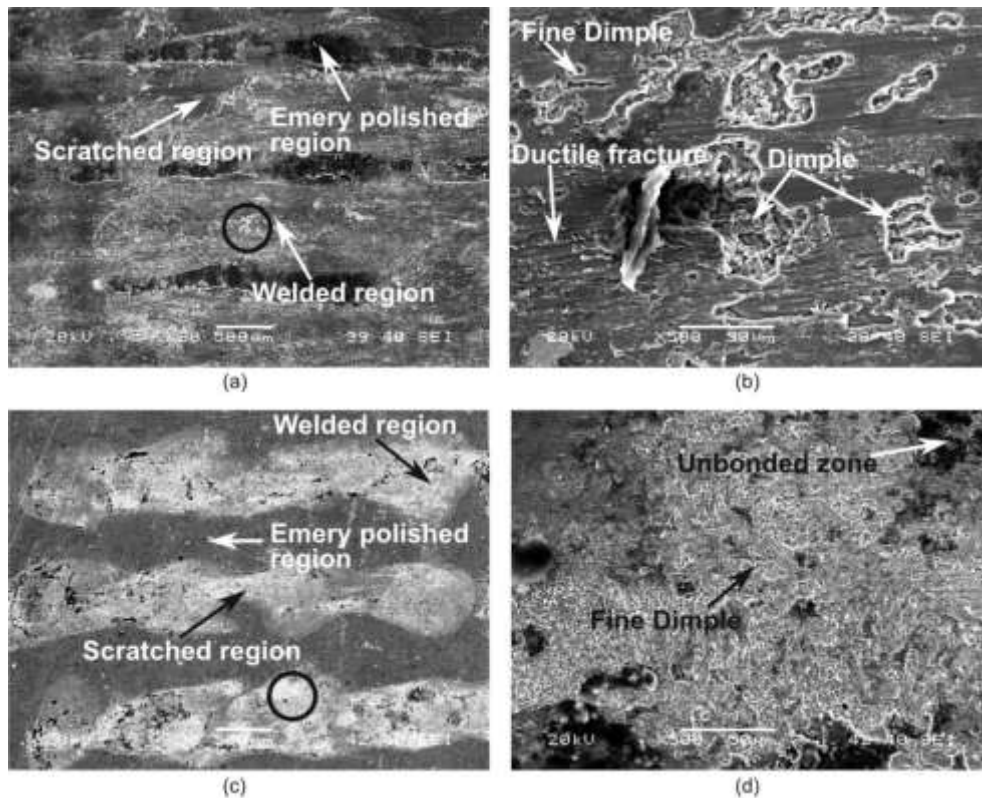


Fig. 5.54 Fractured surfaces of ultrasonically welded specimens in emery surface condition (a) Al side surface with 30X zoom; (b) Magnified image of a; (c) Cu side surface with 30X zoom; (d) Magnified image of c

### 5.4.6.5 Shear force determination during USMW for various surface conditions

From previous experiments, it is clearly observed that the weld surface conditions have a significant effect on the mechanical properties of joint as well as on the weld quality. From the above microstructural analysis, one can clearly notice the scratched region around the weld spot. But, this scratched zone is indistinctive for lubricating condition showing less friction has happened. Meanwhile, the amount of abrasion depends on shear force results. These shear forces are generally developed due to the ultrasonic vibration of sheets. Thus, to get shear force data, lathe tool dynamometer (Appendix B) has been used with a backing plate and anvil. Fig. 5.55 illustrates the total set up for shear force measurement.

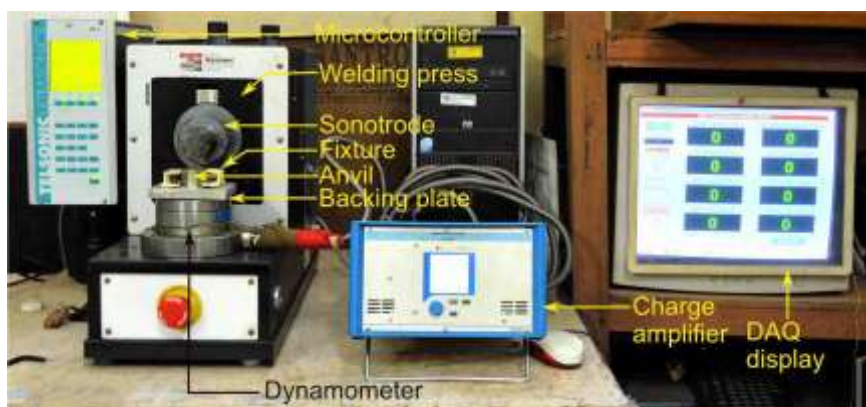


Fig. 5.55 Complete setup for shear force measurement during welding

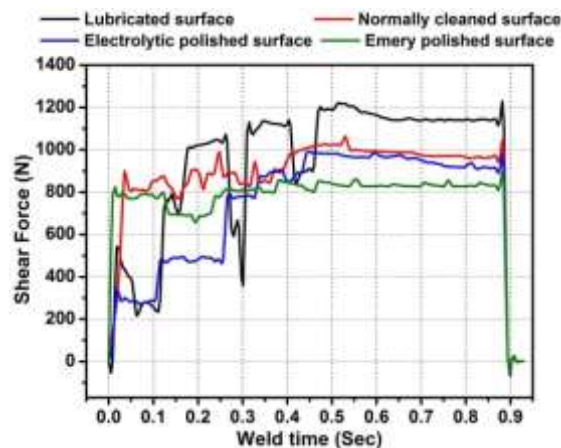


Fig. 5.56 Shear force variation of 0.7Al-0.4Cu weld coupons with weld time for different surface conditions

Likewise, in the previous section, the shear force measurements have been taken at  $68 \mu\text{m}$  and  $0.38 \text{ MPa}$ . Fig. 5.56 depicts the resulting shear force curves for different surface conditions throughout the weld cycle of 0.9 sec. It is observed that the shear force data is somewhat erratic up to 0.5 sec weld time, but towards the end, these data converge to a constant value. Thus, it is believed that, at the end of weld cycle, the weld area is fully developed. In this context, it can be said that the normal force may not be

is selected after simulating the model and observing the time period at which adequate plastic deformation has taken place.

#### 5.4.8.1 Measurement of sheet width increment

An optical image of each welded sample produced with different surface conditions has been selected to measure the average width increase near to the weld spot. This is done by using Image J software. Fig. 5.77 displays a sample image used to calculate average width after welding. It was noticed that although original width ( $W_0$ ) of the specimen was 20 mm, after welding, the width ( $W_0 + \Delta W$ ) became 20.8 mm.

#### 5.4.8.2 Effect of acoustic softening parameters on reduction of yield strength

In this section, the effect of acoustic softening parameter using Eq. (3.149) is described by using thermo-mechanical model. Thus, to validate it, steady state temperature (T) and  $\Delta W/W_0$  are calculated for the 0.7Al-0.4Cu sheets. Meantime, for establishing the acoustic softening parameter, it is necessary to convert the vibration amplitude and weld pressure to a dimensionless form. Firstly, the dimensionless vibration amplitude ( $\psi$ ) can be found out by dividing the amplitude ( $\xi$ ) with initial foil thickness (t). Mathematically, it can be expressed as:

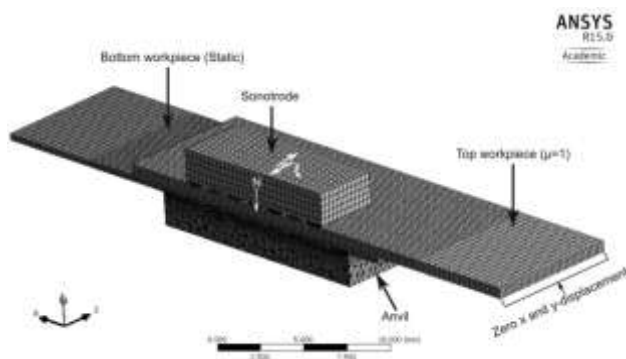


Fig. 5.76 Boundary conditions of the numerical model used for acoustic softening analysis

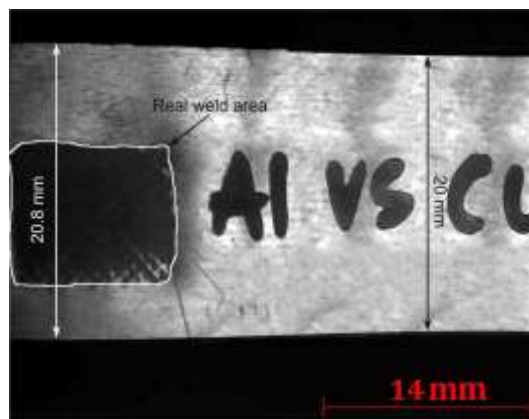


Fig. 5.77 Sample image used to calculate average width after welding in Image J

$$\Psi = \frac{\xi}{t} = \frac{68 \times 10^{-3}}{0.7} = 0.09 \quad (5.19)$$

Likewise, the dimensionless weld pressure (P) can be written as the division between weld pressure (WP) and yield strength ( $\sigma_y$ ) of the material ( $\sigma_y=34$  MPa at room temperature). Therefore, the mathematical expression is:

$$P = \frac{WP}{\sigma_y} = \frac{0.38}{34} = 0.01 \quad (5.20)$$

The coefficient of friction values those described previously are used in this section, and acoustic softening parameter ( $\beta$ ) is solved by decreasing the  $\beta$  value incrementally. This will be carried out until the predicted  $\Delta W/W_0$  and experimental  $\Delta W/W_0$  is a good match. Thus, to enlighten the effect of acoustic softening Fig. 5.78 represents the experimental as well as predicted  $\Delta W/W_0$  with three  $\beta$  values for different surface conditions.

The various  $\beta$  values are fed to the explicit dynamics model of ANSYS® and the corresponding deformation in the width of the sheet is observed. For all the surface conditions,  $\psi$  is 0.09 and  $P$  is 0.01. Thus, the model with  $\beta=1$  severely under predicts the sheet width increase as comparable to  $\beta=0.13$ . As it is previously described that when  $\beta=1$ , there is no acoustic softening happened. Meanwhile, if this value is decreased, the acoustic softening will play a vital role. It clearly perceives the figure that majority of the material softening and reduction in yield strength happened due to acoustic softening effect. To test the model results for different surface conditions, it is important to compare the modelled decrease in the thickness of the top sheet and the experimentally measured sheet thickness. This checking has been done after fixing the  $\beta$  value for minimization of error between the modelled and experimental  $\Delta W/W_0$  results. This comparison is displayed in Fig. 5.79 for 0.7Al-0.4Cu sheets.

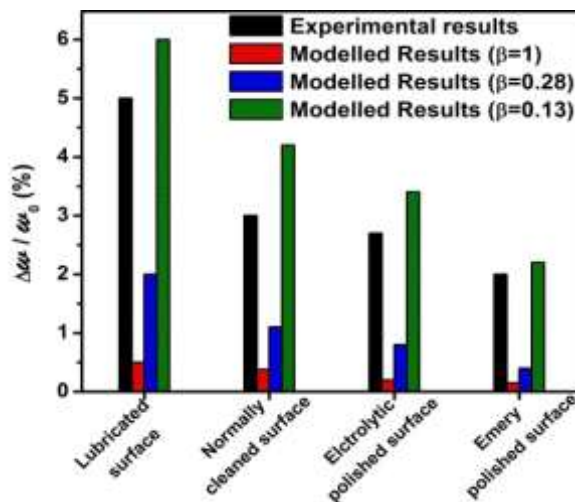


Fig. 5.78 Comparison of  $\Delta W/W_0$  between modelled and experimental results using three acoustic softening parameter ( $\beta$ ) values for various surface conditions

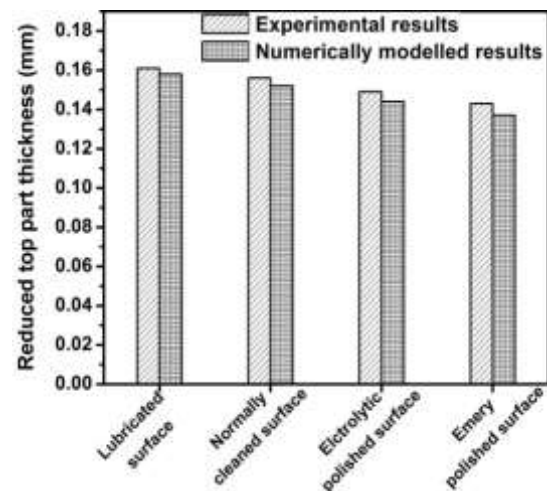


Fig. 5.79 Comparison of reduced top part thickness values between modelled and experimentally measured results for various surface conditions

Table 5.15 compares the effects of thermal and acoustic softening on strength coefficient ( $K_s$ ) which is provided in Eq. (3.149). It can be noticed that in the case of lubricating condition, there is a significant acoustic softening (53.73%) in AA1100



aluminium sheet at 375.37 °C as compared to room temperature (20 °C) properties. Likewise, in the case of normally polished, electrolytic polished and emery polished surface conditions, acoustic softening effects of 45.75%, 37.76% and 29.78% are observed. But when the  $\beta=0.13$ , there is a considerable reduction in the yield strength of the material for different surface condition values, and these are 87%, 93.98%, 92.95%, 91.91%, 90.87% while doing a comparison study with the normal temperature properties.

Table 5.15 Effect of acoustic softening parameter ( $\beta$ ) on strength coefficient( $K_s$ )

Temperature ( $T_s$ ) (°C)	Acoustic softening parameter ( $\beta$ )	Strength coefficient ( $K_s$ ) (MPa)	% $K_s$ reduction from room condition
20	1	157.8	0
375.37	1	73	53.73
350.35	1	85.6	45.75
319.09	1	98.2	37.76
295.08	1	110.8	29.78
20	0.13	20.51	87
375.37	0.13	9.49	93.98
350.35	0.13	11.12	92.95
319.09	0.13	12.76	91.91
295.08	0.13	14.40	90.87

## 5.5 Summary

The present study deals with the extensive analysis on a different aspect of USMW of Al-Cu dissimilar sheet metals. This study includes the exploration of impelling process parameters of the welding process on the responses like tensile shear and T-peel strength failure loads with providing information on the weld area and temperature during the process. The microstructural study also has been carried out to reveal the quality of weld. Likewise, the modelling of the results has been explored by ANN and ANFIS. The outcomes from these analyses have been compared with the results acquired from a traditional method called regression analysis. Additionally, the FEM analysis for the welding is carried out on the basis of its mechanics. The following conclusions can be extracted from the present investigation:

- AA1100 and UNS C10100 sheets are welded successfully under different process parameter combinations. From the experimental research, the maximum values of tensile shear stress, T-peel failure loads are obtained as 482.65 N and 141.32 N for 0.3Al-0.3Cu similar thickness materials at 0.24 MPa weld pressure and at 68  $\mu\text{m}$  amplitude. Similarly, the maximum values of these failure loads are obtained as 564.6

N and 193.52 N for 0.45Al-0.45Cu similar thickness materials at 0.34 MPa weld pressure and at 68  $\mu\text{m}$  amplitude.

- Furthermore, the dissimilar thickness sheets are also welded to reveal its weld strengths. Thus, the maximum values for tensile shear and T-peel failure loads are achieved as 953.8 N and 235.85 N for 0.6Al-0.4Cu materials at 0.26 MPa weld pressure and at 68  $\mu\text{m}$  amplitude. Likewise, the highest values of tensile shear and T-peel failure loads among all the thickness combinations are obtained as 1512 N and 280.83 N for 0.7Al-0.4Cu materials at 0.38 MPa weld pressure and at 68  $\mu\text{m}$  amplitude. It is noticed that when the thickness of the weld materials increased, then more amount of ultrasonic energy is required to remove the oxide film present on the surface, and a satisfactory weld can be achieved.
- The microscopic analysis also has been done for 0.7Al-0.4Cu because; it provides the maximum tensile shear and T-peel failure loads for the weld joint. A quality classification of welding like “under weld”, “good weld” and “over weld” is proposed with respect to the formation of micro bonds and absence of gaps. It is observed that at the starting stage of USMW, the hardness shows 57% higher results than the hardness of the parent materials and it is due to severe cold working at the interface.
- To reveal the quality of welding and confirms the presence of IMCs on either side of the fracture surface EDS analysis have been performed. It proves that the deformation in the weld coupon of softer metal (AA1100) is more than the harder metal (UNS C10100). This is due to the factor like the hardness of material and oxide layer. Moreover, the EDS line scan result also revealed that there is a formation of about 1.5  $\mu\text{m}$  thick  $\text{Al}_2\text{Cu}$  IMC layer for the good weld joint. Meanwhile, XRD analysis is also carried out to validate the results; those are already obtained in SEM and EDS analyses.
- Various methods like regression, ANN and ANFIS are used as to develop the models for an accurate prediction after tuning the various parameters. The average absolute errors of TS are obtained as 0.47%, 0.48% and 0.07% for regression, ANN and ANFIS respectively. Likewise, these values of TP are varied as 1.89%, 1.44% and 0.22% for regression, ANN and ANFIS respectively. Thus, it is confirmed that ANFIS can predict most accurately among ANN and regression for the current domain of experiments. Moreover, to demonstrate the highest level of accuracy among the proposed predictive models, the parity graphs are plotted between the experimental and predicted values for TS and TP. The  $R^2$  values of TS for regression, ANN and ANFIS are obtained as 91.47%, 98.30% and 99.98% respectively. Similarly, in the case of TP results also, ANFIS is more accurate than other two techniques with an  $R^2$

value of 99.79%. Eventually, the ANN modelling has given comparatively accurate result than regression modelling with  $R^2$  values of 99.36% and 93.77% respectively.

- The maximum failure loads for each anvil are observed at the weld time of 0.75 sec and the vibration amplitude of 68  $\mu\text{m}$ . Among all the tested anvils, anvil 1 (knurling angle is  $75^\circ$ , cutting width is 0.55 mm and non-cutting width is 1 mm) shows the highest failure load requirement. The weld time, vibration amplitude and geometry of anvil tip pattern are also examined for the cause of plastic deformation and sticking of tip part. For higher weld time, the temperature is found to be more which results in the increase of weld area. But, at a higher temperature, ample extrusion occurs, and it leads to crack formation at the periphery of the weld spot. Microhardness distribution also shows that sufficient plastic deformation occurs at the interface due to the significant amount cold work in this zone. It also revealed the softening of the material at higher weld time.
- The tensile shear and T-peel failure loads decrease as the surface roughness of the material increases. Though in lubricating (with ethanol) condition, initially the mechanical strength take a little bit longer period of time to increase, but after the evaporation of ethanol, the highest strength is obtained. The interface temperature achieved during welding with the addition of ethanol is the highest among all surface conditions. Initially, the temperature profile of the emery polished surface suddenly increases but as the relative motion between the sheets vanishes, the temperature comes to a steady state and finally, it is the lowest among others. Due to the formation of highest temperature at the interface region, the maximum grain refinement takes place for the lubricating condition. Thus, the maximum hardness is observed at the faying surface than other conditions. Moreover, it can be said that the joint strength is directly related to the hardness of the weld interface. The microstructural analysis also reveals that, at the initial stage of welding using ethanol, the increased relative motion between the sheets is observed. Due to it, WI regions are generated and, later on, they are converted to D and FD regions. These regions with ductile fractures are more often observed as comparable to other conditions. Thus, these regions make the weld strength maximum among normal; EP and emery polished conditions.
- A welding mechanics based numerical model has been explained that can predict the temperatures during the USMW process for various surface conditions. The maximum experimental temperatures measured at the end of weld time by thermocouples shows a close fit with the predicted results. The errors are obtained as 0.80%, 2.35%, 0.78% and 0.72% for lubricating, normally polished, electrolytic polished and emery polished surface conditions respectively. Thus, it is confirmed that the boundary conditions which applied to this thermo-mechanical problem are reasonable.

Furthermore, the acoustic softening analysis shows that in the case of lubricating condition, there is a significant acoustic softening (53.73%) in AA1100 aluminium sheet at 375.37 °C as compared to room temperature (20°C) properties. Likewise, in the case of normally polished, electrolytic polished and emery polished surface conditions, acoustic softening effects of 45.75%, 37.76% and 29.78% are observed. But when the acoustic softening parameter ( $\beta=0.13$ ) is introduced, there is a considerable reduction in the yield strength of the material for different surface condition values, and these are 87%, 93.98%, 92.95%, 91.91% and 90.87% while doing a comparison study with the standard temperature properties. Thus, it clearly signifies that majority of the material softening and reduction in yield strength happened due to acoustic softening effect.



## Chapter 7

# Experimental and Numerical Investigations on Al-SS Weld Coupons

## 7.1 Introduction

Recently, there is considerable interest in reducing the weight of the automotive structures by introducing an advanced method of joining metals. This technique includes various materials such as aluminium, magnesium, steel and reinforced composites [187]. Typically, the structures of an automobile contribute nearly 20 % of its total and usually, these structures are made up of steel [188]. Thus, replacing steel with other lightweight materials such as aluminium alloy and magnesium enriched composites may be a potential solution for weight reduction in future vehicle design. Till now, resistance spot welding (RSW) is widely used in these automobile industries due to its simplicity and speed. However, RSW faces difficulty in welding of aluminium alloys due to its inconsistent weld behaviour, shorter electrode life and high production cost [189]. Furthermore, it is hard to apply this technique for joining of ferrous and non-ferrous materials, as there is a tendency of forming intermetallic compounds (IMCs) and large amounts of distortion [190]. USMW has received much consideration as alternative joining techniques to resistance spot welding for ferrous and non-ferrous materials. [155,156]. These methods solve many of the issues like IMC formation, the occurrence of distortion, etc. because of the absence of liquid phase formation [98,191]. So far, only a few reports have been published in the field of joining of aluminium alloy with steel using high power ultrasonics for automotive applications [192]. Not only in USMW, but other joining methods also show the formation IMC like  $\text{Fe}_2\text{Al}_5$  when aluminium is tried to be weld with steel in both solid and liquid state [193-196]. The present study deals with the high power ultrasonic metal welding of aluminum (AA1100) and stainless steel (SS304) to investigate the effects of individual input parameters like amplitude, weld pressure and weld time on different output parameters such as tensile shear and T-peel failure loads by using a full factorial design of experiment.

## 7.2 Problem Definition

Welding of dissimilar materials has been emerged as a key topic for the researchers as well as for the industry persons. Determination of suitable welding parameters is one of the most vital elements in the weldability study of metals. However, it has been observed

that lesser attention has given to the ultrasonic welding of Al-SS combinations with the variation of various control parameters. Thus, the primary focus of this study is to get high tensile shear and T-peel failure loads with a considerable amount of weld area and interface temperature. Meanwhile, other analyses such as the effects of various anvil knurl patterns and surface conditions on these responses have been studied for a selected material thickness combination. Metallurgical analyses of these conditions have also been performed to demonstrate the quality of the weld. Furthermore, predictive analysis and numerical analysis have been accomplished to validate the experimental results.

## **7.3 Experimentation**

In the current research work, a handful number of experiments have been executed to analyse the responses like tensile shear failure load, T-peel failure load, weld area and interface temperature during the welding of Al-SS metal sheets of various thickness combinations.

### **7.3.1 Design of experiment**

A lateral drive ultrasonic metal welder (Telsonic® Ultrasonics, Switzerland, model: M4000) (Fig. 4.1) with flat and knurled weld tip size of 11 mm× 9 mm is employed to carry out welding experiments of Al-SS combination. As the Al is a softer material than SS thus, Al is placed on the SS side. Meantime, the working range of input parameters such as weld pressure (WP), weld time (WT) and vibration amplitudes (A) have been selected in such a way that, the good welding can be obtained in that range, and it has been found from trial experiments. As far as input parameters are concerned, three welding pressures, seven welding times and four vibration amplitudes are chosen based on the trial experiments (Table 7.1). These tests are conducted using a full factorial design with six replicates for each condition, and the total of 504 samples is prepared for the determination optimum process parameters and its effect on weld quality.

### **7.3.2 Workpiece and tool material**

The various weld joints are produced between the 0.45 and 0.7 mm thick AA1100 aluminium sheets with 0.1 and 0.2 mm thick SS304 sheets. These sheets cut into 80 mm × 20 mm rectangles. To get a sound weld, the contaminants, and other greasing agents present over the weld surface are removed by acetone. There is also a formation of a thin oxide layer on the surface of SS304 but, as the aluminum material is softer than it, more amount of aluminum is diffused into the SS304. The specimens after welding are shown

in Fig. 7.1. Table 7.2 represents the mechanical, thermal and physical properties and Table 7.3 shows the chemical compositions of specimens used in this study.

### 7.3.3 Welding performance evaluation characteristics

The tensile shear and T-peel tests have been carried out on the welded samples using a universal testing machine with a fitted load cell of 100 kN. Tests are performed under the standard atmospheric condition with a uniaxial shear in the rolling direction of the samples. The load-displacement graphs are used to determine the failure load of the welded samples, and each test is repeated three times to achieve better accuracy in results. K-type thermocouples are embedded into the weld spot of two materials to measure the temperature rise during the welding. These temperature values are recorded by the data acquisition system (DAQ). The metallographic analysis has been performed on the weld cross-sections of the selected samples using JEOL JSM-6084LV<sup>®</sup> scanning electron microscope. Likewise, the average weld area is observed by an optical stereo microscope shown in Appendix B, and the grabbed image is analysed as well as its dimensions are quantified by Image J<sup>®</sup> software package. A computerized Vickers microhardness machine is employed to measure microhardness values on the polished cross-sections.

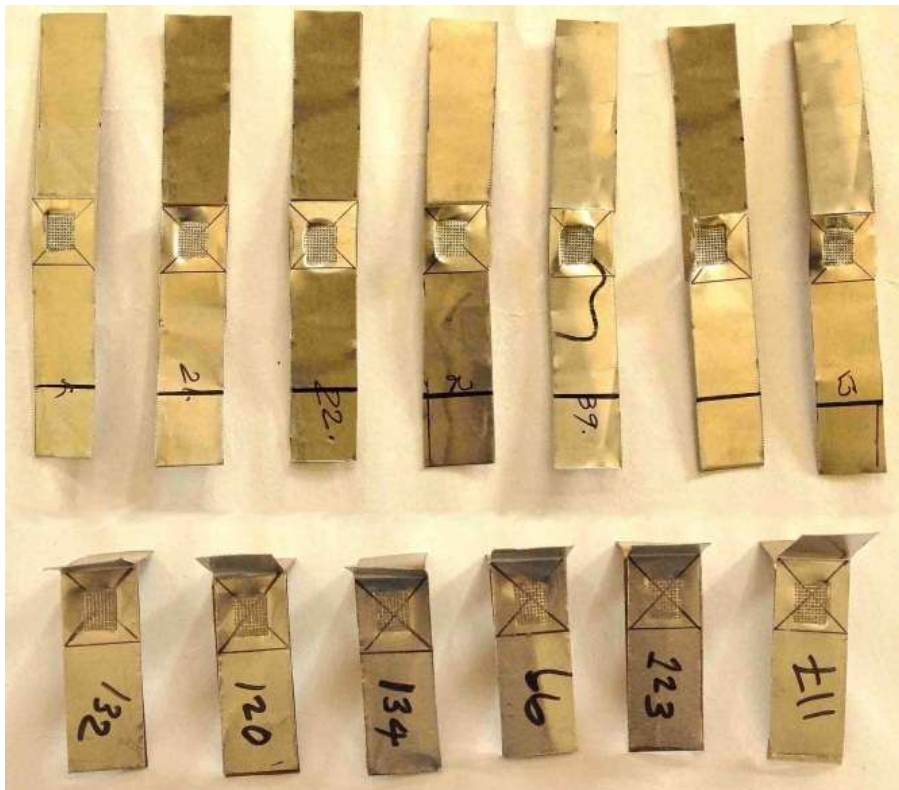


Fig. 7.1 Welded samples



Table 7.1 Domain of experiments adopted for USMW of dissimilar thickness Al-SS weld coupons

Thickness	0.45Al Vs 0.1SS							0.7Al Vs 0.2SS						
Factors	Level 1	Level 2	Level 3	Level 4	Level 5	Level 6	Level 7	Level 1	Level 2	Level 3	Level 4	Level 5	Level 6	Level 7
Amplitude ( $\mu\text{m}$ )	47	54	60	68	...	...	...	47	54	60	68	...	...	...
Weld pressure (MPa)	0.2	0.22	0.24	...	...	...	...	0.26	0.32	0.38	...	...	...	...
Weld time (sec)	0.3	0.35	0.4	0.45	0.5	0.55	0.6	0.52	0.62	0.72	0.78	0.82	0.85	0.92

Table 7.2 Physical, mechanical and thermal properties of specimens

Properties	Unit	AA1100	SS304
Density	Kg/m <sup>3</sup>	2710	8000
Young's modulus	GPa	68.9	193
Poisson's ratio		0.33	0.29
UTS	MPa	135.5	858.1
YS	MPa	115.2	649.4
Co-efficient of thermal expansion	°C <sup>-1</sup>	23.6 × 10 <sup>-6</sup>	17.3 × 10 <sup>-6</sup>
Thermal conductivity	W/m°C	220	16.2
Specific heat	J/Kg°C	904	500

Table 7.3 Chemical compositions of specimens

Component Elements Symbol	Composition (%) in AA1100	Composition (%) in SS304
Al	99	...
Cu	≤0.05-0.20	...
Mn	0.05	2
Zn	0.10	...
Si	0.3	1
Fe	0.3	66
Ni	...	8
Cr	...	18
Others	≤0.3	...

## 7.4 Results and Discussion

### 7.4.1 0.45Al-0.1SS and 0.7Al-0.2SS dissimilar thickness weld coupons

The similar thickness weld samples of aluminium and steel are considered for the first set of experimental runs. As the soundness of the joints depends on the control of process parameters in the forthcoming sections, the effects of these control parameters on the various aspects of weld attributes are described along with illustrating the quality of the weld through microstructural analysis.

#### 7.4.1.1 Influence of process parameters on tensile shear and T-peel failure load

The results of the peak tensile shear and T-peel failure loads for 0.45Al-0.1SS and 0.7Al-0.2SS USW joints at different values of process parameters are shown in Fig. 7.2 and Fig.

7.3. In those figures, the solid lines represent tensile shear failure loads, and dotted lines show T-peel failure loads. It is noted that these loads increase with the increase in vibration amplitude and reach maximum values of 500.17 N and 207.63 N at the 68  $\mu\text{m}$  amplitude for 0.45Al-0.1SS combination due to high relative motion between the sheets. Similarly, the maximum tensile shear failure load of 582.9 N and T-peel failure load of 217.12 N are obtained for 0.7Al-0.2SS combination at the 68  $\mu\text{m}$  amplitude. These maximum failure values of mechanical strengths also depend on the formation of IMCs. It is well understood that in the dissimilar welding process, the presence and growth of a thin IMC layer are an evidence of sound metallurgical joining [197]. But these strengths are increased with the rise of weld time up to 0.4 sec for 0.45Al-0.1SS and 0.72 sec for 0.7Al-0.2SS followed by decreasing trend due to the substantial formation of the IMCs. Meantime, the density of micro bonds increases with the rise in weld pressure up to 0.22 MPa for 0.45Al-0.1SS and 0.32 MPa for 0.7Al-0.2SS followed by gradually decreasing trend. Conventionally, with the increase of weld pressure, the weld strength is improved due to the transfer of ultrasonic energy to the faying surface effectively. Thus, it produces higher temperature at the weld zone, which is responsible for decreasing the material deformation resistance and enhancing the plastic flow. However, the excessive weld pressure causes significant friction between the specimens, and ultimately the relative motion between them disappears, leading to interlocking between the surfaces.

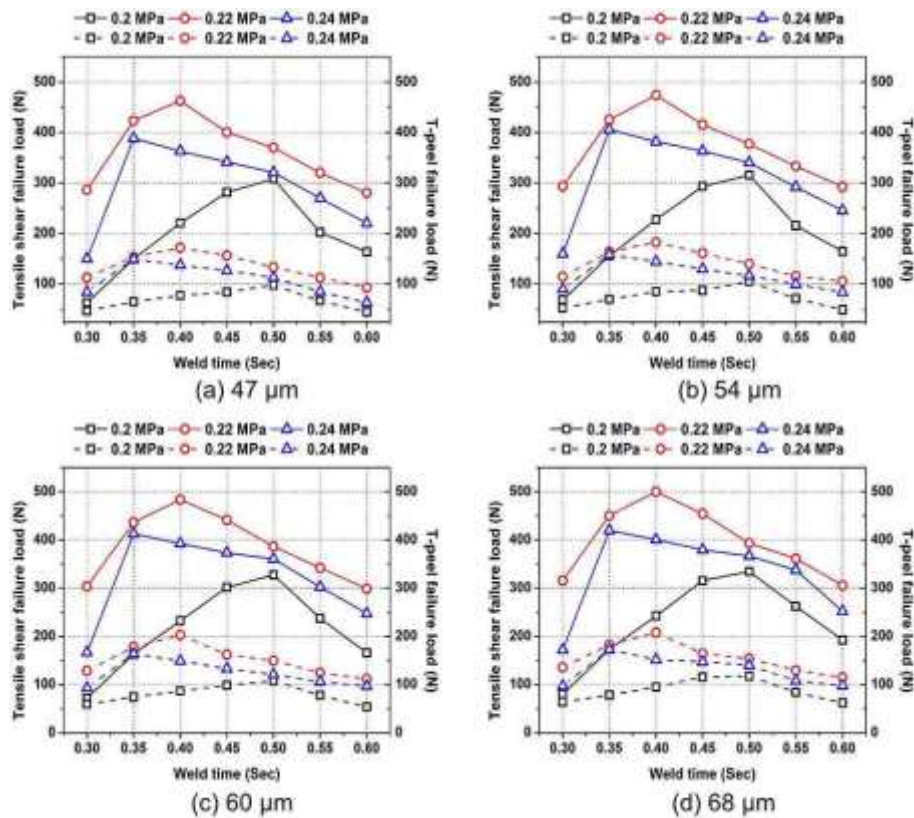


Fig. 7.2 Tensile shear and T-peel failure loads of 0.45Al-0.1SS weld coupons for different vibration amplitudes

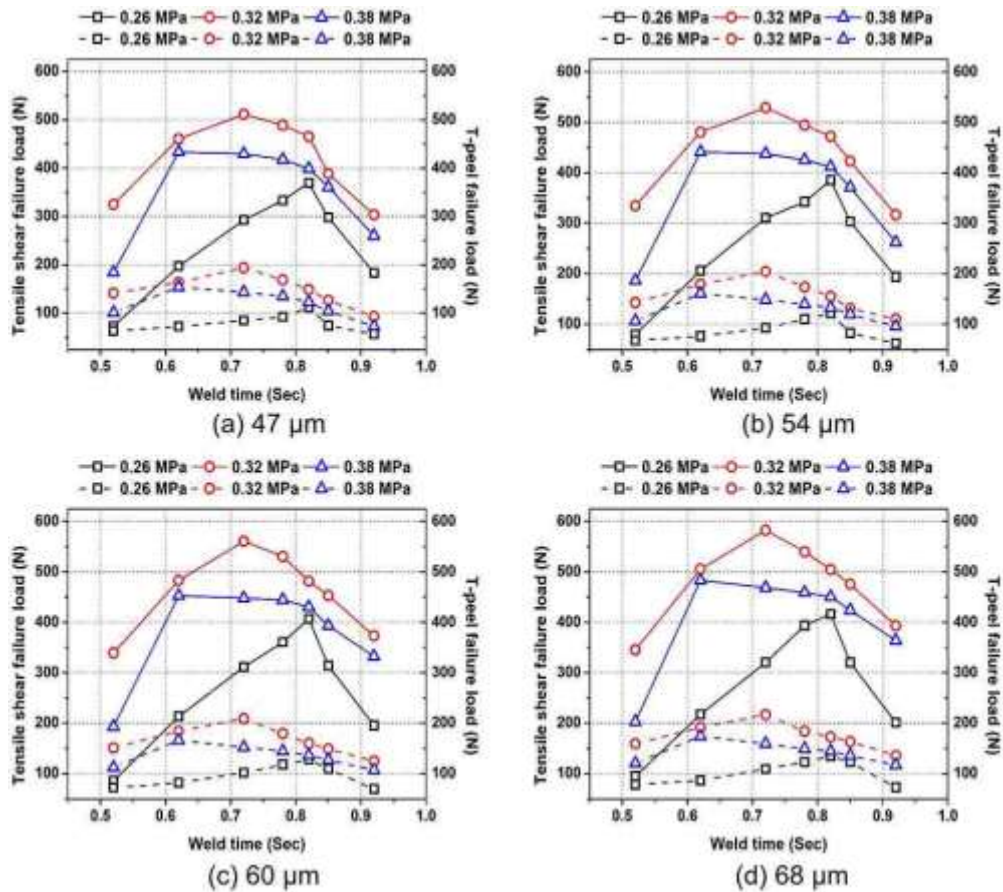


Fig. 7.3 Tensile shear and T-peel failure loads of 0.7Al-0.2SS weld coupons for different vibration amplitudes

#### 7.4.1.2 Influence of process parameters on weld area

A comparison of the weld areas is shown in Fig. 7.4 for 0.45Al-0.1SS. As discussed earlier, the experiments are conducted using four different vibration amplitudes of 47  $\mu\text{m}$ , 54  $\mu\text{m}$ , 60  $\mu\text{m}$ , 68  $\mu\text{m}$  and the relevant weld areas are measured by multiplying one micro bond area with a number of points present on the horn tip. Initially, the weld area is continued to increase, and maximum value of 54.63  $\text{mm}^2$  is obtained at 0.6 sec of weld time, 0.22 MPa of weld pressure and 47  $\mu\text{m}$  of vibration amplitude. Likewise, the weld areas noticed at 54  $\mu\text{m}$ , 60  $\mu\text{m}$  and 68  $\mu\text{m}$  are 59.12  $\text{mm}^2$ , 61.29  $\text{mm}^2$ , and 69.53  $\text{mm}^2$  respectively. The reasons for these phenomena are quite same as described in the previous section.

Fig. 7.5 illustrates the graphs between different process parameters with weld areas for the weld coupons of 0.7Al-0.2SS. As like before, the weld area begins to rise and reaches the peak value of 59.82  $\text{mm}^2$  at maximum weld time of 0.92 sec, weld pressure of 0.32 MPa and 47  $\mu\text{m}$  of vibration amplitude. Likewise, the weld area exhibits higher values of 65.53  $\text{mm}^2$ , 72.92  $\text{mm}^2$ , and 76.83  $\text{mm}^2$  respectively when the vibration amplitude values increased to 54  $\mu\text{m}$ , 60  $\mu\text{m}$ , and 68  $\mu\text{m}$ .

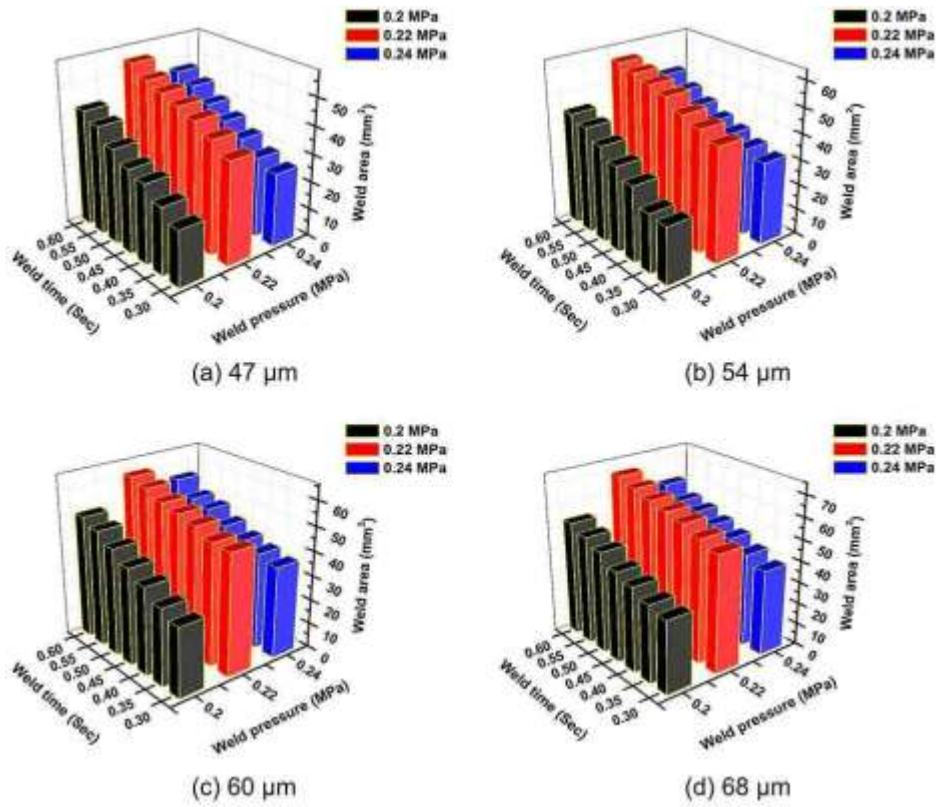


Fig. 7.4 Weld areas of 0.45Al-0.1SS weld coupons for different vibration amplitudes

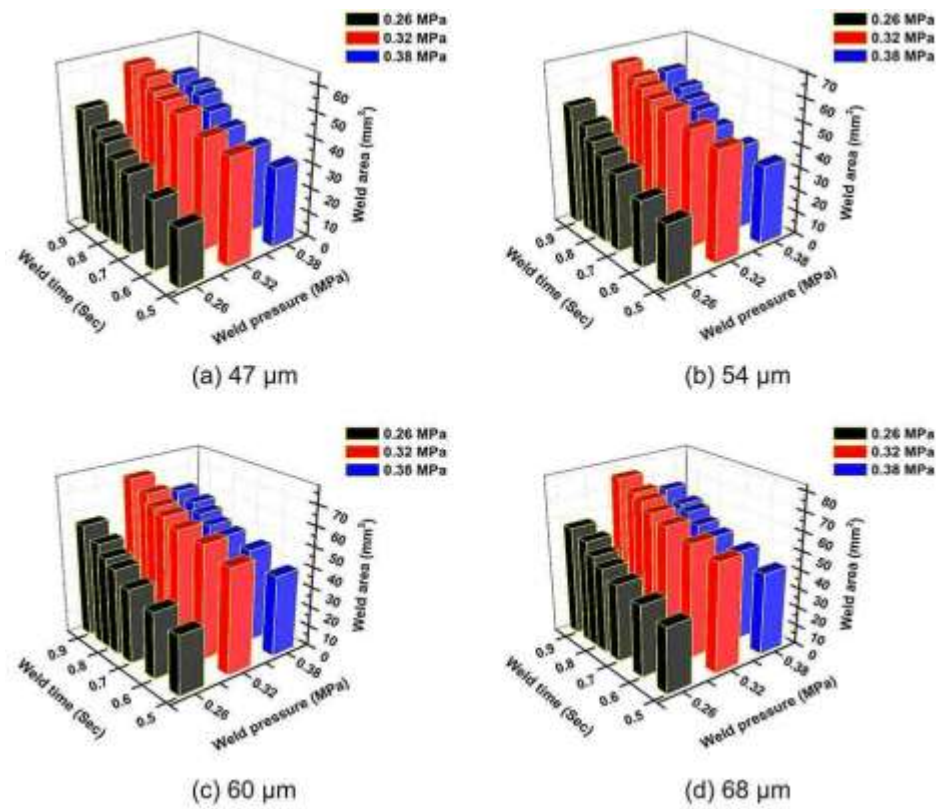


Fig. 7.5 Weld areas of 0.7Al-0.2SS weld coupons for different vibration amplitudes

### 7.4.1.3 Effect on weld interface temperatures by process parameters

To further comprehend the welding procedure and the evolution of IMCs at the weld interface, the temperatures are detected by sacrificial thermocouple implanted at the weld spot precisely Fig. 7.6.

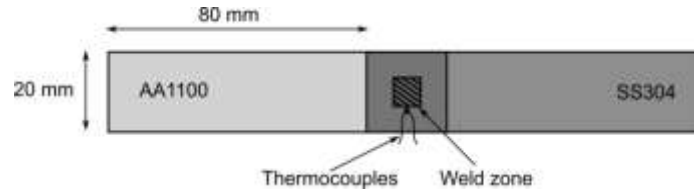


Fig. 7.6 Weld samples with positions of thermocouples for temperature measurement

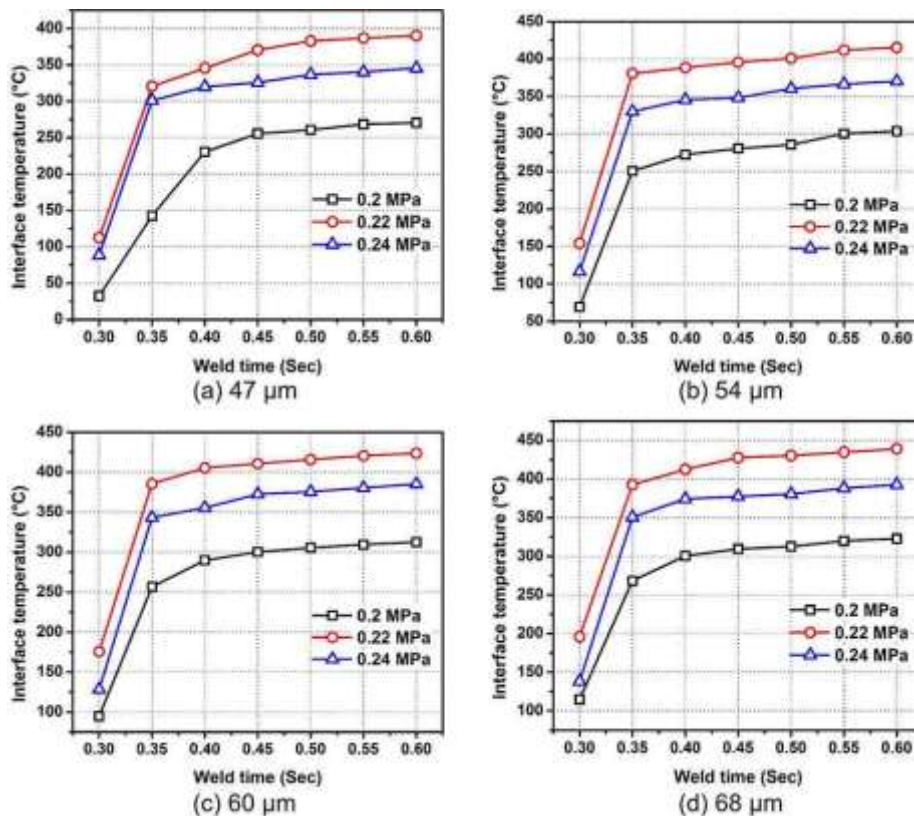


Fig. 7.7 Weld interface temperatures for 0.45Al-0.1SS weld coupons at different vibration amplitudes

Fig. 7.7 and Fig. 7.8 represent the peak temperatures at each condition of process parameters. It has been observed that increasing weld time results in an increase of interface temperature, and the maximum temperature of 438.94 °C is observed at 68  $\mu\text{m}$  vibration amplitude, 0.22 MPa of weld pressure and 0.6 sec of weld time for 0.45Al-0.1SS samples. Likewise, the peak temperature of 440.6 °C is achieved at the same vibration amplitude with 0.32 MPa of weld pressure and 0.92 sec of weld time for 0.7Al-0.2SS samples. The temperature increasing rate is faster at the initial phase of welding, and thus it delivers more energy to the weld zone, and more plastic deformation occurs. But prolonged weld time and high weld pressures hinder the motion between the specimens

and provide high contact resistance between tool and specimens. Therefore, it results in slowing down the temperature rate, more heat dissipation and providing less input energy to the weld zone.

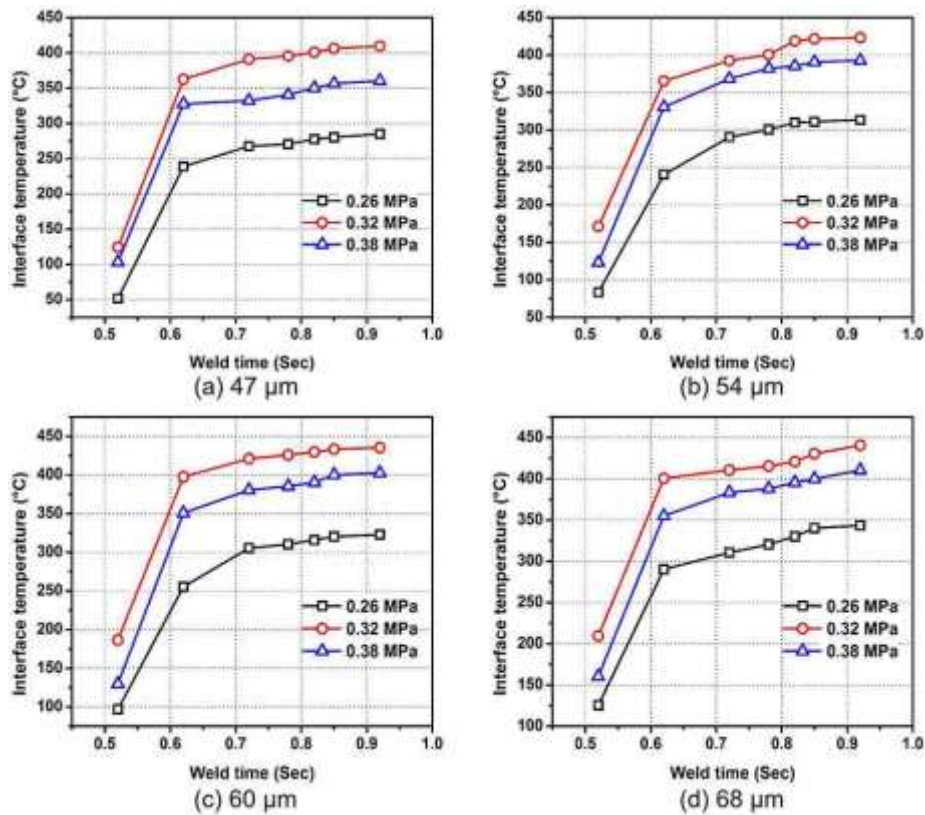


Fig. 7.8 Weld interface temperatures for 0.7Al-0.2SS weld coupons at different vibration amplitudes

#### 7.4.1.4 Microscopic investigations on weld quality

As like before, three types of weld specimens such as “under”, “good” and “over” are selected for 0.45Al-0.1SS and 0.7Al-0.2SS based on the tensile shear and T-peel failure loads. The SEM images of all these samples are shown in Fig. 7.9. These qualities of the weld are characterised based on the density of microbonds present at the interface. If the density of micro bonds is less then it is treated as “under weld” condition, and if the density of the micro bonds is dense then it may be considered as “good weld” or “over weld” condition. However, in “over weld” condition, cracks and severe plastic deformation are observed.

#### 7.4.2 Weld quality determination for 0.7Al-0.2SS weld coupons

The quality of welding depends on the correct selection of materials, its thickness and process parameters. Improper selection of these parameters may result in inferior welding. Thus, in this analysis, 0.7Al-0.2SS weld combination is selected based on its

highest tensile shear and T-peel failure loads. Moreover, microhardness distribution, fractographic and X-ray diffraction (XRD) analyses of weld surfaces are discussed in the forthcoming sections.

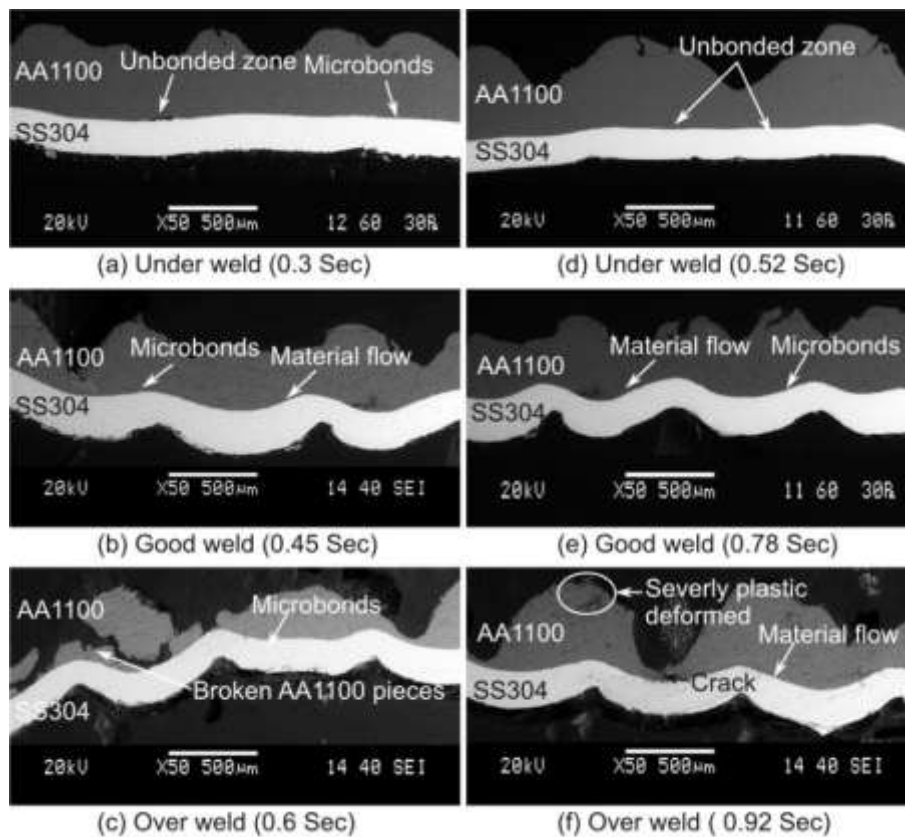


Fig. 7.9 SEM micrographs of weld cross-sections for (a)-(c) 0.45Al-0.1SS joints and (d)-(f) 0.7Al-0.2SS joints

#### 7.4.2.1 Microhardness distribution in weld zone

During USMW of 0.7Al-0.2SS sheets, the interface temperature developed is beyond the recrystallization temperature of Al. Thus, due to this elevated temperature and plastic deformation, work hardening of the specimen is occurred followed by softening. The microscopic observation of grains around the weld interface with respect to various weld times is shown in Fig. 7.10.

Fig. 7.11 depicts the microhardness results for “under”, “good” and “over” weld samples against the weld time. From this figure, it is noticed that at the starting stage of USMW, the hardness shows 56% higher results than the hardness of the parent materials and it is due to severe cold working at the interface. Meanwhile, when the weld time is increased further, then the hardness value is drastically reduced due to material softening.

The hardness variations along the weld interface in a horizontal manner with respect to various weld times for these three weld conditions are shown in Fig. 7.12. For the



shorter weld time, there is a much fluctuation in the hardness value observed than the results obtained at higher weld time. But, one common feature noticed for all the conditions is that the region under the peak of the sonotrode experiences a higher hardness value than the crest position. It is due to the fact that the plastic deformation starts from the center of the trough position and gradually proceeds towards the crest position as the welding progresses.

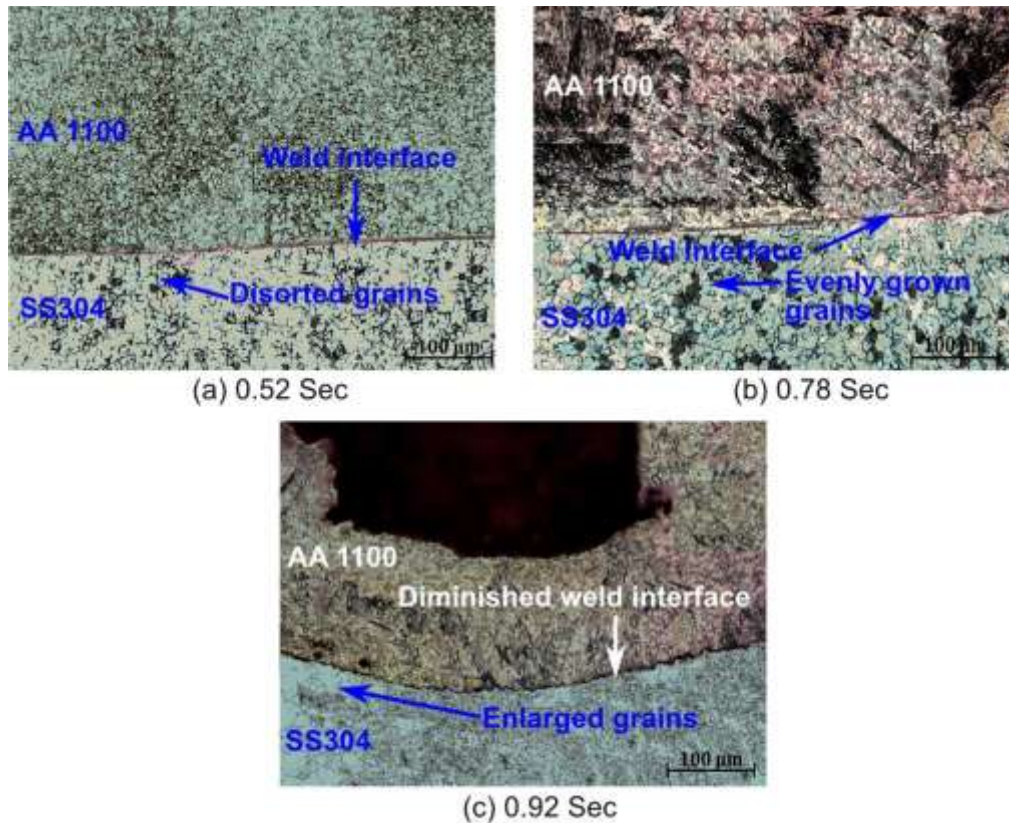


Fig. 7.10 Optical microscopic images of 0.7Al-0.2SS weld specimens with increase in weld time

The measurements are also taken in the vertical direction of the weld cross-section. Thus, Fig. 7.13 reveals the variations of hardness with time at various locations below the crest zone. This vertical measurement showed that the hardness value is very high in the bottom surface zone for shorter welding time, and it is drastically reduced towards weld interface due to material softening. It shows the same hardness profile as reported by Hall [198]. When the temperature of the metal increases, the grain growth occurs, and it softens the material decreasing hardness. But for higher welding times, there is an extraneous amount of cold work hardening at the surface region of crest zone. Thus, there is less difference observed between the surface and interface zone for welding times.

Hardness distribution also reveals the effective plastic deformation of the material at the weld zone and due to it, dislocation density plays a vital role than the grain size refinement. It is also observed that there is little change in the microhardness of AA1100

when compared to SS304. The possible reason behind it is the soft annealing of AA1100 sheet at a higher temperature, and therefore, the welding temperature may not be adequate to modify the original recrystallized grain size [154].

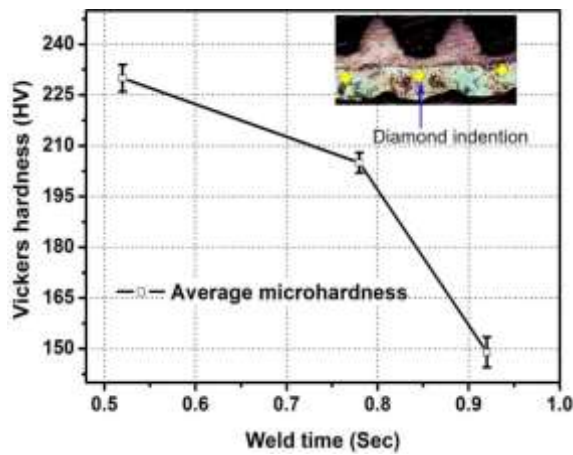


Fig. 7.11 Average microhardness of peaks beneath sonotrode tip for different weld times

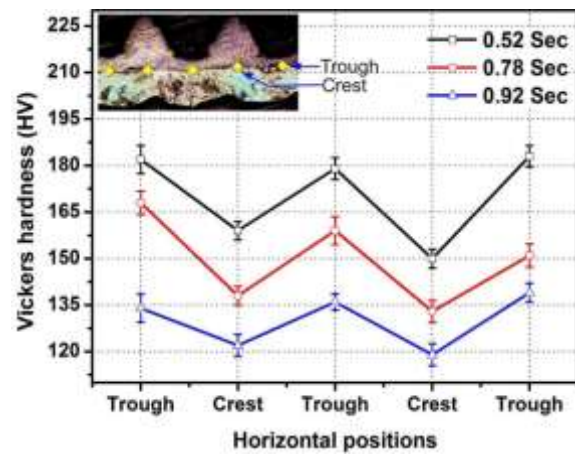


Fig. 7.12 Hardness distribution along the horizontal direction for 0.7Al-0.2SS weld samples

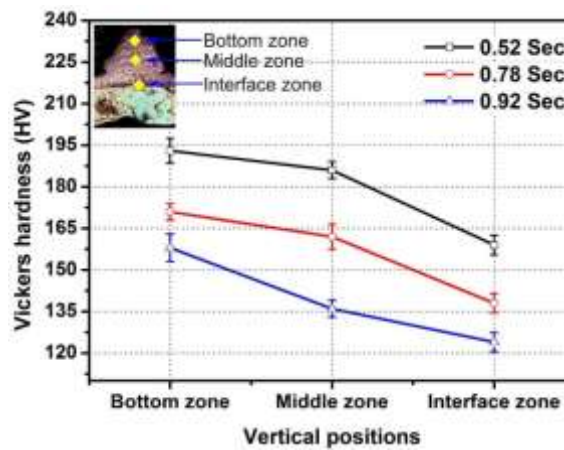


Fig. 7.13 Hardness distribution along the vertical direction for 0.7Al-0.2SS weld samples

#### 7.4.2.2 Fractographic analysis of weld surface

The fractographic analysis has been done on the good weld sample where the tensile shear and T-peel failure loads are maximum, and this joint is produced under the welding pressure of 0.32 MPa, weld time of 0.72 sec and vibration amplitude of 68  $\mu\text{m}$ . Fig. 7.15 (a) and (b) depicts the overall fractured surfaces of Al side and SS side respectively. From Fig. 7.15 (a), it is noticed that Al is more plastically deformed than SS. Meantime, the higher magnification images of Al and SS i.e. Fig. 7.15 (c) and Fig. 7.15 (d) shows the weld spots in Al fractured surface is having more denser micro bonds than the SS fractured surface. It can be clearly observed from higher magnification image presented in Fig. 7.15 (e)-(h). in these figures, Al side fracture surface contains more dimple (D) and fine dimple (FD) like features than SS fractured surface. The possible reason is that as

the temperature generated in this stage is 410.55 °C (much higher than the recrystallization temperature of Al) thus, this temperature is sufficient enough to increase the flowability of the specimen. The impression marks on the top surface by sonotrode knurls are fully composed of peaks and valleys as seen in Fig. 7.14 It is believed that in the valley region, plastic deformation takes place.

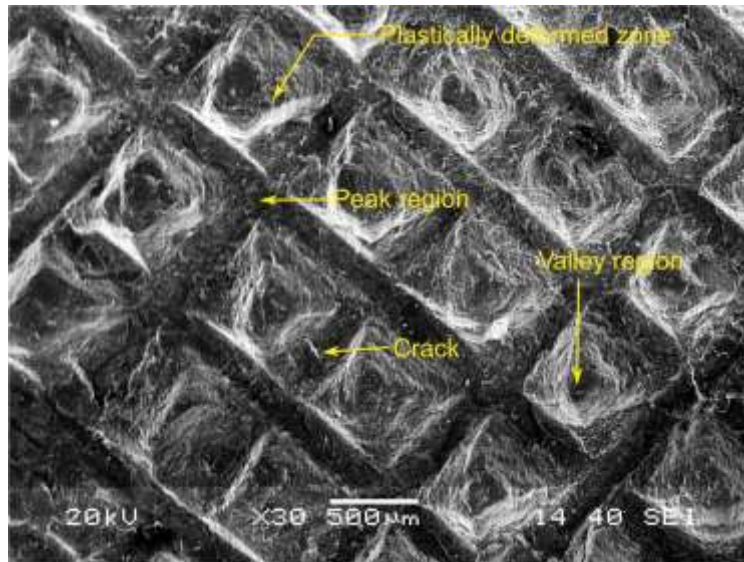


Fig. 7.14 Typical SEM image of top surface of Al sheet under sonotrode tip showing peak and valley regions

#### 7.4.2.3 Scanning electron microscopy (SEM) with EDS investigation of fractured surface

Energy dispersive spectroscopy (EDS) analysis has been used to detect a number of materials present on either side of the fractured surface and in this analysis, only good samples are considered. Fig. 7.16 (a) illustrates a small amount of Fe i.e. 26.37 (wt %) and 7.71 (wt %) of Cr present on the fracture surface of Al side. Likewise, Fig. 7.16 (b) also confirms a 62.63 (wt %) of Al is deposited on the SS surface. These results reveal that, as Al is a softer material than SS, its weld surface is more quickly deformed plastically during ultrasonic welding. So, most of the fracture occurs on the low strength Al side during testing.

The metallographic observations of the weld cross-section were observed to understand the amount of diffusion across the interface. The SEM micrographs were taken with the backscattered electrons (BSE) mode of the sample whose tensile shear strength and T-peel strengths are maximized.

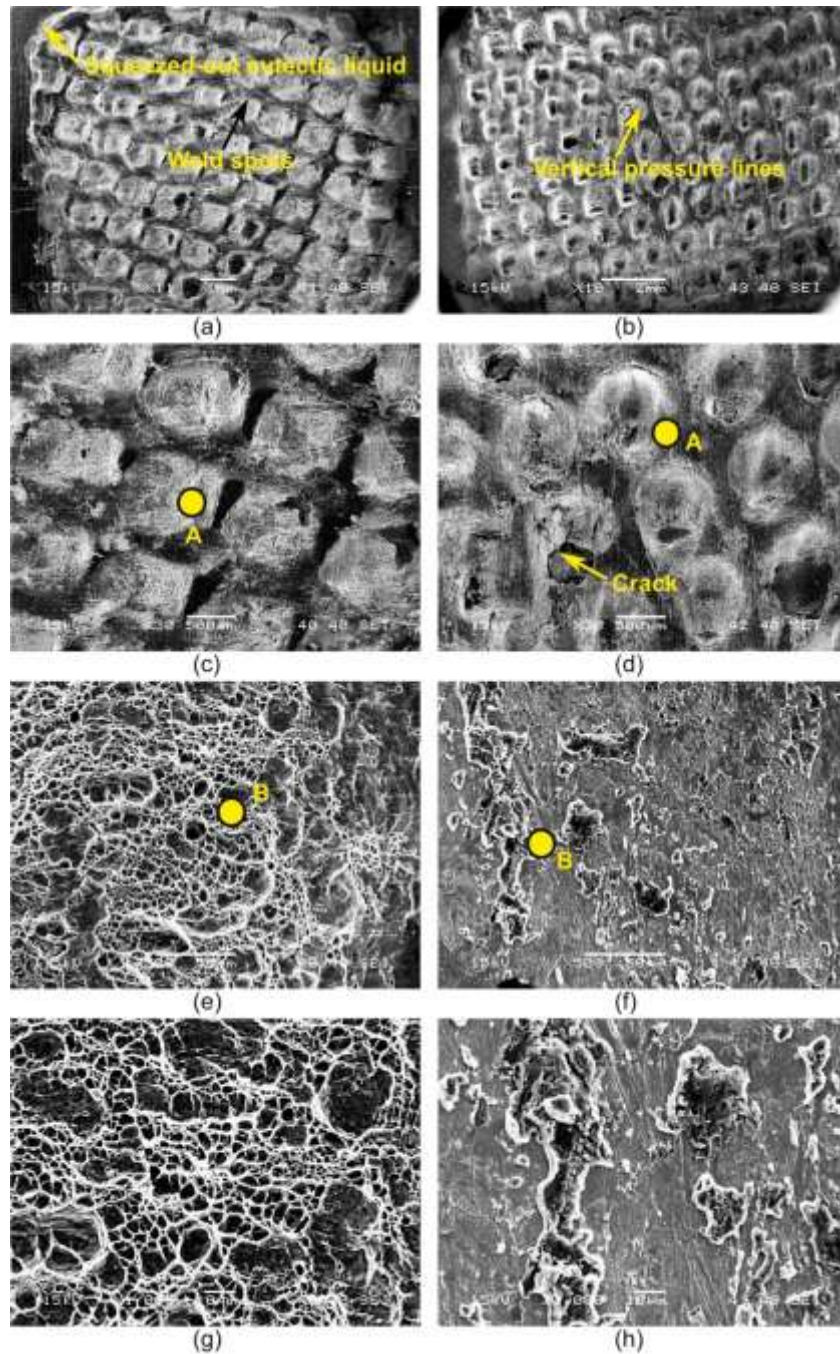


Fig. 7.15 Overall fractured surface SEM images of tensile shear failed samples (a) Al side and (b) SS side; (c) magnified image of (a) showing weld spots; (d) magnified image of (b) indicating squeezed-out eutectic liquid feature; (e) and (f) magnified images of spot A denoted in (c) and (d); (g) and (h) higher magnification images of spot B indicated in (e) and (f)

Fig. 7.17 shows the SEM image and the result of SEM-EDS mapping of the weld cross-sectional area. A thin layer of IMCs is clearly visible and continuously distributed along the joint interface between aluminium and steel (Fig. 7.17 (a)). The thickness of this diffusion interlayer is about 1  $\mu\text{m}$ . EDS analysis also distinguishes the IMC phases by line scan analysis (Fig. 7.17 (b)). The chemical composition (wt %) detected by EDS in this layer is 64.84Al-30.39Fe and 4.77Cr. This means, the primary constituents of the IMCs are Fe and Al and its composition may be  $\text{FeAl}_3$  and  $\text{Fe}_2\text{Al}_5$ . At higher welding time, the

mechanical strengths decrease because, on maximum occasions, the nugget pullout type fracture occurred at the aluminum side due to the soundness of the bond and comparably softer material than steel. In some cases, the fracture also happened at the interface due to its brittleness by the formation of FeAl phase.

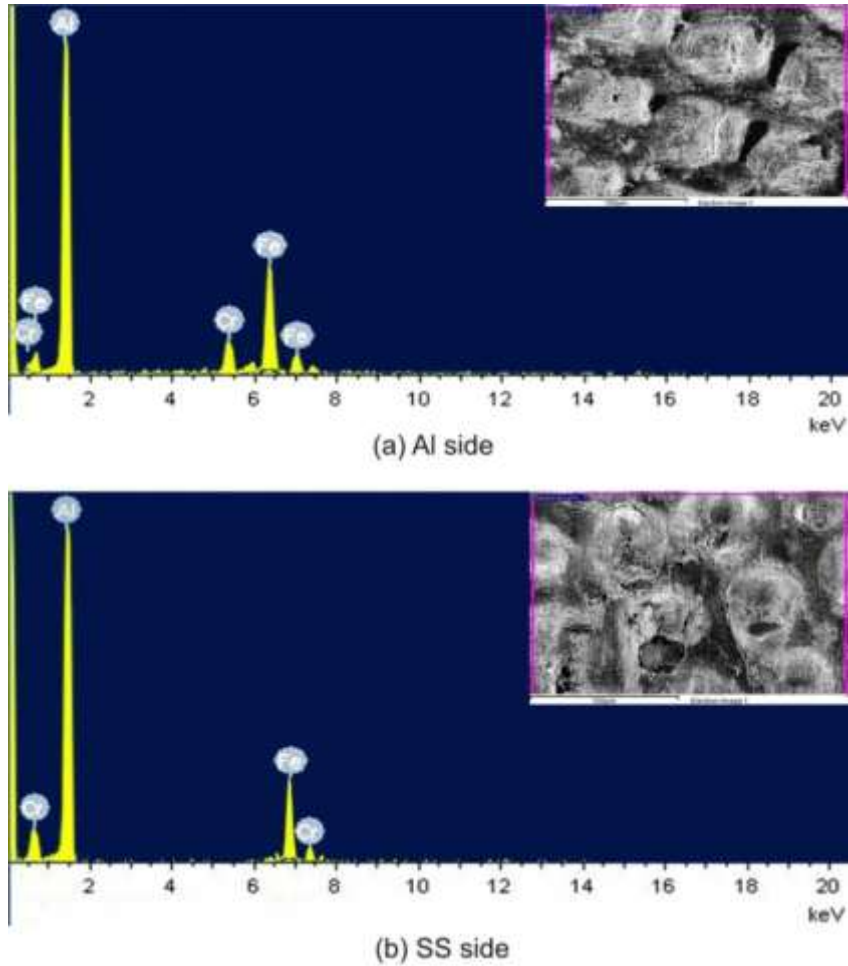


Fig. 7.16 EDS analysis of fractured surfaces of good weld sample

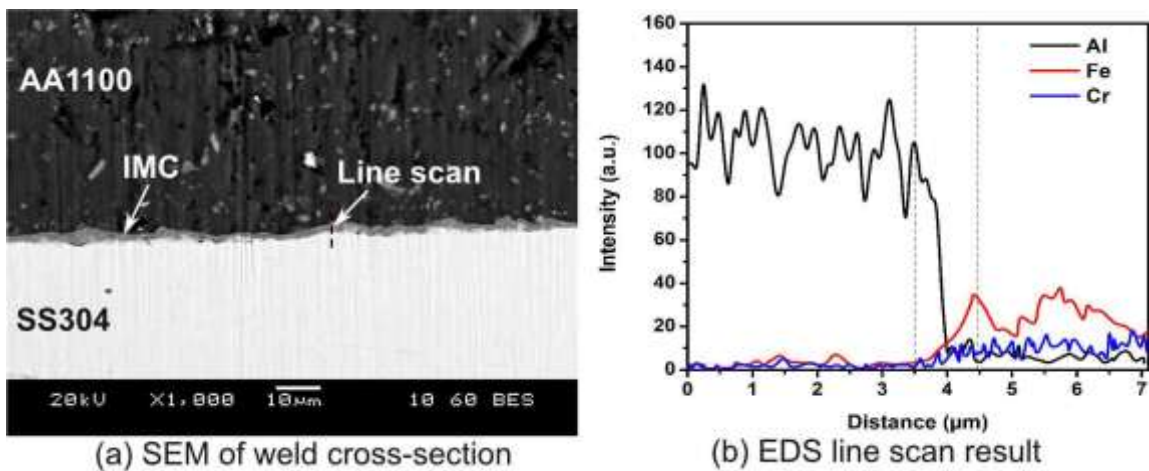


Fig. 7.17 (a) High magnification SEM image and (b) EDS line analysis of weld interface for good weld joint

Agudo et al. [199] described the failure pattern in the welds by the formation of this phase, and this phase exhibits lower toughness value as compared to Fe-rich intermetallic compounds. The growth of the reaction layer is a favourable factor for the ultrasonic welding, and it can be achieved in two ways. Firstly, an increment of temperature brought about by Joule heat and plastic deformation of the weld surface and secondly, an increase in the concentrations of lattice defects like dislocations, vacancies and grain boundaries.

#### 7.4.2.4 X-ray diffraction (XRD) analysis of fractured surface

The purpose of the XRD analysis is to confirm the IMCs formed at the weld interface. Thus, the XRD analysis is carried out on the fractured surfaces of Al and SS, which are previously described as the good weld samples. Fig. 7.18 (a) and (b) depicts the peak intensities of various compounds with respect to diffraction angle  $2\theta$ . The intermetallic compounds (IMCs) observed in the weld interface are  $\text{FeAl}_3$  and  $\text{Fe}_2\text{Al}_5$ . The other compounds observed are the Al on SS fracture surface. As reported by previous literature,  $\text{FeAl}_3$  brittle IMC forms faster than  $\text{Fe}_2\text{Al}_5$  because it has the largest negative free Gibbs energy and kinetically active [188,200,201]. During the experiment, when the metal to metal contact happens, then the first phase i.e.  $\text{FeAl}_3$  is formed due to most negative heat formation at the lowest eutectic point in a binary system [202]. In the next stage,  $\text{FeAl}_3$  react with Fe and forms  $\text{Fe}_2\text{Al}_5$  phase which are closest to the lowest eutectic composition.

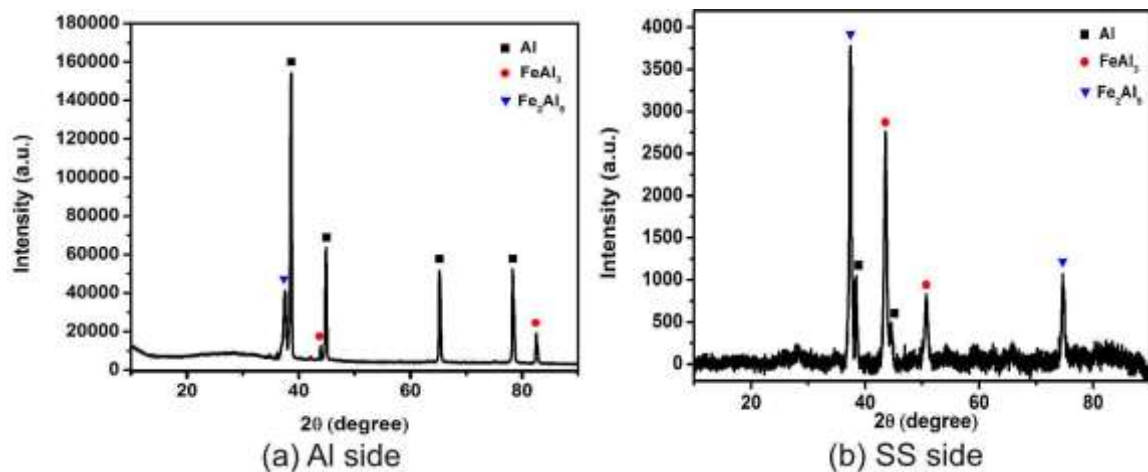


Fig. 7.18 XRD results showing the presence various elements on (a) Al fractured surface, (b) SS fractured surface

#### 7.4.3 Prediction of responses for 0.7Al-0.2SS weld coupons

To model the real world problems accurately, techniques like regression analysis, artificial neural network (ANN) and adaptive neuro-fuzzy inference system (ANFIS) are typically

used. The regression analysis is inefficient to solve complicated problems while soft computing methods like ANN and ANFIS are quite useful to address them. The objective of the current research is to urge predictive models between multiple inputs and a single output. A comparative study based on regression, ANN, and ANFIS approaches are also discussed and described in the forthcoming sections.

**7.4.3.1 Prediction of responses by regression analysis**

The coefficient of determination ( $R^2$ ) and adjusted  $R^2$ -statistic ( $R^2_{adj}$ ) for TS and TP are determined and compared in Table 7.4 for the various regression models. From this comparison, it is observed that second order polynomial regression model is best suited for the current problem, where  $R^2=92.85\%$  means, this model can be able to explain the response up to 92.85%. However,  $R^2_{adj}=91.98\%$  represents the number of predictors those can express the significance of the relationship between the input variables and responses.

Table 7.4  $R^2$  and  $R^2_{adj}$  values for various regression models of TS

Degree of model	$R^2$ (%)	$R^2_{adj}$ (%)
Linear	23.58	20.71
Linear+interaction	25.12	19.29
Quadratic	92.85	91.98

Table 7.5 summarizes the ANOVA for tensile shear failure load (TS). The factors having P-values more than 0.05 are treated as the insignificant terms and represented in “\*” symbol. Therefore, these insignificant terms are eliminated from the table by the backward stepwise model fitting process.

Table 7.6 depicts the ANOVA table with the terms after elimination. Therefore, the  $R^2$  and  $R^2_{adj}$  values are 92.50% and 91.92% respectively. Thus these two values obtained here are below than the values obtained in the full quadratic model (i.e. 92.85% and 91.98%) unveiling the significance of relationship between the responses and the input variables after elimination of terms like  $A \times WP$ ,  $A \times WT$  and  $A^2$ . Eq. (7.1) depicts the TS model in the un-coded unit.

$$\begin{aligned}
 TS = & -6804.76 + 2.30 \times A + 25335.12 \times WP + 8111.23 \times WT - 2066.34 \times WP \times WT - 35700.12 \\
 & \times WP^2 - 5040.23 \times WT^2
 \end{aligned}
 \tag{7.1}$$

Later on, these parameters are removed from the table through the backward elimination process. The modified table after removal is shown in Table 7.9 which consists of only significant terms and their F and P-values. This table indicates the two interaction terms like  $A \times WP$  and  $A \times WT$  with one square term  $A^2$  are insignificant.

Meanwhile,  $R^2$  and  $R_{adj}^2$  values found in this table are 89.85 % and 89.06 % respectively. These values are less than that of the values obtained from the full quadratic model. Eq. (7.2) represents the TP model in the un-coded unit.

$$TP = -2211.87 + 1.21 \times A + 9749.11 \times WP + 2012.02 \times WT - 791.26 \times WP \times WT - 13788.45 \times WP^2 - 1249.69 \times WT^2 \quad (7.2)$$

Table 7.5 ANOVA table for TS (before elimination of insignificant terms)

Source	Sum of Squares	DF	Mean Square	F-Value	p-value
Model	1.10E+06	9	1.22E+05	106.83	< 0.0001
A-Amplitude	372.42	1	372.42	0.33	0.5698
B-Weld pressure	2.91E+05	1	2.91E+05	254.29	< 0.0001
C-Weld time	3.38E+05	1	3.38E+05	296.01	< 0.0001
AB	602.21	1	602.21	0.53	0.4702*
AC	3535.46	1	3535.46	3.09	0.0827*
BC	14183.72	1	14183.72	12.41	0.0007
A <sup>2</sup>	4.4	1	4.4	3.85E-03	0.9507*
B <sup>2</sup>	3.08E+05	1	3.08E+05	269.78	< 0.0001
C <sup>2</sup>	4.93E+05	1	4.93E+05	431.54	< 0.0001
Residual Error	84574.65	74	1142.9		
Total Error	1.18E+06	83			
R <sup>2</sup> =92.85 %, R <sub>adj</sub> <sup>2</sup> = 91.98 %					

Table 7.6 ANOVA table for TS (after elimination of insignificant terms)

Source	Sum of Squares	DF	Mean Square	F-Value	p-value
Model	1.10E+06	6	1.83E+05	158.36	< 0.0001
A-Amplitude	26727.52	1	26727.52	23.2	< 0.0001
B-Weld pressure	3.44E+05	1	3.44E+05	298.53	< 0.0001
C-Weld time	4.79E+05	1	4.79E+05	416.04	< 0.0001
BC	14183.72	1	14183.72	12.31	0.0008
B <sup>2</sup>	3.08E+05	1	3.08E+05	267.61	< 0.0001
C <sup>2</sup>	4.93E+05	1	4.93E+05	428.07	< 0.0001
Residual Error	88716.72	77	1152.17		
Total Error	1.18E+06	83			
R <sup>2</sup> =92.50 %, R <sub>adj</sub> <sup>2</sup> = 91.92 %					

Fig. 7.19 (a) reveals the normal probability plot for TS to check the deviation of data from normality. From this plot, it can be noticed that all the residuals are situated near to the straight line except two data points. These encircled outliers exhibit significant deviation from the mean line because of the presence of measurement error in the testing



results. Residual versus fitted values plot in Fig. 7.19 (b) represents the relatively constant variance, and non-linear relationship also exists as no outlier data exist. In addition, the residual versus run order illustrates that there is no unusual type of structure present in the data and are scattered randomly around zero (Fig. 7.19 (c)). Histogram plot in Fig. 7.19 (d) explores the symmetry of residuals on both the sides of zero mean line. This plot is in the form of Gaussian distribution.

Likewise, for T-peel failure load (TP),  $R^2$  and  $R^2_{adj}$  are reviewed and compared in Table 7.7 for choosing the degree of the regression model. It can be clearly noticed that the quadratic model has the highest  $R^2$  and  $R^2_{adj}$  value of 90.27 % and 89.08 % among all the models. Thus, this model is selected for further analysis as described before. Table 8.8 represents the ANOVA table for T-peel failure load with all terms. The terms whose P-values greater than 0.05 are treated as insignificant terms and are marked with “\*”.

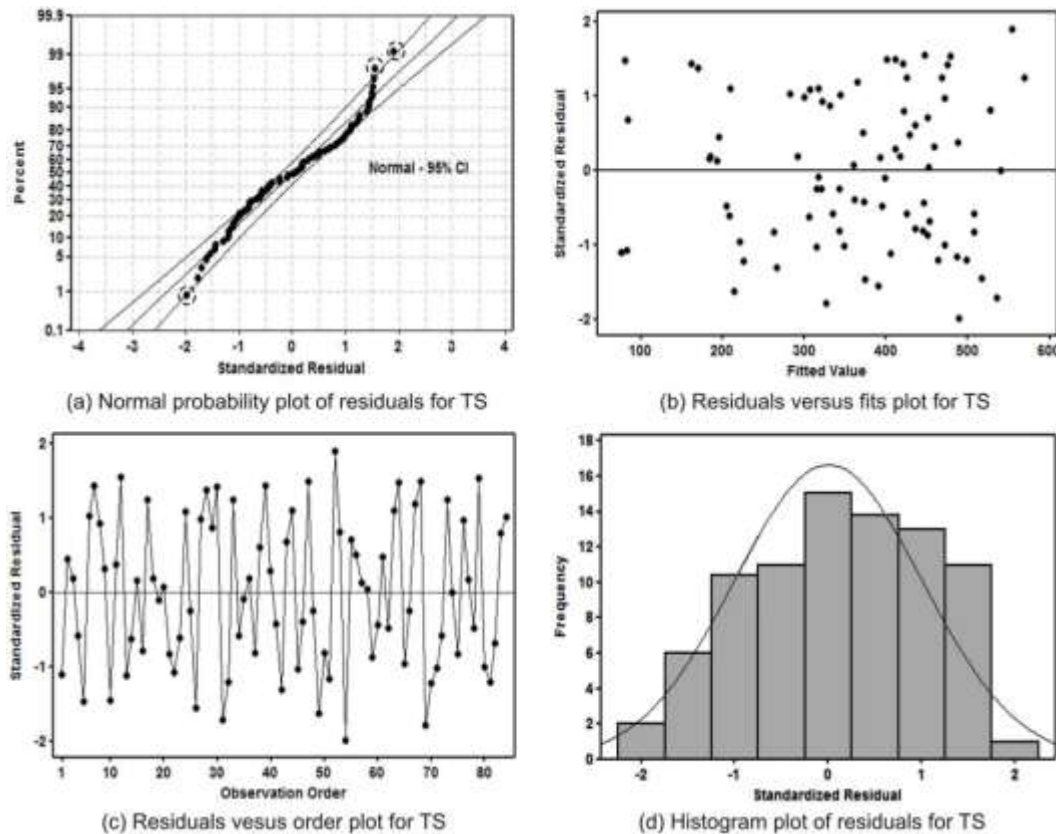


Fig. 7.19 Various residual plots for TS

Table 7.7  $R^2$  and  $R^2_{adj}$  values for various regression models of TP

Degree of model	$R^2$ (%)	$R^2_{adj}$ (%)
Linear	25.57	22.78
Linear+interaction	27.69	22.05
Quadratic	90.27	89.08

Table 7.8 ANOVA table for TP (before elimination of insignificant terms)

Source	Sum of Squares	DF	Mean Square	F-Value	p-value
Model	1.10E+05	9	12233.21	76.27	< 0.0001
A-Amplitude	5.35	1	5.35	0.033	0.8556
B-Weld pressure	45051.22	1	45051.22	280.87	< 0.0001
C-Weld time	19833.73	1	19833.73	123.65	< 0.0001
AB	16.14	1	16.14	0.1	0.752*
AC	485.25	1	485.25	3.03	0.0861*
BC	2079.84	1	2079.84	12.97	0.0006
A <sup>2</sup>	12.14	1	12.14	0.076	0.784*
B <sup>2</sup>	45994.21	1	45994.21	286.75	< 0.0001
C <sup>2</sup>	30320.37	1	30320.37	189.03	< 0.0001
Residual Error	11869.33	74	160.4		
Total Error	1.22E+05	83			
R <sup>2</sup> =90.27 %, R <sub>adj</sub> <sup>2</sup> = 89.08 %					

Table 7.9 ANOVA table for TP (after elimination of insignificant terms)

Source	Sum of Squares	DF	Mean Square	F-Value	p-value
Model	1.10E+05	6	18264.23	113.57	< 0.0001
A-Amplitude	7425.01	1	7425.01	46.17	< 0.0001
B-Weld pressure	50931.79	1	50931.79	316.71	< 0.0001
C-Weld time	29494.19	1	29494.19	183.4	< 0.0001
BC	2079.84	1	2079.84	12.93	0.0006
B <sup>2</sup>	45994.21	1	45994.21	286	< 0.0001
C <sup>2</sup>	30320.37	1	30320.37	188.54	< 0.0001
Residual Error	12382.86	77	160.82		
Total Error	1.22E+05	83			
R <sup>2</sup> =89.85 %, R <sub>adj</sub> <sup>2</sup> = 89.06 %					

The residual plot of TP is presented in Fig. 7.20. From these graphs, one can confirm about the model describing the adequacy of results. Furthermore, these plots also show similar characteristics as already discussed before.

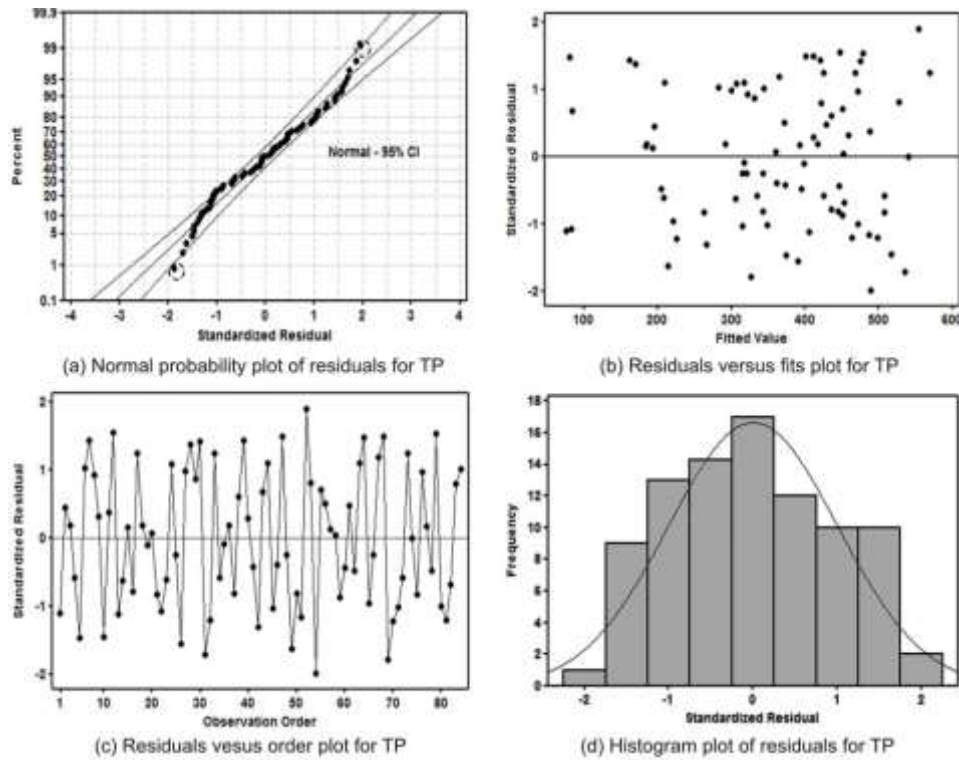


Fig. 7.20 Various residual plots for TP

#### 7.4.3.2 Prediction of responses by ANN approach

A multi-layer feed forward neural network (MLNN) with three input neurons, one hidden layer, and one output neuron is used. Like before, the input layer receives signals from three parameters (i.e. A, WP, and WT) and passes this information to the network for further processing. In this analysis, Levenberg-Marquardt back propagation (LMBP) algorithm, weights, learning rate and momentum factors are selected based on their accuracy of predicting the output. Meantime, 70 % of the total data has been taken for training purpose while 15 % of the total data has been considered for testing and validation purpose. As the efficiency of predicting results by ANN depend on the number of hidden neurons thus, a trial and error method is followed to minimize the mean squared error (MSE). Fig. 7.21 illustrates the graph between MSE and number of hidden neurons. In this case, ten number hidden neurons are sufficient enough to predict TS and TP accurately.

The MSE variation with a number of iterations plots for TS and TP with 10 number of hidden neurons are illustrated in Fig. 7.22. It can be observed from the plot that the MSE converges and attains a stabilized value after 50 epochs for TS and 80 epochs for TP. The best MSE for TS and TP are  $9.7 \times 10^{-4}$  and  $9.3 \times 10^{-4}$ , and these are achieved at 51 and 89 epochs respectively.

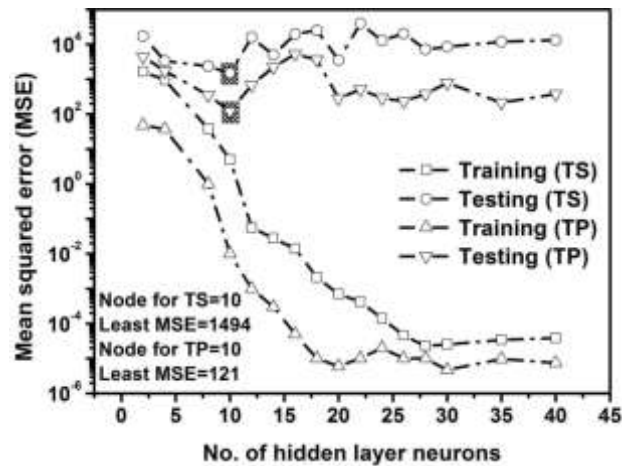


Fig. 7.21 Optimal number of hidden neurons for TS and TP in ANN model

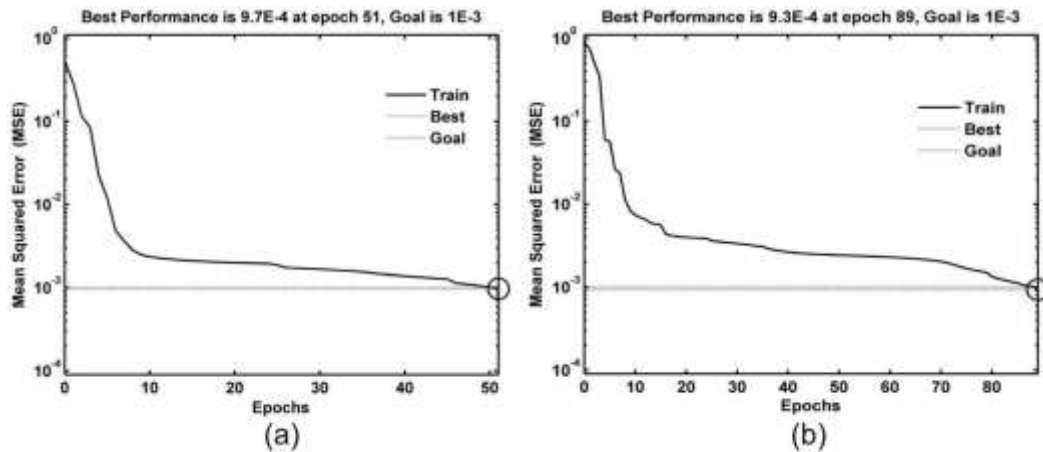


Fig. 7.22 MSE variation with number of iterations for (a) TS and (b) TP

#### 7.4.3.3 Prediction of responses by fuzzy neural network

The major advantage of ANFIS is the expression of parameters in the fuzzy linguistic terms and it is chosen by the designer. However, the accuracy of predicting the result depends on the number of membership functions (MFs). The number of MFs for responses like TS, TP is illustrated in Fig. 7.23. It can infer from the figure that the 4 number of MFs are sufficient to get the least MSE. This Takagi-Sugeno ANFIS modelling was accomplished by MATLAB 2014b using bell type MFs to fuzzify the input parameters.

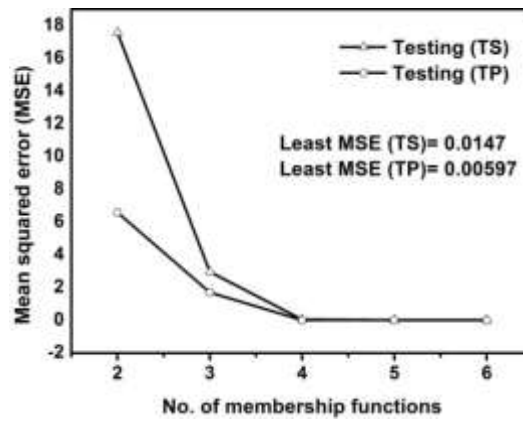


Fig. 7.23 Optimal number of MFs for TS and TP in ANFIS model

#### 7.4.3.4 Overall comparison of prediction techniques results for model validation

For checking the efficiency and exactness of the proposed model, a set of 20 experimental data is chosen randomly from the total number of experiments and these are not also used in training as well as testing purpose. Fig. 7.24 depicts the graph obtained from residuals for these 20 experimental input parameter conditions.

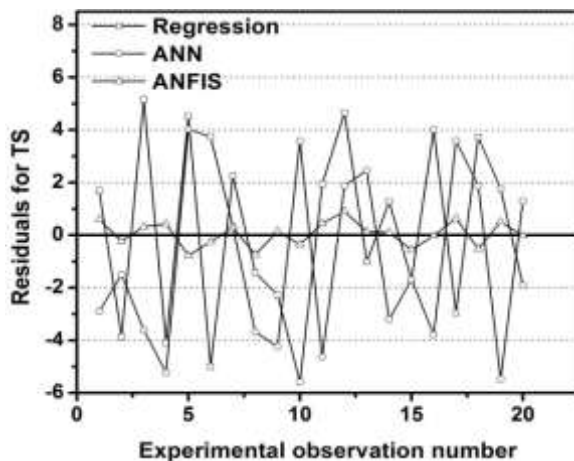


Fig. 7.24 Error profile of validation data on TS for different models

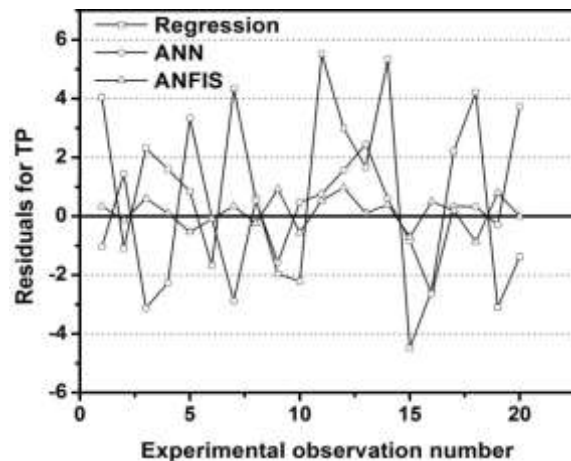


Fig. 7.25 Error profile of validation data on TP for different models

These residuals are calculated by taking the difference between experimental and predicted values of TS for regression, ANN and ANFIS model. It can be observed from the figure that the residuals for regression vary from -5.58 to 5.15 and for ANN, it ranges from -5.47 to 4.03. But for ANFIS, it ranges from -0.77 to 0.89 which is the minimum variation among all models. Thus, it can be outlined that the ANFIS is the best model which can accurately predict the experimental TS with a little deviation. Likewise, the residual values for TP are represented in Fig. 7.25. It can be inferred from the figure that the regression, ANN and ANFIS residual values are varied from -4.48 to 5.51, -3.12 to 3.73 and -0.87 to 0.97 respectively. Again ANFIS model approximate better results than the ANN and regression model results for TP.

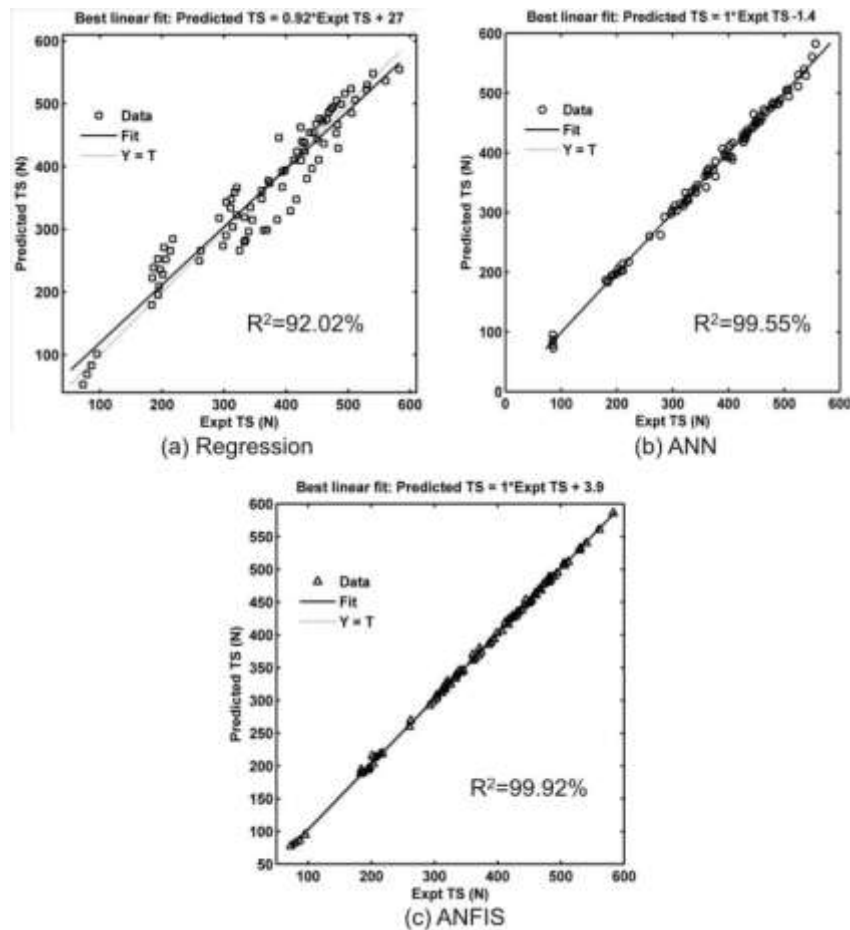


Fig. 7.26 Comparison of various model predicted values with experimental results for TS

To demonstrate the highest level of accuracy among the proposed predictive models, the parity graphs are plotted between the experimental and predicted values for TS, and it is shown in Fig. 7.26. Conclusively, it can be inferred from the figure that both ANN and ANFIS are more accurate than the regression model. The  $R^2$  values for regression, ANN and ANFIS are obtained as 92.02 %, 99.55 % and 99.92 % respectively. Therefore, these models can be ranked as ANFIS, ANN and regression in terms of accuracy for predicting TS.

Likewise, Fig. 7.25 illustrates the parity plot for TP. From this graph, all models show an excellent fit between predicted and experimental values. Among all the models, the predicted values of ANN models are closer to the line than the values obtained in ANFIS and regression modelling. Thus, it can be said that ANN is more accurate than other two techniques with an  $R^2$  value of 99.58 %. Eventually, the ANFIS modelling has given comparatively accurate result than regression modelling with  $R^2$  values of 99.31% and 89.80 % respectively. Hence, in this case, ANN has occupied the first position followed by ANFIS and regression based on the accuracy of predicting the TP.

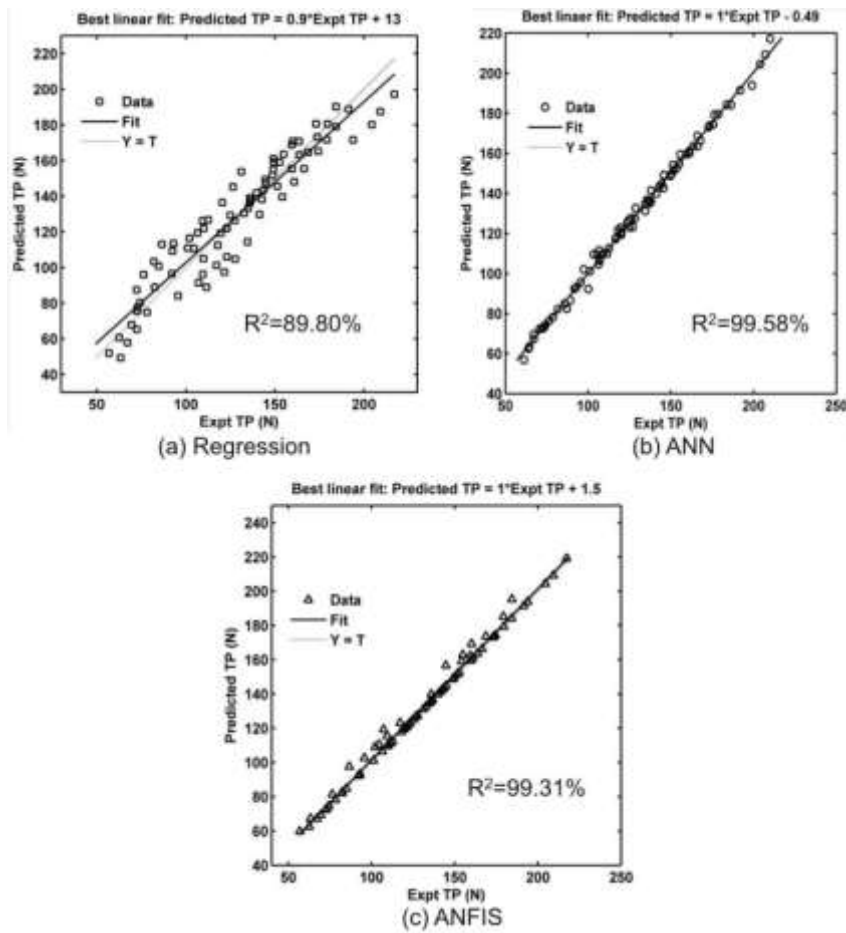


Fig. 7.27 Comparison of various model predicted values with experimental results for TP

Absolute error for the proposed models can be calculated as per the Eq. (5.3). In this case, the data set which is already considered for finding residuals is taken. These values along with experimental and residuals are listed in Table 7.10 and Table 7.11. The absolute error values of TS are obtained as 1.07 %, 1.13 % and 0.14 % for regression, ANN and ANFIS respectively. Likewise, the average absolute errors of TP are varied as 2.32 %, 1.37 % and 0.37 % for regression, ANN and ANFIS respectively.

Table 7.10 Accuracy testing of all proposed models for prediction of TS

Run No	Input parameters			Exp. TS	Residuals for TS			% Absolute error for TS		
	A	WP	WT		Regression	ANN	ANFIS	Regression	ANN	ANFIS
1	47	0.26	0.52	72.83	1.68	-2.89	0.60	2.31	3.97	0.82
2	47	0.26	0.62	197.1	-3.85	-1.50	-0.23	1.95	0.76	0.12
10	47	0.32	0.72	511.6	5.15	-3.60	0.32	1.00	0.70	0.06
18	47	0.38	0.78	417.73	-4.08	-5.23	0.42	0.97	1.25	0.10
19	47	0.38	0.82	398.81	4.52	4.03	-0.77	1.13	1.26	0.19
23	54	0.26	0.62	206.12	-4.99	3.73	-0.25	2.42	1.81	0.12
29	54	0.32	0.52	334.83	2.25	0.32	0.28	0.67	0.09	0.08

32	54	0.32	0.78	494.56	-1.42	-3.68	-0.74	0.28	0.74	0.15
35	54	0.32	0.92	317.13	-2.27	-4.24	0.14	0.71	1.33	0.04
44	60	0.26	0.62	213.39	-5.58	3.57	-0.35	2.61	1.67	0.16
46	60	0.26	0.78	360.73	1.93	-4.63	0.44	0.53	1.56	0.12
47	60	0.26	0.82	406.83	4.64	1.88	0.89	1.14	0.46	0.22
49	60	0.26	0.92	195.56	-1.01	2.45	0.13	0.52	1.25	0.06
51	60	0.32	0.62	483.12	1.27	-3.20	0.10	0.26	0.66	0.02
59	60	0.38	0.72	448.19	-1.70	-1.68	-0.56	0.37	0.37	0.12
65	68	0.26	0.62	217.44	4.00	-3.79	-0.02	1.84	1.74	0.01
68	68	0.26	0.82	416.6	-2.94	3.58	0.62	0.70	0.86	0.15
71	68	0.32	0.52	345.63	3.72	1.87	-0.52	1.07	0.54	0.15
77	68	0.32	0.92	393.49	1.75	-5.47	0.50	0.44	1.39	0.12
80	68	0.38	0.72	468.45	-1.91	1.28	-0.01	0.40	0.27	0.00
Average absolute error (%)								1.07	1.13	0.14

Table 7.11 Accuracy testing of all proposed models for prediction of TP

Run No	Input parameters			Exp. TS	Residuals for TS			% Absolute error for TS		
	A	WP	WT		Regression	ANN	ANFIS	Regression	ANN	ANFIS
1	47	0.26	0.52	63.39	4.04	-1.03	0.34	6.38	1.63	0.54
2	47	0.26	0.62	72.42	-1.08	1.44	-0.13	1.50	1.99	0.18
10	47	0.32	0.72	193.92	2.31	-3.12	0.61	1.19	2.64	0.31
18	47	0.38	0.78	135.06	1.60	-2.26	0.11	1.18	1.67	0.08
19	47	0.38	0.82	122.78	0.84	3.33	-0.53	0.69	2.71	0.43
23	54	0.26	0.62	76.36	-1.66	-0.06	-0.10	2.18	0.07	0.13
29	54	0.32	0.52	142.63	4.34	-2.88	0.34	3.04	2.01	0.24
32	54	0.32	0.78	173.78	0.60	0.53	-0.23	0.34	0.30	0.13
35	54	0.32	0.92	110.02	-1.96	-1.56	0.91	1.78	1.42	0.83
44	60	0.26	0.62	82.12	-2.20	0.47	-0.55	2.68	0.58	0.67
46	60	0.26	0.78	117.92	5.51	0.75	0.53	4.67	0.64	0.45
47	60	0.26	0.82	127.66	2.98	1.56	0.97	2.33	1.22	0.76
49	60	0.26	0.92	69.52	1.66	2.45	0.10	2.39	3.52	0.15
51	60	0.32	0.62	184.33	5.32	0.58	0.40	2.89	0.31	0.21
59	60	0.38	0.72	152.59	-4.48	-0.84	-0.70	2.93	0.55	0.46
65	68	0.26	0.62	86.56	-2.50	-2.64	0.49	2.89	3.05	0.57
68	68	0.26	0.82	134.63	2.22	0.34	0.19	1.65	0.25	0.14
71	68	0.32	0.52	159.53	4.21	0.32	-0.87	2.63	0.20	0.54
77	68	0.32	0.92	135.92	-3.10	-0.28	0.79	2.28	0.20	0.58
80	68	0.38	0.72	159.43	-1.37	3.73	-0.00	0.86	2.34	0.00
Average absolute error (%)								2.32	1.37	0.37



#### 7.4.4 Impact of various anvil designs for 0.7Al-0.2SS weld coupons

In this study, the tensile shear failure load and T-peel failure load of the weld joint have been examined by varying different input parameters as well as anvil knurl patterns. A lot of trial experiments are performed carefully to select the range of process parameters for welding. For this study, a constant weld pressure of 0.32 MPa and vibration amplitude of 68  $\mu\text{m}$  are selected with only one variable factor i.e. weld time. The effects of this parameter on the weld strength may be investigated for different anvils.

##### 7.4.4.1 Effect of weld time on tensile shear and T-peel failure loads

The specifications of anvil knurl patterns are given in Table 3.5. The tensile shear and T-peel failure load curves as a function of weld time for these three anvil patterns are shown in Fig. 7.28. It is observed that these two strengths increase with weld time up to 0.72 sec, after this value, these strengths gradually decrease due to formations of cracks around the weld zone. As the non-cutting width and angle of the knurls are higher in the case of anvil 1, the material flows freely and allows the horn tips to indent further. Thus, anvil 1 produces a greater failure load than anvil 2 and 3. The maximum tensile shear strength of 803.61 N and T-peel strength of 270.87 N are obtained for anvil 1 at 68  $\mu\text{m}$  of vibration amplitude. The more strength values at higher amplitude are attributed to the larger frictional heat that gives rise to more plastic deformation at the interface layer. But at the highest weld time of 0.92 sec, relatively lesser failure loads are obtained due to gradual softening and thinning of the material. Therefore, it can be considered as over weld condition.

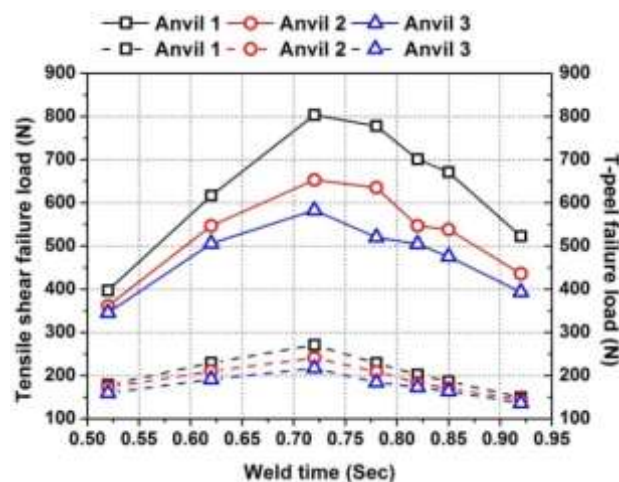


Fig. 7.28 Tensile shear and T-peel failure loads of 0.7Al-0.2SS weld coupons with weld time for various anvil patterns

#### 7.4.4.2 Effect of weld time on weld area

The weld areas of different anvils are presented in Fig. 7.29. It shows that anvil 1 exhibits the highest weld area at the end of the weld time of 0.9 sec because it is believed that the aluminium sheet is adequately plastically deformed. On the other hand, lower non-cutting width and anvil knurl angle only produce friction between the sheets with extrusion of Al sheet. Thus, the growth of weld area is also less in anvil 2 and anvil 3.

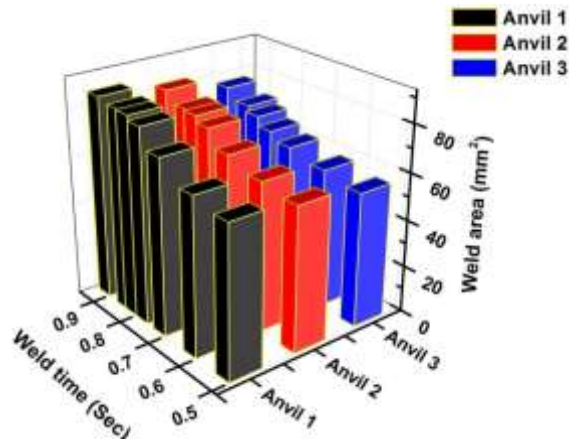


Fig. 7.29 Weld area as a function of weld time of 0.7Al-0.2SS weld coupons for different anvil patterns

#### 7.4.4.3 Effect of weld time on interface temperature

The temperatures obtained in the weld zone by a number of K-type thermocouples at various amplitudes and weld times for respective anvil patterns are represented in Fig. 7.30. A maximum temperature of 487.03 °C was measured when the anvil 1 used 68  $\mu\text{m}$  of vibration amplitude and 0.92 Sec of weld time. This temperature is equal to the 73 % of the melting point of the aluminum sheet. Similarly, a temperature of 466.93 °C and 440.6 °C have been achieved for anvil 2 and anvil 3 respectively at 68  $\mu\text{m}$  amplitude and 0.92 sec of weld time.

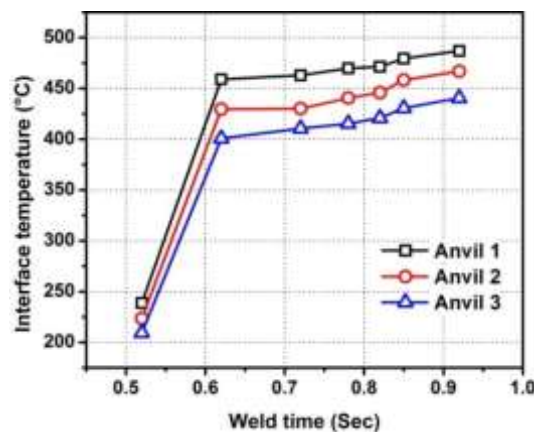


Fig. 7.30 Temperatures measured at weld interface with time of 0.7Al-0.2SS weld coupons for different anvil patterns

### 7.4.5 Impact of different surface conditions for 0.7Al-0.2SS weld coupons

From the earlier observation, it is found that the ultrasonic vibration energy and weld time are the correlated parameters which have major contributions towards the formation of good joints between 0.7Al and 0.2SS sheets. The aim of the present study is to weld Al and SS using ultrasonic welding method and to investigate the effects of various welding parameters and surface conditions on the tensile shear and T-peel strength of the joint. Furthermore, the metallurgical analysis of the welded zone is analysed in detail. The experimental domain is presented in Table 7.12. During the experiment, the weld time is the varying factor to control weld energy which is transferred to the faying surface while other two parameters are kept constant.

Table 7.12 Experimental domain for specimens used in different surface conditions

Parameters	Terms	Domain of experiment
Amplitude ( $\mu\text{m}$ )	A	68
Weld pressure (MPa)	P	0.32
Weld time (Sec)	T	0.52-0.92
Frequency (kHz)	f	20

#### 7.4.5.1 Influence of weld time on tensile shear and T-peel failure loads

Fig. 7.31 shows the relationship between tensile shear and T-peel failure loads with the variation of weld time for four different conditions. These readings have taken in 68  $\mu\text{m}$  of vibration amplitude and weld pressure of 0.32 MPa. For the lubricating condition, when ethanol is added to the faying surface, the two failure loads remain relatively constant up to 0.72 sec of weld time. This is because at the initial stage of welding, complete lubrication was not achieved due to infiltration of ethanol and as it has an alkyl group; it efficiently prevents any direct contact between the faying surfaces. Subsequently, these loads increased sharply up to the weld time of 0.85 Sec, and maximum values of 620.95 N and 230.46 N are obtained for the tensile shear and T-peel failure loads respectively. For the normal condition case, both tensile shear and T-peel failure loads show a maximum load of 582.9 N and 217.12 N respectively at 0.72 Sec. Afterwards, the loads gradually decrease with weld time as described before. In electrolytic polished (EP) condition, maximum tensile shear failure load of 540.87 N and T-peel failure load of 201.49 N are observed. Those maximum values are obtained at the weld time of 0.72 Sec, which is identical to the normal condition. Likewise, maximum loads of 463.39 N and 183.48 N are observed at 0.62 Sec for tensile shear and T-peel conditions in emery paper polished case.

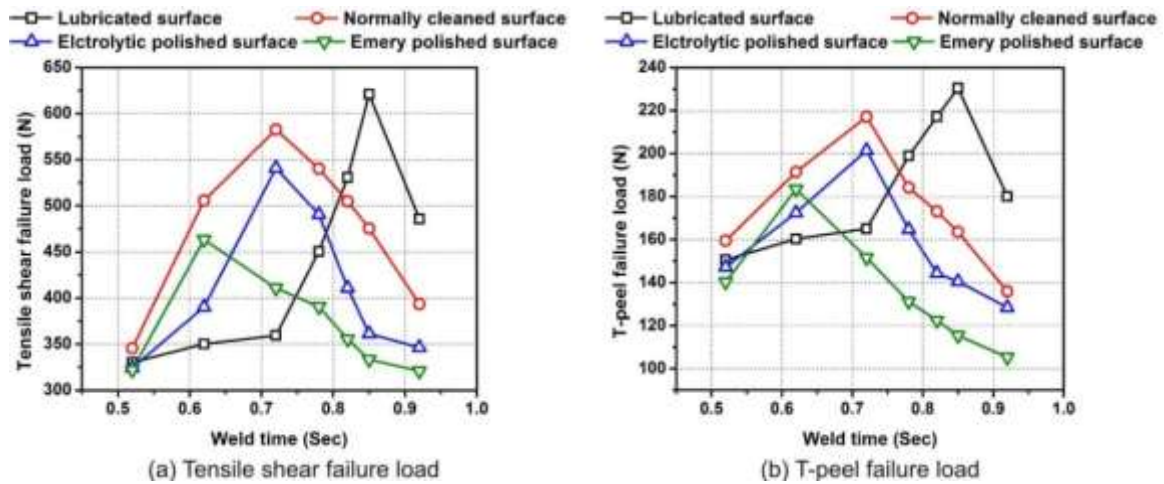


Fig. 7.31 Tensile shear and T-peel failure loads of 0.7Al-0.2SS weld coupons for different surface conditions (a) Tensile shear failure load; (b) T-peel failure load

#### 7.4.5.2 Relationship between welding time and weld interface temperature

Fig. 7.32 shows the interface temperatures for various surface conditions. For the lubricating condition, the maximum temperature of 462.37 °C is obtained, and it creates a suitable environment for plastic flow. In normally cleaned condition, 440.6 °C is observed as the highest temperature at the end of 0.92 Sec. This temperature is below than the temperature produced by ethanol adhesion. As the surface roughness of emery paper is more than that of electrolytically polished one, the initial temperature rise is also very high for the emery paper polished surface. But gradually when the time increased the rise of temperature is not uniform, and finally a maximum temperature of 389.58 °C is obtained for emery condition as comparable to 408.14 °C of EP state. The reason for lowering the heat generation is that the relative motion between the sheets got obstructed due to high surface roughness.

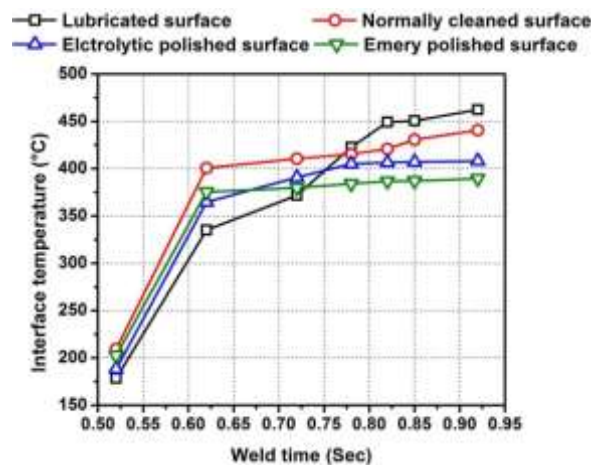


Fig. 7.32 Interface temperatures of welded specimens at various surface conditions

### 7.4.5.3 Measurement of weld interface microhardness

Fig. 7.33 represents the Vickers microhardness distribution of the joint interface in a longitudinal direction. The readings are taken at a clamping pressure of 0.32MPa, vibrational amplitude of 68  $\mu\text{m}$  and weld time of 0.92 sec. It is worth noting that, the average hardness of the joint interface under these four conditions is HV159.5. In all the cases, grain refining took place due to severe plastic deformation, and consequently, the hardness value increased. The hardness of the joint produced by lubricating condition shows the maximum hardness than other conditions. Because in this condition, the temperature generation is maximum and it creates a suitable environment for plastic deformation.

### 7.4.5.4 Analysis of fractured surfaces

The fractured surface analysis for the various surface conditions at 0.32 MPa weld pressure and 68  $\mu\text{m}$  of vibration amplitude has been persuaded. Fig. 7.34 shows the SEM micrographs of the fractured surface for the lubricating condition. Fig. 7.34 (a) reveals a low magnification photograph of the bottom surface of the top specimen in which there are three regions clearly visible, and they are: welded region (WR), base material (BM) and dimple (D). In it, the black circled region is the weld zone and magnified image of it is shown in Fig. 7.34 (b). The darker flat region is the BM where no welding has been taken place. This is to say; a substantial plastic deformation is observed at the WR due to the high temperature of 462.37  $^{\circ}\text{C}$ , and thus, it facilitates the rupture of the oxide film. Due to it, grain refinement has been taken place; some cracks are formed inside the weld spot. Similarly, Fig. 7.34 (c) represents the fractured surface of the bottom specimen and Fig. 7.34 (d) is the magnified image of the black circled region in it. Due to the ethanol adhesion, an island type of irregularities is scattered on SS surface. This weld island (WI), also sometimes referred to nucleation sites.

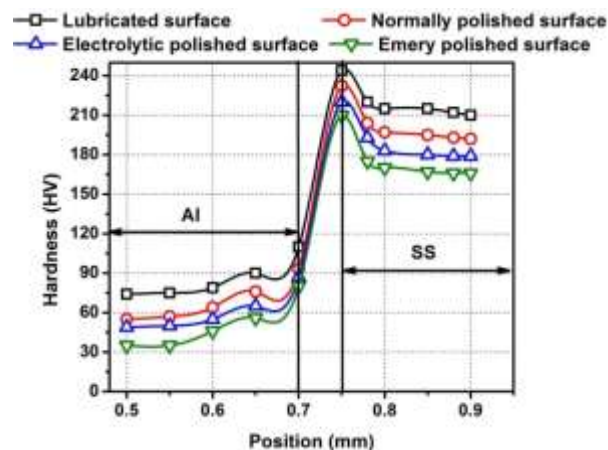


Fig. 7.33 Microhardness distribution across the 0.7Al-0.2SS interface for different surface conditions

The SEM micrograph for normal conditions is represented in Fig. 7.35. As the Al is softer material than SS, thus it is more plastically deformed, and ductile fractures can be seen from Fig. 7.35 (a) and (b). In both of these cases, the WR can be observed clearly with black looked like region as the BM. From Fig. 7.35 (a), the weld spots observed on the bottom surface of the Al sheet appear to be mirror images of the knurl patterns of horn tip those are penetrated into Al material. But in this surface condition, one other type of region observed and that is called scratched region (SR). In this region, only friction between the sheets happened, and no welding has taken place. Fig. 7.35 (b) and (d) are the magnified images of the circled zone. In these photographs, the vertically fractured patterns are found. Due to heavy plastic deformation and elevate temperature, cracks are also formed just around the welding spot with irregularities like dimple (D) and fine dimple (FD) in SS material. Therefore, WI and abraded regions are distinguished clearly.

In EP condition, as the surface roughness is modified by the electrolytic polishing, more scattered regions are observed in Fig. 7.36 (a) and (c). The black spotted region is the EP region where no welding has taken place. Thus, ductile fracture with D and FD are observed and could be seen from Fig. 7.36 (b). In comparison with this figure, less plastically deformed zone was noticed in Fig. 7.36 (d).

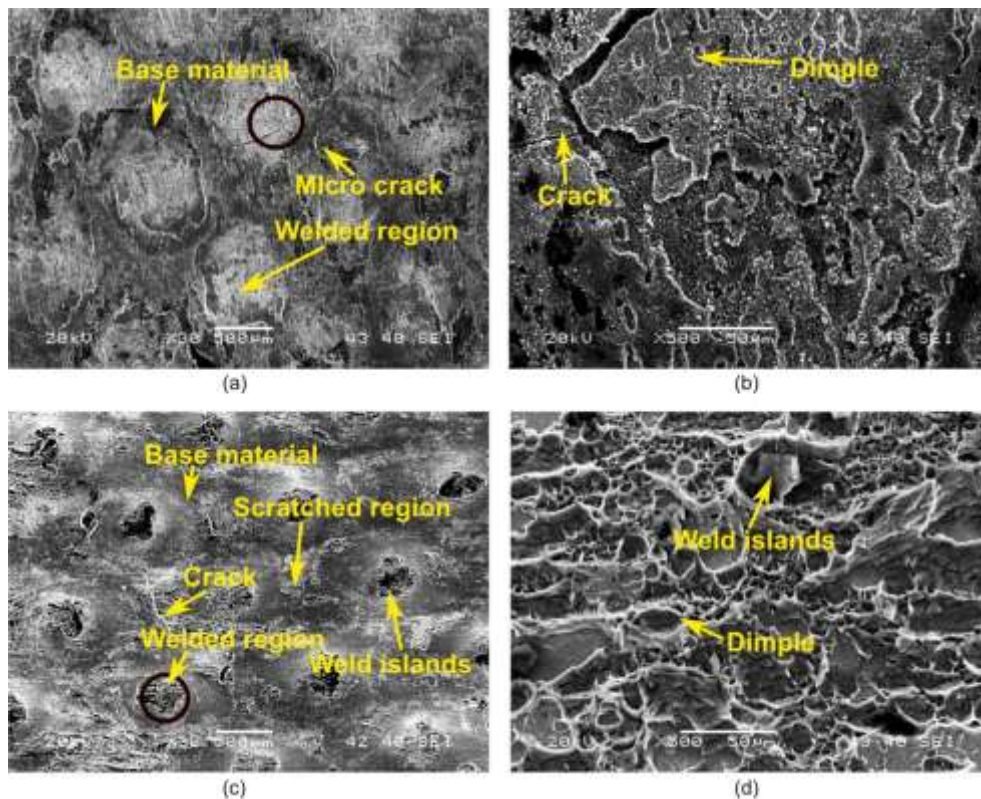


Fig. 7.34 Fractured surfaces of ultrasonic welded specimens in lubricating surface condition (a) Al side surface with 30X zoom; (b) Magnified image of a; (c) SS side surface with 30X zoom; (d) Magnified image of c

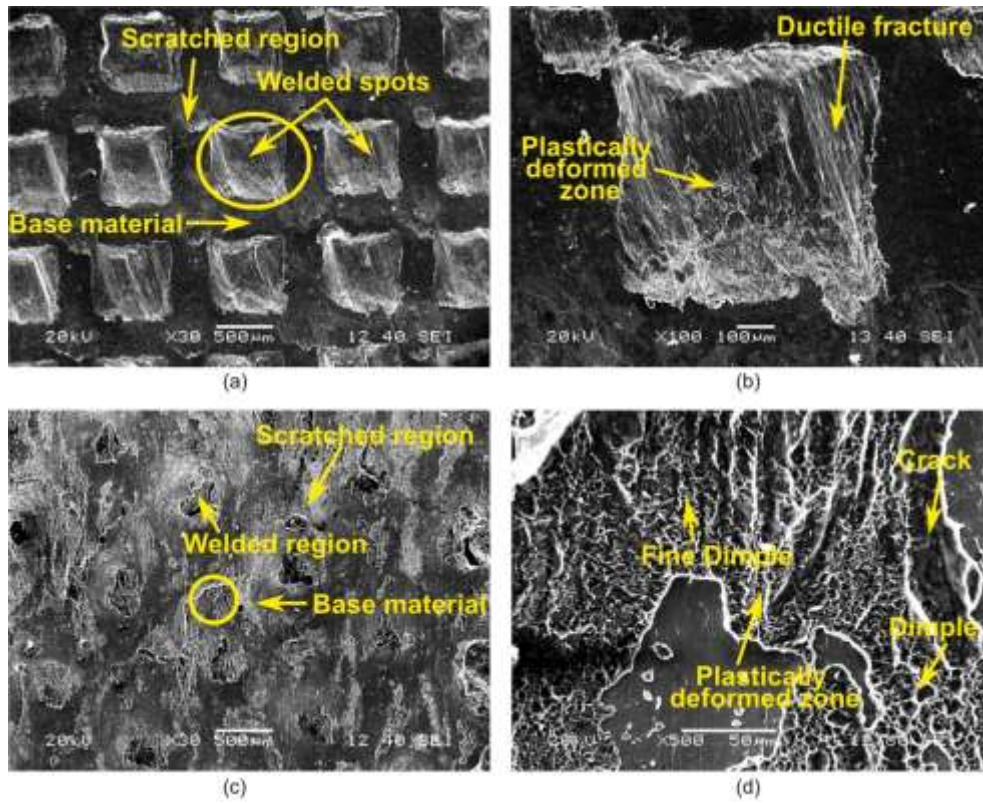


Fig. 7.35 Fractured surfaces of ultrasonic welded specimens in normal surface condition (a) Al side surface with 30X zoom; (b) Magnified image of a; (c) SS side surface with 30X zoom; (d) Magnified image of c

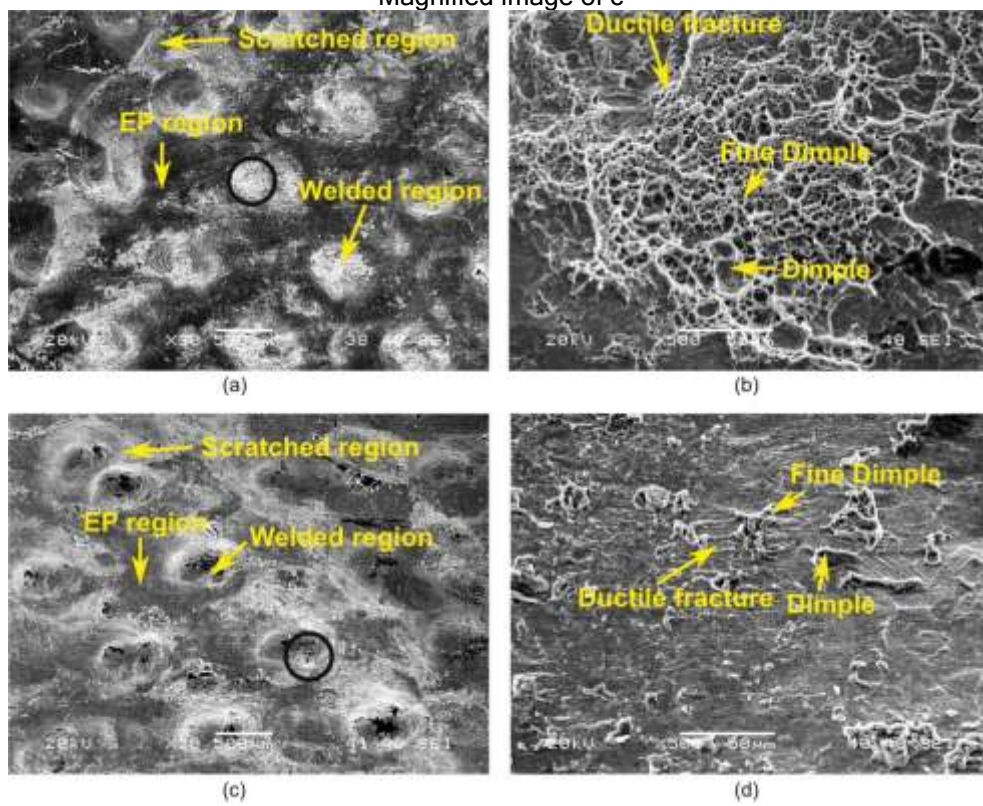


Fig. 7.36 Fractured surfaces of ultrasonic welded specimens in EP surface condition (a) Al side surface with 30X zoom; (b) Magnified image of a; (c) SS side surface with 30X zoom; (d) Magnified image of c

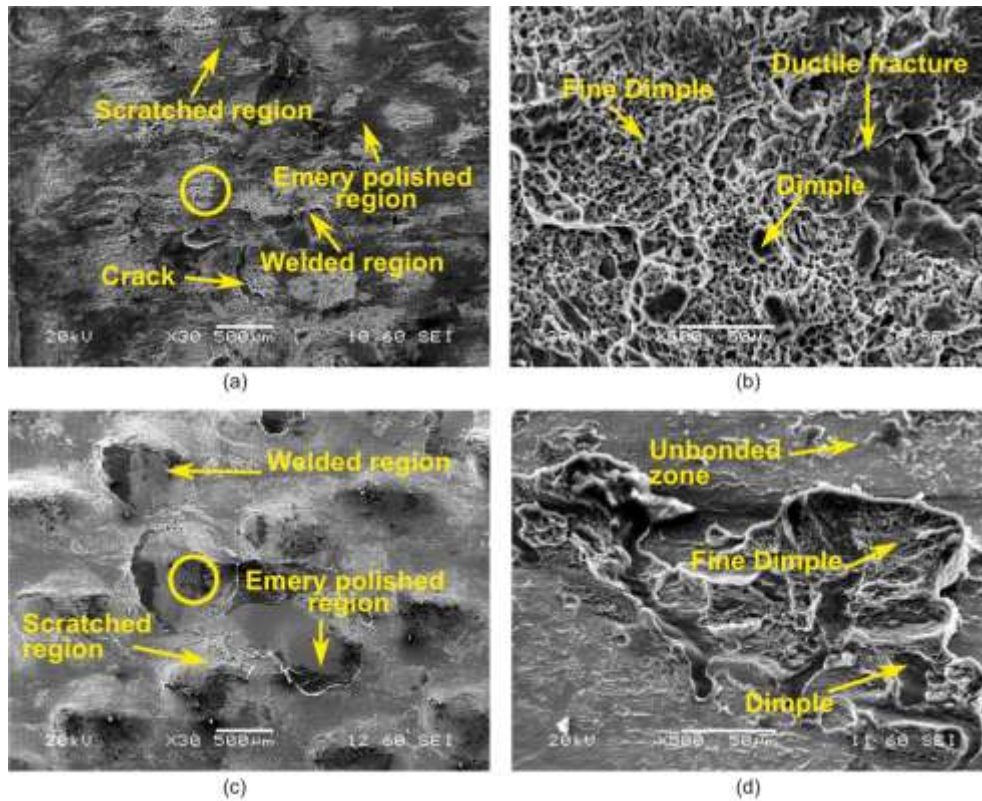


Fig. 7.37 Fractured surfaces of ultrasonic welded specimens in emery surface condition (a) Al side surface with 30X zoom; (b) Magnified image of a; (c) SS side surface with 30X zoom; (d) Magnified image of c

Similarly in emery polished condition, the surface peaks formed by polishing are readily crushed and become flat during the welding. Fig. 7.37 (a) and (c) show the surfaces in which the scratched region becomes more prevalent than the welded area. This is because of high surface roughness, which enhanced friction between the sheets and due to it, the relative motion between the sheets disappeared. It can also be seen from Fig. 7.37 (b) that, due to the softness of the Al material, ductile fractures happen with some D and FD regions. It can be clearly observed from Fig. 7.37 (d). These results, therefore, demonstrate that surface roughness of the material played a vital role in deciding the joint strength in USMW.

#### 7.4.5.5 Shear force determination during USMW for various surface conditions

The shear forces are generally developed due to the ultrasonic vibration of sheets. Thus, to get shear force data, lathe tool dynamometer (Appendix B) is used with a backing plate and anvil. The total set up for shear force measurement is illustrated in Fig. 5.55. Fig. 7.38 depicts the resulting shear force curves for different surface conditions throughout the weld cycle of 0.92 sec. It is observed that the shear force data is somewhat erratic up to 0.45 sec weld time, but towards the end, these data converge to a constant value. Thus, it is believed that, at the end of weld cycle, the weld area is fully developed.





## Chapter 8

# Comparison of Results for Various Weld Coupon Combinations

## 8.1 Introduction

During the ultrasonic welding, the rupture of the oxide layer present on the faying surfaces, final strength of joint and the frictional heat depend on the physical and mechanical properties of the parent materials. Hence, the ability of the materials to make bonds with each other also varies. Thus, there is a need to establish a relationship between weld strength and the properties like material hardness and thermal conductivity. The objective of this study is to make a qualitative comparison of the results those are already obtained for 0.7Al-0.4Cu, 0.7Al-0.4Br and 0.7Al-0.2SS weld samples (Although, thickness of the stainless steel sample is less than other two samples, the comparisons can be seen as a qualitative trends). Meantime, the effects of material hardness, thermal conductivity and amount of extrusion on the tensile shear and T-peel failure loads are also compared.

## 8.2 Comparison of Various Performance Characteristics

In this section, attempts have been made to compare the mechanical and metallurgical properties of the joints where the maximum tensile shear and T-peel failure loads are obtained. Thus, the highest vibrational amplitude with a moderate amount of weld pressure and weld time are taken for each material combination. The details of these process parameters effects on the mechanical strengths along with the temperature evolution and weld area growth are described in the subsequent sections.

### 8.2.1 Results from tensile shear and T-peel failure loads analyses

Fig. 8.1 demonstrates the effects of welding time and weld pressure on the tensile shear and T-peel failure loads for different weld combinations at the maximum amplitude of 68  $\mu\text{m}$ . Meanwhile, the adopted weld pressures for 0.7Al-0.4Cu, 0.7Al-0.4Br and 0.7Al-0.2SS are 0.38 MPa, 0.36 MPa and 0.32 MPa respectively. These weld pressures are selected because, in these pressures, the maximum tensile shear and T-peel failure loads are observed. Furthermore, at the welding times of 0.75 sec, 0.55 sec and 0.72 sec, the 0.7Al-0.4Cu, 0.7Al-0.4Br and 0.7Al-0.2SS weld combinations exhibit highest tensile shear

failure loads of 1512 N, 615 N and 582.9 N respectively. Likewise, at these input parameters combinations, 280.83 N, 260.05N and 217.12 N T-peel failure loads are also observed for the respective weld combinations. It is clearly observed that the 0.7Al-0.4Cu weld coupon shows the maximum tensile shear and T-peel failure loads because the initial hardness of Cu (i.e. 67HV) is quite lower than the brass (100HV) and SS304 (141HV). Thus, the oxide layer which is present on the Cu surface can readily disperse. On the other hand, the hardness values of the brass and SS304 are more thus, to disperse the oxide layer on these surfaces require more time. Meantime, some cracks are also noticed around the weld zone for Al-Br and Al-SS samples because of the severe plastic deformation, and these are spotted by scanning electron microscope (SEM).

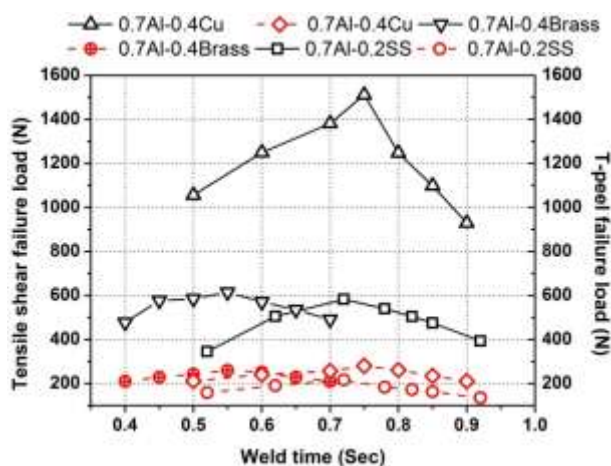


Fig. 8.1 Comparison of tensile shear and T-peel failure loads results for different weld coupons

The microscopic photographs of 0.7Al-0.4Cu, 0.7Al-0.4Br and 0.7Al-0.2SS are illustrated in Fig. 8.2 respectively. These fractographs are taken at 0.9 sec because it is believed that at the end of this weld time, the plastic deformation takes place entirely, and the weld zone is fully covered by microbonds. From these figures, it can be observed that the amount of scratching increases from Al-Cu weld specimens to Al-SS specimens. Due to it, some micro cracks are noticed around the weld zone of the brass and SS304 fractured surface. That is the primary reason for lowering the tensile shear and T-peel strength. Another feature such as the plastic deformation is more severe in the case of 0.7Al-0.4Cu specimen because Cu is softer as comparable to brass and SS304.

### 8.2.2 Results from interface temperature analysis

The temperature measurements in the welded zone have been performed at the maximum amplitude of 68  $\mu\text{m}$  and at the same weld pressure values as described before. Fig. 8.3 depicts the temperature profiles for different weld combinations with respect to weld time. From this figure, one interesting feature is noticed i.e. the maximum

temperature of 440 °C is obtained for 0.7Al-0.2SS samples followed by 410.93 °C for 0.7Al-0.4Br and 350.35 °C for 0.7Al-0.4Cu respectively.

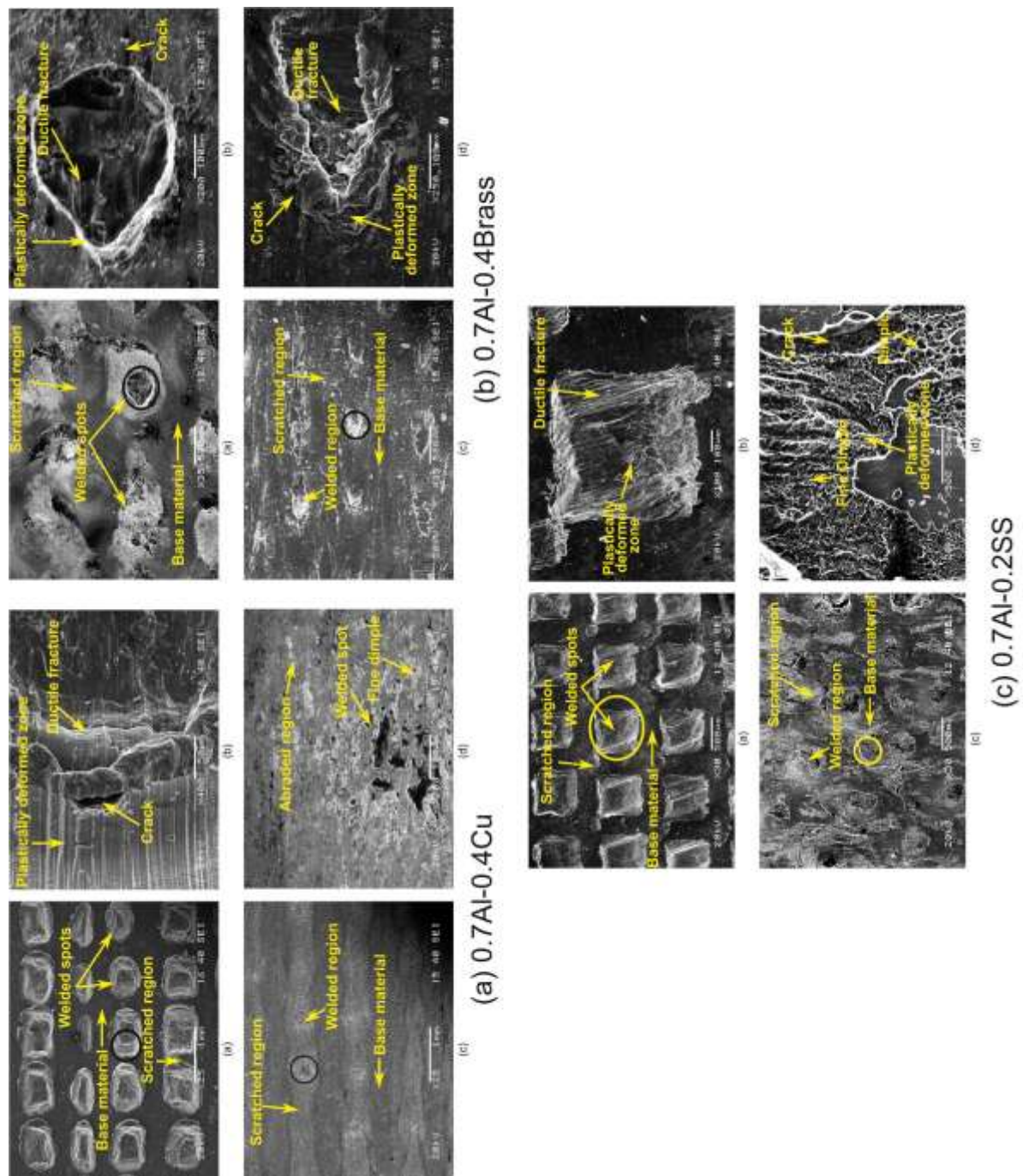


Fig. 8.2 Comparison of microscopic photographs for different weld coupons

This is because of SS304 has a low thermal conductivity (16.2 W/m°C) than the brass (116 W/m°C) and copper (391 W/m°C). Due to this low thermal conductivity nature, it is accumulated at the weld zone only. It is well known that the commercial aluminium starts to soften near 240 °C (i.e. recrystallization temperature of Al) [178] and in the Al-SS combination, as the interface temperature is far above than this recrystallization temperature, there is a substantial loss in strength observed.

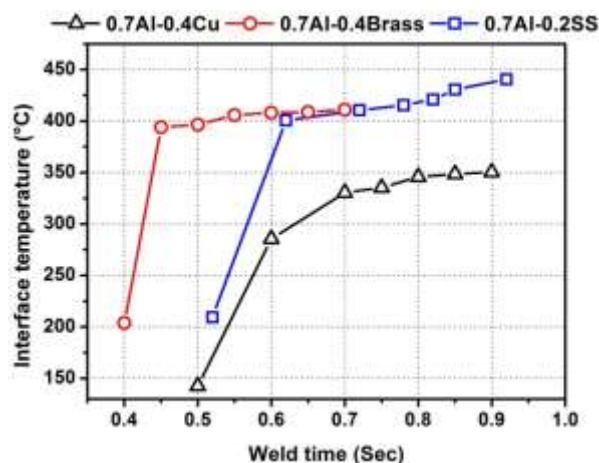


Fig. 8.3 Comparison of interface temperature results for different weld coupons

### 8.2.3 Results from weld area analysis

Fig. 8.4 shows the experimentally measured values of average weld areas obtained at maximum vibration amplitude of  $68 \mu\text{m}$  at the weld pressures as mentioned in the previous section. When the welding time increases, Al-SS weld combinations depicts a maximum increment in weld area of around 28.11 % followed by 26.23 % for Al-Br combination and 25.24 % for Al-Cu combination. This is due to the fact that as the hardness of SS304 is higher than Al thus, Al material is more susceptible to plastic deformation. Furthermore, it is described earlier that the interface temperature obtained for Al-SS is the highest than other two combinations, and it also exceeds the recrystallization temperature of Al. thus, the oxide layer easily ruptures and creates a favourable condition for metal to metal contact.

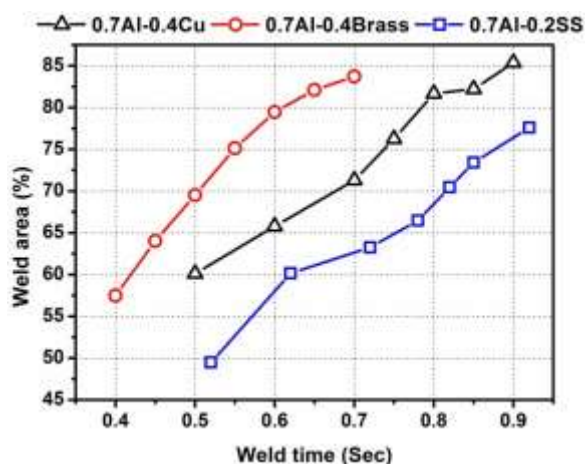


Fig. 8.4 Comparison of weld areas for different weld coupons

### 8.2.4 Results from microhardness analysis

Microhardness measurements across the weld cross-sections of Al-Cu, Al-Br and Al-SS dissimilar metal combinations at different locations are illustrated in Fig. 8.5. These values are taken at the highest vibration amplitude, moderate amount of weld pressure and at the end of weld time (good weld condition). From this figure, an asymmetric type of hardness distribution can be clearly noticed across the joint interface with an average hardness of around 59.48 HV for Al, 103.23 HV for Cu and 155.83 HV for Brass and 202.23 HV for SS. These results signify that no noticeable increase in hardness values is observed for all the materials. Thus, it is believed that no heat affected zone (HAZ) is formed during the welding process. With support for this feature, various researchers are also reported the USMW as the process in which no degradation of bond strength happens due to HAZ while it is more frequent in resistance spot welding (RSW) [202,204]. Usually, the hardness values are supposed to decrease with the increase in temperature because of the increase in grain size at the interface [205,206]. However, in the present study, the hardness values of each metal are increased, and the maximum values are obtained near the interface. Out of the three currently described weld combinations, SS304 shows the highest hardness value and the reasons behind this phenomenon are the formations of a solid solution composed of Cr and the highest ultimate strength of SS304 itself.

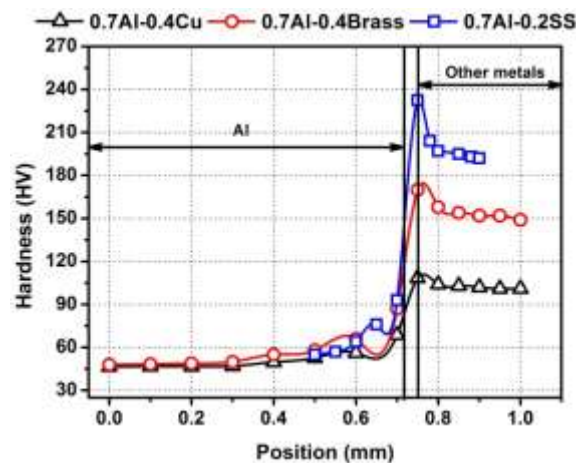


Fig. 8.5 Comparison of microhardness results for different weld coupons

### 8.2.5 Results from energy dispersive X-ray spectroscopy (EDS) analysis

EDS line scan analysis has been performed at the weld interface of 0.7Al-0.4Cu, 0.7Al-0.4Br and 0.7Al-0.2SS samples to verify the interface diffusion as well as different phases formed during the ultrasonic welding process. These readings are taken for good weld samples where the maximum weld tensile shear and T-peel failure loads are obtained,

and these are represented in Fig. 8.6. It can be observed from the figure that the interface diffusion layer for the different weld combinations are not same, and the highest diffusion thickness of around 1.5  $\mu\text{m}$  is noticed for 0.7Al-0.4Cu followed by 1  $\mu\text{m}$  diffusion thickness for 0.7Al-0.4Br and 0.7Al-0.2SS combinations. Usually, due to comparatively, low melting point temperature of Al, it is readily diffused to the Cu and Fe lattice because Al atoms are more energetic during the welding process [207]. In this zone, some intermetallic compounds (IMCs) such as  $\text{Al}_2\text{Cu}$ ,  $\text{AlCu}$  and  $\text{Al}_4\text{Cu}_9$  are formed during the welding of Al-Cu, Al-Br and Al-SS weld coupons. Many studies reported that the IMC, which is formed between Al and SS, causes the fracture around the weld zone [208]. However, the IMCs formed between Al-Cu and Al-Br have no significant effect on the weld strength. Thus, the lowest strength is obtained for Al-SS combination.

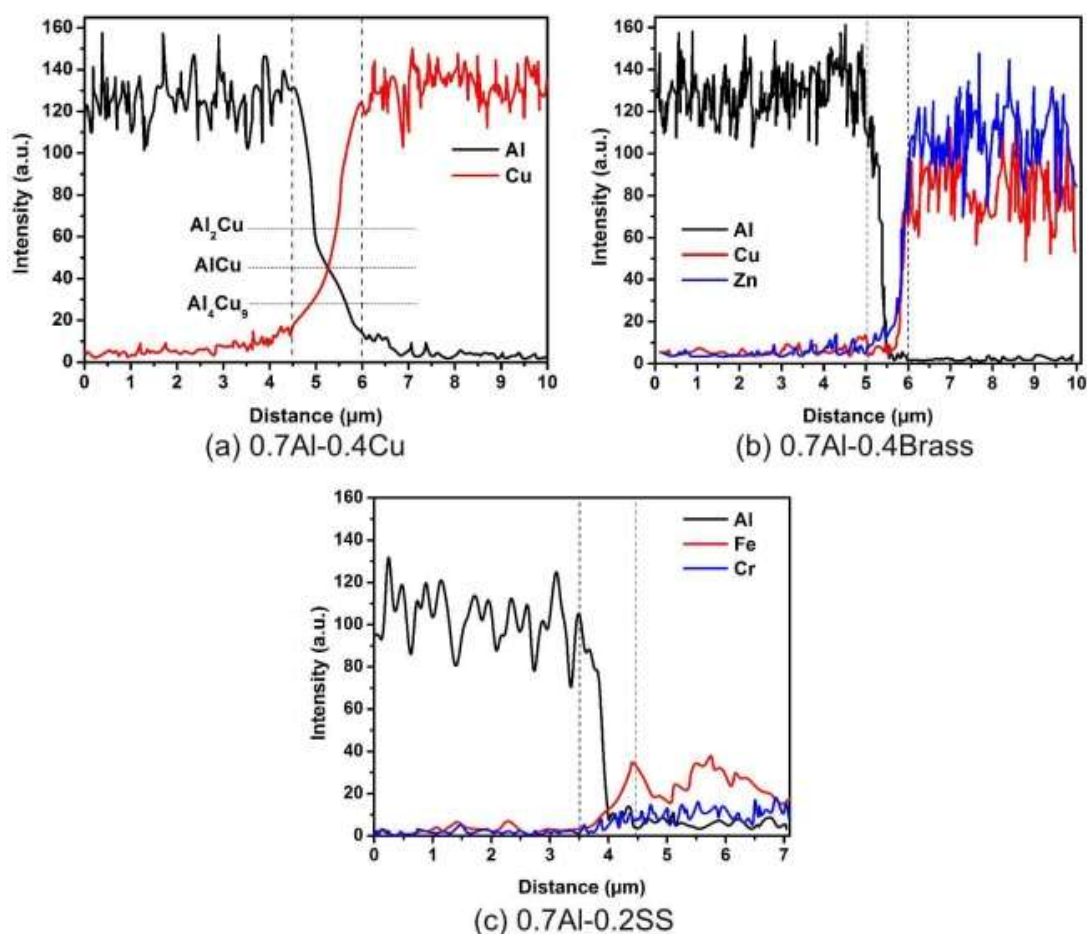


Fig. 8.6 Comparison of EDS results for different weld coupons

### 8.3 Summary

Ultrasonic welding is used successfully to weld aluminium, copper, brass and stainless steel at various input parameter combinations. Meanwhile, a comparison study also has

been done on the various aspects of weld attributes. The following conclusions could be derived from the present study:

- The highest tensile shear and T-peel failure loads of 1512 N and 280.83 N have been obtained for 0.7Al-0.4Cu weld sample which is the highest among 0.7Al-0.4Br and 0.7Al-0.2SS combinations. It is due to the fact that Cu is the softer material as comparable to brass and SS. Thus, it is readily crushed and plastically deformed under the application of high-frequency energy and normal weld pressure.
- From the fractographic study of weld surfaces, it is observed that for Al-Cu weld samples, the weld area is fully covered with microbonds while, in the case of Al-Br and Al-SS weld specimens, a number of scratch marks increase and it leads to the formation of cracks around the weld zone. Thus, it is the primary reason for lowering the tensile shear and T-peel failure loads in Al-Br and Al-SS weld coupons.
- The interface temperature results reveal that the highest temperature of 440 °C is obtained for 0.7Al-0.2SS samples. Thus, a substantial loss in strength is observed due to the thermal softening phenomenon.
- There is a maximum increment of 28.11m % weld area occurred for 0.7Al-0.2SS weld coupons which suggest that Al material is severely plastically deformed in the weld combination than the other two weld coupons.
- 0.7Al-0.2SS sample showed the highest microhardness value as comparable to 0.7Al-0.4Cu and 0.7Al-0.4Br weld coupons due to the formation of a solid solution composed of Cr and the highest ultimate strength of SS304.
- Regardless of fast welding time and solid state nature of the USMW process, the weld interface reveals an IMC diffusion layer of 1.5  $\mu\text{m}$  for 0.7Al-0.4Cu weld coupon. Meantime, for Al-Br and Al-SS weld combinations, 1  $\mu\text{m}$  thick IMC diffusion layer also obtained. Despite forming this low thickness IMC layer with respect to Al-Cu weld coupon, the element such as  $\text{FeAl}_3$  (formed during Al-SS welding) has more adverse effect on the bond strength.





## Chapter 9

# Conclusions

### 9.1 Introduction

Ultrasonic metal welding (USMW) is considered to be one of the novel and innovative techniques which involve the solid state joining process. In this process, the metals are held together by the application of moderate amount of pressure with high-frequency shear vibrations between them. This high-frequency relative motion between the sheets disperses oxides and contaminants present over the surface and thus pure metal to metal contact happens. USMW draws significant attention in the area of joining of dissimilar metals such as plates, sheets, wires, etc. Moreover, this process is also best suited for joining of soft metals such as copper, aluminium, gold, and silver for application ranging from automotive to aerospace industries. One of the current challenges faced by the industries relates to the control of process parameters and to ensure the associated qualities of the joints. Thus, the present work critically examine the mechanical and metallurgical qualities of the dissimilar metal welded joints, proposing design improvements in USMW components along with fine tuning of the process parameters.

### 9.2 Executive Summary

The understandings acquired from the present work describe not only the complex USMW mechanism but also represent the in-depth study of controlling parameters' effects on the responses and associated mechanical and metallurgical joint qualities. The major observations obtained from the entire work have been summarized and presented below:

- The theoretical governing equation to design the horn and booster is explained and by using the derived equations the lengths of both parts are estimated as 130 and 126.8 mm respectively. These results are again verified numerically by using finite element method and the theories behind these numerical analyses have also been successfully demonstrated.
- Using the correct material properties and the theoretical dimensions of both parts, the modal analysis has been performed to find out the natural frequency of the horn and booster, which comes out to be 20004 and 19999 Hz respectively. These frequencies are obtained by gradually reducing the lengths and increasing the radius of curvatures. Hence, the final lengths of horn and the booster are found to be 126.8 and

125.4 mm respectively and in a similar way, the radius of curvatures are also found to be 4.5 and 5.5 mm respectively. While adjusting the length, errors by 2.46 % and 1.10 % are noticed for both parts.

- The frequency response analysis also has been executed to discover the stress distribution in both the parts. The maximum stresses are obtained at the nodal regions of both the parts and they are found to be 196.67 and 576.6 MPa. From this analysis, output vibration amplitudes of 68.86 and 47.35  $\mu\text{m}$  are also obtained for horn and booster respectively. As these components are under repeated elastic cyclic loading of 20000 cycles/sec, cumulative damages of the parts are located in the nodal regions. These are found to be 1.111 and 1.175 for horn and booster respectively, suggesting failures of both parts at the given working frequencies and amplitudes.
- The temperatures developed in the nodal regions for both the components due to the repeated loading are found to be 63.5 °C and 49.8 °C. The possible reason behind this phenomenon is the internal damping coefficient, which is higher in D2 steel horn than titanium booster. To validate these results, the temperatures of 64.85 °C and 50.24 °C are measured experimentally, and errors of 2.08 % and 0.24 % are being reported.
- The friction between the sheets is one of the causes for heat generation and subsequently it leads to the plastic deformation. Along with this thermo-mechanical analysis, one other phenomenon called acoustic softening analysis is also applied for accurate prediction of stress field, plastic deformation and yield stress of the material.
- The material combinations such as Al-Cu, Al-Brass and Al-SS are welded successfully under different process parameter combinations of weld pressure, weld time and vibration amplitude. From the experimental investigation, the maximum values for tensile shear (TS), T-peel (TP) failure loads are obtained as 1512 N and 280.83 N for 0.7Al-0.4Cu, 615.3 N and 260.05 N for 0.7Al-0.4Brass along with 582.9 N and 217.12 N for 0.7Al-0.2SS sheets. All these strengths are noticed at maximum vibration amplitude of 68  $\mu\text{m}$  with a moderate amount of weld pressure and weld time. It can also be observed that the thermal conductivity of the copper is the highest, and its hardness is the lowest among brass and SS. Thus, the Al-Cu combination is more amenable to plastic deformation and produced minimum failure load.
- The microscopic analysis also has been done for all the above-described specimen thickness combinations because; they provide the maximum tensile shear and T-peel failure loads for the weld joint. It is observed that at the starting stage of USMW, the hardness values of Al-Cu, Al-Brass and Al-SS show 57 %, 47.61 % and 56 % higher results than the hardness values of the parent materials and it was due to severe cold working at the interface. Moreover, the EDS line scan results of the good weld joint

also revealed that there are the formations of 1.5  $\mu\text{m}$  thick  $\text{Al}_2\text{Cu}$  IMC layer for Al-Cu, 1  $\mu\text{m}$  thick  $\text{Al}_2\text{Cu}$  and  $\text{Cu}_5\text{Zn}_8$  IMC layer for Al-Brass and 1  $\mu\text{m}$  thick  $\text{FeAl}_3$  and  $\text{Fe}_2\text{Al}_5$  IMC layer for Al-SS. Meanwhile, XRD analysis is also carried out to validate the results; those are already obtained in SEM and EDS analyses.

- Various methods like regression, ANN and ANFIS are used as to develop the models for an accurate prediction after tuning the various parameters. It is seen that ANFIS is more accurate than other two techniques with an  $R^2$  value of 99.79 % for Al-Cu, 99.54 % for Al-Brass. Meanwhile, the ANN modelling gives comparatively accurate result than ANFIS and regression modelling with an  $R^2$  value of 99.54 % for Al-SS.
- The maximum failure loads for each anvil are observed at the end of weld time with a vibration amplitude of 68  $\mu\text{m}$  because it is believed that the most plastic deformation occurred at the end of weld time. Among all the tested anvils, first anvil design shows the highest failure loads of 2148.1 N and 376.88 N for 0.7Al-0.4Cu, 851.4 N and 305.84 N for 0.7Al-0.4Brass along with 803.61 N and 270.87 N for 0.7Al-0.2SS sheets.
- Similarly, TS and TP failure loads decrease as the surface roughness of the material increases. Though in lubricating (with ethanol) condition, initially the mechanical strength take a little bit longer period of time to increase, but after the evaporation of ethanol, the highest strengths of 1550.48 N and 370.46 N for 0.7Al-0.4Cu, 642.37 N and 280.86 N for 0.7Al-0.4Brass along with 620.95 N and 230.46 N for 0.7Al-0.2SS sheets are obtained. The interface temperatures achieved during welding of these sheets with the addition of ethanol are the highest among normally polished, electrolytic polished and emery polished surface conditions.
- A welding mechanics based numerical model has been explained that can predict the temperatures during the USMW process for various surface conditions. The maximum errors of 2.16 %, 0.59 % and 0.92% are obtained for Al-Cu, Al-Brass and Al-SS respectively while comparing the experimental temperature results with the simulated values. Likewise, due to the acoustic softening effects, there is a considerable reduction in the yield strength of the material obtained for different material combinations. The results show a maximum reduction of 93.98 % for Al-Cu, 96.71 % for Al-Brass and 96.55 % for Al-SS combinations while doing a comparison study with the standard temperature properties.

### 9.3 Conclusions

The important findings from the present investigation can be summarized as below:

- The research work provides an in-depth analysis of design, modeling, characterization and testing of ultrasonic spot welded dissimilar metal joints (Al-Cu, Al-Br and Al-SS) performed by means of a lateral drive system. This system is capable of joining relatively thin metal sheets.
- The mechanics of the ultrasonic welding process is fully explored keeping the trail of experimental conditions. Experimental observations indicate that good weld strengths can be achieved by USMW applied to Al-Cu, Al-Br and Al-SS dissimilar coupons to get the essential advantages instead of following the present conventional welding techniques.
- Traditional as well as soft computing techniques have been adopted for predictive modeling of tensile shear and T-peel failure loads. The results confirm the suitability of the proposed techniques (regression, ANN and ANFIS) for the effective prediction of tensile shear and T-peel failure loads.
- The metallurgical analyses of the fractured surfaces and the quality characterization of the welded joints reveal that soundness of the USMW is affected by surface conditions and anvil knurl patterns.
- Numerically estimated temperature, stress, and deformation during the welding process effectively take care of plastic deformation, friction effects, acoustic softening and yield strength reduction, and remain within the engineering accuracy limit comparing with the experimental results.
- Finally, the metallurgical investigations of the joints also strengthen the appropriateness of the proposed welding method, windows of process parameters for the different working conditions.

### 9.4 Contributions to Knowledge Enhancement

The contributions of this dissertation in light of above summary and findings have been discussed as follows:

- The major contribution of the current study is to replace the principle of 'welder's intuition', followed by various industries, with a methodical analysis for the determination of various control parameters and processing it to produce high-quality ultrasonic spot welded dissimilar metal joints between Al-Cu, Al-Br and Al-SS sheets.
- An effective method of design and fabrication of USMW components (sonotrode with booster, anvil, specimen holder, and backing plate) for successful welding of thin

sheets to get its inherent advantages like low heat affected zone and less welding time in comparison to other conventional welding processes.

- A 3D finite element formulation with sufficient precision is prescribed to explore the effects of ultrasonic energy on fatigue life of sonotrode, temperature generation under the cyclic loading of 20 kHz and vibro-thermographic property.
- The knowledge of acoustic softening is coupled with USMW process for better prediction of force as well as temperature during the welding.
- Generate a database of numerous experiments by USMW process using various process parameters such as weld pressure, weld time and vibration amplitude for dissimilar metal joints between Al-Cu, Al-Br and Al-SS sheets.
- Enhancing the metallurgical characterizing information about various weld cross-sections and fractured surfaces obtained by the proposed methods.
- Provide polynomial regression, ANN, and ANFIS models to predict the responses of USMW under different process parameters accurately.
- The results not only enhance the confidence to weld dissimilar metal sheets (Al-Cu, Al-Br and Al-SS) by USMW with required joint qualities but also solve some of the relevant issues faced by microelectronics, aviation, and automotive industries. It opens a pathway for further research in this area.

## 9.5 Scope for Further Research

The current research work will encourage the future researchers and have broad scope to explore the various aspects of USMW process. Several suggestions for further investigations are:

- Typically, the ultrasonic welding power can be improved up to 8 kW by designing the relevant components to weld thicker and advanced alloys.
- There is countless other tool materials present which may have significant effects on the weld strength, and these can be revealed.
- More detailed metallurgical studies like electron backscatter diffraction (EBSD) and texture analysis of the fractured surfaces and weld cross-sections are recommended.
- Finite element analysis can be extended further to model the process under various sonotrode and anvil knurls.
- Soft computing modeling with other hybridization techniques and optimization of process parameters can be explored for all weld combinations.



# Appendix A

## Drawings

### A.1 Ultrasonic Horn Design

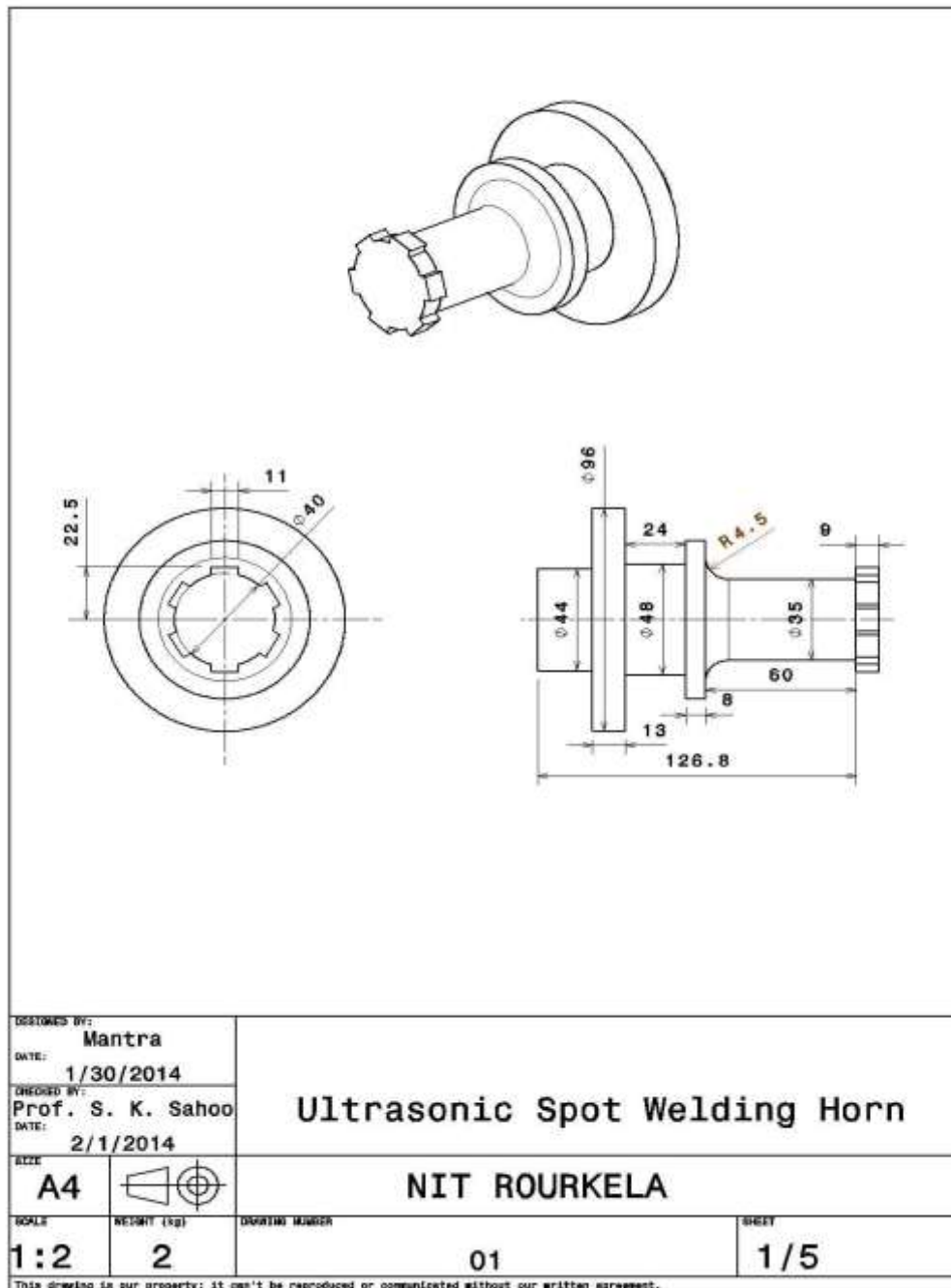


Fig. A.1 Ultrasonic horn



## A.2 Ultrasonic Horn Tips

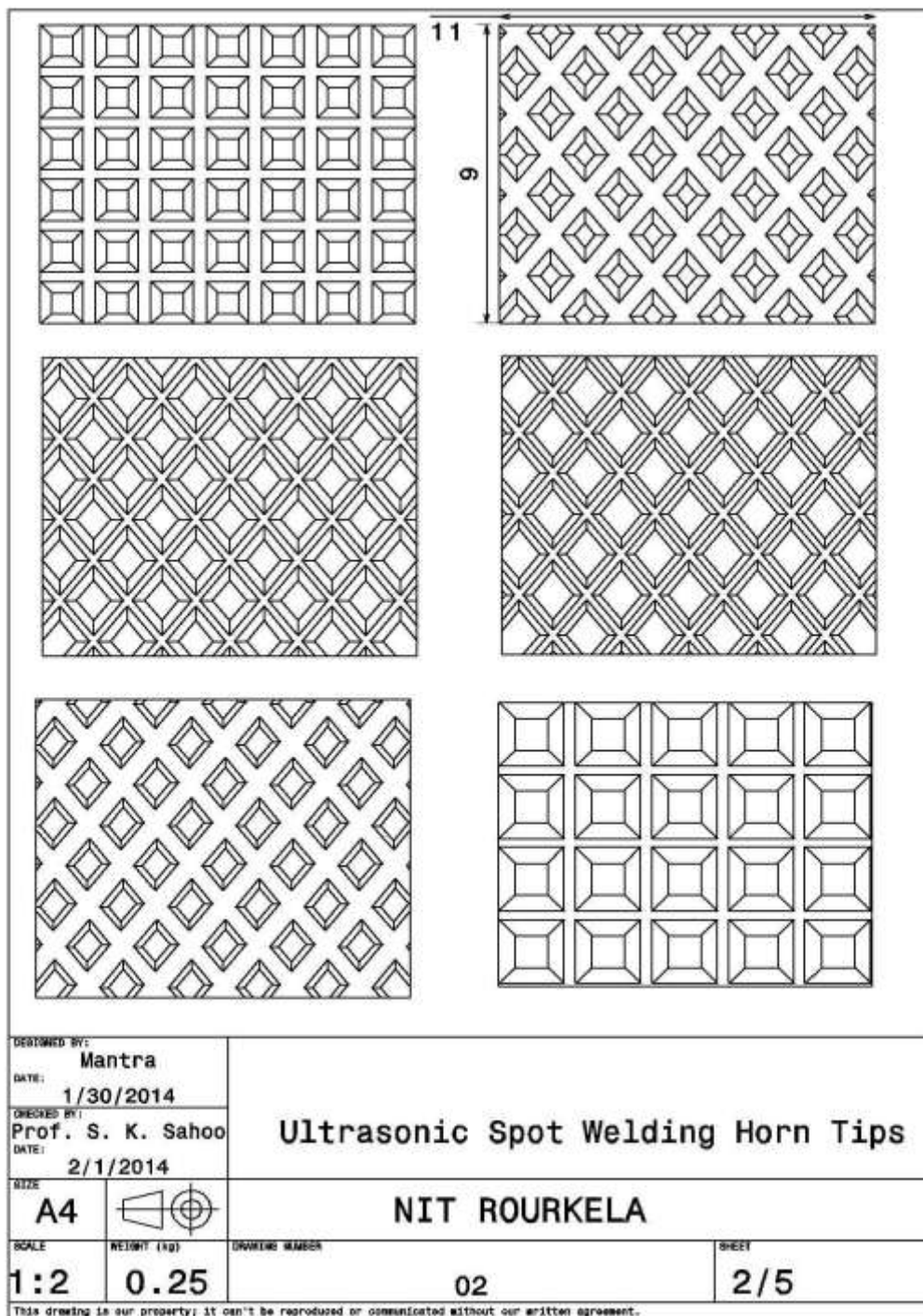


Fig. A.2 Ultrasonic spot welding horn tips

### A.3 Booster Design

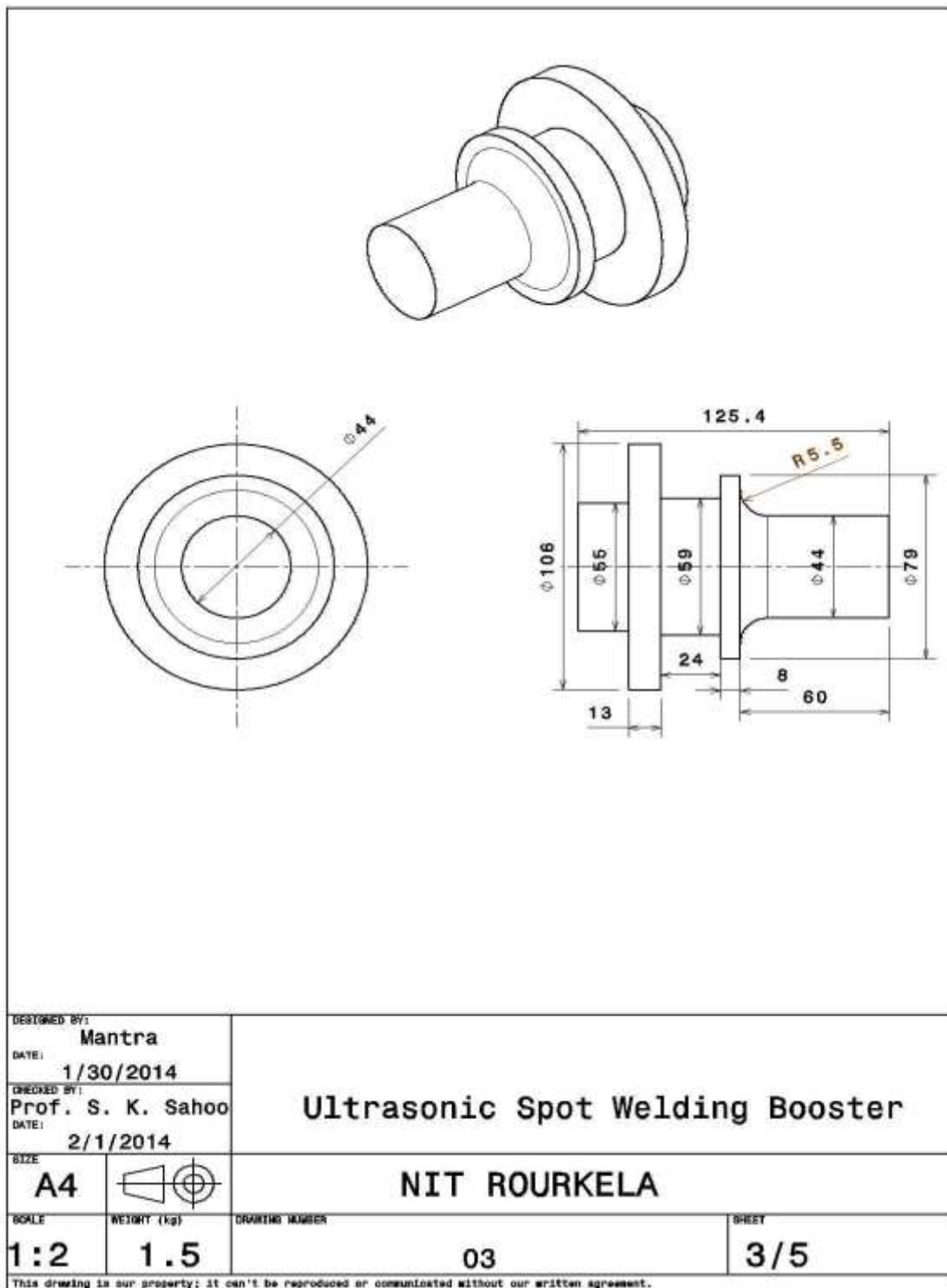


Fig. A.3 Ultrasonic spot welding booster

### A.4 Anvil Designs

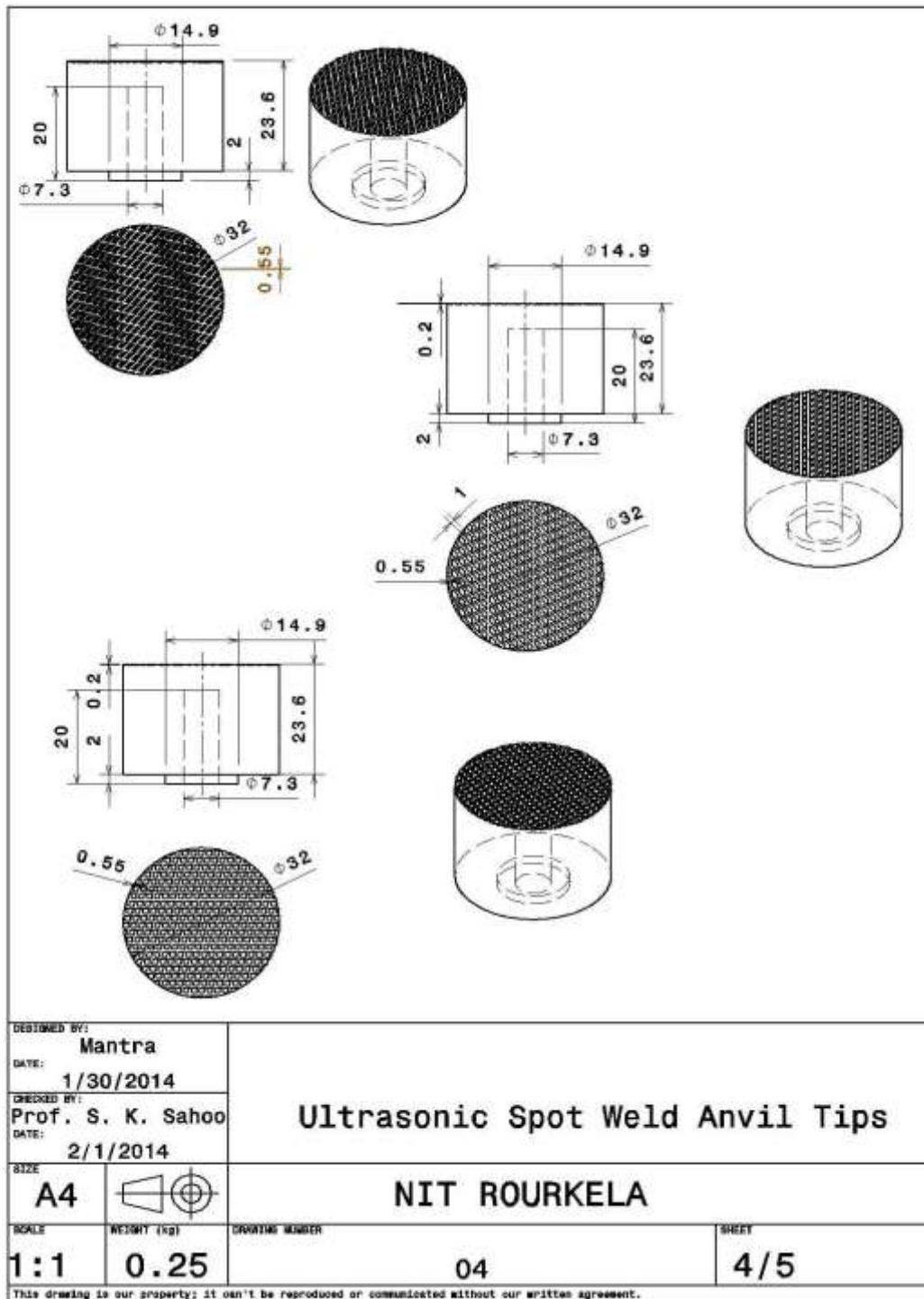


Fig. A.4 Anvil designs for ultrasonic spot welding

### A.5 Backing Plate Designs

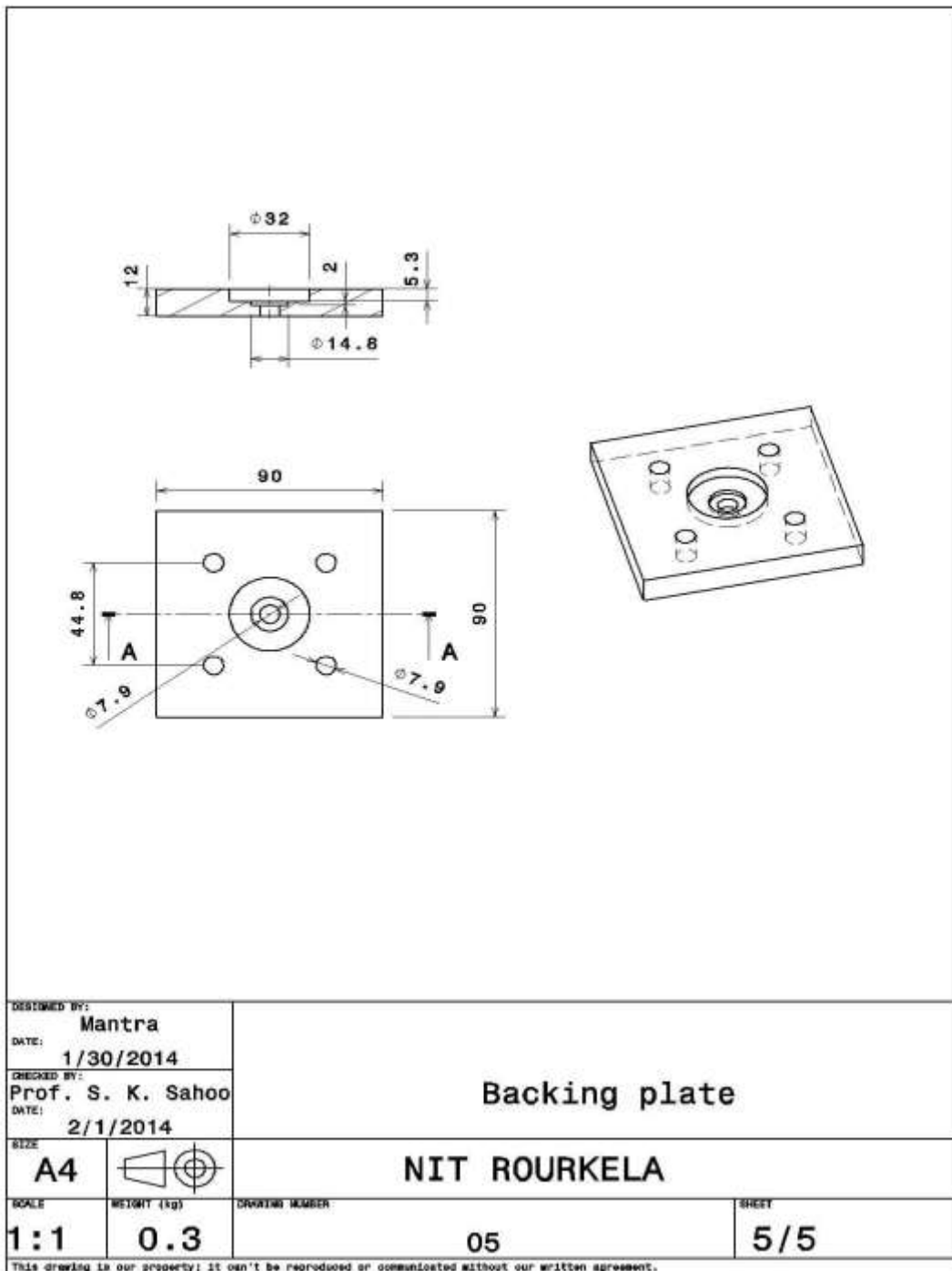


Fig. A.5 Backing plate design



## Appendix B

# Equipment used

### B.1 Horizontal Band Saw

It is otherwise known as power hacksaw. It was used to cut the SS304 stainless steel bar into two pieces for further machining operations.



Fig. B.1 Horizontal metal cutting band saw

Table B.1 Technical specifications of horizontal metal cutting band saw machine

Brand	Laxmen
Model	LX-1HS
Capacity	200 mm
Motor power	0.75 KW

### B.2 Computer Numerical Control (CNC) Machine

The CNC milling machine was used to step the anvil and also applied for making a backing plate.



Fig. B.2 CNC milling machine

Table B.2 Technical specifications of CNC milling machine

Brand	MTAB
Model	MAXMILL
X axis travel (longitudinal)	300 mm
Y-axis travel (cross)	250 mm
Z-axis travel (vertical)	250 mm
Repeatability	$\pm 0.005$ mm
Positional accuracy	0.01 mm
Motor power	3.7 kW

### B.3 Lathe Machine

This machine was used for turning and facing purpose of the anvil.



Fig. B.3 Lathe machine

Table B.3 Technical specifications of lathe machine

Brand	Tussor Pinacho
Model	Rocio(180×750)
Centre height	180 mm
Centre distance	750 mm
Swing over bed	400 mm
Swing over gap	500 mm
Swing over carriage	335 mm
Swing over cross slide	245 mm
Main motor power	4 KW
Coolant motor power	0.06 KW

### B.4 Holding Device and Backing Plate

Holding device was used to hold the workpiece firmly during the cutting operation performed in WEDM machine. Backing plate was employed to join the anvil with lathe tool dynamometer during the measurement of shear force.



Fig. B.4 Mild steel holding device



Fig. B.5 Aluminum backing plate

## B.5 Wire Electro-Discharge Machine (WEDM)

This is one of the important machines for making the knurling type of features on the surface of the anvil surface.



Fig. B.6 WEDM machine employed for making knurling features

Table B.4 Technical specifications of WEDM machine

Make	Electronica, EIPULS 15
Model	Ecocut
X × Y	250 × 230 mm
Max Workpiece height	200 mm
Max table size	370 × 600 mm
Max cutting speed	70mm/min
Taper	±8° over 50 mm
Best surface finish	1.2 μ R <sub>a</sub>

## B.6 Optical Stereo Microscope

Optical stereo microscope was used to grab the image of the weld area after the welding operation.



Fig. B.7 Optical microscope for measuring weld area

Table B.5 Technical specifications of optical microscope

Make	Radical Instruments
Model	0M-19
Camera	Samsung CCD (SDC-313B)
Zoom range	7x to 45x
Max X × Y size	150 × 150 mm
Least count	0.001 mm



## B.7 Lathe Tool Dynamometer

Lathe tool dynamometer equipped with charge amplifier was used to measure shear force during the welding process.



Fig. B.8 Lathe tool dynamometer



Fig. B.9 Charge amplifier

Table B.6 Technical specifications of lathe tool dynamometer

Brand	Kistler
Model	Type 9272
Measuring range ( $F_x$ and $F_y$ )	-5 to 5 kN
Measuring range ( $F_z$ )	-5 to 20 kN
Sensitivity ( $F_x$ and $F_y$ )	-7.8 pC/N
Sensitivity ( $F_z$ )	-3.5 pC/N

Table B.7 Technical specifications of charge amplifier

Brand	Kistler
Model	Type 5070A
Measuring range	$\pm 200$ pC
Measuring range ( $F_z$ )	-5 to 20 kN
Frequency range	0 to 45 kHz
Output signal	$\pm 10$ V

## B.8 Microhardness Tester

Microhardness tester was used to measure the microhardness of the welded samples.



Fig. B.10 Microhardness testing equipment

Table B.8 Technical specifications of microhardness tester

Make	Vaiseshika, India
Model	7005
Range	25HV-1500HV
Magnification	400x
Loading	10 gm-200 gm
Accuracy	$\pm 10$

## B.9 Scanning Electron Microscope (SEM)

Scanning electron microscope (SEM) was employed to reveal the quality of weld. It is also equipped with energy dispersive spectroscopy (EDS) technology for quantitative analysis of fractured surfaces.



Fig. B.11 Scanning electron microscope

Table B.9 Technical specifications of SEM

Make	Jeol, Japan
Model	JSM-6480LV
Resolution	SEI, BEI
Voltage	30 kV
Working distance	5 to 8 mm
Probe current	1 pA to 1 $\mu$ A
Vacuum pressure	10 to 270 Pa

## B.10 Multipurpose X-Ray Diffraction System (XRD)

X-ray diffraction (XRD) system was used to validate the results; those are already obtained in SEM and EDS analyses.



Fig. B.12 XRD machine

Table B.10 Technical specifications of XRD

Make	Rigaku, Japan
Model	Ultima IV

## B.11 Advanced Optical Microscope

Optical microscope was employed to reveal the microstructural features of weldment.



Fig. B.13 Optical microscope for measuring weld area

Table B.11 Technical specifications of optical microscope

Make	Carl Zeiss, Germany
Model	Axiotech, 100HD-3D
Magnification	10X, 20X, 50X, 100X

## B.12 Surface Roughness Tester

Surface roughness tester was used to measure the average roughness of the weld samples prepared in various conditions before the welding.



Fig. B.14 Zeiss Handysurf surface roughness tester

Table B.12 Technical specifications of optical microscope

Make	Carl Zeiss, Germany
Model	E-35B
Resolution	0.01 $\mu\text{m}$ -0.08 $\mu\text{m}$
Evaluation length	0.4 mm-6.1 mm

# References

- [1] Sound Waves For Brain Waves <http://www.biotele.com/usstim.html> (accessed February 27, 2013).
- [2] Goldman R. Ultrasonic technology. New York: Reinhold, London; 1962.
- [3] Leighton TG. What is ultrasound? *Prog Biophys Mol Biol* 2007;93:3-83. doi:10.1016/j.pbiomolbio.2006.07.026.
- [4] Nagy PB. Introduction to ultrasonics. Grad Course Notes, Univ Cincinnati 2001.
- [5] Cardoni A. Characterising the dynamic response of ultrasonic cutting devices. University of Glasgow, 2003.
- [6] Abramov O V. High-intensity ultrasonics: theory and industrial applications. vol. 10. CRC Press; 1999.
- [7] McCulloch E. Experimental and finite element modelling of ultrasonic cutting of food. University of Glasgow, 2008.
- [8] Ahmed N. New developments in advanced welding. England: Elsevier; 2005.
- [9] The Process of Ultrasonic Welding <http://www.weldmyworld.com/blog/2012/01/the-process-of-ultrasonic-welding.html> (accessed April 6, 2013).
- [10] Society AW. Welding handbook. vol. 3. American Welding Society; 1950.
- [11] Understanding ultrasonic welding [www.thefabricator.com/article/arcwelding/understanding-ultrasonic-welding](http://www.thefabricator.com/article/arcwelding/understanding-ultrasonic-welding) (accessed June 20, 2013).
- [12] Graff K. Development of Advanced Joining Processes for AHSS and UHSS. Columbus: Edison Welding Institute (EWI); 2007.
- [13] Bloss MC. Ultrasonic Metal Welding: The Weldability of Stainless Steel, Titanium, and Nickel-Based Superalloys. The Ohio State University, 2008.
- [14] Short M. EWI Advanced Ultrasonics - Capabilities overview n.d.
- [15] Graff K. Introduction to High Power Ultrasonics. Columbus: Edison Welding Institute; 1999.
- [16] Graff K. Ultrasonic metal welding, in *New developments in advanced welding*. Woodhead: Cambridge; 2005.
- [17] Janaki Ram GD, Robinson C, Yang Y, Stucker BE. Use of ultrasonic consolidation for fabrication of multi-material structures. *Rapid Prototyp J* 2007;13:226-35.
- [18] De Vries E. Mechanics and mechanisms of ultrasonic metal welding. The Ohio State University, 2004.
- [19] Derks PLLM. The design of ultrasonic resonators with wide output cross-sections. Technische Hogeschool Eindhoven, 1984.
- [20] Ultrasonic metal welding applications [http://www.telsonic.com/en/application-finder/#metal\\_welding](http://www.telsonic.com/en/application-finder/#metal_welding) (accessed August 9, 2013).
- [21] Matsuoka S, Imai H. Direct welding of different metals used ultrasonic vibration. *J Mater Process Technol* 2009;209:954-60. doi:10.1016/j.jmatprotec.2008.03.006.
- [22] Matheny M. Ultrasonic Metal Welding Foils to Tabs for Lithium-Ion Battery Cells. EWI Summ Rep SR1301 2012.
- [23] Haddadi F, Strong D, Prangnell PB. Effect of zinc coatings on joint properties and interfacial reactions in aluminum to steel ultrasonic spot welding. *JOM* 2012;64:407-13.
- [24] Bakavos D, Prangnell PB. Mechanisms of joint and microstructure formation in high power ultrasonic spot welding 6111 aluminium automotive sheet. *Mater Sci Eng A* 2010;527:6320-34.
- [25] Froes FH. Advanced metals for aerospace and automotive use. *Mater Sci Eng A* 1994;184:119-33.

- [26] O'Brien RL. *Jefferson's Welding Encyclopedia*. American Welding Society; 1997.
- [27] Lucas M, Cardoni A, McCulloch E, Hunter G, MacBeath A. Applications of power ultrasonics in engineering. *Appl. Mech. Mater.*, vol. 13, 2008, p. 11-20.
- [28] Lin SY. Sandwiched piezoelectric ultrasonic transducers of longitudinal-torsional compound vibrational modes. *IEEE Trans Ultrason Ferroelectr Freq Control* 1997;44:1189-97.
- [29] Merkulov LG. Design of ultrasonic concentrations. *Sov Physics-Acoustics* 1957;4:246-55.
- [30] Nad M. Ultrasonic horn design for ultrasonic machining technologies. *Appl Comput Mech* 2010;4:79-88.
- [31] Sherrit S, Askins SA, Gradziol M, Dolgin BP, Bao X, Chang Z, et al. Novel horn designs for ultrasonic/sonic cleaning, welding, soldering, cutting, and drilling. *SPIE's 9th Annu. Int. Symp. Smart Struct. Mater.*, 2002, p. 353-60.
- [32] Amin SG, Ahmed MHM, Youssef HA. Computer-aided design of acoustic horns for ultrasonic machining using finite-element analysis. *J Mater Process Technol* 1995;55:254-60. doi:10.1016/0924-0136(95)02015-2.
- [33] Lin S. Study on the longitudinal-torsional composite mode exponential ultrasonic horns. *Ultrasonics* 1996;34:757-62.
- [34] Amza G, Drimer D. The design and construction of solid concentrators for ultrasonic energy. *Ultrasonics* 1976;14:223-6.
- [35] Satyanarayana A, Reddy BGK. Design of velocity transformers for ultrasonic machining. *Electr India* 1984;24:11-20.
- [36] Ensminger D. Solid Cone in Longitudinal Half-Wave Resonance. *J Acoust Soc Am* 1960;32:194-6.
- [37] Alexandru N, Nicolae S, Marinescu I. Study on Ultrasonic Stepped Horn Geometry Design and FEM simulation. *Nonconv Technol Rev* 2011:25-30.
- [38] Belford JD. The stepped horn-Technical Publication TP-214 2011.
- [39] Shu K, Hsiang W-, Chen CC. The design of acoustic horns for ultrasonic insertion. *J Chinese Soc Mech Eng* 2010:338-42.
- [40] Woo J, Roh Y, Kang K, Lee S. Design and Construction of an Acoustic Horn for High Power Ultrasonic Transducers. *Ultrason. Symp. 2006. IEEE, 2006*, p. 1922-5.
- [41] Adachi K, Ueha S, Mori E. Modal vibration analysis of ultrasonic plastic welding tools using the finite element method. *Proc. Ultrason. Int.*, 1986, p. 727-32.
- [42] Gourley B, Rushton A. Solve ultrasonic horn problems with finite element analysis. *Plast Technol* 2006;52:49-50.
- [43] Roopa Rani M, Rudramoorthy R. Computational modeling and experimental studies of the dynamic performance of ultrasonic horn profiles used in plastic welding. *Ultrasonics* 2013;53:763-72. doi:10.1016/j.ultras.2012.11.003.
- [44] da Silva JB, Franceschetti NN, Adamowski JC. Numerical Analysis of a High Power Piezoelectric Transducer Used in the Cutting and Welding of Thermoplastic Textiles. *ABCM Symp. Ser. Mechatronics*, vol. 2, 2006, p. 142-9.
- [45] Wang D, Chuang W-Y, Hsu K, Pham H-T. Design of a Bézier-profile horn for high displacement amplification. *Ultrasonics* 2011;51:148-56. doi:10.1016/j.ultras.2010.07.004.
- [46] Nguyen H-T, Nguyen H-D, Uan J-Y, Wang D-A. A nonrational B-spline profiled horn with high displacement amplification for ultrasonic welding. *Ultrasonics* 2014;54:2063-71. doi:10.1016/j.ultras.2014.07.003.
- [47] Balandin GF, Kuznetsov VA, Silin LL. Fretting action between members in ultrasonic welding of metals. *Weld Prod* 1967;10:77-80.
- [48] Pfluger AR, Sideris XN. New developments in ultrasonic welding. *Sampe Q* 1975;7:9-19.
- [49] Neville SW. *Ultrasonic welding*. British Welding Research Assoc.; 1960.
- [50] Jones JB, Powers JJ. Ultrasonic welding. *Weld J* 1956;35:761-6.

- [51] Antonevich JN. Ultrasonic welding equipment. *Ultrason Eng IRE Trans* 1960;7:26-31.
- [52] Ginzburg SK, Mitskevich AM, Nosov YG. Formation of the joint in ultrasonic welding. *Weld Prod* 1967;14:83-7.
- [53] Weare NE, Antonevich JN, Monroe RE. Fundamental studies of ultrasonic welding. *Weld J* 1960;39:331.
- [54] Chang UI, Frisch J. On optimization of some parameters in ultrasonic metal welding. *Weld J* 1974;53:24.
- [55] de Vries E. Development of ultrasonic welding process for stamped 6000 series Aluminum. Diploma Thesis, University of Applied Science, Emden, 2000.
- [56] Harthoorn JL. Ultrasonic metal welding. Technische Hogeschool Eindhoven, 1978.
- [57] Komiyama K, Sasaki T, Watanabe Y. Effect of tool edge geometry in ultrasonic welding. *J Mater Process Technol* 2016;229:714-21. doi:http://dx.doi.org/10.1016/j.jmatprotec.2015.10.031.
- [58] Sasaki T, Hosokawa Y. Effect of Relative Motion between Weld Tool and Work Piece on Microstructure of Ultrasonically Welded Joint. *Mater Sci Forum* 2014;783-786:1782-7. doi:10.4028/www.scientific.net/MSF.783-786.1782.
- [59] Jahn R, Cooper R, Wilkosz D. The Effect of Anvil Geometry and Welding Energy on Microstructures in Ultrasonic Spot Welds of AA6111-T4. *Metall Mater Trans A* 2007;38:570-83. doi:10.1007/s11661-006-9087-0.
- [60] Watanabe T, Itoh H, Yanagisawa a., Hiraishi M. Ultrasonic welding of heat-treatable aluminium alloy A6061 sheet. *Weld Int* 2009;23:633-9. doi:10.1080/09507110902842802.
- [61] Lum I, Mayer M, Zhou Y. Footprint study of ultrasonic wedge-bonding with aluminum wire on copper substrate. *J Electron Mater* 2006;35:433-42.
- [62] Heymann E, Koehler B. Influence of the workpiece separation on ultrasonic welding. *ZIS-Mitteilungen* 1969;11:180-90.
- [63] Hiraishi M, Watanabe T. Improvement of ultrasonic weld strength of Al-Mg alloys by alcohol adhesion - ultrasonic welding of Al-Mg alloys. *Weld Int* 2004;18:357-63. doi:10.1533/wint.2004.3257.
- [64] Watanabe T, Yanagisawa A, Konuma S, Yoneda A, Ohashi O. Ultrasonic welding of Al-Cu and Al-SUS304. Study of ultrasonic welding of dissimilar metals (1st Report). *Weld Int* 1999;13:875-86. doi:10.1080/09507116.2012.708491.
- [65] Bakavos D, Prangnell PB. Mechanisms of joint and microstructure formation in high power ultrasonic spot welding 6111 aluminium automotive sheet. *Mater Sci Eng A* 2010;527:6320-34. doi:10.1016/j.msea.2010.06.038.
- [66] Shakil M, Tariq NH, Ahmad M, Choudhary MA, Akhter JI, Babu SS. Effect of ultrasonic welding parameters on microstructure and mechanical properties of dissimilar joints. *Mater Des* 2014;55:263-73. doi:10.1016/j.matdes.2013.09.074.
- [67] Kong CY, Soar RC, Dickens PM. Characterisation of aluminium alloy 6061 for the ultrasonic consolidation process. *Mater Sci Eng A* 2003;363:99-106.
- [68] Yang Y, Janaki Ram GD, Stucker BE. An analytical energy model for metal foil deposition in ultrasonic consolidation. *Rapid Prototyp J* 2010;16:20-8.
- [69] Patel VK, Bhole SD, Chen DL. Ultrasonic Spot Welding of Aluminum to High-Strength Low-Alloy Steel: Microstructure, Tensile and Fatigue Properties. *Metall Mater Trans A* 2013;45:2055-66. doi:10.1007/s11661-013-2123-y.
- [70] Tsujino J, Hidai K, Hasegawa a, Kanai R, Matsuura H, Matsushima K, et al. Ultrasonic butt welding of aluminum, aluminum alloy and stainless steel plate specimens. *Ultrasonics* 2002;40:371-4. doi:Pii S0041-624x(02)00124-5\nDoi 10.1016/S0041-624x(02)00124-5.
- [71] Panteli A, Chen YC, Strong D, Zhang X, Prangnell PB. Optimization of aluminium-to-magnesium ultrasonic spot welding. *Jom* 2012;64:414-20. doi:10.1007/s11837-012-0268-6.
- [72] Gunduz IE, Ando T, Shattuck E, Wong PY, Doumanidis CC. Enhanced diffusion and phase

- transformations during ultrasonic welding of zinc and aluminum. *Scr Mater* 2005;52:939-43.
- [73] Zhao YY, Li D, Zhang YS. Effect of welding energy on interface zone of Al-Cu ultrasonic welded joint. *Sci Technol Weld Join* 2013;18:354-60. doi:10.1179/1362171813Y.0000000114.
- [74] Graff K. Ultrasonic metal welding. In: Ahmed N, editor. *New Dev. Adv. Weld.*, Woodhead: Cambridge; 2005, p. 241-69.
- [75] Graff KF, Devine JF, Kelto J, Zhou NY. *Ultrasonic welding of metals*. vol. 3. Elsevier Ltd.; 2007. doi:10.1016/B978-1-78242-028-6.00011-9.
- [76] Bloss M, Graff K. Ultrasonic metal welding of advanced alloys: the weldability of stainless steel, titanium, and nickel-based superalloys. *Trends Weld. Res. Proc. 8th Int. Conf.*, 2009, p. 348-53.
- [77] Patel VK, Bhole SD, Chen DL, Ni DR, Xiao BL, Ma ZY. Solid-state ultrasonic spot welding of SiCp/2009Al composite sheets. *Mater Des* 2015;65:489-95. doi:10.1016/j.matdes.2014.09.049.
- [78] Wodara J. Relation between component geometry and the quality of ultrasonically welded metallic joints. *Wissenschaftliche Zeitschrift Der Tech Univ Otto von Guericke Magdebg* 1989;33:64-8.
- [79] Okada M, Shin S, Miyagi M, Matsuda H. Joint mechanism of ultrasonic welding. *Trans Japan Inst Met* 1963;4:250-5.
- [80] Harman G, Albers J. The ultrasonic welding mechanism applied to aluminium and gold-wire bonding in microelectronics. *IEEE Trans Parts, Hybrid Packging* 1977;13:406-12.
- [81] Rozenberg L, Mitskevich A. *Ultrasonic Welding of Metals*. vol. 1. Plenum Press: Moscow; 1973.
- [82] What is an Ultrasonic weld? <http://jascoes.com/datasheets/WhatIsAnUltrasonicWeld.pdf> (accessed August 2, 2014).
- [83] Siddiq A, Ghassemieh E. Fibre embedding in aluminium alloy 3003 using ultrasonic consolidation process—thermo-mechanical analyses. *Int J Adv Manuf Technol* 2011;54:997-1009.
- [84] Park DS, Jang HS, Park WY. Tensile Strength of Cu Sheets Welded by Ultrasonic Metal Welding. *Adv Mater Res* 2013;658:202-8. doi:10.4028/www.scientific.net/AMR.658.202.
- [85] Hetrick E, Jahn R, Reatherford L, Skogsmo J, Ward S, Wilkosz D, et al. Ultrasonic spot welding: a new tool for aluminum joining. *Weld J* 2005;84:26-30.
- [86] Kodama M. Ultrasonic welding of non-ferrous metals. *Weld Int* 1989;3:853-60.
- [87] Barnes TA, Pashby IR. Joining techniques for aluminium spaceframes used in automobiles: Part I—solid and liquid phase welding. *J Mater Process Technol* 2000;99:62-71.
- [88] Zhang CY, Chen DL, Luo AA. Joining 5754 Automotive Aluminum Alloy 2-mm-Thick Sheets Using Ultrasonic Spot Welding. *Weld J* 2014;93:131-8.
- [89] Siddiq A, Ghassemieh E. Theoretical and FE Analysis of Ultrasonic Welding of Aluminum Alloy 3003. *J Manuf Sci Eng Asme* 2009;131:41007. doi:DOI 10.1115/1.3160583.
- [90] Tsujino J, Sano T, Ogata H, Tanaka S, Harada Y. Complex vibration ultrasonic welding systems with large area welding tips. *Ultrasonics* 2002;40:361-4.
- [91] Al-Sarraf Z, Lucas M. A study of weld quality in ultrasonic spot welding of similar and dissimilar metals. *J Phys Conf Ser* 2012;382:012013. doi:10.1088/1742-6596/382/1/012013.
- [92] Seo JS, Jang HS, Park DS. Ultrasonic Welding of Ni and Cu Sheets. *Mater Manuf Process* 2015;30:1069-73. doi:10.1080/10426914.2014.880466.
- [93] Elangovan S, Prakasan K, Jaiganesh V. Optimization of ultrasonic welding parameters for copper to copper joints using design of experiments. *Int J Adv Manuf Technol* 2010;51:163-71. doi:10.1007/s00170-010-2627-1.
- [94] Lee SS, Kim TH, Hu JS, Cai WW, Abell J a., Li J. Characterization of Joint Quality in

- Ultrasonic Welding of Battery Tabs. *J Manuf Sci Eng* 2013;135:1-13. doi:10.1115/1.4023364.
- [95] Annoni M, Carboni M. Ultrasonic metal welding of AA 6022-T4 lap joints: Part I - Technological characterisation and static mechanical behaviour. *Sci Technol Weld Join* 2011;16:107-15. doi:10.1179/1362171810Y.0000000015.
- [96] Chen Y-C, Bakavos D, Gholinia A, Prangnell PB. HAZ development and accelerated post-weld natural ageing in ultrasonic spot welding aluminium 6111-T4 automotive sheet. *Acta Mater* 2012;60:2816-28.
- [97] Watanabe T, Sakuyama H, Yanagisawa A. Ultrasonic welding between mild steel sheet and Al-Mg alloy sheet. *J Mater Process Technol* 2009;209:5475-80. doi:10.1016/j.jmatprotec.2009.05.006.
- [98] Daniels HPC. Ultrasonic welding. *Ultrasonics* 1965;3:190-6.
- [99] Zhou B, Thouless MD, Ward SM. Predicting the failure of ultrasonic spot welds by pull-out from sheet metal. *Int J Solids Struct* 2006;43:7482-500.
- [100] Kim TH, Yum J, Hu SJ, Spicer JP, Abell J a. Process robustness of single lap ultrasonic welding of thin, dissimilar materials. *CIRP Ann - Manuf Technol* 2011;60:17-20. doi:10.1016/j.cirp.2011.03.016.
- [101] Siddiq AM, Ghassemieh E. Modelling and characterization of ultrasonic consolidation process of Aluminium alloys. *Mater. Res. Soc. Symp. Proc.*, vol. 1079, 2008, p. 125-32.
- [102] Zhu Z, Lee KY, Wang X. Ultrasonic welding of dissimilar metals, AA6061 and Ti6Al4V. *Int J Adv Manuf Technol* 2012;59:569-74. doi:10.1007/s00170-011-3534-9.
- [103] Al-Sarraf Z, Lucas M, Harkness P. A numerical and experimental study of ultrasonic metal welding. *IOP Conf Ser Mater Sci Eng* 2012;42:012015. doi:10.1088/1757-899X/42/1/012015.
- [104] Collins FR, Dowd JD, Brennecke MW. Ultrasonic welding of aluminum. *Weld J* 1959;38:969.
- [105] Tsujino J, Ueoka T. Ultrasonic multi-spot continuous welding of metal plate specimens using a two-vibration-system welding equipment. *Ultrasonics* 1996;34:229-33.
- [106] Flood G. Ultrasonic energy welds copper to aluminium. *Weld J* 1997;76.
- [107] Elangovan S, Anand K, Prakasan K. Parametric optimization of ultrasonic metal welding using response surface methodology and genetic algorithm. *Int J Adv Manuf Technol* 2012;63:561-72. doi:10.1007/s00170-012-3920-y.
- [108] Norouzi A, Hamed M, Adineh VR. Strength modeling and optimizing ultrasonic welded parts of ABS-PMMA using artificial intelligence methods. *Int J Adv Manuf Technol* 2012;61:135-47. doi:10.1007/s00170-011-3699-2.
- [109] Elangovan S. Experimental and theoretical investigations on temperature distribution at the joint interface for copper joints using ultrasonic welding. *Manuf Rev* 2014;1:1-13.
- [110] Jedrasiak P, Shercliff HR, Chen YC, Wang L, Prangnell P, Robson J. Modelling of the Thermal Field in Dissimilar Alloy Ultrasonic Welding. *J Mater Eng Perform* 2015;24:799-807.
- [111] Elangovan S, Semeer S, Prakasan K. Temperature and stress distribution in ultrasonic metal welding-An FEA-based study. *J Mater Process Technol* 2009;209:1143-50. doi:10.1016/j.jmatprotec.2008.03.032.
- [112] Chen K, Zhang Y. Mechanical analysis of ultrasonic welding considering knurl pattern of sonotrode tip. *Mater Des* 2015;87:393-404. doi:10.1016/j.matdes.2015.08.042.
- [113] Chen KK, Zhang YS. Numerical analysis of temperature distribution during ultrasonic welding process for dissimilar automotive alloys. *Sci Technol Weld Join* 2015;20:522-31.
- [114] Konchakova N, Balle F, Barth FJ, Mueller R, Eifler D, Steinmann P. Finite element analysis of an inelastic interface in ultrasonic welded metal/fibre-reinforced polymer joints. *Comput Mater Sci* 2010;50:184-90. doi:10.1016/j.commatsci.2010.07.024.



- [115] Blaha F, Langenecker B. Tensile deformation of zinc crystal under ultrasonic vibration. *Naturwissenschaften* 1955;42:0.
- [116] Kirchner HOK, Kromp WK, Prinz FB, Trimmel P. Plastic deformation under simultaneous cyclic and unidirectional loading at low and ultrasonic frequencies. *Mater Sci Eng* 1985;68:197-206.
- [117] Izumi O, Oyama K, Suzuki Y. Effects of superimposed ultrasonic vibration on compressive deformation of metals. *Trans Japan Inst Met* 1966;7:162-7.
- [118] Doumanidis C, Gao Y. Mechanical modeling of ultrasonic welding. *Weld J* 2004;83:140-6.
- [119] Zhang C, Li L. A friction-based finite element analysis of ultrasonic consolidation. *Weld J* 2008;87:187.
- [120] Merkulov LG, Yakovlev LA. Propagation and reflection of ultrasonic beams in crystal. *Sov Phys Acoust* 1962;8:72-7.
- [121] Cardoni A. Characterising the dynamic response of ultrasonic cutting devices. 2003.
- [122] ANSYS R. 11.0 Documentation, SAS IP 2007.
- [123] ANSYS. ANSYS Mechanical APDL Theory Reference 2013;15317:724-46. doi:www.ansys.com.
- [124] Troughton MJ. Handbook of plastics joining: a practical guide. William Andrew; 2008.
- [125] Phillips AL, Kearns WH, Weisman C. Welding handbook. vol. 2. American Welding Society; 1976.
- [126] Material property data [www.matweb.com](http://www.matweb.com) (accessed April 6, 2013).
- [127] Nishihara K, Watanabe T, Sasaki T. Effect of Weld Tip Geometry on Ultrasonic Welding between Steel and Aluminum Alloy. *Adv Mater Res* 2010;89-91:419-24. doi:10.4028/www.scientific.net/AMR.89-91.419.
- [128] Kremer D, Saleh SM, Ghabrial SR, Moisan A. The state of the art of ultrasonic machining. *CIRP Ann Technol* 1981;30:107-10.
- [129] Hibbeler RC. *Mechanics of Materials*. Prentice Hall, Upper Saddle River; 2011.
- [130] Ming Y, Fu LS, Zheng S. A new optimization method for horn designs in ultrasonic welding systems. *Singapore Inst Manuf Technol* 2002:1-6.
- [131] Stephens RI, Fatemi A, Stephens RR, Fuchs HO. *Metal fatigue in engineering*. John Wiley & Sons; 2000.
- [132] Military Handbook SF. *Metallic Materials and Elements for Aerospace Vehicle Structures*. Washington DC: Department of Defense; 1972.
- [133] Miner MA. Cumulative damage in fatigue. *J Appl Mech* 1945;12:159-64.
- [134] Dulieu-barton JM. Introduction to thermoelastic stress analysis. *Strain* 1999;35:35-9. doi:10.1111/j.1475-1305.1999.tb01123.x.
- [135] Serra E, Bonaldi M. A finite element formulation for thermoelastic damping analysis. *Int J Numer Methods Eng* 2009;78:671-91.
- [136] Greitmann MJ, Adam T, Holzweißig HG, Stroh D, Wanger G, Wiesner P, et al. Present status and future prospects of special welding processes: Ultrasonic welding. *Weld Cut* 2003;55:268-74.
- [137] Ely K. *Ultrasonic Welding Development for Aluminum Automotive Structures*. Columbus: 2000.
- [138] O'Brien RL. *AWS Welding Handbook: Welding Process, Vol. 2* 1991:783-812.
- [139] *ASM Handbooks Online*. USA: ASM International; 2011.
- [140] Okafor UC. *Mechanical Characterization of A2 and D2 Tool Steels by Nanoindentation*. University of North Texas, 2012.
- [141] Langenecker B. Effects of ultrasound on deformation characteristics of metals. *Sonics Ultrason IEEE Trans* 1966;13:1-8.

- [142] Hockett JE. On relating the flow stress of aluminum to strain, strain rate, and temperature. 1966.
- [143] Methods for calibration and grading of extensometers for testing of metals 1985.
- [144] Standard A. E8m-09: Standard Test Methods for Tension Testing of Metallic Materials. Annu B ASTM Stand ASTM, West Conshohocken, PA 2009:127.
- [145] J. Gillbert Kaufman. Properties of aluminum alloys. ASM International and aluminum association Inc.; 2006.
- [146] Handysurf: The Small, Portable Surface Measuring Unit n.d.
- [147] Sahin M. Joining of aluminium and copper materials with friction welding. *Int J Adv Manuf Technol* 2010;49:527-34.
- [148] Chang UI, Frisch J. On optimization of some parameters in ultrasonic metal welding. *Weld J* 1974;53:24.
- [149] Neppiras EA. Ultrasonic welding of metals. *Ultrasonics* 1965;3:128-35.
- [150] Cheng X, Li X. Investigation of heat generation in ultrasonic metal welding using micro sensor arrays. *J Micromechanics Microengineering* 2007;17:273-82.
- [151] Jata K V, Sankaran KK, Ruschau JJ. Friction-stir welding effects on microstructure and fatigue of aluminum alloy 7050-T7451. *Metall Mater Trans A* 2000;31:2181-92.
- [152] Truog AG. Bond improvement of Al/Cu joints created by very high power ultrasonic additive manufacturing. The Ohio State University, 2012.
- [153] Funamizu Y, Watanabe K. Interdiffusion in the Al--Cu system. *Trans Japan Inst Met* 1971;12:147-52.
- [154] Balasundaram R, Patel VK, Bhole SD, Chen DL. Effect of zinc interlayer on ultrasonic spot welded aluminum-to-copper joints. *Mater Sci Eng A* 2014;607:277-86.
- [155] Yang JW, Cao B, He XC, Luo HS. Microstructure evolution and mechanical properties of Cu-Al joints by ultrasonic welding. *Sci Technol Weld Join* 2014;19:500-4.
- [156] Xue P, Ni DR, Wang D, Xiao BL, Ma ZY. Effect of friction stir welding parameters on the microstructure and mechanical properties of the dissimilar Al--Cu joints. *Mater Sci Eng A* 2011;528:4683-9.
- [157] Montgomery DC. Design and analysis of experiments. John Wiley & Sons; 2008.
- [158] Sugeno M, Kang GT. Structure identification of fuzzy model. *Fuzzy Sets Syst* 1988;28:15-33.
- [159] Hagan MT, Demuth HB, Beale MH, De Jesús O. Neural network design. vol. 20. PWS publishing company Boston; 1996.
- [160] Tsai K-M, Wang P-J. Predictions on surface finish in electrical discharge machining based upon neural network models. *Int J Mach Tools Manuf* 2001;41:1385-403.
- [161] Sheela KG, Deepa SN. Review on methods to fix number of hidden neurons in neural networks. *Math Probl Eng* 2013;2013.
- [162] Haykin S. Neural networks: A comprehensive approach. IEEE Comput Soc Press 1994.
- [163] Gill SS, Singh R, Singh J, Singh H. Adaptive neuro-fuzzy inference system modeling of cryogenically treated AISI M2 HSS turning tool for estimation of flank wear. *Expert Syst Appl* 2012;39:4171-80.
- [164] Takagi T, Sugeno M. Fuzzy identification of systems and its applications to modeling and control. *Syst Man Cybern IEEE Trans* 1985:116-32.
- [165] Sugeno M. Industrial applications of fuzzy control. Elsevier Science Inc.; 1985.
- [166] Jang J-SR. ANFIS: adaptive-network-based fuzzy inference system. *Syst Man Cybern IEEE Trans* 1993;23:665-85.
- [167] Ying L-C, Pan M-C. Using adaptive network based fuzzy inference system to forecast regional electricity loads. *Energy Convers Manag* 2008;49:205-11.

- [168] Sengur A. Wavelet transform and adaptive neuro-fuzzy inference system for color texture classification. *Expert Syst Appl* 2008;34:2120-8.
- [169] Buragohain M, Mahanta C. A novel approach for ANFIS modelling based on full factorial design. *Appl Soft Comput* 2008;8:609-25.
- [170] Zhou M, Zhang H, Hu SJ. Relationships between quality and attributes of spot welds. *Weld J* 2003;82:72-7.
- [171] Kreye H. Melting Phenomena in Solid State Welding Processes. *Weld J* 1977;56:154-8.
- [172] Joshi KC. The formation of ultrasonic bonds between metals. *Weld J* 1971;50:840-8.
- [173] Igari S, Mori S, Takikawa Y. Effects of molecular structure of aliphatic diols and polyalkylene glycol as lubricants on the wear of aluminum. *Wear* 2000;244:180-4. doi:10.1016/S0043-1648(00)00458-0.
- [174] Abdollah-Zadeh a., Saeid T, Sazgari B. Microstructural and mechanical properties of friction stir welded aluminum/copper lap joints. *J Alloys Compd* 2008;460:535-8. doi:10.1016/j.jallcom.2007.06.009.
- [175] Yilbas BS, Sahin AZ, Kahraman N, Al-Garni AZ. Friction welding of St-Al and Al-Cu materials. *J Mater Process Technol* 1995;49:431-43. doi:10.1016/0924-0136(94)01349-6.
- [176] Jedrasiak P, Shercliff HR, Chen YC, Wang L, Prangnell P, Robson J. Modeling of the Thermal Field in Dissimilar Alloy Ultrasonic Welding. *J Mater Eng Perform* 2015;24:799-807.
- [177] Khanna SK, Long X, Porter WD, Wang H, Liu CK, Radovic M, et al. Residual stresses in spot welded new generation aluminium alloys Part A--thermophysical and thermomechanical properties of 6111 and 5754 aluminium alloys. *Sci Technol Weld Join* 2005;10:82-7.
- [178] Callister WD. *Callister's Materials Science and Engineering*. Wiley-India; 2010.
- [179] Lindeburg, Michael R. *Mechanical engineering reference manual for the PE exam*. www.ppi2pass.com; 2013.
- [180] Jones JB, Maropis N. *Fundamentals of Ultrasonic Welding*. 1960.
- [181] AMBEKAR THHSM. Additional studies on interface temperatures and bonding mechanisms of ultrasonic welds. *WELD J* 1970;49.
- [182] Pao YH, Gilat A. Modeling 1100-0 aluminum over a wide range of temperatures and strain rates. *Int J Plast* 1989;5:183-96.
- [183] Puchi ES, Staia MH, Villalobos C. On the mechanical behavior of commercial-purity aluminum deformed under axisymmetric compression conditions. *Int J Plast* 1997;13:723-42.
- [184] Andersson CG, Andrews RE, Dance BGI, Russell MJ, Olden EJ, Sanderson RM. A comparison of copper canister fabrication by the electron beam and friction stir processes. *Proc. 2nd Int. Symp. "Friction Stir Welding"*, Gothenbg., 2000.
- [185] Elrefaey A, Takahashi M, Ikeuchi K. Preliminary investigation of friction stir welding aluminium/copper lap joints. *Weld World* 2005;49:93-101.
- [186] Harding RA, Homer C, Baudelet B. Recrystallization of 70/30 brass during induction heating. *J Mater Sci* 1980;15:1804-13.
- [187] Burger GB, Gupta AK, Jeffrey PW, Lloyd DJ. Microstructural control of aluminum sheet used in automotive applications. *Mater Charact* 1995;35:23-39.
- [188] Haddadi F. Rapid intermetallic growth under high strain rate deformation during high power ultrasonic spot welding of aluminium to steel. *Mater Des* 2015;66:459-72.
- [189] Bakavos D, Prangnell PB. Effect of reduced or zero pin length and anvil insulation on friction stir spot welding thin gauge 6111 automotive sheet. *Sci Technol Weld Join* 2009;14:443-56.
- [190] Peng J, Fukumoto S, Brown L, Zhou N. Image analysis of electrode degradation in resistance spot welding of aluminium. *Sci Technol Weld Join* 2004;9:331-6.

- [191] Gerlich A, Avramovic-Cingara G, North TH. Stir zone microstructure and strain rate during Al 7075-T6 friction stir spot welding. *Metall Mater Trans A* 2006;37:2773-86.
- [192] Wright NW, Robson JD, Prangnell PB. Effects of Thickness Combinations on Joint Properties and Process Windows in Ultrasonic Metal Welding. 2009.
- [193] Bozzi S, Helbert-Etter AL, Baudin T, Criqui B, Kerbiguet JG. Intermetallic compounds in Al 6016/IF-steel friction stir spot welds. *Mater Sci Eng A* 2010;527:4505-9.
- [194] Qiu R, Shi H, Zhang K, Tu Y, Iwamoto C, Satonaka S. Interfacial characterization of joint between mild steel and aluminum alloy welded by resistance spot welding. *Mater Charact* 2010;61:684-8.
- [195] Naoi D, Kajihara M. Growth behavior of Fe<sub>2</sub>Al<sub>5</sub> during reactive diffusion between Fe and Al at solid-state temperatures. *Mater Sci Eng A* 2007;459:375-82.
- [196] Springer H, Kostka A, Dos Santos JF, Raabe D. Influence of intermetallic phases and Kirkendall-porosity on the mechanical properties of joints between steel and aluminium alloys. *Mater Sci Eng A* 2011;528:4630-42.
- [197] Laurila T, Vuorinen V, Kivilahti JK. Interfacial reactions between lead-free solders and common base materials. *Mater Sci Eng R Reports* 2005;49:1-60.
- [198] Hall EO. Variation of hardness of metals with grain size 1954.
- [199] Agudo L, Eyidi D, Schmaranzer CH, Arenholz E, Jank N, Bruckner J, et al. Intermetallic Fe x Al y-phases in a steel/Al-alloy fusion weld. *J Mater Sci* 2007;42:4205-14.
- [200] Prangnell P, Haddadi F, Chen YC. Ultrasonic spot welding of aluminium to steel for automotive applications—microstructure and optimisation. *Mater Sci Technol* 2011;27:617-24.
- [201] Macwan A, Jiang XQ, Chen DL. Interfacial Characterization of Dissimilar Joints Between Al/Mg/Al-Trilayered Clad Sheet to High-Strength Low-Alloy Steel. *JOM* 2015;67:1468-77.
- [202] Patel VK, Bhole SD, Chen DL. Ultrasonic spot welding of aluminum to high-strength low-alloy steel: microstructure, tensile and fatigue properties. *Metall Mater Trans A* 2014;45:2055-66.
- [203] Nanda G, Nanda A, Kumar S. Optimizing the mechanical properties of AISI 304 steel in gas metal arc welding process. *Int J Emerg Technol* 2013;4:112-22.
- [204] Jahn R, Cooper R, Wilkosz D. The Effect of Anvil Geometry and Welding Energy on Microstructures in Ultrasonic Spot Welds of AA6111-T4. *Metall Mater Trans A* 2007;38:570-83. doi:10.1007/s11661-006-9087-0.
- [205] Patel VK, Bhole SD, Chen DL. Microstructure and mechanical properties of dissimilar welded Mg-Al joints by ultrasonic spot welding technique. *Sci Technol Weld Join* 2012;17:202-6. doi:10.1179/1362171811Y.0000000094.
- [206] Patel VK, Bhole SD, Chen DL. Improving weld strength of magnesium to aluminium dissimilar joints via tin interlayer during ultrasonic spot welding. *Sci Technol Weld Join* 2012;17:342-7.
- [207] Tsujino J, Hidai K, Hasegawa a, Kanai R, Matsuura H, Matsushima K, et al. Ultrasonic butt welding of aluminum, aluminum alloy and stainless steel plate specimens. *Ultrasonics* 2002;40:371-4. doi:Pii S0041-624x(02)00124-5\nDoi 10.1016/S0041-624x(02)00124-5.
- [208] Xu L, Wang L, Chen Y-C, Robson JD, Prangnell PB. Effect of Interfacial Reaction on the Mechanical Performance of Steel to Aluminum Dissimilar Ultrasonic Spot Welds. *Metall Mater Trans A* 2015. doi:10.1007/s11661-015-3179-7.



# Dissemination

## Internationally indexed journals (*Web of Science, SCI, Scopus, etc.*)<sup>1</sup>

1. **M P Satpathy**, S K Sahoo, S Datta, "Optimization of tensile strength during ultrasonic lap welding of dissimilar metals using Taguchi's philosophy", *Applied Mechanics and Materials*, 2014, vol. 592, pp. 652-657.
2. **M P Satpathy**, S K Sahoo, S Datta, "Acoustic horn design and effects of process parameters on properties of dissimilar ultrasonic welding aluminium to brass", *Materials and Manufacturing Processes*, 2015, vol. 31(3), pp. 283-290.
3. **M P Satpathy**, S K Sahoo, "Microstructural and mechanical performance of ultrasonic spot welded Al-Cu joints for various surface conditions", *Journal of Manufacturing Processes*, 2016, vol. 22, pp. 108-114.
4. **M P Satpathy**, S K Sahoo, "Ultrasonic spot welding of dissimilar materials: characterization of welded joints and parametric optimization", *IOP Conf. Series: Materials Science and Engineering*, 2016, vol. 115, pp. 1-9.
5. **M P Satpathy**, S K Sahoo, "Parametric analysis on plastic deformation of materials during ultrasonic spot welding with different anvil geometries", *International Journal of Manufacturing Technology and Management*, 2015.
6. **M P Satpathy**, S K Sahoo, "An experimental investigation on joining of aluminum with steel using ultrasonic metal welding", *International Journal of Mechatronics and Manufacturing Systems*, 2016, vol. 9(4), pp. 299-309.
7. **M P Satpathy**, S K Sahoo, S.B Mishra, K D Mohapatra, "Interfacial characterization and mechanical properties of joint quality in ultrasonic welding of aluminum to brass", *Materials Today: Proceedings*, 2016.
8. **M P Satpathy**, B R Moharana, S Dewangan, S K Sahoo, "Modelling and optimisation of ultrasonic metal welding on dissimilar sheets using fuzzy based genetic algorithm approach", *Engineering Science and Technology, an International Journal*, 2015, vol. 18, pp. 634-647.
9. **M P Satpathy**, S K Sahoo, "Mechanical performance and metallurgical characterization of ultrasonically welded dissimilar joints", *Journal of Manufacturing Processes*, 2017, vol. 25, pp. 443-451

## Conferences<sup>1</sup>

1. **M P Satpathy**, S K Sahoo, "Ultrasonic Spot Welding of Dissimilar Metals: Mechanical Behaviour and Microstructural Analysis", 6th International & 27th All India Manufacturing Technology, Design and Research Conference (AIMTDR 2016), December 16-18, 2016, College of Engineering Pune, Pune.
2. **M P Satpathy**, S K Sahoo, A Pattanaik, S B Mishra, "Effect of process parameters on mechanical strength of Al-SS ultrasonic spot welded joint", 1st International Conference on Emerging Trends in Mechanical Engineering (ICETiME 2016), September 23-24, 2016, Faculty of Science and Technology, ICFAI Foundation of Higher Education (IFHE), Hyderabad.
3. **M P Satpathy**, S K Sahoo, S B Mishra, K D Mohapatra, "Mechanical properties and interfacial characterization of aluminum-brass joint in ultrasonic welding", ICEMS 2016, Jaipur National University, Jaipur.
4. **M P Satpathy**, S K Sahoo, "Mechanical properties and microstructural characterization of ultrasonic spot welded Al-Cu joints used for battery electric vehicles", 57<sup>th</sup> Annual Technical Session 2016, IEI, Bhubaneswar, Odisha.
5. **M P Satpathy**, S K Sahoo, "Characterization and parametric optimization of dissimilar material joints using Ultrasonic spot welding", NCPCM 2015, NIT Rourkela, Odisha.

6. **M P Satpathy**, K T Irshad, S K Sahoo, "Design and simulation of acoustic horn with booster used for used for lap welding of dissimilar materials", AMMA 2015, NIT Tiruchirappalli, Tamilnadu.
7. **M P Satpathy**, S K Sahoo, "Numerical Modelling of a novel horn and parametric optimization of ultrasonic welding process using desirability approach", NCPCM 2014, NIT Rourkela, Odisha.
8. **Mantra Prasad Satpathy**, Susanta Kumar Sahoo, Saurav Datta, "Desirability approach based Taguchi philosophy for optimization of weld strength in ultrasonic metal welding of dissimilar metals", IMEC2014, NIT Tiruchirappalli, Tamilnadu.
9. **M P Satpathy**, S K Sahoo, K C Nayak, "FEM simulation of ultrasonic stepped sonotrode used for plastic welding", AIS2013, IEI, Bhubaneswar, Odisha.

#### Article under preparation<sup>2</sup>

1. **M P Satpathy**, S K Sahoo, "Experimental and numerical studies on enhancement of weld quality using ultrasonic metal welding applied to dissimilar metals", *International Journal of Advanced Manufacturing Technology*.
2. **M P Satpathy**, S K Sahoo, "Temperature field Modeling in ultrasonic dissimilar metal welding: exploration of thermo-mechanical approach", *Journal of Manufacturing Science and Engineering*.
3. **M P Satpathy**, Abhisek, S K Sahoo, "Effect of brass interlayer sheet on microstructure and joint performance of ultrasonic spot welded copper-steel joints", *Journal of Materials Engineering and Performance*.
4. **M P Satpathy**, S K Sahoo, "Prediction of joint strength in ultrasonic spot welding process using regression and artificial intelligence methods", *Journal of Intelligent Manufacturing*.

---

<sup>1</sup>Articles already published, in press, or formally accepted for publication.

<sup>2</sup>Articles under review, communicated, or to be communicated.